





This is to certify that the  
dissertation entitled

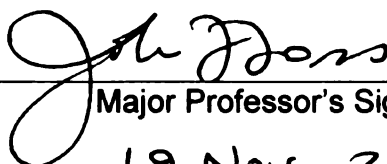
THE EFFECTS OF ROTATION ON THE FLOW FIELD OVER  
A CONTROLLED-DIFFUSION AIRFOIL

presented by

DOUGLAS R. NEAL

has been accepted towards fulfillment  
of the requirements for the

Doctoral degree in Mechanical Engineering



Major Professor's Signature

19 Nov. 2010

Date

*MSU is an Affirmative Action/Equal Opportunity Employer*

LIBRARY  
Michigan State  
University



**PLACE IN RETURN BOX** to remove this checkout from your record.  
**TO AVOID FINES** return on or before date due.  
**MAY BE RECALLED** with earlier due date if requested.

DATE DUE	DATE DUE	DATE DUE



THE EFFECTS OF ROTATION ON THE FLOW FIELD OVER A  
CONTROLLED-DIFFUSION AIRFOIL

By  
Douglas R. Neal

A DISSERTATION

Submitted to  
Michigan State University  
in partial fulfillment of the requirements  
for the degree of

DOCTOR OF PHILOSOPHY

Mechanical Engineering

2010



**ABSTRACT**

**THE EFFECTS OF ROTATION ON THE FLOW FIELD OVER A  
CONTROLLED-DIFFUSION AIRFOIL**

By  
**Douglas R. Neal**

An experiment has been designed, fabricated, instrumented and validated to study the effects of rotation on a controlled-diffusion (CD) cambered airfoil. This experiment, called the rotating CD blade, (RCDB) allows for detailed measurements of temperature, pressure and velocity to be collected using instrumentation that is: i) rotating with the blade and ii) stationary. The former provides time-resolved data in the rotating reference frame and the latter provides ensembles of values at designated positions with respect to the rotating blade. The RCDB was designed so that the operating conditions make it a true rotating analog of the stationary CD airfoil experiment and therefore suitable comparisons between the two experiments can be found. A second (and extensive) body of experimental data were obtained with the same airfoil shape fixed in open-jet wind tunnel configuration. Hence the comparative measurements reveal the effects of rotation, as well as other subtle geometric features, on the flow over the CD airfoil.

These comparative measurements have been carried out using conventional hot-wire anemometry (HWA) techniques and also particle image velocimetry (PIV). Additionally, a new measurement technique that utilizes four-sensor HWA probes in a double X-array (2X-probe) configuration has been developed and used in this study. A comprehensive methodology for both efficient calibration and high accuracy data processing of the 2X-probe has been developed. These techniques have been evaluated against other four-wire techniques that are found in the open literature and have subsequently been shown to have both a higher accuracy and a much lower computational time. The 2X-probe has been used in the wake of the stationary CD airfoil



and RCDB to provide detailed information on the three-dimensional flow field of the rotating and stationary experiments. The differences found between measurements collected with a conventional X-probe and similar measurements with a 2X-probe reveal the limitations of using two-dimensional measurement techniques in a three-dimensional flow field.

The data collected with the 2X-probe include the three components of velocity and also the full Reynolds stress tensor in the wake of the stationary and rotating experiments. These measurements reveal that the wake of the RCDB is initially more energetic (lower peak velocity deficit) and has a higher semi-width than the wake of the stationary CD airfoil. The wake of the RCDB is also shown to be slightly asymmetric upstream and it becomes increasingly asymmetric further downstream. In contrast, the wake of the CD airfoil is consistently symmetric at both upstream and downstream locations. Different rates decay rates for the peak velocity deficit were also found for the stationary CD airfoil and the RCDB. This study is the first to compare the flow fields of a stationary lift generating body and an equivalent body under rotation with equivalent operating conditions.



Copyright by

DOUGLAS RICHARD NEAL

2010

## DEDICATION

Dedicated to Karen and David, my mother and father, who always encouraged me to pursue my passions and have provided me considerable love and support throughout my entire life.



## ACKNOWLEDGMENTS

I would like to acknowledge Prof. John Foss, who has been an outstanding mentor and friend throughout much of my time at MSU. I have had the opportunity to work with him in several different capacities and each of those experiences have been extremely fulfilling. The attention he gives to all of his graduate students is truly unique and exceptional.

My other committee members Prof. Ahmed Naguib, Prof. Charles Petty and Prof. Farhad Jaberli have also been very influential in my career. I was fortunate enough to have each of them in the classroom and also interactions at conferences and other professional events. As a result, I learned a tremendous amount from each of them.

A very special thanks to Prof. Stéphane Moreau, who also served on my committee, but who is particularly important. His research vision made this project possible and without his support, this unique experiment would never have come to fruition. In addition to this work, I was fortunate to work with him while living in France, collaborate together at Stanford University, and publish numerous papers together. I have a huge amount of professional respect for him, but I am also pleased to call him a good friend.

A project as involved as this could also not have been accomplished by a single person. Manuel Henner, Aurélien Levasseur, and Bruno Demory at Valeo have worked diligently on the design of the RCDB. In particular I must acknowledge Bruno Demory for his true mastery with the 3D CAD.

Special thanks to Alan Lawrenz, who I have worked closely with throughout my time in the Turbulent Shear Flows Laboratory. I am continually amazed by the range of his skills - he is truly one of the best engineers I know. Work with him for even just an afternoon and you will see why the foreign students call him "MacGyver".

I have worked with a large number of undergraduates at MSU over the years. In particular, Andrew Cawood worked closely with me on much of the testing and implementation of the rotating CD blade experiment and also was a great help in the data processing. Also John Schultz, who makes the best hot-wire probes that I have ever seen! He also worked with me on sorting out the final comparisons with other published 4-wire techniques. There are other TSFL alumni who I have also enjoyed interacting with over the years including Kyle Bade, Aren Hellum and Scott Treat.

I would also like to acknowledge the extremely talented stream of students who have visited from various engineering schools in France, in particular ECAM. These students include J  r  my Servettaz, Philippe Rochat, J  r  me de Laborderie, J  r  me Genin, and Lo  c Paccard. Their attention to detail has really enabled this work.

The assistance of Stefan Reiber from Technische Universit  t Kaiserslautern in Germany was also an important part of this project. He worked with me on a significant portion of the data collection for my dissertation and his carefulness and attention to detail are greatly appreciated.

A very special thanks to Richard Prevost and Callum Gray of LaVision, Inc. for loaning me some of the equipment I would otherwise not have had at my disposal. Richard also took several days out of his busy schedule to lend his expertise in collecting PIV measurements in the RCDB experiment, which proved to be quite challenging.

I also wish to acknowledge Prof. Philippe Lavoie, whose work I discovered during this dissertation. I was quite pleased to also meet and become friends with the person behind that work.

Thanks to Michael Bilka for visiting for a summer from Belgium and working with me to derive the Reynolds stress equations in a cylindrical rotating coordinate system - can't beat a night of beer and formulas!

I would also like to acknowledge fellow fluid mechanician and kayaker Kristofer

Dressler. Discussions (both on the water and on dry land) with him have helped ease my mind and keep my focus. I always enjoy another good discussion on the physics of beer, paddling or turbulence.

Special thanks to James and Harriet Neal. Discussions with each of them inspired my continued interest in higher education and they have always shown a particular interest in my endeavors. James Neal also shares the distinction of being an MSU alumnus (M.S. 1959) and I will enjoy having another publication that shares a space in the MSU library alongside his thesis.

Finally, a very special thanks to Samantha Tank for showing me love and support during the writing process, which seemingly took twice as long as it should have. You showed up when I least expected it and I could not be happier!

# TABLE OF CONTENTS

<b>List of Tables</b> . . . . .	xii
<b>List of Figures</b> . . . . .	xiii
<b>Nomenclature</b> . . . . .	xxii
<b>1 Introduction</b> . . . . .	<b>1</b>
1.1 Motivation . . . . .	1
1.2 Stationary airfoils . . . . .	2
1.3 Rotating blades . . . . .	4
1.4 4-wire probe techniques for measuring turbulent flows . . . . .	7
1.5 Overview . . . . .	9
<b>2 Analysis</b> . . . . .	<b>10</b>
2.1 Effects of rotation on turbulent flow fields . . . . .	10
2.2 Low-speed airfoils . . . . .	15
2.3 Characteristics of the asymmetric wake of an airfoil . . . . .	17
<b>3 Design of the Rotating CD Blade (RCDB)</b> . . . . .	<b>19</b>
3.1 Initial design using radial equilibrium equations . . . . .	19
3.2 Modified design using computational fluid dynamics (CFD) . . . . .	24
3.3 RCDB Final Design . . . . .	28
<b>4 Experimental Apparatus and Methodologies</b> . . . . .	<b>37</b>
4.1 Controlled-diffusion (CD) airfoil . . . . .	37
4.1.1 CD airfoil configuration at the ECL . . . . .	37
4.1.2 CD airfoil configuration at MSU . . . . .	38
4.1.2.1 Coordinate system . . . . .	40
4.1.2.2 Reference pressure . . . . .	40
4.1.3 Surface pressure taps and RMPs . . . . .	40
4.1.4 Comparison of CD airfoil configuration at ECL and MSU . . . . .	42
4.2 Rotating CD Blade (RCDB) experimental configuration . . . . .	43
4.2.1 Axial Fan Research and Development (AFRD) facility . . . . .	43
4.2.2 Instrument cluster in the RCDB hub . . . . .	45
4.2.2.1 Slip ring . . . . .	45
4.2.2.2 Level 1: A/D board . . . . .	48
4.2.2.3 Level 2: Pressure and temperature mezzanine board . . . . .	48
4.2.2.4 Level 3: Hot-wire constant temperature anemometers . . . . .	50
4.2.2.5 Level 4: Pressure reference chamber . . . . .	50
4.2.3 Centrifugal correction for pressure transducers . . . . .	51



4.2.4	RCDB coordinate systems . . . . .	53
4.2.4.1	Conventional turbomachinery coordinates . . . . .	53
4.2.4.2	Rotated coordinates for comparisons with stationary CD airfoil . . . . .	55
4.2.5	Rotating hot-wire traverse . . . . .	55
4.3	Particle Image Velocimetry (PIV) . . . . .	57
4.3.1	CD Airfoil in the $0.61m \times 0.61m$ wind tunnel . . . . .	58
4.3.2	RCDB in the AFRD Facility . . . . .	60
4.4	Conventional Hot-wire Anemometry (SN-Probe and X-Probe) . . . .	62
4.4.1	Calibration . . . . .	62
4.4.2	Data reduction . . . . .	64
4.5	4-sensor HWA probe: The 2X-probe . . . . .	65
4.5.1	A new calibration strategy for the 2X-probe . . . . .	65
4.5.2	A new data reduction technique for the 2X-probe: MSU spline search . . . . .	70
<b>5</b>	<b>Results . . . . .</b>	<b>79</b>
5.1	Development of 2X-probe calibration and data reduction techniques .	79
5.1.1	Data reduction using only the cross calibration . . . . .	81
5.1.2	Data reduction using the TSFL Spline Search method . . . . .	86
5.1.2.1	Comparisons with published results . . . . .	86
5.1.3	Tests of elapsed time between cross and full calibrations . . . .	87
5.1.3.1	Same-day tests (0 elapsed days) . . . . .	87
5.1.3.2	Tests after 5 elapsed days . . . . .	92
5.1.3.3	Tests after 7 elapsed days . . . . .	92
5.2	Controlled-Diffusion (CD) Airfoil . . . . .	95
5.2.1	Inlet data . . . . .	95
5.2.2	Suction side boundary layer data . . . . .	96
5.2.3	Very near wake data . . . . .	105
5.2.4	Near and far wake data - mean velocity and related wake pa- rameters . . . . .	108
5.2.5	Near and far wake data - turbulence properties . . . . .	118
5.3	Rotating CD Blade (RCDB) . . . . .	127
5.3.1	Performance data ( $\Delta P$ vs. $\dot{m}$ ) . . . . .	127
5.3.2	Surface pressure ( $C_p$ ) data . . . . .	128
5.3.3	Phase-averaged mean velocity in the wake . . . . .	129
5.3.4	Phase-averaged turbulence properties . . . . .	141
5.3.5	Time-resolved turbulence properties from the rotating X-probe measurements . . . . .	146
5.4	Comparison of the Rotating CD Blade (RCDB) and the CD Airfoil .	148
5.4.1	Comparison of mean wake parameters . . . . .	148
5.4.2	Comparison of turbulence parameters . . . . .	153
5.5	Comparison of the measurements from the 1X and 2X probes . . . .	155
5.5.1	Comparison of measured velocities: 1X and 2X . . . . .	155

5.5.2	Uncertainty considerations: 1X and 2X . . . . .	160
<b>6</b>	<b>Conclusions . . . . .</b>	<b>165</b>
<b>A</b>	<b>Effect of probe quality on data reduction methodologies for 4-wire probes . . . . .</b>	<b>172</b>
	<b>References . . . . .</b>	<b>183</b>

## LIST OF TABLES

5.1	Total uncertainty on test data #1: 0 elapsed days . . . . .	92
5.2	Total uncertainty on test data #2: 5 elapsed days . . . . .	92
5.3	Total uncertainty on test data #3: 7 elapsed days . . . . .	94
5.4	Comparison of peak turbulence intensities at upstream and downstream locations (CD airfoil) . . . . .	122
5.5	Comparison of peak turbulence intensities at upstream and downstream locations (RCDB) . . . . .	143
5.6	Comparison of the peak turbulence intensities of the RCDB and CD airfoil . . . . .	154

## LIST OF FIGURES

Images in this dissertation are presented in color

1.1	Axial engine cooling fan - upstream view (left); side view (right). . . .	6
2.1	Relationship between inertial ( $X,Y,Z$ ) and rotating ( $x',y',z'$ ) coordinate systems. . . . .	11
2.2	Vector diagram of Coriolis and centrifugal forces. . . . .	13
2.3	Description of the laminar separation bubble on low-speed airfoils. . .	16
3.1	Stationary and rotating flow fields (left - RCDB; right - CD Airfoil). .	20
3.2	Vector diagram of relative ( $W$ ) and absolute ( $V$ ) inlet velocities for the RCDB. . . . .	21
3.3	Computational domain for the RCDB design. . . . .	25
3.4	Relative Inlet Velocity ( $W$ ) for RCDB from CFD simulations. . . . .	26
3.5	Exit radial velocity for RCDB (CFD simulations). . . . .	27
3.6	Calculated angle of incidence for the RCDB. . . . .	27
3.7	Inlet axial velocity for the RCDB (CFD simulations). . . . .	28
3.8	RCDB final design CAD (left - upstream view; right - downstream view).	29
3.9	RCDB final design installed (left - upstream view; right - downstream view). . . . .	29



3.10	RCDB rotor design showing modular capability. . . . .	30
3.11	The large and small anechoic wind tunnels at the Ecole Centrale de Lyon. . . . .	31
3.12	$C_p$ data showing the effect of the inlet jet width. . . . .	32
3.13	CFD simulations showing the velocity contours. . . . .	33
3.14	CFD RCDB $C_p$ data for various blade configurations. . . . .	33
3.15	Leading edge region showing the CFD RCDB $C_p$ data for various blade configurations. . . . .	34
3.16	Experimental RCDB $C_p$ data for various blade configurations. . . . .	36
3.17	$C_p$ data final RCDB configuration and the CD airfoil. . . . .	36
4.1	ECL Large Anechoic Wind Tunnel. . . . .	38
4.2	The free jet configuration for the CD airfoil (left - MSU, right - ECL). . . . .	39
4.3	Coordinate system used for the CD Airfoil experiments. . . . .	40
4.4	Location of Pitot tube used in CD airfoil experiments. . . . .	41
4.5	Locations of measurement stations on the CD airfoil. . . . .	42
4.6	CD Airfoil with RMP probes (pressure taps at mid-span region). . . . .	42
4.7	CD Airfoil $C_p$ data in the MSU and ECL wind tunnels). . . . .	43
4.8	The Axial Fan Research and Development (AFRD) Facility. . . . .	44
4.9	RCDB mounted in the AFRD (left - upstream view, right - downstream view . . . . .	45
4.10	RCDB instrument cluster . . . . .	46
4.11	Slip ring assembly (left - uninstalled, right - installed in the AFRD Facility) . . . . .	47
4.12	Pressure taps embedded into RCDB . . . . .	48

4.13	Allsensors MEMS-based pressure transducer . . . . .	49
4.14	Compact anemometers in RCBD instrument cluster . . . . .	50
4.15	Isobaric reference chamber in the RCDB . . . . .	51
4.16	Description of centrifugal correction terms . . . . .	54
4.17	Polar coordinate system typically used for turbomachinery studies . .	55
4.18	Coordinate system used for comparisons with CD airfoil data . . . . .	56
4.19	Rotating traverse assembly used for rotating X-probe measurements (see Sec. 4.2.5 for the legend entries A-E). . . . .	57
4.20	Close-up view of the fine positioning assembly of the rotating traverse.	58
4.21	Two measurement planes used for PIV experiments . . . . .	59
4.22	Left: PIV set-up for the CD Airfoil. Right: PIV set-up during data collection. . . . .	59
4.23	Reflected laser light near the CD airfoil trailing edge region . . . . .	60
4.24	PIV set-up for the RCDB in the AFRD Facility . . . . .	61
4.25	Left: $\Theta$ - $z$ plane for RCDB PIV data Right: $r$ - $z$ plane for RCDB PIV data . . . . .	61
4.26	Calibration facility for quasi-steady calibration on standard X-probes	63
4.27	Calibration data for $E_1$ and $E_2$ showing dependence on $\alpha$ . . . . .	64
4.28	2X-Probe (left - top view; right - side view) . . . . .	66
4.29	2X-probe calibration facility . . . . .	68
4.30	Description of indexing algorithm for creating the pseudo-full calibration	71
4.31	left - Cross calibration; right - Full calibration . . . . .	71
4.32	Mapping of $\Psi(\alpha, \beta)$ . . . . .	75

4.33 Spline search method. The initial guess is in the middle and neighboring knots are evaluated ("d" varies). . . . .	76
4.34 Left: Current location (K0) and neighbors (K1 & K2) Right: A lower value for $\Psi$ is found and K1 is the new location. . . . .	77
4.35 Neighboring vertical values of $\Psi$ are evaluated and K4 becomes the new location. . . . .	77
4.36 First diagonal check - location, K4 is retained since no lower value is found. . . . .	77
4.37 Second diagonal check - K6 is the new location. This cycle is repeated for multiple values of "d". . . . .	78
5.1 Joint-angle error plotting used for 2X-probe . . . . .	82
5.2 Pitch-yaw results for test data processed with a cross calibration ( $Q = 12$ m/s). . . . .	83
5.3 The effect of off-axis (bi-normal) cooling X-probe processing. . . . .	84
5.4 Overall uncertainty on the velocity magnitude for cross calibration. . . . .	85
5.5 Overall uncertainty on the yaw angle for cross-calibration. . . . .	86
5.6 Overall uncertainty on the pitch angle for cross calibration. . . . .	87
5.7 Pitch-yaw results for test data processed with TSFL Spline Search. . . . .	88
5.8 Overall uncertainty on the velocity magnitude for full calibration. . . . .	88
5.9 Overall uncertainty on the yaw angle for for full calibration. . . . .	89
5.10 Overall uncertainty on the pitch angle for full calibration. . . . .	89
5.11 Pitch-yaw results for test data #1: processed with cross calibration. . . . .	91
5.12 Pitch-yaw results for test data #1: processed with pseudo-full calibration (0 days elapsed between cross and full calibrations). . . . .	91
5.13 Pitch-yaw results for test data #2: processed with cross-calibration. . . . .	93

5.14 Pitch-yaw results for test data #2: 5 days elapsed between cross and full calibrations. . . . .	93
5.15 Pitch-yaw results for test data #3: processed with cross-calibration. .	94
5.16 Pitch-yaw results for test data #3: 1 week elapsed between cross and full calibrations. . . . .	95
5.17 Comparison of the inlet ( $x/c = -2.5$ ) velocity profiles for the MSU and ECL experiments. . . . .	96
5.18 Comparison of the freestream turbulence intensity profiles for the MSU and ECL experiments (measured at $x/c = -2.5$ ). . . . .	97
5.19 Measurement locations for boundary layer surveys above the RMP locations. . . . .	98
5.20 Normalized mean velocity profile at the RMP #5 location . . . . .	99
5.21 Normalized RMS velocity profile from HW data at the RMP #5 location.	99
5.22 Mean velocity profile at RMP #6 (HW data and LES). . . . .	101
5.23 Mean velocity profile at RMP #7 (HW data and LES). . . . .	101
5.24 Mean velocity data at RMP #7 fitted to the Blasius and Falkner-Skan solutions. . . . .	102
5.25 Mean velocity profile at RMP #9 (HW data and LES). . . . .	103
5.26 Mean velocity profile at RMP #11 (HW data and LES). . . . .	104
5.27 Mean velocity profile at RMP #21 (HW data and LES). . . . .	104
5.28 Composite of mean velocity profiles at the suction-side RMP locations.	105
5.29 Orientation of HW probe near the TE for near wake experiments (mm units on reference scale). . . . .	106
5.30 Coordinate system for near wake measurements. . . . .	107
5.31 Top view of HW probe traversing the near wake region. . . . .	107
5.32 Mean streamwise velocity profile in the near wake region . . . . .	108



5.33	Mean streamwise velocity profiles. . . . .	109
5.34	Mean streamwise velocity profiles, wake center aligned ( $n = y - y_c$ ). .	110
5.35	Close-up view of the velocity just outside the CD airfoil wake on the pressure side. . . . .	111
5.36	Explanation for increasing velocity on the pressure side of the CD airfoil.	111
5.37	Mean transverse velocity profiles ( $n = y - y_c$ ). . . . .	112
5.38	Mean spanwise velocity profiles ( $n = y - y_c$ ). . . . .	113
5.39	Self-similarity for the mean velocity profiles of the CD airfoil. . . . .	114
5.40	Decay of the wake centerline velocity defect for the CD airfoil. . . . .	115
5.41	Momentum thickness and shape factor for the CD airfoil. . . . .	117
5.42	PIV data showing the normalized velocity magnitude. . . . .	118
5.43	Streamwise turbulence intensity ( $n = y - y_c$ ). . . . .	119
5.44	Transverse turbulence intensity ( $n = y - y_c$ ). . . . .	120
5.45	Spanwise turbulence intensity profiles ( $n = y - y_c$ ). . . . .	120
5.46	Instantaneous PIV data for the CD airfoil . . . . .	121
5.47	Streamwise velocity spectra in CD airfoil wake at $x/c = 0.075$ . . . . .	122
5.48	$\overline{u'v'}$ shear stress distribution ( $n = y - y_c$ ). . . . .	123
5.49	Wake half-width based on $\left  \overline{u'v'}/U_\infty^2 \right  > 0$ . . . . .	124
5.50	Sketch of the unstable condition for $\overline{u'v'}$ region in curved streamlines.	126
5.51	$\overline{u'w'}$ shear stress distribution ( $n = y - y_c$ ). . . . .	126
5.52	$\overline{v'w'}$ shear stress distribution ( $n = y - y_c$ ). . . . .	127
5.53	Performance data ( $\Delta P$ vs. $\dot{m}$ ) for the 3-blade RCDB configuration. .	128

5.54	Comparison of the $C_p$ distributions for various RCDB configurations.	129
5.55	Locations of wake velocity surveys for the RCDB experiments. . . . .	131
5.56	Phase-averaged $\langle u \rangle$ data for all 3 blades of the RCDB experiment (wakes are indicated by the arrows). . . . .	131
5.57	Data used to determine the location of the RCDB trailing edge. . . .	133
5.58	Phase-averaged $\langle u \rangle$ data for a single blade of the RCDB experiment. .	133
5.59	Phase-averaged $\langle u \rangle$ for a single blade wake at multiple downstream locations. . . . .	134
5.60	RCDB wake PIV data in the absolute velocity frame. . . . .	135
5.61	Relationship between the absolute and relative reference frame veloci- ties in the RCDB. . . . .	136
5.62	RCDB wake PIV data in the relative velocity frame. . . . .	137
5.63	Wake-centered phase-averaged $\langle u \rangle$ for a single blade wake ( $n = r\theta - r\theta_c$ ). 138	
5.64	Phase-averaged $\langle v \rangle$ for a single blade wake ( $n = r\theta - r\theta_c$ ). . . . .	138
5.65	Phase-averaged $\langle w \rangle$ in the wake of a single blade ( $n = r\theta - r\theta_c$ ). . . .	139
5.66	Close-up view of the phase-averaged $\langle w \rangle$ in the wake of a single blade ( $n = r\theta - r\theta_c$ ). . . . .	140
5.67	Similarity for the mean velocity profiles of the RCDB. . . . .	141
5.68	Phase-averaged streamwise turbulence intensity in the wake . . . . .	143
5.69	Phase-averaged transverse turbulence intensity in the wake of a single blade ( $n = r\theta - r\theta_c$ ). . . . .	144
5.70	Phase-averaged radial (spanwise) turbulence intensity in the wake of a single blade ( $n = r\theta - r\theta_c$ ). . . . .	144
5.71	Phase-averaged Reynolds shear stress in the wake of a single blade ( $n = r\theta - r\theta_c$ ). . . . .	145

5.72	Phase-averaged Reynolds shear stress $\langle u'w' \rangle$ in the wake of a single blade ( $n = r\theta - r\theta_c$ ). . . . .	145
5.73	Phase-averaged Reynolds shear stress in the wake of a single blade ( $n = r\theta - r\theta_c$ ). . . . .	146
5.74	Streamwise velocity spectra in RCDB wake at $z/c = 0.05$ . . . . .	147
5.75	Streamwise velocity profiles. (left - CD airfoil, right - RCDB). . . . .	150
5.76	RCDB wake PIV data - relative velocity in $(x/c, y/c)$ coordinates. . .	150
5.77	Location of the wake centerline: RCDB & CD . . . . .	151
5.78	Wake semi-width for the RCDB and CD airfoil. . . . .	152
5.79	Decay of wake centerline velocity defect: RCDB & CD . . . . .	153
5.80	Momentum Thickness for the CD and RCDB. . . . .	154
5.81	Streamwise velocity profiles for the CD airfoil measured by the 1X and 2X-probes ( $n = y - y_c$ ). . . . .	158
5.82	Transverse velocity profiles for the CD airfoil measured by the 1X and 2X-probes ( $n = y - y_c$ ). . . . .	159
5.83	Streamwise turbulence intensity profiles for the CD airfoil measured by the 1X and 2X-probes ( $n = y - y_c$ ). . . . .	160
5.84	Streamwise turbulence intensity profiles for the CD airfoil measured by the 1X and 2X-probes ( $n = y - y_c$ ). . . . .	161
5.85	Effect of measurement uncertainties on $\bar{u}$ data collected with a 1X and 2X-probe. . . . .	163
5.86	Effect of measurement uncertainties on $\bar{v}$ data collected with a 1X and 2X-probe. . . . .	164
A.1	Close-up view of 2X-probe with “S-wire” defect. . . . .	173
A.2	Pitch-yaw results for test data processed with TSFL Spline Search using the probe shown in Fig. A.1. . . . .	174

A.3	Close-up view of 2X-probe with improved sensor mounting (note the absence of the “S-wire” defect seen in Fig. A.1)	174
A.4	Pitch-yaw results for test data processed with TSFL Spline Search using the probe shown in Fig. A.3	175
A.5	Comparison of pitch-yaw results for test data processed with TSFL Spline Search. Left: Original wire-mounting, Right: Improved wire-mounting.	176

## NOMENCLATURE

### Roman symbols

$A$	calibration coefficient for a hot-wire sensor (see Fig. 4.12)
$B$	calibration coefficient for a hot-wire sensor (see Fig. 4.12)
$C_p$	mean pressure coefficient = $(p_s - p_r)/\frac{1}{2}\rho U_\infty^2$
$E$	voltage
$L$	wake semi-width
$P$	pressure
$Q$	convective cooling velocity as measured by a hot-wire sensor
$U_1$	RCDB rotational speed for inlet velocity triangle (see Fig. 3.1)
$U_e$	wake edge velocity
$U_\infty$	freestream velocity upstream of the CD airfoil
$V_1$	RCDB inlet velocity in the stationary reference frame (see Fig. 3.1)
$\vec{V}_{a/b}$	velocity of the air with respect to the blade
$\vec{V}_{a/g}$	velocity of the air with respect to the ground
$\vec{V}_{b/g}$	velocity of the blade with respect to the ground
$V_r, V_\theta, V_z$	velocity components in a polar coordinate system
$W_1$	RCDB inlet velocity in the rotating reference frame (see Fig. 3.1)
$W_\infty$	freestream velocity (rotating reference frame) upstream of the RCDB
$l_p$	wake semi-width on pressure side
$l_s$	wake semi-width on suction side
$n$	calibration coefficient for a hot-wire sensor (see Fig. 4.12)
$p_e$	effective pressure (see Eq. 2.5 on pg. 13)
$u, v, w$	velocity components in a Cartesian coordinate system
$x', y'$	rotated coordinate system at trailing edge (see Fig. 5.30)

## Greek symbols

$\Psi$	Minimization parameter for 2X-probe data reduction (see Fig. 4.16)
$\Omega$	rotational speed measured in RPM (revolutions per minute)
$\alpha$	yaw angle for 2X-probe
$\alpha_g$	geometric angle of attack
$\beta$	pitch angle for 2X-probe
$\gamma$	yaw angle for 1X-probe
$\delta^*$	displacement thickness
$\theta$	momentum thickness
$\vartheta$	total uncertainty (see Eq. 5.3)
$\rho$	density
$\omega$	rotational speed measured in rad/s

## Other notations

$\langle x \rangle$	phase-averaged quantity
$\bar{x}$	time-averaged quantity



# Chapter 1

## Introduction

### 1.1 Motivation

Axial fans are utilized in an exceptionally wide range of applications. Adequate performance of such fans can be gained with relatively unsophisticated design tools. However, as reduced aeroacoustic emissions and higher efficiencies are sought, a much better understanding of the fundamental flow physics for these fans must be established. This study was carried out to further improve this basic understanding.

The focus of the work is to explore the differences between the flow field around a stationary lift generating body and that of a similar body under rotation. The selected geometry is a controlled diffusion (CD) airfoil designed by Valeo. The CD airfoil is the shape that is found at the mid-span region of axial turbomachinery (cooling fans) designed by Valeo and this profile is used for the pitchline (chord line at the designated angle of attack) analysis in their preliminary design process. Controlled diffusion airfoils are a class of cambered airfoils that employ specific design characteristics to carefully control the flow around the airfoil surface. The term *diffusion*, which is also referred to as *aerodynamic diffusion*, describes the general process that occurs when a subsonic fluid enters a region of increasing flow area. As the flow area increases, the

velocity of the fluid will decrease and the static pressure will increase. This exchange of fluid velocity (kinetic energy) for static pressure rise (flow work) is commonly called diffusion, as in the term “diffuser”. If the process occurs at a constant total pressure and constant density, this exchange can be computed by the well-known Bernoulli equation. Otherwise compressible flow equations must be used (see the chapter by Wisler in Johnson (1998)). Controlled diffusion airfoils have their camber and thickness distributions tailored to avoid boundary layer separation on the suction surface by controlling diffusion (deceleration) from the peak velocity point to the trailing edge (Johnson, 1998; Gelder *et al.*, 1987).

The reduction of noise emitted by an axial fan is a major objective in the design process of fans that are used in an automotive engine cooling system, along with other fans such as those used to cool electronic components (Moreau *et al.*, 2006c). The noise generated by the scattering of boundary layer disturbances past the trailing edge, called trailing edge noise or broadband self-noise, is a major source of the overall noise generated by fans (Sharland, 1964; Wright, 1976; Fukano *et al.*, 1977; Caro & Moreau, 2000), wind turbines (Glegg *et al.*, 1987; Hubbard & Shepherd, 1991; Parchen *et al.*, 1999), and other high lift devices (Pérennès & Roger, 1998; Singer *et al.*, 2000). This noise can be reduced or controlled by properly identifying the sources of self-noise and modifying the associated design parameters that affect these noise sources.

## 1.2 Stationary airfoils

Trailing edge noise sources have been studied primarily through the use of nominally two-dimensional airfoils in open-jet anechoic tunnels (Arbey & Bataille, 1983; Blake, 1975; Brooks & Hodgson, 1981; Schlinker & Amiet, 1981; Roger & Moreau, 2004; Moreau & Roger, 2005). The experimental studies have focused on incident velocity fluctuations, wall pressure fluctuations, and far field sound. One study (Moreau

*et al.*, 2006a) describes details of the velocity profile in the airfoil wake. Sophisticated computational methods of trailing edge aeroacoustics have involved the use of Large Eddy Simulations (LES) (Wang & Moin, 2000; Manoha *et al.*, 2001; Oberai *et al.*, 2002); however the large computational costs of LES have limited previous studies to simplified devices like airfoils. Since it is too costly to do an extensive experimental campaign or a computationally expensive unsteady Navier Stokes simulation in an industrial design cycle, there has been a focus on developing analytical noise models based on the acoustic analogies. This approach uses limited data in the near-field of the airfoil to predict the far-field acoustic data. Several of these models were developed and reviewed by Howe (Howe, 1978). These models evolved in complexity and accuracy with the availability of Reynolds Averaged Navier Stokes (RANS) simulations used in conjunction with acoustic analogies (Casper & Farassat, 2004; Zhou & Joseph, 2007). However, studies that compared measurements in the near wake to CFD simulations showed that commonly-used turbulence closure models did not adequately account for important characteristics of the wake (Hah & Lakshminarayana, 1982). These types of analytical noise models have been applied by only a few researchers for rotating blades (Zhou & Joseph, 2006; Schlinker & Amiet, 1981; Moreau & Roger, 2007).

Airfoil trailing edge studies that employ an open-jet wind tunnel configuration have different boundary conditions than other trailing edge airfoil studies, such as isolated airfoil studies (Hah & Lakshminarayana, 1982) or cascade studies (Raj & Lakshminarayana, 1973). The airfoil in the open-jet wind tunnel will have a blade loading and a wake that are influenced by the jet width (Moreau *et al.*, 2003, 2006a). In these experiments, the bounding shear layers at the edges of the jet are deflected by the lift associated with the flow over the airfoil. In contrast, isolated airfoil experiments involve mounting the airfoil in the closed test section of the wind tunnel. Here the effect of the lift will be manifest in the surface pressure distribution on the

bounding walls of the wind tunnel. In this case, the opposing surfaces provide the upper and lower boundary condition for the far-field region on the pressure and suction side of the airfoil. Cascade studies also differ from both of the above experimental configurations since they have an airfoil (with identical shape and incidence angle) for the upper and lower bounding surfaces. Therefore, the use of open-jet airfoil configurations to validate trailing edge noise models requires extensive experimental data that can provide the required details of the flow field. To date, there exist very few studies that can provide these necessary details.

### 1.3 Rotating blades

A recent study (Rozenberg, 2007) has begun to validate analytical models for rotating blades. These results have focused primarily on the pressure on the surface of the blade using microphones. This study did not examine the details of the turbulent velocity field in the vicinity of the rotating blade. The proper validation of these models does require detailed data of the trailing edge region and the downstream wake. However, a number of studies have measured the detailed velocity field in the near wake of an axial turbomachine (Raj & Lakshminarayana, 1976; Reynolds *et al.*, 1980; Ravindranath & Lakshminarayana, 1980, 1981). Yet these studies lack a comparable stationary analog by which the effects of rotation can be evaluated. Lakshminarayana & Reynolds (1980) present data for an axial turbomachine, based on a symmetric NACA 0012 and compared these results with the isolated airfoil (NACA 0012) study of Hah & Lakshminarayana (1982). The authors used a triaxial hot-wire probe in the rotating reference frame and provide some results for the mean flow and turbulence statistics in the wake. Another study by Lakshminarayana *et al.* (1982) studied an axial turbomachine at three different rotational speeds and two different blade loadings. The authors also use a triaxial probe, but in the stationary

reference frame, to collect phase-averaged data in the wake. This study showed the combined effects of rotation and Reynolds number on the wake, although the authors claim the effects of Reynolds number should be small in the range of Reynolds number employed in their experiments. They also note that it is difficult to separate these effects (rotation and Reynolds number) in turbomachinery (Lakshminarayana *et al.*, 1982). Raj & Lumley (1978) conducted an analytical study of the mean flow and turbulent characteristics of axial turbulent wakes behind a rotating fan. Their results show the additional Coriolis terms that appear when the equations for the components of the Reynolds stress are derived in coordinate system rotating with the fan.

The review article by (Johnston, 1998) and also chapter 14 in the handbook of Tropea *et al.* (2007) provide a good overview of the experimental and numerical studies conducted on the effects of rotation relevant to turbomachinery. In particular, (Johnston, 1998) notes that “although some excellent data sets have been obtained by means of laser anemometry in real compressor and turbine rotors, these flow fields are too complex to allow for the study of the basic physical phenomena systematically, one at a time”. Consequently basic research investigations have made use of geometrically simple flows. These investigations have used a variety of experimental techniques and also direct numerical simulation (DNS) of the Navier-Stokes (N-S) equations. The simple geometries studied to-date include: developed and developing channel flows (Johnston *et al.*, 1972), turbulent boundary layers in straight channels (Koyama *et al.*, 1979; Watmuff *et al.*, 1985; Koyama *et al.*, 1995), boundary layer transition in straight channels, plane walled (2D) diffusers focusing on the region between separation and reattachment (Rothe & Johnston, 1979), curved wall (2D) diffusers, pipes and conical diffusers, and free shear layer flows (Witt & Joubert, 1985). A recent study by Di Sante *et al.* (2008) measured the effects of rotation on channel flow, using high-speed particle image velocimetry (PIV) techniques in the rotating reference frame to measure the instantaneous relative velocity field. Despite the numerous papers in this

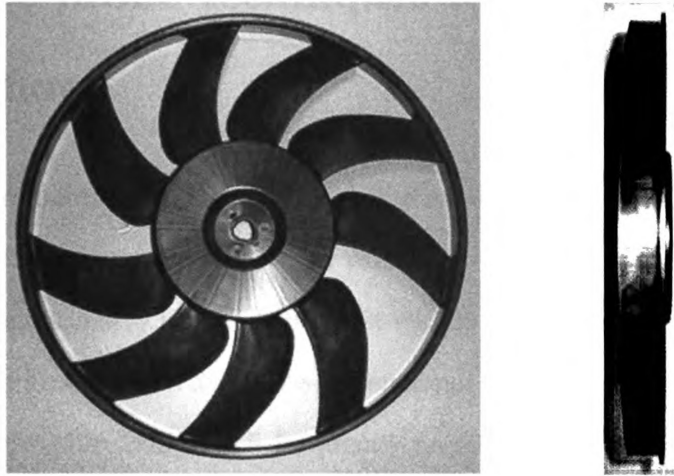


**Figure 1.1:** Axial engine cooling fan - upstream view (left); side view (right).

general area, there exists a need for a comprehensive study that can examine, in detail, the flow field associated with a stationary lift-generating body and an equivalent rotating body.

The focus of this work is to thoroughly study the turbulent flow field around the stationary CD airfoil and then compare these results with a rotating version of the same blade profile. A unique experiment, called the rotating CD blade (RCDB) has been designed, built, instrumented and evaluated specifically for the purpose of having a rotating analog of the stationary CD airfoil. The RCDB experiment represents one additional step of complexity between an airfoil and a modern axial turbomachine. This allows for the effect of rotation to be separated from other complexities that are added in the design process, which begins with the CD airfoil and ends up as a modern axial turbomachine as shown in Fig. 1.1. These complexities include blade sweep (either forward or backward), variable chord length, variable chord shape, and modifications to the tip region, such as the addition of a banded ring at the maximum radius of the blades.

## 1.4 4-wire probe techniques for measuring turbulent flows

Accurate measurements in the wake of either a stationary airfoil or a rotating blade require experimental equipment that can reliably resolve the three-dimensional flow field. Hot-wire anemometry is one of the most widely used techniques for the measurement of turbulent flows, which are three-dimensional in nature. Hot-wire anemometry is relatively inexpensive, has a high frequency response and unlike laser-based diagnostics, does not require the addition of particles in the flow field to measure the velocity. The most commonly used probes, single-normal (SN) probes, and crossed-wire (X) probes, can reliably measure one and two-components of velocity (Bruun, 1995). These probes are sensitive to bi-normal cooling effects caused by off-axis velocity fluctuations that cannot be resolved by these probes, as documented by Tutu & Chevray (1975); Ovink *et al.* (2001) and most recently by Zhao & Smits (2006). Extensive efforts have been made to develop a probe that can simultaneously measure three components of velocity. Initial efforts focused on the use of three-wire probes and numerous studies have used these probes in the near wake region of airfoils and turbomachinery (Lakshminarayana & Reynolds, 1980; Lakshminarayana *et al.*, 1982). However, four wire probes are preferred over three wire probes since they have been shown to be more accurate and also they have a larger acceptance domain, which is the range of incoming velocity angles that can be reliably resolved (Maciel & Gleyzes, 2000). Researchers have both developed their own versions of the four wire probe and there are also commercially available models.

Four-sensor hot-wire probes require that four separate voltage signals must be reduced to a three component velocity vector by solving a set of four non-linear, over-determined equations. Note that this calculation is considerably more difficult than standard (one or two sensor) hot-wire techniques. These data reduction schemes are

typically based on analytical equations or they employ look-up table methods. These data reduction schemes have been explored by a number of researchers (Döbbeling *et al.*, 1990a,b; Marasli *et al.*, 1993; Wittmer *et al.*, 1998; Beharelle, 1999; Maciel & Gleyzes, 2000). An overview of many of the techniques for four-sensor probe measurements was described by Maciel & Gleyzes (2000). Depending on the assumptions that are implicit in the various reduction schemes and also which pieces of information are used, it is reasonable to expect that variations in accuracy will be experienced. A detailed study was undertaken by Lavoie & Pollard (2003) to determine the differences in the accuracy of four different data reduction schemes that were published in the literature (and also referenced above). They reported the accuracy of these four data reduction schemes using experimental data available in the literature and also using LES data for a free, round jet.

A custom-designed four wire probe was designed and fabricated by the Turbulent Shear Flows Laboratory (TSFL) for use in the present work and also other studies. This probe has previously been used by Dusel (2005) to make measurements of the flow field of a cooling fan from an off-highway vehicle. He used a calibration and data reduction scheme similar to that of Rajagopalan *et al.* (1998). The errors associated with this data reduction scheme are evaluated and the effects of bi-normal cooling are quantified. A new calibration method has been developed for use with four-sensor probes and its efficacy is presented. A new data reduction scheme has also been developed and tested using the methods established in Lavoie & Pollard (2003). This data reduction scheme is compared with two of the published approaches (Döbbeling *et al.*, 1990b; Wittmer *et al.*, 1998) described above and its accuracy and computational time are compared and contrasted. Together, this new calibration and data reduction scheme provide a comprehensive technique for four-wire calibration and data processing.



## 1.5 Overview

This document is divided into six chapters. Chapter 2 presents the necessary background that brings together the characteristics of rotating flows and also low-speed airfoils. Chapter 3 provides the details of the design of the rotating CD blade (RCDB) experiment, along with the validation data that show it truly is the rotating analog of the stationary CD airfoil experiment. Chapter 4 describes the experimental facilities and specialized equipment, much of which was custom-designed, that was used for these experiments. Chapter 4 also describes the calibration and data reduction methodologies that were developed for the 4-wire probe used in these experiments. Chapter 5 presents the following results:

1. A detailed comparison of the calibration and data reduction methodologies developed in this dissertation vs. existing techniques found in the literature.
2. Measurements on the suction side boundary layer of the stationary CD airfoil.
3. Data in the wake of the stationary CD airfoil measured using the methodologies in (1).
4. Data in the wake of the rotating CD blade (RCDB) measured using measured using the methodologies in (1).
5. Comparisons between the data in the wake of the stationary CD airfoil and the wake of the RCDB.
6. Comparisons between data collected using a 2X-probe and a 1X-probe.

Finally, these results are concluded in Chapter 6 along with an overview of future measurement possibilities for the RCDB facility. Appendix A presents a very important finding, discovered during the course of this work, related to the effect of probe quality on the results presented in Chapter 5.

# Chapter 2

## Analysis

### 2.1 Effects of rotation on turbulent flow fields

Rotating flows are encountered in many applications of interest in engineering fluid mechanics. In many of these applications (e.g. compressors, turbines, pumps), system rotation is a critical aspect of the design and the performance. The vast majority of engineering applications have the dynamical system cast in an inertial reference frame. However, the flow fields of rotating machinery are most conveniently studied in a rotating reference frame, where the coordinates are fixed to the rotating blade. These coordinate systems can be related in the following manner. Consider a rotating reference frame which moves with velocity  $\vec{U}_o$  and accelerates with  $\vec{a}_o$  relative to the inertial reference frame. Velocities in the rotating reference frame,  $\vec{U}$  can be related to the velocities in the inertial reference frame  $\vec{U}_I$  according to:

$$\vec{U}_I = \vec{U}_o + \vec{\Omega} \times \vec{r} + \vec{U} \quad (2.1)$$

$\vec{\Omega}$  is the angular velocity vector that indicates the rate of rotation and the direction of the moving reference frame. The time rate-of-change of  $\vec{U}_I$ , i.e. the acceleration

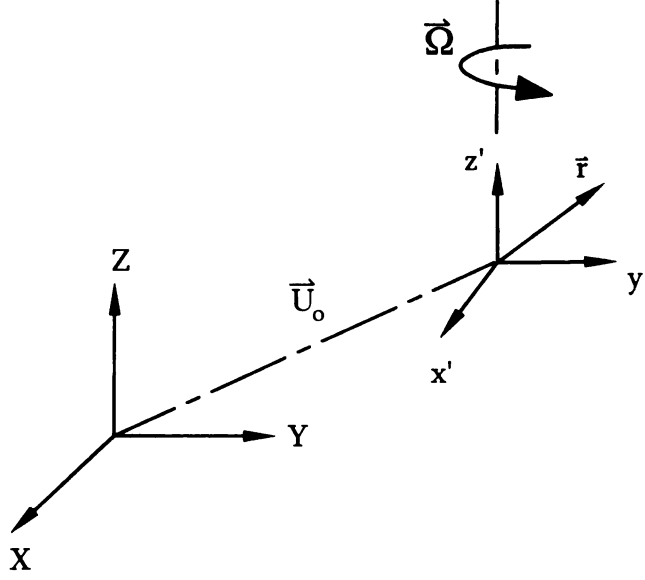


**Figure 2.1:** Relationship between inertial  $(X, Y, Z)$  and rotating  $(x', y', z')$  coordinate systems.

$\vec{a}_I$  can be written as:

$$\vec{a}_I = \vec{a}_o + \vec{\Omega} \times \vec{r} + \vec{\Omega} \times (\vec{\Omega} \times \vec{r}) + \underbrace{2\vec{\Omega} \times \vec{U}}_{\text{Coriolis acceleration}} + \vec{a} \quad (2.2)$$

Eqs. 2.1 and 2.2 represent kinematic relationships which are essential for describing flows in rotating reference frames. The present analysis will consider a steady angular velocity,  $\Omega$ , about the axis of a turbomachine in a rotating reference frame. Additionally, several simplifying assumptions can be made:

- **Incompressible flow.** This assumption means that  $D\rho/Dt = 0$ , which further implies low Mach number flows for air ( $M \leq 0.3$ ) at standard atmospheric conditions ( $T = 293.15$  K and  $P_{abs} = 101.325$  KPa).
- **Fixed rotation axis.** The rotation axis can be changing in geophysical flows, but turbomachinery flows almost invariably involve a fixed rotation axis.
- **Unstratified flow.** No stratifications due to temperature variations are consid-

ered. In water flows, salinity, in addition to temperature variations, can cause stratifications.

- Body forces such as gravity, magnetic and electric fields are not considered. These can be of primary importance in some problems, such as astrophysical flows.

The dynamic equation of motion for a fluid particle in a rotating reference frame can be written as (Johnston 1998):

$$\frac{D\vec{U}}{Dt} = 2\vec{U} \times \vec{\Omega} + \nabla \frac{\Omega^2 r^2}{2} - \frac{\nabla p}{\rho} + F_{vis} \quad (2.3)$$

These equations are the well-known Navier-Stokes equations and relate the forces (per unit volume) acting on a fluid particle to the motion of the fluid. The term on the left-hand side represents the acceleration of the fluid particle with respect to the rotating reference frame and the four terms on the right-hand side represent the forces per unit mass: Coriolis, centrifugal, pressure and viscous. The Coriolis and centrifugal forces are “virtual” forces that result from the rotating reference frame, whereas the pressure and viscous forces are felt by the fluid particle in any reference frame. The last term, the viscous force per unit mass, can be written as:

$$F_{vis} = \nu \nabla^2 \vec{U} \quad (2.4)$$

for the incompressible, constant viscosity, Newtonian fluid described by the Navier-Stokes equations. The kinematic viscosity is defined as  $\nu = \mu/\rho$ . The centrifugal force acts along the local radial direction and has a magnitude of  $\Omega^2 r$ , as seen in Fig. 2.2. The Coriolis force has a magnitude of  $2U\Omega \sin \alpha$  and is perpendicular to the plane formed by the  $\vec{U}$  and  $\vec{\Omega}$  vectors. Its vector direction follows the right-hand rule and is oriented as shown in Fig. 2.2. The angle between  $\vec{U}$  and  $\vec{\Omega}$ , shown as

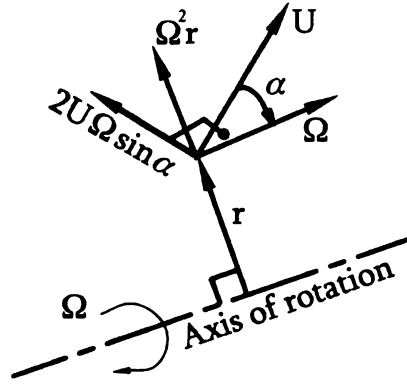


**Figure 2.2:** Vector diagram of Coriolis and centrifugal forces.

$\alpha$  in Fig. 2.2, can range between 0 and  $\pi/2$ . The effect of the Coriolis force will vary depending on the angle between the various velocity components and the axis of rotation. For a velocity component that is parallel to the axis of rotation (axial component, the magnitude of this force will be zero). The radial component will be maximally affected, since it will be perpendicular to this force. In radial flow turbomachines, these effects can be very large.

For flows where  $\rho$  is constant, the centrifugal force can be combined with the pressure force term to form a single term,  $-\nabla(p_e/\rho)$ , where  $p_e$  is called an “effective pressure” Johnston (1998) and is defined by:

$$p_e = p + \frac{\rho(\Omega^2 r^2)}{2} \quad (2.5)$$

The resulting Navier-Stokes equations now become:

$$\frac{D\vec{U}}{Dt} = 2\vec{U} \times \vec{\Omega} - \frac{\nabla p_e}{\rho} + \nu \nabla^2 \vec{U} \quad (2.6)$$

Eq. 2.6 shows that the centrifugal force plays no independent role in the dynamics of motion. Johnston (1998) notes that where density gradients,  $\nabla \rho$ , exist in the

flow, the centrifugal force is similar to a gravitational body force. It is interesting to note that the Coriolis force does not directly affect the energy of the flow in an axial turbomachine (Godeferd & Lollini, 1999). The change of energy in a fluid particle is created by the applied force,  $\vec{F}$ , across some distance  $d\vec{x}$ , given by the work relationship  $\vec{F} \cdot d\vec{x}$ . Since the flow moves instantaneously in the rotating reference frame along the vector  $\vec{U}$ , which is perpendicular to the Coriolis force vector, there can be no work done on the flow by the Coriolis force and subsequently no energy brought to the flow. It follows that both the mean flow and the turbulence kinetic energy,  $k$ , cannot be produced or destroyed by the Coriolis force. However, the individual components of the Reynolds stress tensor,  $-\overline{u'_i u'_j}$ , can be affected by this force (Johnston, 1998). The evolution equations for the normal Reynolds stresses ( $-\overline{u' u'}$  and  $-\overline{v' v'}$ ) will have explicit Coriolis production terms which cancel out when they are summed up to obtain the equation for the turbulent kinetic energy. The equation for the Reynolds shear stress,  $(-\overline{u' v'})$ , also does not have a direct Coriolis production term. Here, the effects of Coriolis come indirectly through its effects on  $(-\overline{u' u'}$  and  $-\overline{v' v'})$ . Raj & Lumley (1978) derived these terms for a low-speed axial fan in rotating coordinates and the complete Reynolds stress equations can be found there.

A common practice in fluid mechanics is to cast the equations of motion in a non-dimensional form. This is accomplished by introducing a characteristic length scale,  $L$  and a characteristic velocity,  $U$ . All pressures can be normalized by  $\rho U^2$  and a characteristic time  $L/U$  is introduced. Noting that  $\nabla^* = L\nabla$ , the Navier-Stokes now become:

$$\frac{D\vec{U}^*}{Dt^*} = -Ro \vec{e}_\Omega \times \vec{U}^* - \frac{\nabla^* p_e^*}{\rho} + \frac{1}{Re} \nabla^{*2} \vec{U}^* \quad (2.7)$$

Where all the independent and dependent variables are dimensionless through the aforementioned scales and denoted by (\*). The unit vector  $\vec{e}_\Omega$  indicates the direc-

tion of the axis of rotation of the reference frame. In the form shown in Eq. 2.7, two important dimensionless numbers are introduced, one of which is the Reynolds number:

$$Re = \frac{\rho LU}{\mu} \quad (2.8)$$

The Reynolds number includes the fluid properties and the length and velocity scales for a particular problem. Since flows in rotating reference frames are affected by the Coriolis force, rotating flows are characterized by the Reynolds number and another dimensionless parameter, the rotation number:

$$Ro = \frac{2|\Omega|L}{U} \quad (2.9)$$

The rotation number is defined so that for a non-rotating case ( $\Omega = 0$ ),  $Ro = 0$ . References on rotating flows will often cite the Rossby number:

$$Ros = \frac{U}{2|\Omega|L} \quad (2.10)$$

It can be seen that the Rossby number is the reciprocal of the rotation number,  $Ro = Ros^{-1}$ . The use of the rotation number is more common for turbomachinery applications and other engineering fluid mechanics studies involving rotation.

## 2.2 Low-speed airfoils

Low-speed airfoils, which are typically considered to be those with Reynolds number based on chord of well below 500,000, have been studied extensively. Lissaman (1983) provides a comprehensive review article, and several of the features of the fundamental fluid mechanics are described here. Since all airfoils provide lift, they correspondingly have regions of low-pressure on the suction side of the airfoil. These low-pressure

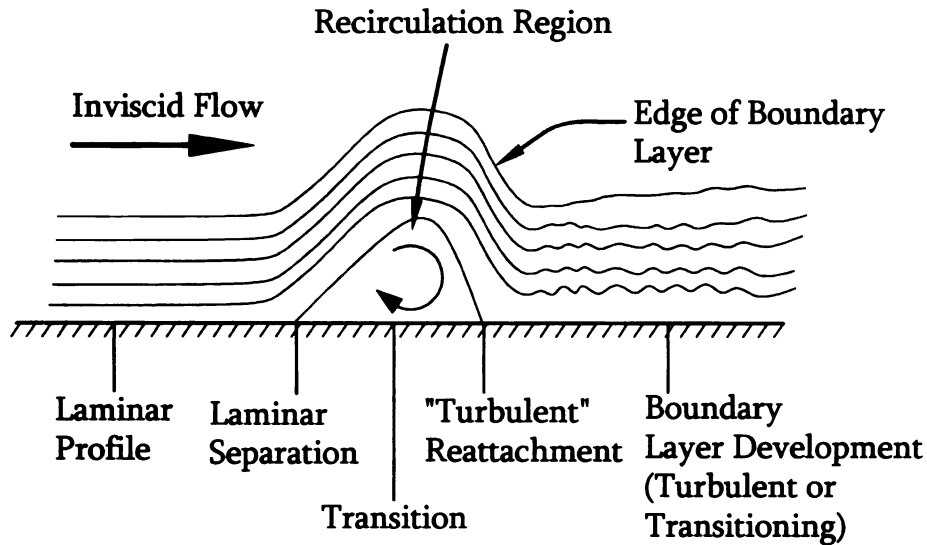


**Figure 2.3:** Description of the laminar separation bubble on low-speed airfoils.

regions will have an associated flow acceleration that will create high speed flow. This high speed flow will undergo a pressure recovery that will bring it back to approximately freestream conditions at the trailing edge for an attached flow. In high Reynolds number airfoils ( $> 10^6$ ), this boundary layer will transition quickly from laminar to turbulent. These turbulent boundary layers near the leading edge can remain attached even in the presence of strong adverse pressure gradients. However, in low Reynolds number airfoils, the boundary layer will often remain laminar near the leading edge. Since a laminar boundary layer has lower momentum in the near wall region (as compared with a turbulent boundary layer) it will undergo a flow separation caused by the adverse pressure gradient. The separated laminar boundary layer becomes a shear layer, which is thought to undergo a rapid transition to a turbulent flow. The increased entrainment from the turbulent flow makes it possible for the flow to reattach to the airfoil as a turbulent boundary layer, as described by Lissaman (1983). This is commonly referred to as a laminar separation bubble, and a brief description of the physics is shown in Fig. 2.3. This reattached boundary layer will reorganize itself into an “approximately normal” turbulent boundary layer.



The reattached turbulent boundary layer will undergo an adverse pressure gradient to bring the low-pressure, accelerated flow back to the (approximately) freestream conditions at the trailing edge. For low angles of attack, this boundary layer will remain attached until the trailing edge, but, as described by Lissaman (1983), there are situations where the laminar separation remains over the entire suction side of the airfoil.

## 2.3 Characteristics of the asymmetric wake of an airfoil

The wake region for an airfoil is defined by the following statements. The irrotational upstream flow that approaches an airfoil interacts with the suction and pressure side surfaces of the airfoil, creating boundary layers on each of these surfaces. These boundary layers will continue to grow and eventually separate at the trailing edge, creating a region of vorticity directly downstream of the airfoil. This region is referred to as the *wake* of the airfoil. If the upstream approach flow were rotational, the interaction of this rotational upstream flow and the airfoil would create distinctive small scale features that could be used to identify the wake fluid. For asymmetric airfoils, such as the cambered CD airfoil, or for symmetric airfoils at non-zero angles of incidence, this wake region will be asymmetric in nature.

The characteristics of an asymmetric wake can be further classified by the following definitions introduced by Hah & Lakshminarayana (1982). Those authors present these three categories:

- (a) *Very near wake*: This is the region directly downstream of the trailing edge.

The wake peak velocity deficit is maximum at this location and the shape of the mean velocity profile is very similar to the upstream boundary layers. The

viscous stresses dominate the Reynolds stresses in the wake center region and the viscous sublayer is not completely mixed with the surrounding inertial sublayer.

- (b) *Near wake:* The evolution of the wake in this region is strongly affected by the physical characteristics of the airfoil (profile shape and chord) and the aerodynamic loading on the airfoil. This region will be asymmetric for cambered airfoils and also symmetric airfoils at non-zero angles of incidence. The absence of the bounding wall (pressure and suction side of the airfoil) means the viscous stresses are negligible and the Reynolds stresses become a higher fraction of the net shear stress.
- (c) *Far wake:* The wake structure in this region is nearly symmetric, regardless of any upstream asymmetries, and the “history effects” (profile shape, aerodynamic loading, etc.) have vanished. Also, the physical characteristics of the airfoil and aerodynamic loading have negligible effects on the evolution of the wake. The peak velocity deficit has decayed considerably and the Reynolds stresses have decreased from the values found in the near wake region

These definitions will be used to describe the areas within the wake where detailed velocity measurements were collected.

## Chapter 3

# Design of the Rotating CD Blade (RCDB)

### 3.1 Initial design using radial equilibrium equations

The Rotating CD Blade (RCDB) experiment was designed with the intent of creating a rotating version of the stationary CD airfoil for use in fundamental studies of rotating machinery. These fundamental studies can provide valuable information for understanding the physics of rotating shear flows since they have a stationary and rotating analog with equivalent operating conditions, making direct comparisons for the same geometry possible. This motivation required that the rotating analog be designed without introducing many of the complexities that are found in modern turbomachines. Figure 1.1 shows a typical engine cooling fan designed and built by Valeo. The CD airfoil is used as the starting profile for the blade design of this cooling fan. The chord shape and relative stagger at the mid-span section (halfway between the tip and the hub) shown in Fig. 1.1 are identical to those shown in Figs. 4.5 and

## Chapter 3

# Design of the Rotating CD Blade (RCDB)

### 3.1 Initial design using radial equilibrium equations

The Rotating CD Blade (RCDB) experiment was designed with the intent of creating a rotating version of the stationary CD airfoil for use in fundamental studies of rotating machinery. These fundamental studies can provide valuable information for understanding the physics of rotating shear flows since they have a stationary and rotating analog with equivalent operating conditions, making direct comparisons for the same geometry possible. This motivation required that the rotating analog be designed without introducing many of the complexities that are found in modern turbomachines. Figure 1.1 shows a typical engine cooling fan designed and built by Valeo. The CD airfoil is used as the starting profile for the blade design of this cooling fan. The chord shape and relative stagger at the mid-span section (halfway between the tip and the hub) shown in Fig. 1.1 are identical to those shown in Figs. 4.5 and

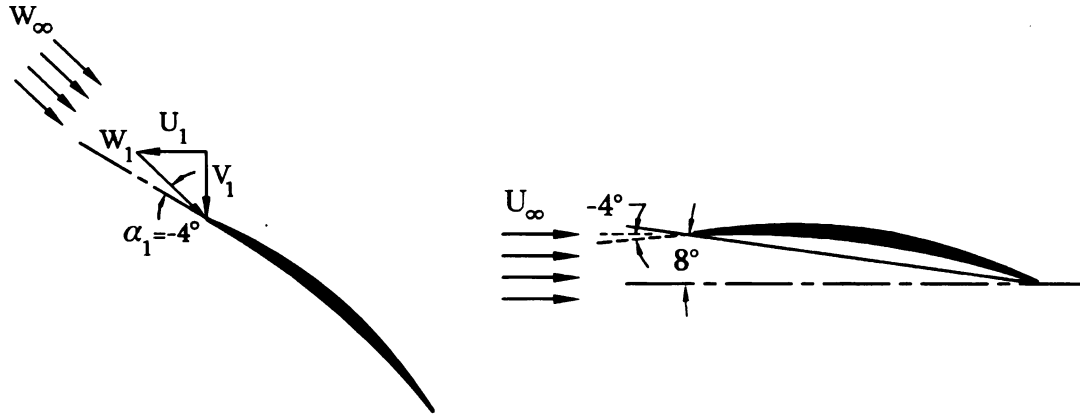


**Figure 3.1:** Stationary and rotating flow fields (left - RCDB; right - CD Airfoil).

4.6. However, the blade shape in Fig. 1.1 changes significantly in both the positive radial direction (towards the tip) and the negative radial direction (towards the hub). In particular, the blade shape has a higher camber and increased blade thickness for sections that are close to the hub. Also, the blade of Fig. 1.1 exhibits “sweep”, which means that the center of the chord line of the blade does not lie along a radial line, but rather follows a curvilinear path from the hub to tip. This particular fan has a forward swept characteristic and is often referred to as a “forward swept” fan. The fan in Fig. 1.1 also has unevenly spaced blades, meaning that the boundary conditions for each individual blade are not consistent. Finally, this fan has a bounding outer ring at the tip. All of the described features are essential parts of many modern axial turbomachines; however, each additional design feature represents another level of complexity when contrasted to the stationary original shape at the mid-span: the CD airfoil.

The motivation for the present study is to compare the flow fields of a stationary lift generating body and an equivalent rotating lift generating body. These comparisons are difficult to determine if the rotating body contains the additional design complexities shown in Fig. 1.1. Once these basic two flow fields are characterized, additional design features (as described above) can be systematically added to un-

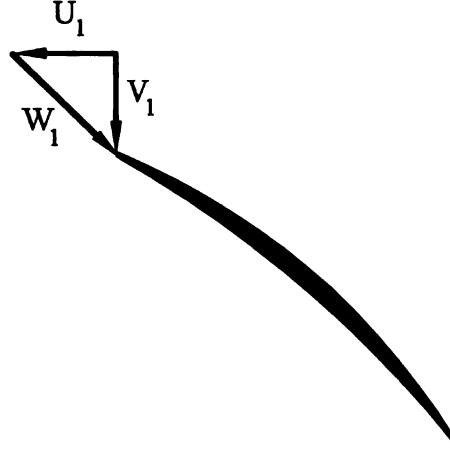


**Figure 3.2:** Vector diagram of relative ( $W$ ) and absolute ( $V$ ) inlet velocities for the RCDB.

derstand their effect on the turbulent flow field and the aeroacoustic noise levels. In order to create a true rotating analog to the stationary CD airfoil, the following criteria were used in the design process:

- Identical chord length ( $c = 133.9$  mm) and blade shape (as found on the stationary CD Airfoil) across the entire radial span.
- No sweep or lean in the blade stacking (combining the 2D shapes to make the 3D blade geometry).
- Matching Reynolds number based on chord ( $Re_c = 1.5 \times 10^5$ ). This is based on  $U_\infty$  for the stationary CD airfoil and the relative velocity,  $W_\infty$  for the RCDB.
- Matching the angle of attack for the CD airfoil ( $\alpha_g$ ) with the angle of incidence ( $\alpha_1$ ) such that the incoming flow to the blade is  $-4^\circ$  for both experiments.
- Equivalent aerodynamic loading (i.e. mean surface pressure profiles). This is accomplished by comparing the coefficient of pressure ( $C_p$ ) in both experiments.

These criteria and the associated methodologies used in the design process will be

explained and described in the following paragraphs. The initial design was conducted using basic equations and considerations that are standard in the design of conventional turbomachinery. This initial design was then iteratively developed to achieve the best overall match to the aforementioned design criteria (i.e. a trade-off). These iterations and the resulting final configuration were designed by Valeo using a 2.5D code termed EQUIOB developed by G. Meauze. Valeo also used the commercial computational fluid dynamics (CFD) code CFX ANSYS in the design process.

Maintaining the identical chord length and blade shape across the entire radial span was an important starting point in the design of a rotating blade that is geometrically equivalent to the stationary CD airfoil. This chord length provided the length scale used to define the Reynolds number that was matched between the two experiments. The Reynolds number based on the chord length for the stationary CD airfoil experiments is ( $Re_c = 1.5 \times 10^5$ ). The characteristic velocity used in those experiments is the upstream incoming velocity,  $U_\infty \approx 16\text{m/s}$ . However, the characteristic velocity used in the RCDB experiment was the relative inlet velocity, or the velocity of the air with respect to the blade,  $W_1 \approx W_\infty \approx 16\text{m/s}$ . This velocity will vary across the radial span of the blade (i.e. it is a function of radial position) and therefore the Reynolds number can only be matched for one radial location. Since all of the previous experiments (Moreau *et al.*, 2003; Moreau & Roger, 2005; Moreau *et al.*, 2006a,b) for the stationary CD airfoil were conducted at the midpoint between the upper and lower bounding walls of the wind tunnel, the mid-span of the RCDB was chosen as the radial location for establishing a relative inlet velocity that would provide a matching Reynolds number. This also makes the measurement location mostly free of hub and tip effects. The relationship between the relative inlet velocity and the absolute inlet velocity (referenced to the fixed ground) can be written as:

$$\vec{V}_{a/g} = \vec{V}_{a/b} + \vec{V}_{b/g} \quad (3.1)$$

The subscripts  $a/g$ ,  $a/b$  and  $b/g$  in Eq. 3.1 are the relative velocities of the air with respect to the ground, the air with respect to the blade and the blade with respect to the ground. The more common convention in turbomachinery literature (Lakshminarayana, 1996) is to write  $\vec{V}_{a/b}$  as  $\vec{W}$ , the relative velocity, and to denote the inlets and outlets of the various stages with a subscript (“1” would indicate the inlet to the first stage, “2” would be the outlet of the first stage, etc). The relationship between the relative inlet velocity, “W” and the absolute inlet velocity “V” is described by:

$$\vec{V} = \vec{W} + \vec{U} \quad (3.2)$$

In Eq. 3.2,  $\vec{U}$  is the product of the radius and the rotational speed of the fan,  $\vec{r}\vec{\omega}$ , which is  $\approx 13.9$  m/s at the mid-span location. The relationship defined in Eq. 3.2 is shown graphically in Fig. 3.2. Also the RCDB needed to have the same geometric angle of attack,  $\alpha_g = 8^\circ$ . The geometric angle of attack for the RCDB was defined using the relative inlet velocity, as shown on the left-hand side of Fig. 3.1. The more common convention in turbomachinery literature is to refer to this as the “angle of incidence” (Wilson & Korakianitis, 1998) and to designate it with  $\alpha_1$ . In the stationary CD airfoil studies, the blade was oriented at  $-4^\circ$  to account for the camber angle of  $12^\circ$  (see the right-hand side of Fig. 3.1). The CD airfoil also has a 4% thickness to chord ratio. During the initial design process, the radial variations in the vector diagrams and flow properties are calculated by assuming that the pressure gradients, momentum changes and blade forces on the fluid are balanced in the radial direction. This is commonly known as the *radial equilibrium equation of turbomachinery*, and it is simply the radial component of the momentum equation written in cylindrical coordinates (Lakshminarayana, 1996). Assuming the flow upstream and downstream of the blade row is axisymmetric, the terms containing variations in the tangential



direction  $\theta$  are eliminated. The resulting equation can be written as

$$\frac{\partial V_r}{\partial t} + V_r \frac{\partial V_r}{\partial r} + V_z \frac{\partial V_r}{\partial r} - \frac{V_\theta^2}{r} = -\frac{1}{\rho} \frac{\partial p}{\partial r} + F_r \quad (3.3)$$

Equation 3.3 is strictly valid away from the blade row and  $F_r$  is the body force in the radial direction, which can be assumed to be zero for the present analysis. This can be further reduced for the case of steady flow with cylindrical stream surfaces (i.e.  $V_r = 0$ ). The resulting momentum equation is a simplified form of Eq. 3.3 which is commonly referred to as the *simplified radial equilibrium (SRE) equation* (Lakshminarayana, 1996):

$$\frac{V_\theta^2}{r} = \frac{1}{\rho} \frac{\partial p}{\partial r} \quad (3.4)$$

## 3.2 Modified design using computational fluid dynamics (CFD)

The initial design was made using the RE equation (Eq. 3.3) as described above. This design was then subsequently evaluated and iteratively modified by running RANS CFD simulations at Valeo. These simulations used the commercially available CFD solver ANSYS CFX. The computational domain is shown in Fig. 3.3. The flow is moving from left to right in Fig. 3.3. This figure shows that a converging nozzle has been added at the inlet and that there is a centerbody device added upstream of the rotating blade. These were added to the design to ensure that a uniform velocity profile exists at the inlet, as shown in Fig. 3.4. As stated previously, it was critical to keep the same CD profile as the blade section across the entire blade span, which required the large hub-to-tip ratio. This identical blade shape was required to have a matching Reynolds number at the mid-span (halfway between the root and tip of the blade), while maintaining minimal radial flow along the blade and at the

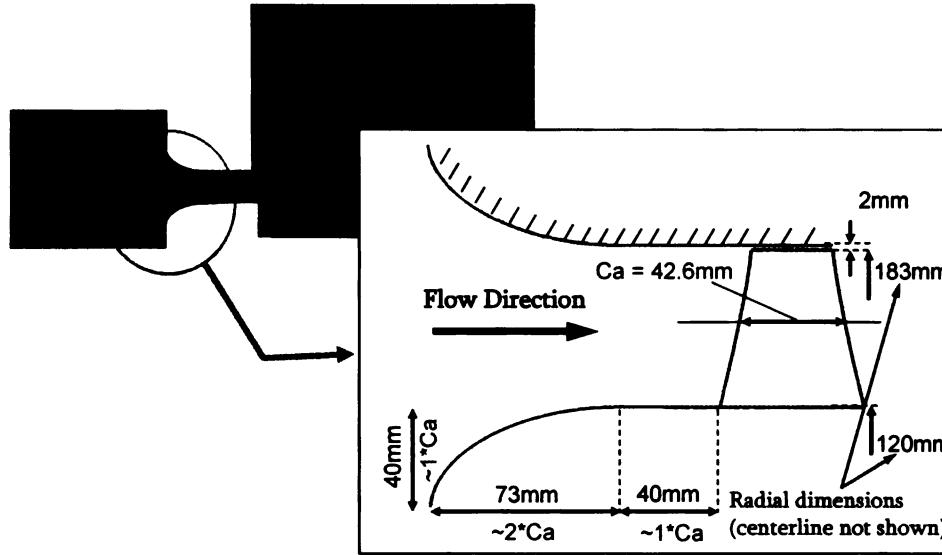


**Figure 3.3:** Computational domain for the RCDB design.

exit of the profile. Also, it was found that the operating conditions (mass flow rate and rotational speed) had to be changed to obtain the correct relative inlet velocity,  $W_1$  at the mid-span. A plot of the relative inlet velocity,  $W_1$ , is shown in Fig. 3.4. The mid-span corresponds to a value of 0.5 on the ordinate of Fig. 3.4. The desired relative inlet velocity at the mid-span is 16 m/s, as shown by the circle labeled 'design target'. The calculated velocity for this location is around 15.95 m/s. By matching this relative inlet velocity, the same Reynolds number could be obtained for both the stationary and rotating CD blades.

The outlet radial velocity is shown in Fig. 3.5. The initial designs using the RE equations assume that because the forces in the radial direction are balancing the pressure gradient, there is no radial momentum. However, this simplification does not include the three-dimensional effects caused by the addition of the tip clearance and hub geometry. Therefore, any "real" turbomachine will exhibit an outlet radial velocity. This was anticipated and an important goal of the design was to minimize this velocity. Because of this, no design target is shown in the figure (ideally it would be zero, but the realistic objective was to make it small compared to the relative inlet

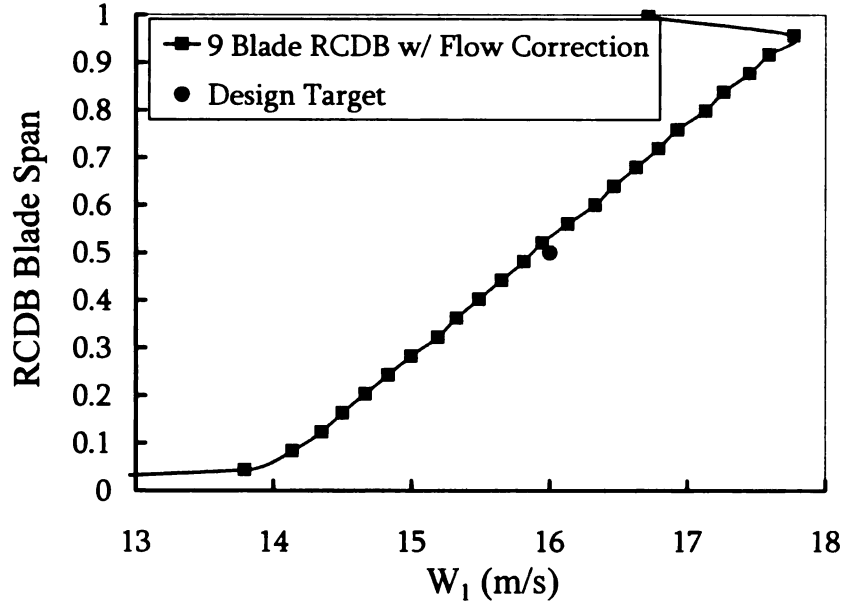


**Figure 3.4:** Relative Inlet Velocity ( $W$ ) for RCDB from CFD simulations.

velocity). Figure 3.5 shows that at the mid-span, the calculated radial velocity is approximately 0.5 m/s, which is roughly 3% of the relative inlet velocity. This very low value was achieved by choosing the proper stagger angle<sup>1</sup> distribution and also by carefully choosing the operating conditions.

The calculated angle of incidence, as shown in Fig. 3.6, varies across the inlet, but it is very close to the design target of  $-4^\circ$  at the mid-span. This plot also shows that the original calculations from the EQUIOB code and the initial CFD simulations closely matched the target; however, as mentioned previously, the operation conditions (mass flow rate and rotational speed) had to be changed to more closely match the target relative inlet velocity. This created a trade-off in the iterative design process, termed “flow correction” in the plots.

A final consideration was the inlet axial velocity, which is shown in Fig. 3.7. This plot shows that the axial velocity profile at the inlet is very uniformly distributed around the mid-span. The design target value of 8 m/s, which is needed for the inlet

<sup>1</sup>The angle between the chord line and the axial direction

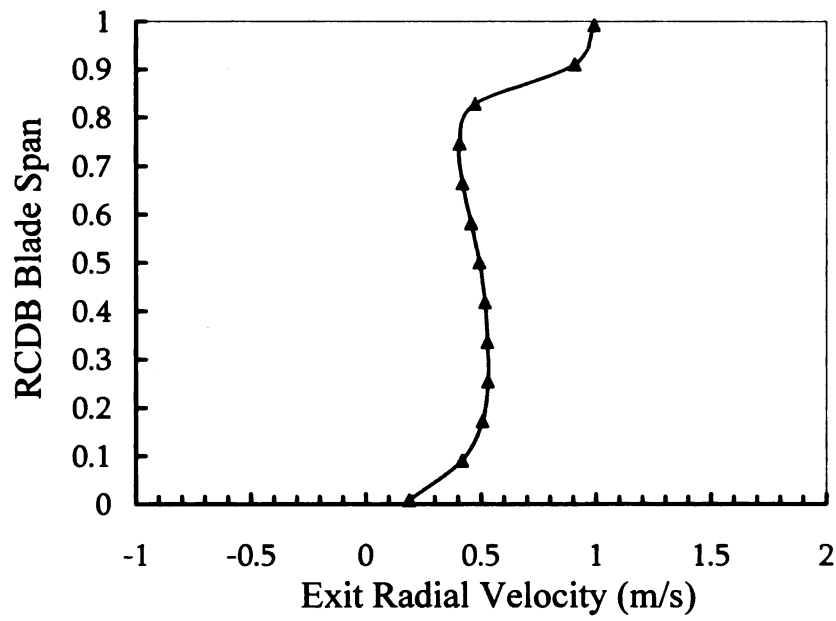


**Figure 3.5:** Exit radial velocity for RCDB (CFD simulations).

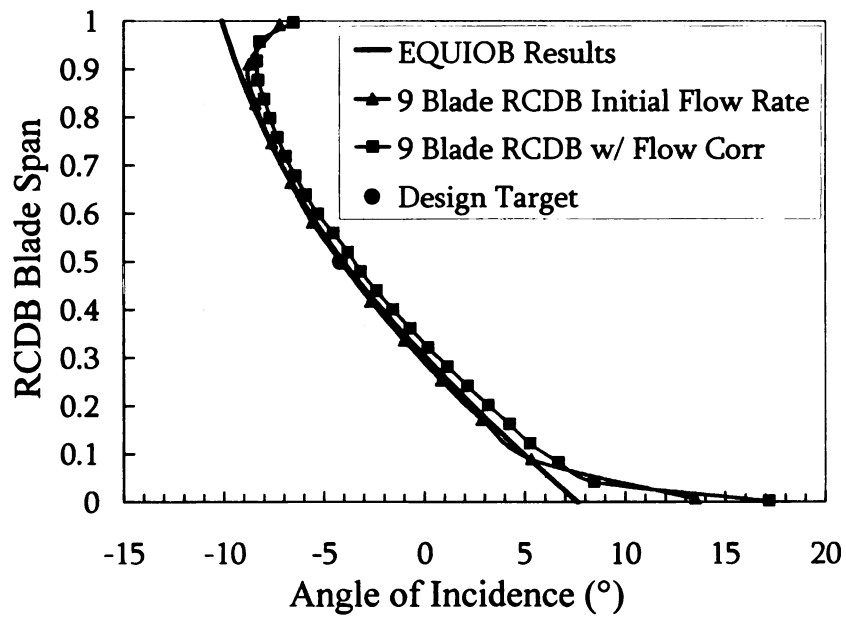


**Figure 3.6:** Calculated angle of incidence for the RCDB.

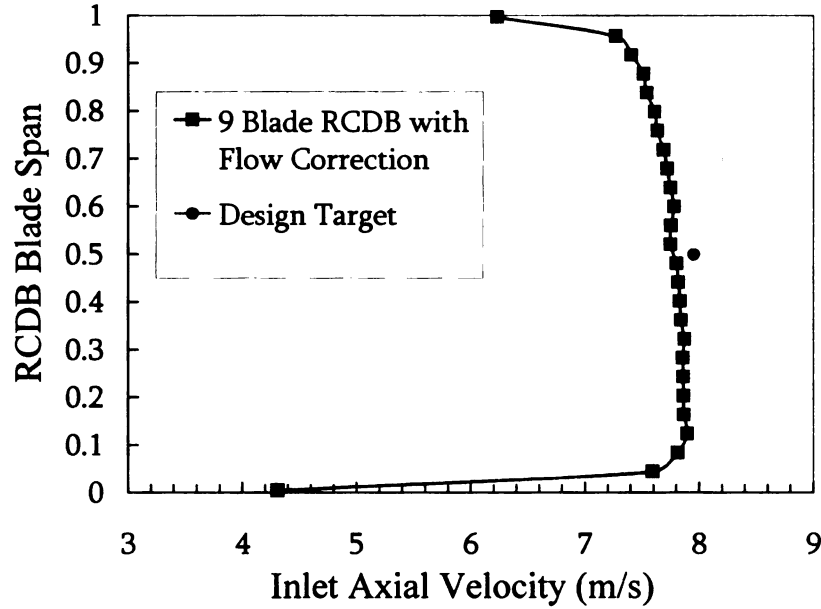


**Figure 3.7:** Inlet axial velocity for the RCDB (CFD simulations).

relative velocity  $W_1 \approx 16$  m/s, is closely matched by the CFD simulations (7.8 m/s).

### 3.3 RCDB Final Design

Figure 3.8 shows the final design obtained from the modified design process using CFD simulations. The final computer generated design shows the hub with 5 blades and the converging inlet nozzle (or shroud) plus the upstream centerbody. This design was prototyped and the physical design is shown installed in the AFRD facility at MSU in Fig. 3.9. The rotor portion of this model has been designed and fabricated such that it is modular and can accommodate any blade combination from 2 to 8 blades. This is accomplished by removing and adding spacer (i.e. hub) sections combined with the blade sections, as shown in Fig. 3.10.

Throughout the design process detailed in Sections 3.1 and 3.2, the 9-blade version of the RCDB was the selected configuration. However, the final design objective

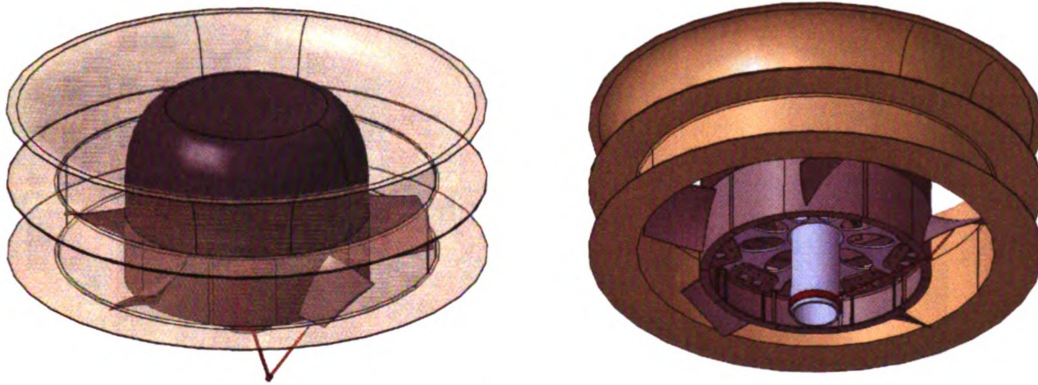


**Figure 3.8:** RCDB final design CAD (left - upstream view; right - downstream view).



**Figure 3.9:** RCDB final design installed (left - upstream view; right - downstream view).



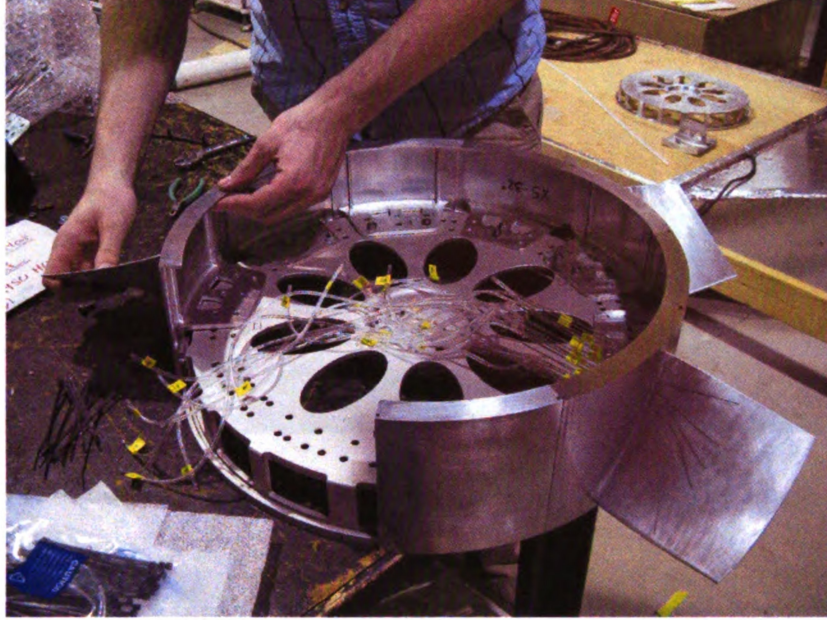


**Figure 3.10:** RCDB rotor design showing modular capability.

(listed above) is to have a rotating version of the CD airfoil that has very similar boundary conditions, or blade loading, which can be represented by the pressure coefficient ( $C_p$  distribution on the suction and pressure sides of the blade). It was noticed in previous experiments on the CD airfoil that the surface pressure distribution varied strongly depending on the inlet nozzle width (Moreau *et al.*, 2003; Moreau & Roger, 2005). This was studied since two different wind tunnels (shown in Fig. 3.11) were used in some of the initial CD airfoil experiments at the Ecole Centrale de Lyon. Additionally, the jet width in each of these tunnels could be varied, so it was important to understand how the varying boundary conditions (i.e. jet width) would affect the experimental results. This effect of the inlet nozzle width in the stationary CD airfoil experiment was further studied using CFD simulations and verified with experimental data as shown in Fig. 3.12. This plot shows that the laminar separation bubble near the leading edge of the airfoil decreases significantly between the free air (infinite inlet nozzle width) and the 13 cm and 50 cm inlet nozzle cases. These data show that the blade loading changes depending on selected inlet nozzle size. These

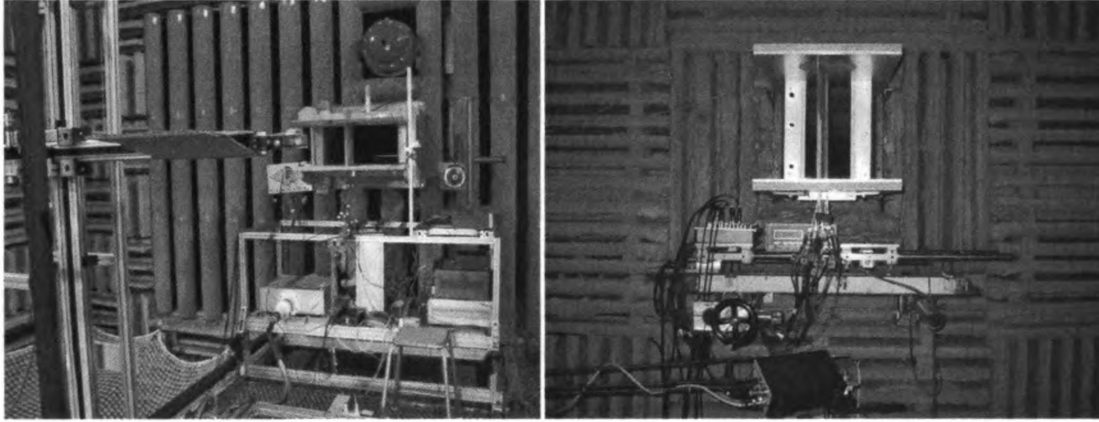


**Figure 3.11:** The large and small anechoic wind tunnels at the Ecole Centrale de Lyon.

results also demonstrate the ability of the CFD simulations to predict the pressure coefficient on both the pressure and suction sides of the stationary CD airfoil. Further insight into the effect of the blade loading as it is influenced by the width of the flow between the shear layers is shown in Fig. 3.13. Note the differences in the velocity contours from the CFD simulations for the various jet widths of the ECL experiments. The stationary CD airfoil setup at MSU is similar to the setup that was used to measure the experimental 50 cm inlet data shown in Fig. 3.12 at the Ecole Centrale de Lyon (ECL). The MSU facility was validated against the ECL facility and this comparison is shown in Section 4. Therefore, the target is to match the  $C_p$  profile of RCDB experiment to the 50 cm inlet data of Fig. 3.12 as closely as possible.

The calculated  $C_p$  distributions for the RCDB are shown in Fig. 3.14 plotted against the experimental 50 cm nozzle data for the CD airfoil. These data show that the 7 and 9 blade configurations have a different overall value for the net lift when compared against the CD airfoil data (both simulation and experiments). Figure 3.15 is zoomed near the leading edge so that the data in the first 20% of the chord are more easily viewed. These data show that the pressure values associated with the laminar



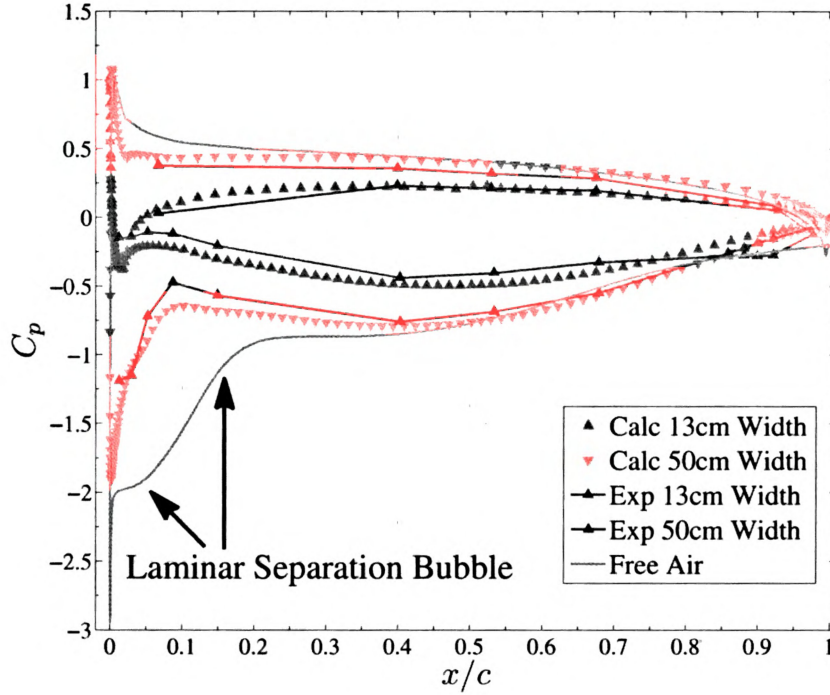


**Figure 3.12:**  $C_p$  data showing the effect of the inlet jet width.

separation bubble are much different for the 7 and 9 blade cases. Additionally, the size of the laminar separation bubble is quite different between the 9 blade case and those with fewer blades. The 9 blade case has a separation bubble which appears to end around  $x/c \approx 0.025$ , whereas the 2 and 5 blade cases are closer to both the calculated and measured values for the stationary CD airfoil ( $x/c \approx 0.05$ ).

These data strongly suggested that the number of blades used in the RCDB experiment has an effect that is similar to varying the inlet nozzle width in the CD airfoil experiment. This indicated that there is a correlation between the nozzle width used in free jet airfoil experiments and the solidity used in an equivalent rotating machine. The lift is reduced for both the narrower jet width in the stationary CD airfoil experiment (13 cm) and it is also reduced for the higher number of blades in the RCDB simulations. Experiments were subsequently conducted on the various blade configurations (2–7 blades) to determine which blade configuration would be closest to the

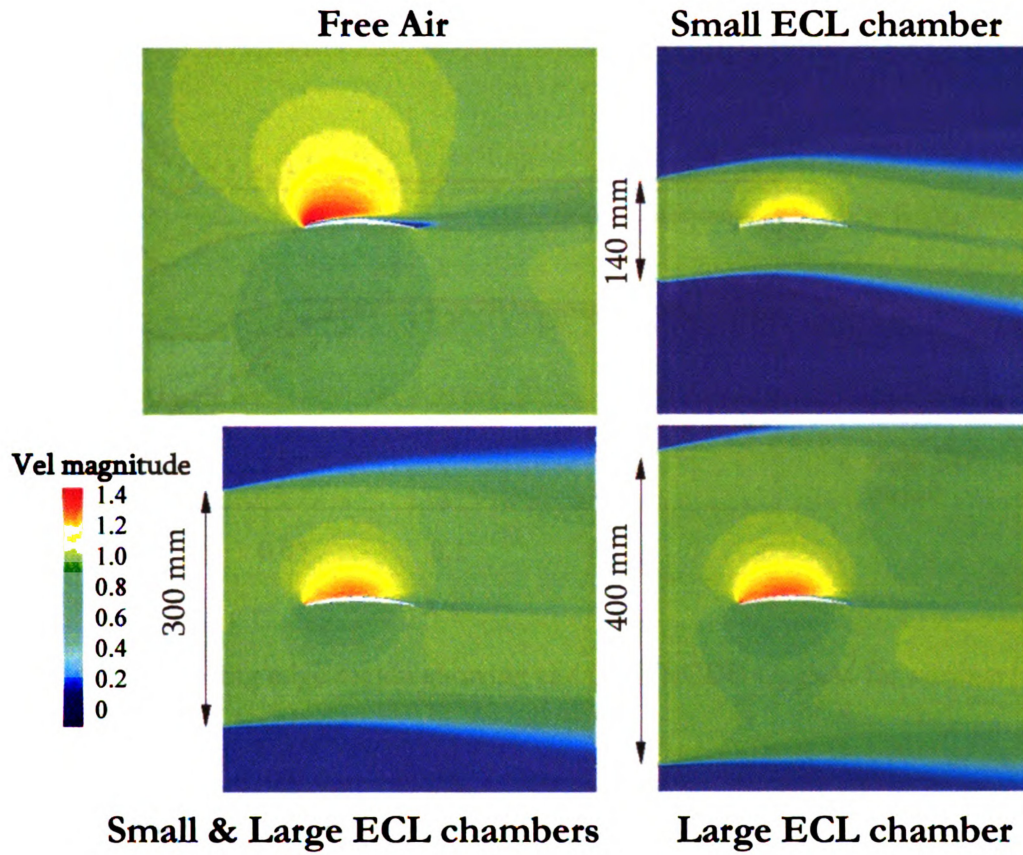


Figure 3.13: CFD simulations showing the velocity contours.

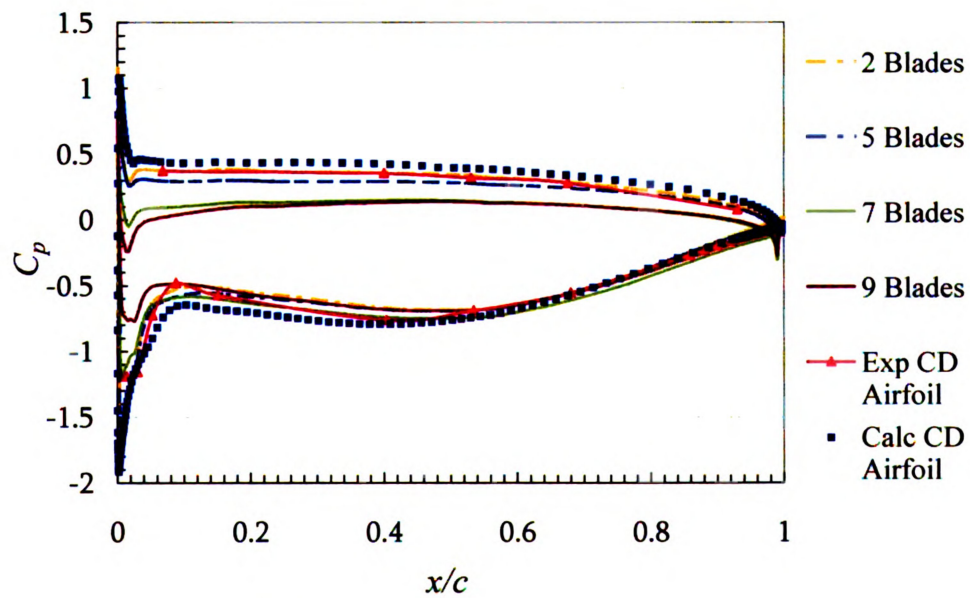
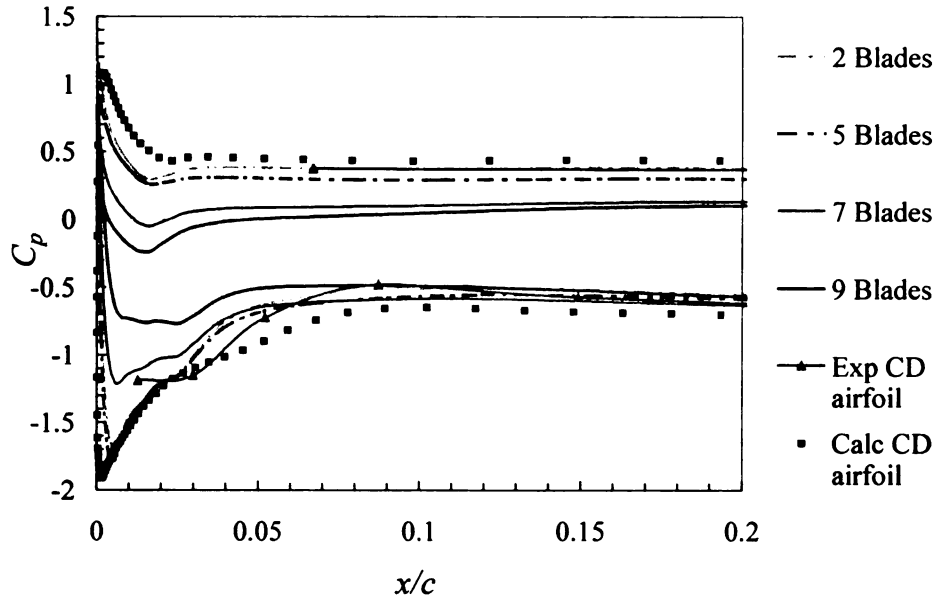


Figure 3.14: CFD RCDB  $C_p$  data for various blade configurations.



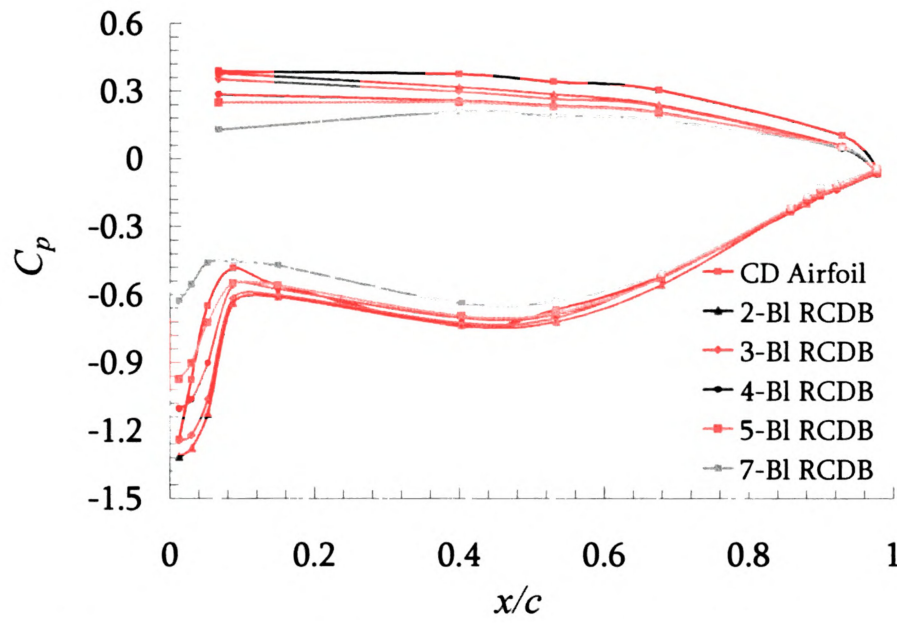
**Figure 3.15:** Leading edge region showing the CFDB RCDB  $C_p$  data for various blade configurations.

50 cm jet width CD airfoil experiment.

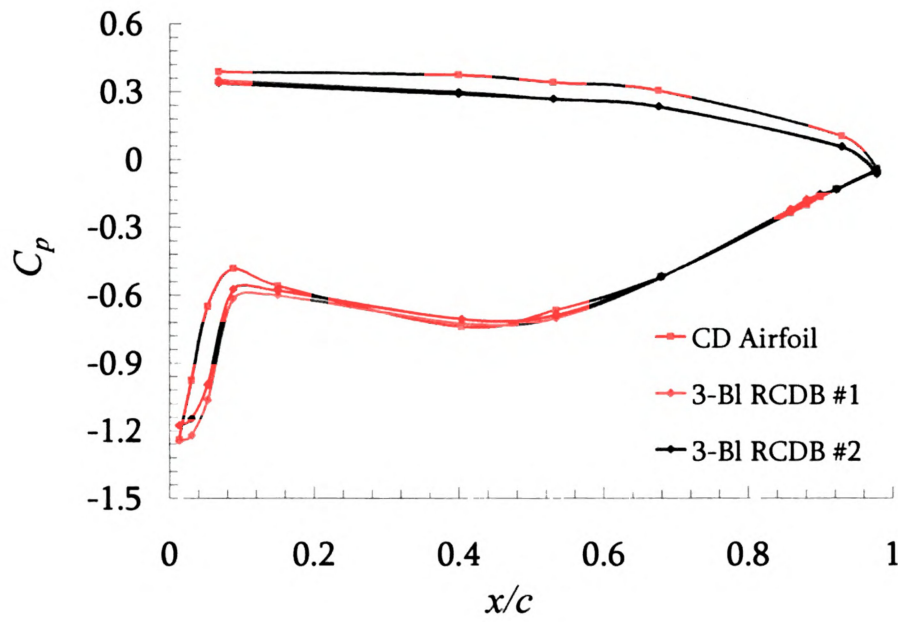
The experimental  $C_p$  for various blade configurations (2–7) are shown in Fig. 3.16. These data confirm the trends predicted by the CFD simulations shown in Fig. 3.14, specifically that the lift is reduced as the number of blades used on the RCDB is increased. The stationary CD airfoil data are also included for comparison purposes. These data further confirm that the overall shape and general trends for the  $C_p$  data of the stationary experiment are matched in the RCDB experiment. These include the separation bubble at the leading edge and also the trends of increasing and decreasing pressure along the suction and pressure side surfaces. These data were used to select the final blade configuration, which is the 3-blade version of the RCDB.

Figure 3.17 shows the  $C_p$  data for the 3-blade RCDB along with the stationary CD airfoil. Two independent tests of the 3-blade configuration, which were shown to be typical tests for repeatability considerations, are also shown. Although the overall agreement is very good between the stationary and rotating experiments, two

notable differences are apparent in Fig. 3.17. First the pressure side values for the  $C_p$  data in the 3-blade RCDB are consistently lower than those for the stationary CD airfoil. This was shown to be true of all configurations of the RCDB (see Fig. 3.16). This is explained by noting that although the effect of solidity (in the RCDB) and jet width (in the CD airfoil) had a similar effect on blade loading, the boundary conditions are distinctly different between these experiments. Furthermore, the lower values measured on the pressure side were also expected per the CFD results shown in Fig. 3.14 (albeit the levels are different). The second difference that is apparent in Fig. 3.17 is the different sizes of the separation bubble at the leading edge. In the RCDB, the laminar separation bubble extends to approximately 8-9% of chord, whereas the separation bubble on the CD airfoil reattaches around 5-6% of chord. Figure 3.17 additionally shows that the pressure at the pressure tap on the suction side that is closest to the leading edge is also very close between the RCDB and the CD airfoil. This was the closest match of all the RCDB configurations and strong variations were noticed between the other blade configurations, as shown in Fig. 3.16.



**Figure 3.16:** Experimental RCDB  $C_p$  data for various blade configurations.



**Figure 3.17:**  $C_p$  data final RCDB configuration and the CD airfoil.

# Chapter 4

## Experimental Apparatus and Methodologies

### 4.1 Controlled-diffusion (CD) airfoil

#### 4.1.1 CD airfoil configuration at the ECL

Initial data were collected in the large anechoic wind tunnel at the Ecole Centrale de Lyon (ECL) in Lyon, France. This tunnel has a free-jet configuration, and the airfoil was held between two horizontal end-plates fixed to the nozzle of the open-jet anechoic wind tunnel as shown in Fig. 4.1. The nozzle dimensions of the tunnel are 50 cm wide by 25 cm tall and the airfoil is mounted so that the airfoil span covers the entire 25 cm height. Initial tests were run in both the large ECL anechoic wind tunnel (nozzle dimensions 50 cm x 25 cm) and the small ECL anechoic wind tunnel (nozzle dimensions 13 cm x 25 cm). However, it was found that the width of the jet had a significant effect on the measured surface pressure distribution ( $C_p$ ) data and also these data varied significantly from previous CFD simulations of the Valeo CD airfoil computed for an infinite jet width (Moreau *et al.*, 2003). Upon realizing the



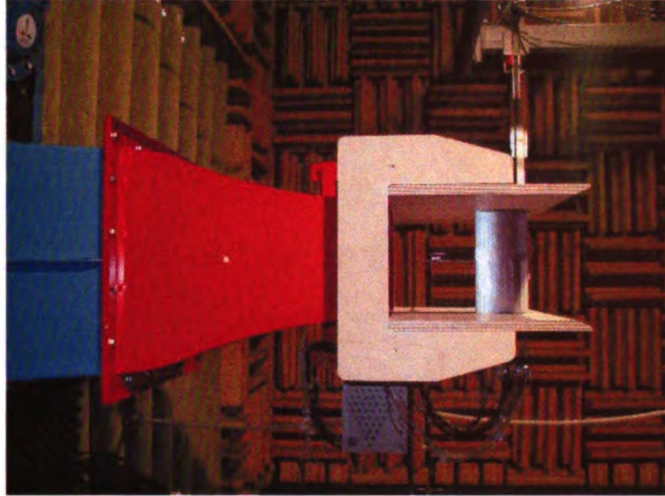


**Figure 4.1:** ECL Large Anechoic Wind Tunnel.

substantial effect that the nozzle width had on the loading of the blade, all subsequent experiments were carried out in the large anechoic wind tunnel (and subsequent CFD simulations included the sidewalls of the nozzle, as described in (Moreau *et al.*, 2003)). It can be noted that an airfoil in open-jet wind tunnel is similar to, but different from isolated airfoil studies (see Raj & Lakshminarayana (1973)) which have a single airfoil installed in closed test sections (i.e. with parallel bounding walls as the boundary conditions on the pressure and suction sides). It is also different from various cascade studies (see Hah & Lakshminarayana (1982)) which have airfoils that are identical to the airfoil being studied as upper and lower boundary conditions. These ideas are further discussed in Sec. 5.3 and comparisons with isolated airfoil and cascade studies are presented.

#### 4.1.2 CD airfoil configuration at MSU

Two different measurement campaigns were conducted in the large ECL anechoic wind tunnel in 2003 and 2005. The former were reported in (Moreau *et al.*, 2006a). The crucial dimensions of the large ECL anechoic wind tunnel were subsequently replicated in the MSU-TSFL, but without the anechoic capability. The MSU facility

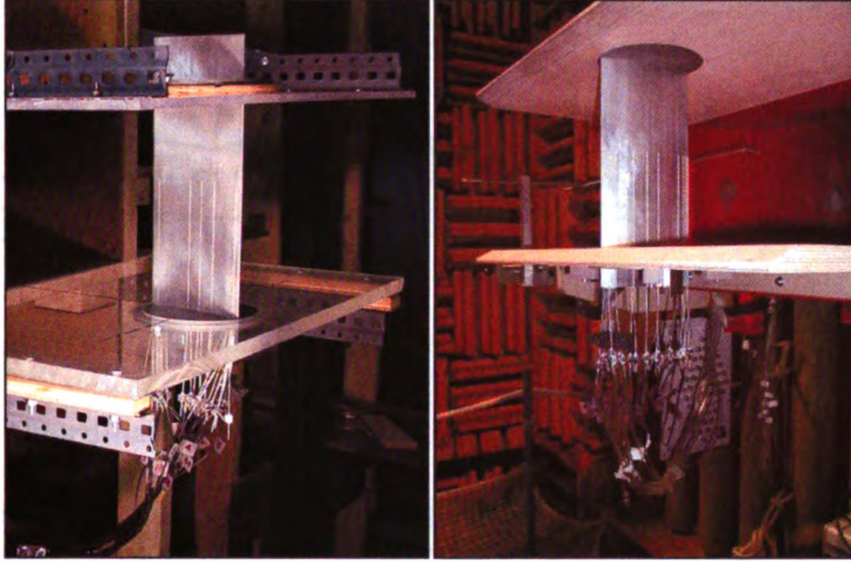


**Figure 4.2:** The free jet configuration for the CD airfoil (left - MSU, right - ECL).

allowed for additional velocity and pressure measurements to be collected. All of the data collected in the MSU facility have the same conditions (free-stream velocity, angle of attack, etc.) as those of the ECL measurements. This configuration is shown in Fig. 4.2. Two disks, with angular positioning capabilities on the end-plates, allow for the adjustment of the angle of attack of the airfoil with respect to the flow. The CD airfoil has a 0.134 m chord length, a 0.3 m span, a 4% thickness-to-chord ratio and a camber angle of  $12^\circ$ . The selected configuration for these studies is the CD airfoil in the large ECL wind tunnel at a nominal speed,  $U_\infty$ , of 16 m/s (corresponding to a Reynolds number based on the airfoil chord length  $Re_c = 1.6 \times 10^5$ ) and a geometric angle of attack,  $\alpha_g$ , of  $8^\circ$ . These conditions corresponded to the largest possible domain within the jet potential core while, at the same time, providing a Reynolds number that allowed for the on-going numerical simulations. In addition, this configuration has a suction side flow with an adverse pressure gradient but the suction side boundary layer is still attached at the trailing edge. The conditions yielded by this configuration are appropriate for noise predictions based on the pressure spectra at the trailing edge (Amiet, 1976).



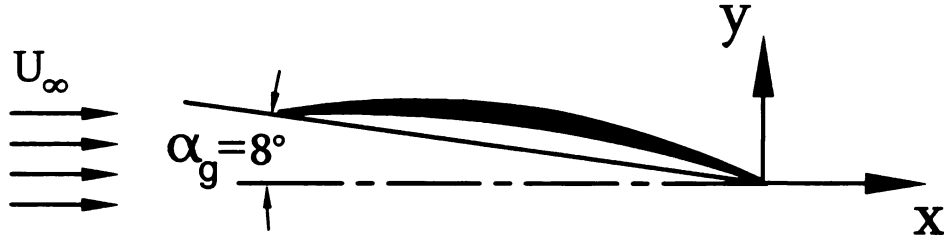


**Figure 4.3:** Coordinate system used for the CD Airfoil experiments.

#### 4.1.2.1 Coordinate system

The coordinate system with the origin at the trailing edge was used for all of the CD airfoil experiments, as shown in in Fig. 4.3. The x-axis is aligned with the upstream flow and its positive direction points downstream. The y-axis is aligned so that the positive direction points towards the suction side of the airfoil. The z-axis (not shown) points out of the page.

#### 4.1.2.2 Reference pressure

The operating conditions of the wind tunnel were established by using an upstream Pitot-static tube shown in Fig. 4.4. This provides the scaling velocity,  $U_\infty$  for normalizing the mean velocity and turbulence data. The location of this Pitot-static probe is approximately the same as for the ECL experiments and its location did not change throughout the data collection.

#### 4.1.3 Surface pressure taps and RMPs

The airfoil is equipped with 21 flush-mounted remote microphone probes (RMPs) (P  renn  s & Roger, 1998) as shown schematically in Fig. 4.5. (Three additional RMPs are located in the spanwise direction at the same streamwise location as RMP No. 25.). These RMPs measure both the mean and fluctuating wall pressures within the frequency range 20 Hz–25 kHz and they characterize the corresponding noise sources.

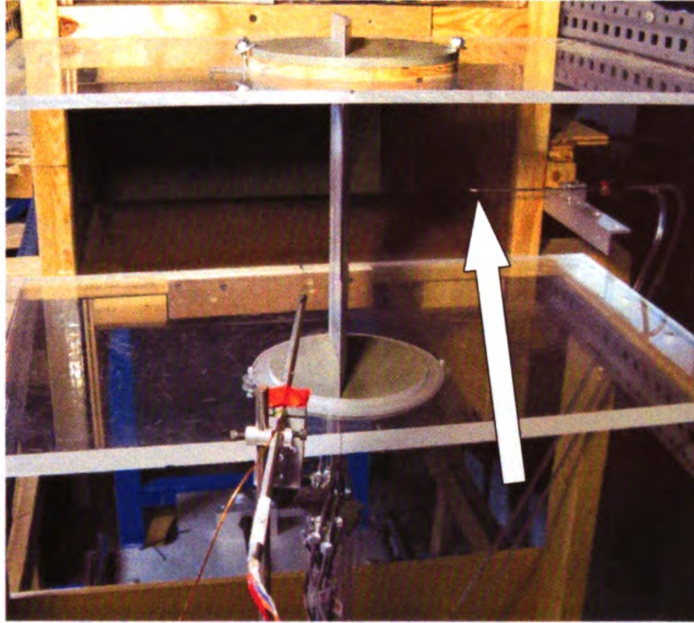


**Figure 4.4:** Location of Pitot tube used in CD airfoil experiments.

The RMP concept was developed for measuring surface pressures in very small areas, such as the trailing edge region of thin airfoils, which can typically have a thickness on the order of 1 mm. The physical configuration is pictured in Fig. 4.6 and the small tubes that are embedded into the airfoil (with the ends protruding out one side) are shown. These regions with very small wall thickness make it very difficult to utilize flush-mounted microphones. Furthermore, the use of “remote” microphones allow for very small spacing of the measurement locations; however, careful in-situ calibrations of the microphones must be carried out. This technique was described in (Hoarau *et al.*, 2006). The present dissertation only used the mean surface pressure capabilities of the RMPs, but the ability to measure unsteady pressure is an important feature of this set-up and a similar capability was implemented into the rotating analog to this experiment, as described in Sec. 4.2.2.3.

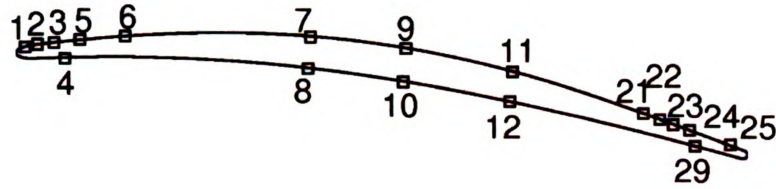


**Figure 4.5:** Locations of measurement stations on the CD airfoil.

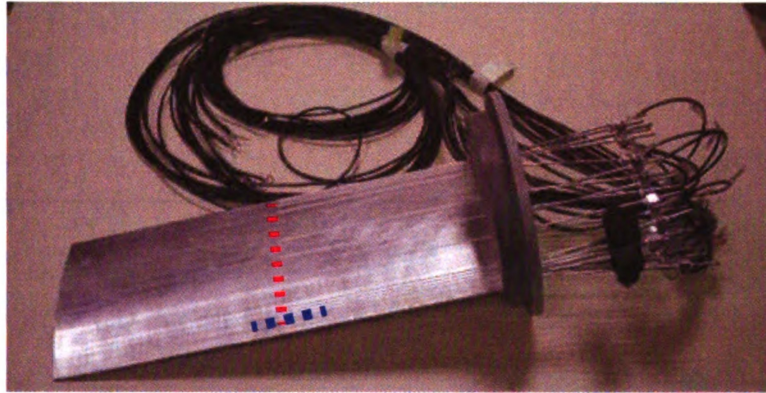


**Figure 4.6:** CD Airfoil with RMP probes (pressure taps at mid-span region).

#### 4.1.4 Comparison of CD airfoil configuration at ECL and MSU

Tests were conducted in the MSU experimental configuration to ensure that the two facilities (ECL and MSU) were equivalent. A comparison of the pressure coefficients measured at MSU and ECL is shown in Fig. 4.7. These data show that there is a good comparison between the pressure coefficient data at MSU and ECL. The absolute values for the ECL data are slightly higher, which is likely a bias error caused by a slightly different calibrations between the pressure transducer used in those experiments and the one used at MSU. There are also some slight differences on the suction side at the leading edge, which could be caused by slight variations in the installation of the airfoil (since the separation and reattachment regions are most likely very sensitive to shifts in boundary conditions). Finally, the MSU data show

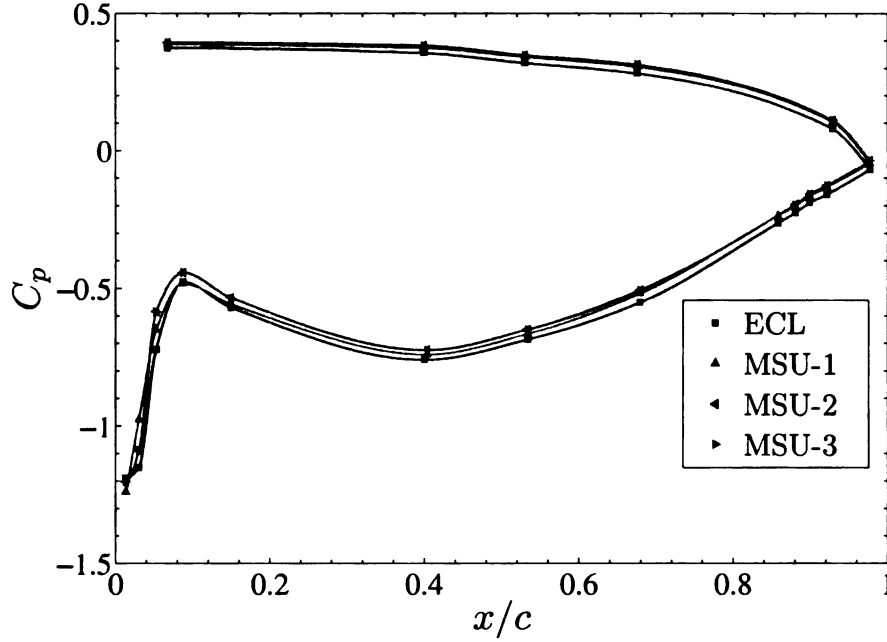


**Figure 4.7:** CD Airfoil  $C_p$  data in the MSU and ECL wind tunnels).

excellent repeatability amongst the three data sets that are shown.

## 4.2 Rotating CD Blade (RCDB) experimental configuration

### 4.2.1 Axial Fan Research and Development (AFRD) facility

The RCDB experiments were conducted in the Axial Fan Research and Development (AFRD) facility at MSU. The facility has been used extensively for a variety of low-speed axial fan studies (Morris & Foss, 2001; Neal & Foss, 2007; Dusel, 2005). The exterior of the AFRD facility is shown in Fig. 4.8 and the salient features are labeled in the right-hand side of that figure. The features are also described in detail in the following paragraphs. The AFRD facility is a vertically mounted wind tunnel that draws air from the atmosphere into an upper receiver. The airflow from the upper



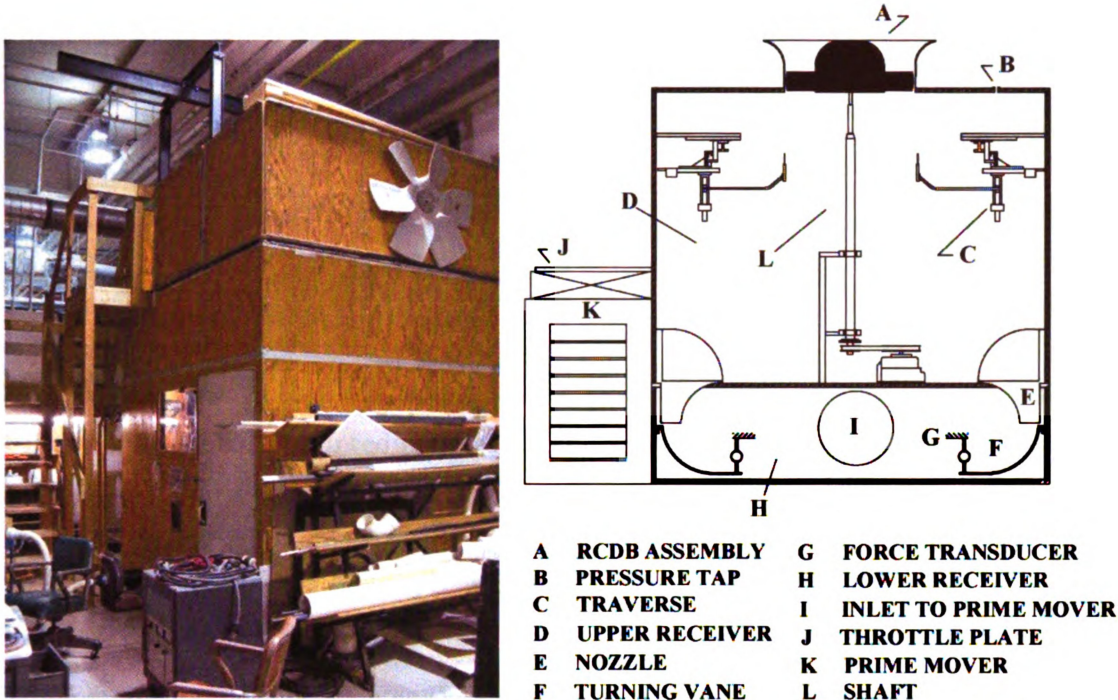


**Figure 4.8:** The Axial Fan Research and Development (AFRD) Facility.

receiver, through the metering system and into the lower receiver is induced by a large (Chicago Design 36 SISW SQA Airfoil) centrifugal fan. A novel flow metering system (see Morris *et al.* (2001)) makes use of the moment-of-momentum flux through a 90-degree turning vane system to measure the total mass flow rate. A wall tap in the ceiling of the AFRD facility is used to evaluate the pressure change across the fan (from atmosphere to receiver). A  $\pm 1\%$  feedback speed control unit powers the 11.2 kw (15 HP) motor that drives the fan. Many of the previous studies have used a Himmelstein 22.5 N-m torque meter to determine the shaft power input to the fan. This was replaced for this study with a slip ring, which is described in Section 4.2.2.1. A once-per-revolution sensor on the main shaft provides the trigger signal needed for phase sampled measurements. The installed traverse system permits radial, axial and azimuthal positions of hot-wire sensors to record the wake region of the fan. The inlet contraction, the hub with its multi-blade attachment capability and the

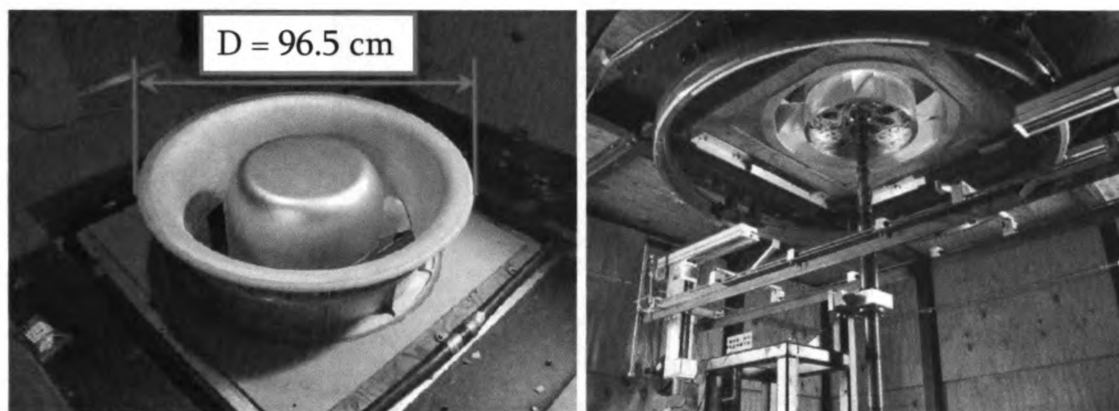


**Figure 4.9:** RCDB mounted in the AFRD (left - upstream view, right - downstream view)

centerbody to cover the installed instrumentation were all supplied to the TSFL by Valeo. These components are shown schematically and via photographs in Fig. 4.9. The installation details, such as the immersion, follow guidelines that were developed during the design process that is described in Chapter 3.

## 4.2.2 Instrument cluster in the RCDB hub

A custom instrumentation cluster was designed and assembled for the RCDB experiment, using a combination of stock components and a custom circuit board. An overview of the cluster can be seen in Fig. 4.10. The details of the various components that comprise this instrumentation cluster can be found in the following sections.

### 4.2.2.1 Slip ring

The design of the instrumentation cluster for the RCDB required electrical connections between the stationary (i.e. lab) and the rotating (RCDB hub) reference frames. This was accomplished through the use of a single shaft-mounted slip ring which is shown in Fig. 4.11. The model used was the SR20M made by Michigan Scientific corporation. The SR20M uses gold alloy rings and precious metal alloy brush contacts. The contact resistance variation is typically 0.05 ohms and the typical contact life

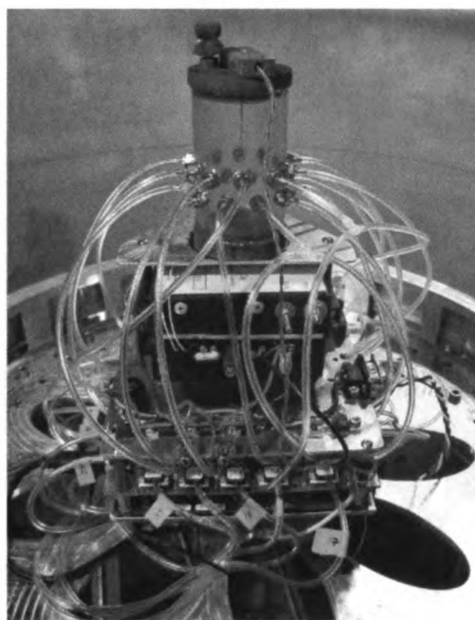


**Figure 4.10:** RCDB instrument cluster

is 200 million revolutions. This assembly imparts very low noise on the transferred signal and also it requires no maintenance to ensure high performance. The SR20M allows for 20 individual circuits to be connected, each with a maximum current draw of 500 mA. This slip ring assembly also mounts on the end of the shaft, as shown in the right-hand side of Fig. 4.11, which allowed it to be retro-fitted into the existing AFRD configuration. This type of slip ring was used by in the paper by Fukano & Jang (2004), where measurements were collected in the rotating reference frame with a single normal (SN) hot-wire probe. In their experiment, the hot-wire cable was split through the slip ring, allowing them to use a stationary anemometer with a rotating probe. The authors noted that the very low-noise characteristics made this particular model desirable. Despite these low-noise characteristics, the design of the RCDB instrumentation cluster omitted the need for transferring analog data connections, which can be adversely affected by the noise (i.e. variable resistance and the corresponding variable impedance) imparted through slip rings. The concern is that this fluctuating resistance would be indistinguishable from any fluctuating flow



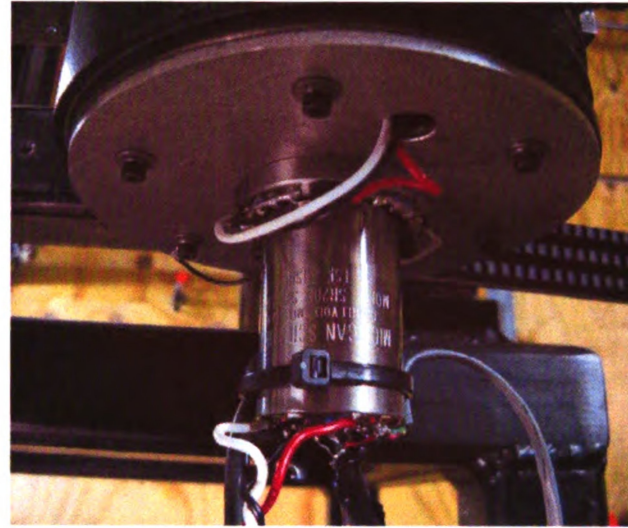


**Figure 4.11:** Slip ring assembly (left - uninstalled, right - installed in the AFRD Facility)

phenomena that may exist in the flow field. Therefore, only three connections were made through the slip ring:

1. The DC power connection that transferred power into the RCDB instrumentation cluster.
2. The USB 2.0 connection for two-way communication between the stationary computer and the rotating (hub mounted) A/D board.
3. The sync line to send the clocking pulse from the stationary A/D to the rotating (hub-mounted) A/D. The stationary A/D was required to measure the needed variables in the stationary reference frame, such as the optical encoder, the AFRD upper receiver pressure and the AFRD flow rate.

The current limit of 500 mA for each circuit on the slip ring required that the DC power connection be divided over several slip ring circuits. Also, both the USB 2.0 and A/D clock use cable types that have multiple wires, so each wire inside these cables used a separate channel on the 20-channel slip ring.



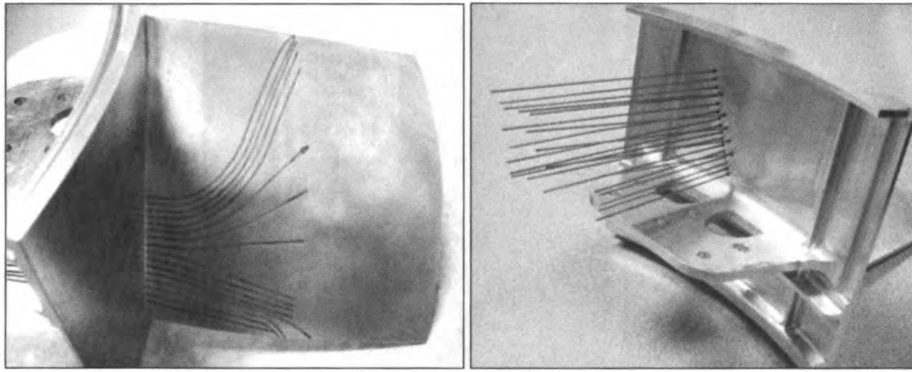


**Figure 4.12:** Pressure taps embedded into RCDB

#### **4.2.2.2 Level 1: A/D board**

All measurements made in the rotating reference frame were digitally sampled by an analog-to-digital (A/D) converter that was mounted in the RCDB hub. The model used was the DaqBoard/3035USB manufactured by IOTech, Inc. This device has 32 differential or 64 single-ended data channels available and its compact design (15.24 cm x 15 cm) was well-suited for mounting in the RCDB. Additionally, this device is both powered by USB 2.0 and also transfers data by USB 2.0. This connection was made using the slip ring described in Section 4.2.2.1.

#### **4.2.2.3 Level 2: Pressure and temperature mezzanine board**

The ability to measure the pressure on the RCDB required the mounting of pressure transducers inside the hub. The RCDB, like the CD airfoil, was equipped with 24 total pressure taps that were embedded into one of the blades of the RCDB. A set of 22 small MEMS-based pressure transducers (see Fig. 4.13) are mounted on the instrumentation cluster. These devices were made by Allsensors Corporation (model-type 1-INCH-D2-4V-MINI) These are capable of measuring pressures ranging from 0–249 Pa, which is nominally the range for most of the surface pressure data, particularly for the operating condition used for the velocity measurements. Two

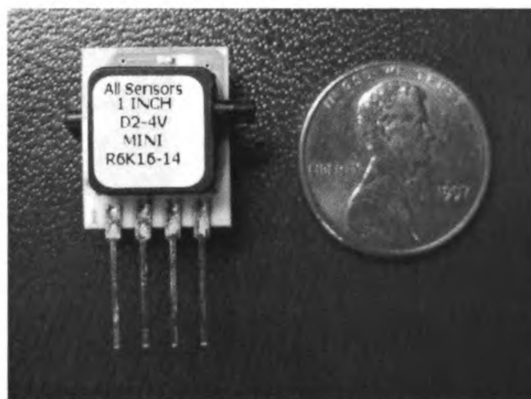


**Figure 4.13:** Allsensors MEMS-based pressure transducer

additional pressure transducers were added to measure the two pressure taps near the leading edge on the suction side, which had values that would saturate the low-range (0–249 Pa) transducers for the lower solidity cases (as seen in Fig. 3.16).

Additionally, a set of amplifiers to be used with condenser microphones are mounted on a platform in the hub. These microphones allow for the unsteady surface pressures to be measured. The MEMS pressure transducers and microphones can be combined using an RMP that is very similar to what was used in the stationary CD airfoil and also described in Sec. 4.1.1 and also in Pérennès & Roger (1998). The amplifiers are installed in the RCDB, but the microphones were not mounted for this study.

Temperature measurements in the rotating reference frame, primarily used for temperature compensation for the rotating reference frame hot-wire anemometry measurements, were accomplished through two small IC thermocouple units. These units were also mounted on the same board/level as the pressure transducers and microphone amplifiers. The specific device is manufactured by Analog Devices (model AD595), and it is a complete instrumentation amplifier and thermocouple cold junction compensator that can be used with type J, K or T thermocouples. Readily available type-T were used in this experiment. Additionally, the AD595 is able to produce a (10 mV/°C) output directly from a thermocouple signal.

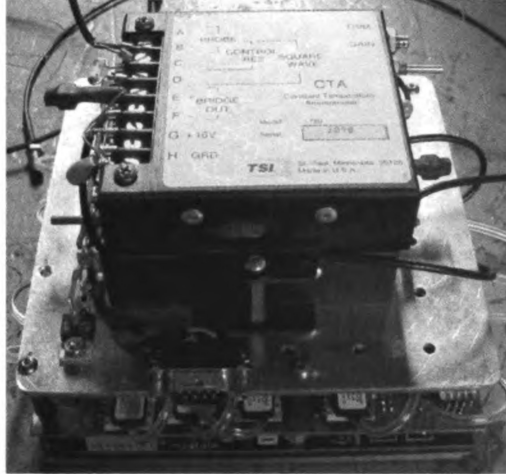


**Figure 4.14:** Compact anemometers in RCBD instrument cluster

#### 4.2.2.4 Level 3: Hot-wire constant temperature anemometers

Two TSI 1750 anemometers were mounted in the instrument cluster in the RCDB. These devices were tested and evaluated in advance and shown to give sufficient frequency response ( $f_c > 20kHz$ ) when used with the custom fabricated probes for the rotating reference frame measurements. These anemometers are shown in Fig. 4.14.

#### 4.2.2.5 Level 4: Pressure reference chamber

The differential pressure transducers require a known reference pressure. The desired reference pressure for the RCDB experiment is the ambient atmospheric pressure,  $P_{atm}$ , since this is used the stationary CD airfoil experiments. However, locating  $P_{atm}$  in the rotating reference frame is a non-trivial task. This was accomplished through the use of an isobaric reference chamber, as shown in Fig. 4.15. This chamber provides a known reference pressure for each of the 22 small pressure transducers. The top of the chamber is left open so that it feels the pressure under the cover of the RCDB hub, which is assumed to be the same as that of the upper receiver of the AFRD. This configuration allows for the surface pressure measurements to be corrected so

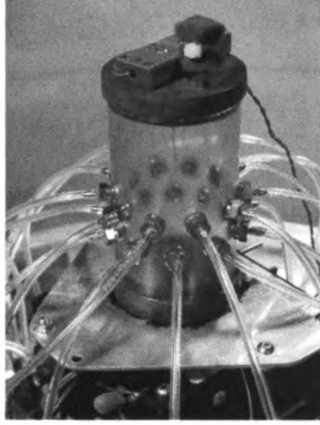


**Figure 4.15:** Isobaric reference chamber in the RCDB

that the reference pressure is the atmospheric pressure, since the relationship of the upper receiver pressure to the atmospheric pressure is known.

### 4.2.3 Centrifugal correction for pressure transducers

The 22 pressure transducers that are mounted in the RCDB hub are used to measure pressures that exist at the mid-span of the blade. There is a radial separation that exists between the pressure taps at the blade's mid-span and the pressure transducers (see Fig. 4.16) and this creates a pressure gradient in the rotating reference frame:

$$\frac{\partial P}{\partial r} = \rho \frac{V^2}{r} \quad (4.1)$$

where  $V = r\omega$ , so Eq. 4.1 becomes:

$$\frac{\partial P}{\partial r} = \rho \frac{r^2 \omega^2}{r} = \rho \omega^2 r \quad (4.2)$$

Separating variables and integrating both sides

$$\int \frac{\partial P}{\partial r} dr = \int \rho \omega^2 r dr \quad (4.3)$$

yields the following relationship:

$$P(r) = P(0) + \frac{\rho\omega^2 r^2}{2} \quad (4.4)$$

Since the radial location of the pressure transducers,  $r_{sensor}$ , is different from the radial location of the pressure taps on the blade,  $r_{taps}$ , the measured pressure will be altered due to the centrifugal accelerations and a correction must be applied. Note that all the taps are at the same radial position ( $r_{taps} = 303$  mm).

$$P_{taps} = P(0) + \frac{\rho\omega^2 r_{taps}^2}{2} \quad (4.5)$$

$$P_{sensor} = P(0) + \frac{\rho\omega^2 r_{sensor}^2}{2} \quad (4.6)$$

Subtracting Eqs 4.6 and 4.5 yields the pressure correction that must be applied to the input pressure:

$$\Delta P_{corr1} = \frac{\rho\omega^2 (r_{taps}^2 - r_{sensor}^2)}{2} \quad (4.7)$$

The pressure correction,  $\Delta P_{corr1}$  represents the correction needed to accurately measure the pressure,  $P_{taps}$  at a smaller radius than where the taps are located (i.e. remote mounting). This correction must also be applied to the reference pressure (since the pressure transducers are differential, i.e.  $\Delta P_{meas} = P_{tap} - P_{ref}$ ), which is measured at a larger radius,  $r_{sensor} > r_{ref}$ . The reference pressure must be corrected to account for the larger radius:

$$\Delta P_{corr2} = \frac{\rho\omega^2 (r_{ref}^2 - r_{sensor}^2)}{2} \quad (4.8)$$

The radial distance from the center of rotation to the measurement locations for  $P_{tap}$  and  $P_{ref}$  is denoted by  $r_{tap}$  and  $r_{ref}$ , resp. Given that the location of the isobaric reference chamber is at the center of rotation,  $r_{ref} = 0$ . In the current configuration

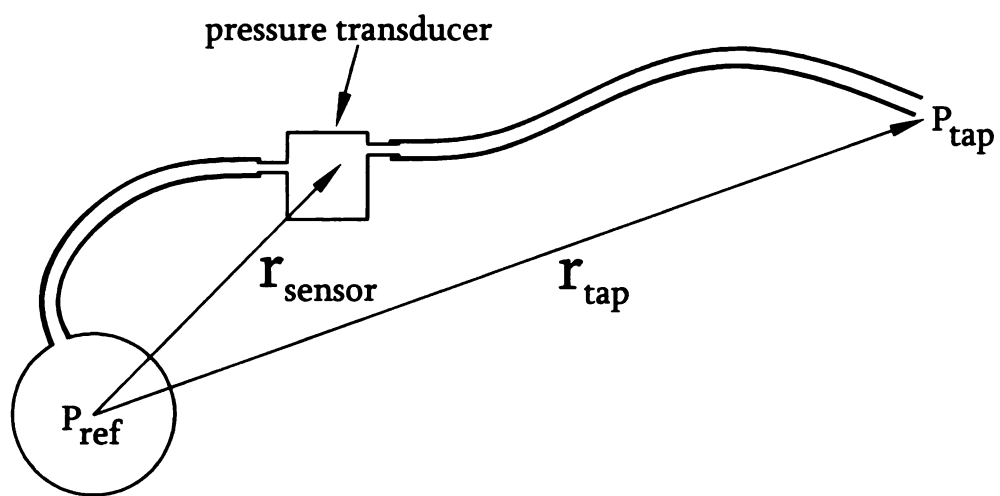


**Figure 4.16:** Description of centrifugal correction terms

$r_{sensor} > r_{ref}$ , so the reference pressure must be reduced to account for the larger radius. These two corrections are combined in the following manner:

$$[P_{taps} - P_{ref}] = \Delta P_{meas} + \Delta P_{corr1} + \Delta P_{corr2} \quad (4.9)$$

The expression  $\Delta P_{meas}$  represents the differential pressure as measured from the MEMS pressure transducers and  $\Delta P_{act}$  is actual pressure difference that would be measured if the both the  $P_{ref}$  and  $P_{taps}$  existed at the same radial location. Eq. 4.9 can be written as follows:

$$\Delta P_{meas} = P_{taps} + \frac{\rho\omega^2(r_{taps}^2 - r_{sensor}^2)}{2} - \left( P_{ref} + \frac{\rho\omega^2(0 - r_{sensor}^2)}{2} \right) \quad (4.10)$$

Which yields the final relationship between the actual differential surface pressure,  $P_{tap}$ , and the measured (in the present experiment) differential surface pressure:

$$[P_{taps} - P_{ref}] = \Delta P_{meas} + \frac{\rho\omega^2 r_{taps}^2}{2} \quad (4.11)$$

## 4.2.4 RCDB coordinate systems

### 4.2.4.1 Conventional turbomachinery coordinates

The conventional coordinate system, used in axial turbomachinery, is a polar coordinate system,  $r$ - $\theta$ - $z$ , where  $z$  is along the axis of rotation,  $\theta$  is in the plane of rotation, and  $r$  is along a radial line that is normal to the axis of rotation. This coordinate system is shown in Fig. 4.17. The data collected for this study have been processed using this coordinate system; however, they are not presented here in this form. It is anticipated that data processed in this coordinate system would be of primary use for CFD simulations. Since the primary purpose of this study is to evaluate the flow field of the RCDB in contrast to that of its stationary analog, a different coordinate

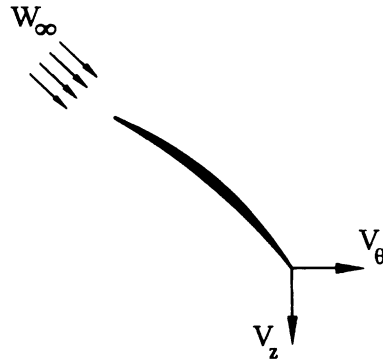


**Figure 4.17:** Polar coordinate system typically used for turbomachinery studies

system is used. This coordinate system is presented in the following section.

#### 4.2.4.2 Rotated coordinates for comparisons with stationary CD airfoil

The coordinate system used to present the data in the RCDB studies is shown in Fig. 4.18. This is unconventional for typical turbomachinery studies, but it allows for the data to be presented in a form which allows for a relatively direct comparison with the CD airfoil. However, one important distinction remains between the two experiments. Because of the limitations of the traverse in the AFRD facility, the  $u-v-w$  velocities are presented in traverses along the  $r-\theta-z$  directions, with the streamwise direction being the  $z$ -direction and the normal direction being the  $\theta$ -direction (typically presented in  $r\theta$  coordinates to yield proper dimensions). The  $r$ -direction in the RCDB is consistent with the  $z$ -direction in the CD airfoil experiment.

#### 4.2.5 Rotating hot-wire traverse

Rotating HWA data were collected using a rotating traverse, shown in Fig. 4.19. This traverse was designed to position the probe at the midspan of the blade ( $r = 303 \text{ mm}$ ), while allowing for the probe to traverse in fine increments in the  $\theta$ -direction. The features of this traverse are marked by letters in Fig. 4.19. The related content is described below:



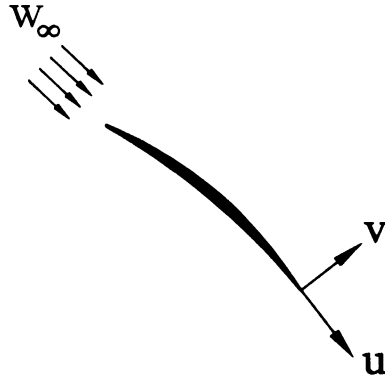


**Figure 4.18:** Coordinate system used for comparisons with CD airfoil data

- (A) Collar that supports the probe positioning assembly. This component was critically important to ensure that fine adjustments could be made during the measurements.
- (B) Counter weight to ensure balance.
- (C) Radial arm that allows the probe tip to be accurately spaced near the blade's trailing edge.
- (D) Vertical support to provide counterweight for centrifugal forces imparted on X-probe. This maintains the radial position of the X-probe.
- (E) Probe used for the measurements.

The vertical alignment of the probe is accomplished by an adjustment that is enabled in the vertical support, shown in item (D). A close-up view of item (A) is shown in Fig. 4.20. This figure shows the lead screw that is positioned between two brass inserts. The two brass inserts and lead screw can be removed prior to spinning the RCDB to reduce the weight (and added potential for imbalance). However, it was found that leaving these pieces installed did not affect the rotational balance of the RCDB experiment. Adjustment of the lead screw (back and forth) allows for the angular position ( $r\Delta\theta$ ) of the rotating X-probe to be moved relative to one

blade of the RCDB assembly. The angular position was adjusted while maintaining a constant radial position ( $r = 303\text{mm}$ ). This allowed for various points in the wake to be measured at the midspan in the rotating reference frame. Angular adjustments of  $r\Delta\theta = 0.4\text{ mm}$  were possible with this rotating traverse.

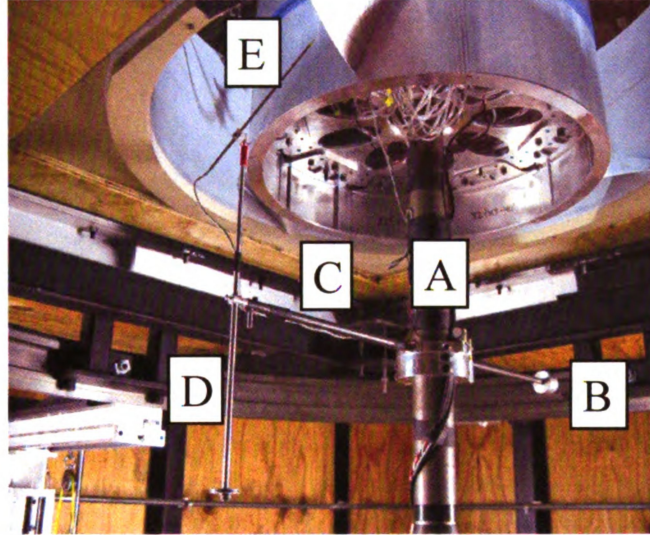


**Figure 4.19:** Rotating traverse assembly used for rotating X-probe measurements (see Sec. 4.2.5 for the legend entries A-E).

### 4.3 Particle Image Velocimetry (PIV)

Planar PIV measurements were collected for both the CD Airfoil and the Rotating CD Blade (RCDB) experiments. A commercially available system from LaVision, consisting of an ND-Yag laser (New Wave Minilase III, 50 mJ/pulse at 532 nm), and a LaVision Imager Intense CCD camera (12-bit,  $1376 \times 1040$  pixels and the ability to collect two images with 500 ns interframing time) were the core components of the system. Proper seeding of the flowfield was accomplished through the use of a Laskin nozzle seeder. Processing was performed using DaVis 7.2 from LaVision, which has the highest accuracy of any commercially available software (Stanislas *et al.*, 2008). In both PIV experiments, it was not easy to directly image at a  $90^\circ$  angle to the laser

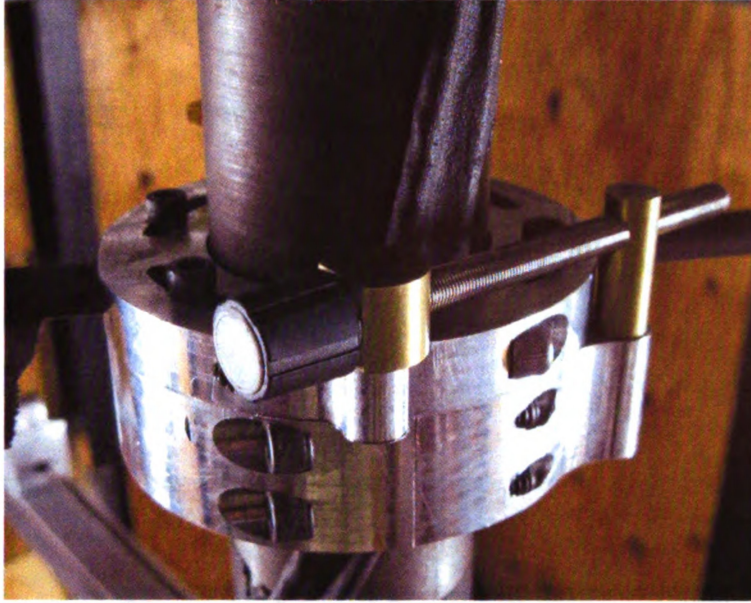


**Figure 4.20:** Close-up view of the fine positioning assembly of the rotating traverse.

plane, so it was necessary to image at an angle substantially greater than  $90^\circ$ . A Scheimpflug adapter was added to the camera to provide a uniform depth-of-field by creating an intersection between the image, subject and lens planes. Image correction was accomplished using DaVis 7.2 to account for distortions introduced using the Scheimpflug adapter and imaging at an obtuse angle.

#### 4.3.1 CD Airfoil in the $0.61m \times 0.61m$ wind tunnel

The PIV experiments for the CD airfoil used two different measurement planes: i) one with the image at the trailing edge and ii) one slightly downstream, as shown in Fig. 4.21. A slight overlap between the two image planes was present. The image planes were slightly trapezoidal, as result of the image correction described above. The general layout of the system is shown in Fig. 4.22. The left picture in Fig. 4.22 shows the experimental configuration in normal lighting conditions. The laser is positioned downstream and fires upstream towards the trailing edge. The CCD camera is positioned below the jet flow and points upward and slightly downstream to properly



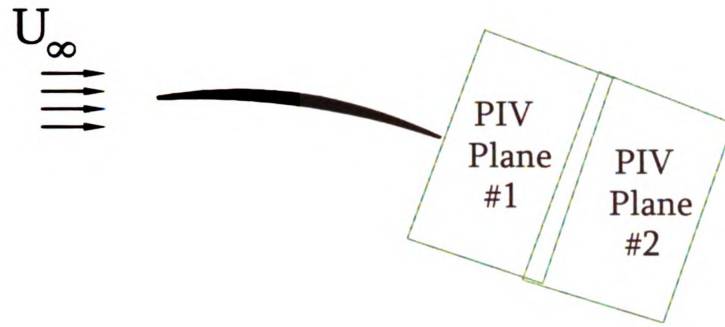


**Figure 4.21:** Two measurement planes used for PIV experiments

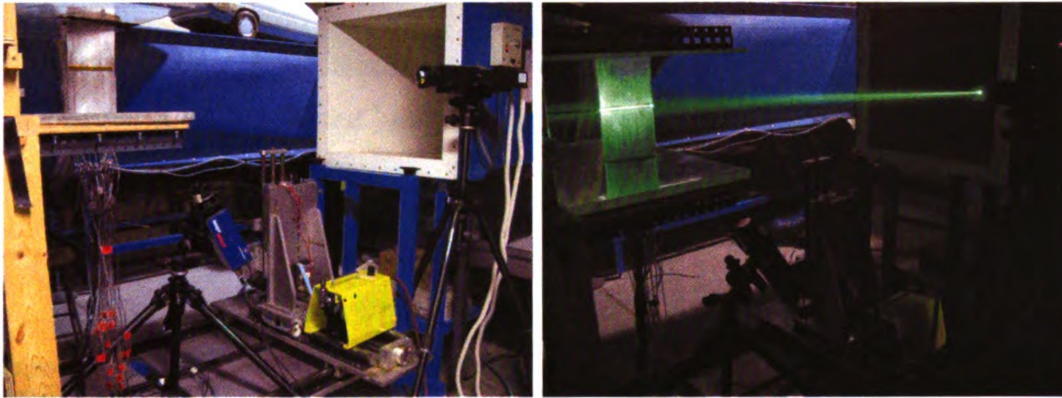


**Figure 4.22:** Left: PIV set-up for the CD Airfoil. Right: PIV set-up during data collection.

image the trailing edge region. The Laskin nozzle seeder is shown just below the downstream tunnel inlet. The smoke particles are introduced downstream and then recirculated through the wind tunnel. The high intensity laser light hitting the aluminum airfoil did cause a considerable amount of reflected light energy, as seen in Fig. 4.23. This caused a slight “washed out” region around the trailing edge where reliable data could not be obtained. This parasitic effect was minimized through the use of a very thin polyimide film tape that had an orange color, providing good absorptive characteristics for the 532 nm (green) wavelength laser light. Very near wake measurements were not possible with the PIV, but reliable data at  $x/c > 0.10$  were possible.

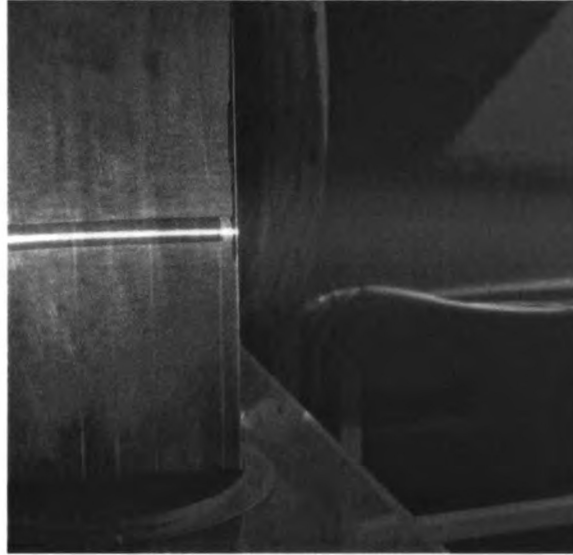


**Figure 4.23:** Reflected laser light near the CD airfoil trailing edge region

### 4.3.2 RCDB in the AFRD Facility

Phase-averaged PIV data were collected for the RCDB in the AFRD facility. The experimental configuration is shown in Fig. 4.24. An optical encoder was used to provide a once-per-revolution trigger signal that was synchronized with the PIV system through the triggering capabilities of the programmable timing unit (PTU) for the PIV system. Two different measurement planes for PIV were collected for the RCDB. The first plane, shown schematically in the left side of Fig. 4.25, provides details of the wake region for the RCDB and is very similar to the PIV plane measured in the CD airfoil experiment. The right side of Fig. 4.25 shows an additional plane, the  $r$ - $z$  plane, which was also measured. Note that the laser light sheet plane (and subsequently the measurement plane) is vertically aligned with the  $z$ -direction defined in Fig. 4.18. For this measurement set, the objective was to see the evolving wake structure as it pass through the vertically aligned measurement plane. This was accomplished by phase-averaging data that were collected for 12 different blade-to-light sheet orientations (for a moving blade passing by the stationary light sheet).

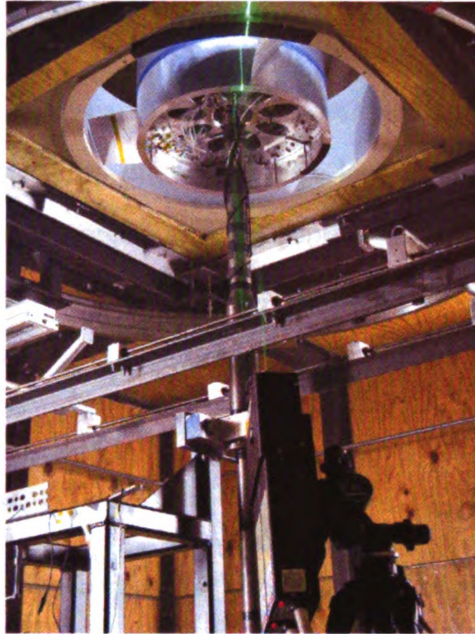


**Figure 4.24:** PIV set-up for the RCDB in the AFRD Facility

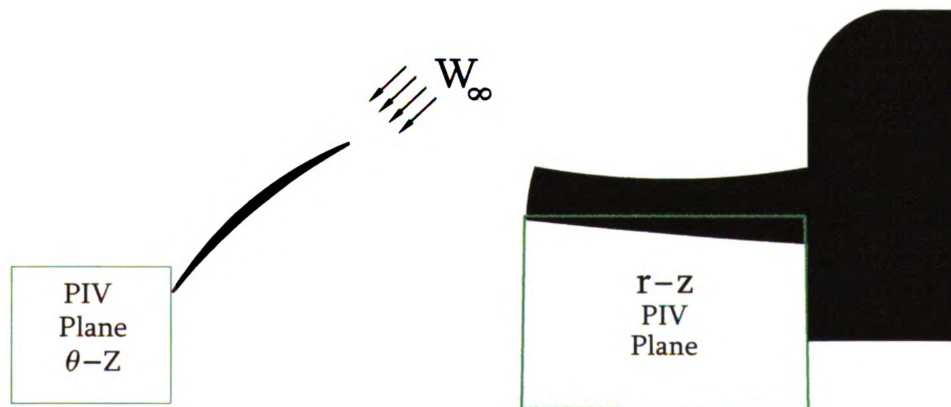


**Figure 4.25:** Left:  $\theta$ - $z$  plane for RCDB PIV data Right:  $r$ - $z$  plane for RCDB PIV data

## 4.4 Conventional Hot-wire Anemometry (SN-Probe and X-Probe)

The X-probes used for this research have been designed and fabricated at the TSFL. They have two 1 mm long  $5\mu\text{m}$  diameter active length tungsten sensors. These are supported, at  $\pm 45^\circ$  from the probe axis, by copper-plated ends that are attached to the prongs, which are separated by 3 mm. The design of this probe follows on the recommendations of Strohl & Comte-Bellot (1973).

### 4.4.1 Calibration

A standard calibration for both speed ( $Q$ ) and angle ( $\alpha$ ) is performed for the X-probes used in this research. This was accomplished using the facility shown in Fig. 4.26. This facility allows for the calibration of X-probes between the yaw angles of  $\pm 36^\circ$  in increments of  $\Delta\alpha = 6^\circ$ . This angle increment is fixed, since it is set by precisely machined holes that line up with the probe-holding mechanism. The result is 13 unique calibration curves for each of the two sensors. X-probes calibrated in this facility make use of the *quasi-steady* calibration technique described in Sec. 5.2.8 of Tropea *et al.* (2007) for standard X-probes (note that this reference refers to this as a *controlled transient* calibration). This approach decreases the time required for calibration while maintaining the accuracy of the technique. The sensor voltage at each yaw and speed combination is correlated with the jet velocity using the following relationship:

$$E_i^2(\alpha) = A_i(\alpha) + B_i(\alpha)Q_i^{n(\alpha)} \quad (4.12)$$

Where  $n$  is treated as a variable parameter that is established by minimizing the sum of errors squared (SES) for the least squares curve-fit. This approach has been attributed to a number of different authors as summarized in Bruun (1995).

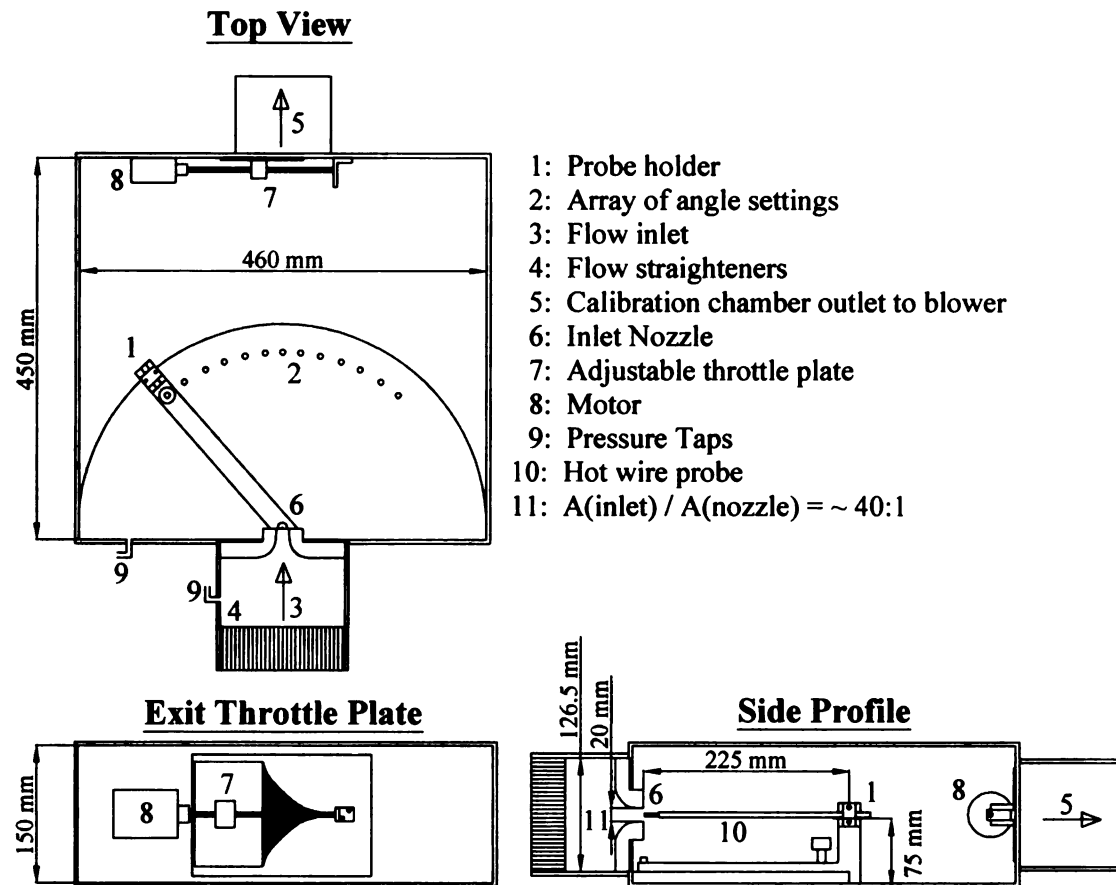


**Figure 4.26:** Calibration facility for quasi-steady calibration on standard X-probes



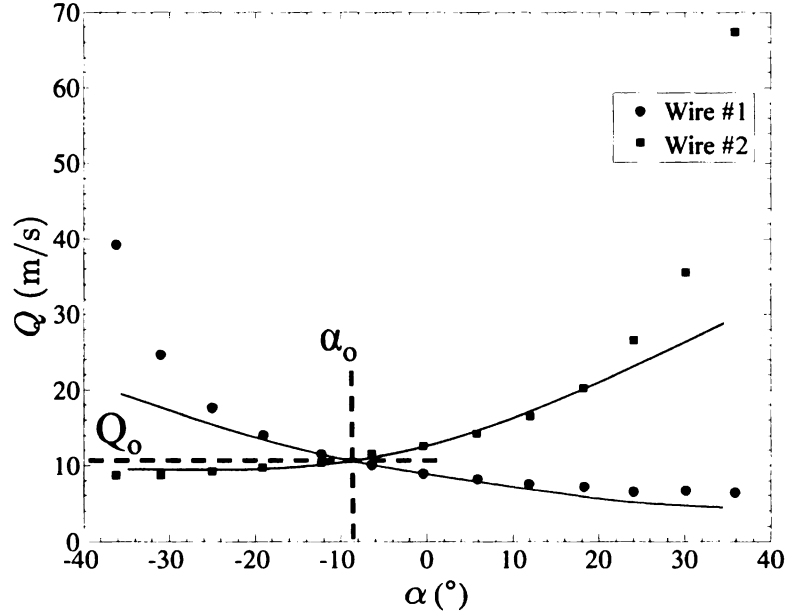


**Figure 4.27:** Calibration data for  $E_1$  and  $E_2$  showing dependence on  $\alpha$

#### 4.4.2 Data reduction

The two voltage signals that are measured by the X-probe are related to the incoming velocity vector using a data reduction method that was introduced by Browne *et al.* (1988) for standard X-probe processing and also developed in the TSFL at MSU and described in Sec. 5.2.8 of Tropea *et al.* (2007). Each sampled voltage pair ( $E_1$  and  $E_2$ ) are processed by each of their 13 calibration curves, described in Sec. 4.4.1. This results in 26 discrete velocity values (13 for each wire). These 26 velocity values can be plotted on common axes, as shown in Fig. 4.27. The 13 velocity values from each sensor form two monotonically varying curves, one that is increasing and one that is decreasing. The intersection of these two curves provide the correct values of ( $Q$ ) and ( $\alpha$ ) for the measured voltages,  $E_1$  and  $E_2$ . This intersection is identified by using a second order curve fit on the three calibration points that are closest to the intersection, as shown in Fig. 4.27. The velocity magnitude,  $Q$ , is then calculated from each of these curvefits for the identified value of  $\alpha$  and averaged.

## 4.5 4-sensor HWA probe: The 2X-probe

Although the use of 4-wire probes are common in the literature (see Döbbeling *et al.* (1990a,b); Marasli *et al.* (1993); Wittmer *et al.* (1998); Beharelle (1999); Maciel & Gleyzes (2000); Lavoie & Pollard (2003)), these investigators have typically used a commercially available probe (AUSPEX AVEP-4-103) or a geometry that is quite similar. The present research used a custom-designed probe that was developed and fabricated in the Turbulent Shear Flows Laboratory (TSFL) at MSU. The probe, as shown in Fig. 4.28, consists of two standard X-arrays that are fabricated such that the active sensor region occupies a small area (approx. 0.75 mm x 0.75 mm). This arrangement requires that the 4th sensor is mounted by threading it underneath one of the previously mounted sensors, a technique that was originally developed for the Mitchell probe (see Bruun (1995)). The 2X-probe design is therefore a hybrid design of two established techniques, the X-probe and the Mitchell probe. As seen in Fig. 4.28, the 2 X-arrays are oriented such that one array (wires 1 & 2) can resolve incoming flow angles in the yaw (i.e. horizontal) plane and the second array (wires 3 & 4) can resolve incoming flow angles in the pitch (i.e. vertical) plane. The challenges to successfully use this probe can be divided into two primary categories: calibration and data processing (typically referred to as data reduction in the literature). The developments that were completed for the 2X-probe in these two areas are described in the following sections.

### 4.5.1 A new calibration strategy for the 2X-probe

The 2X-probe must be calibrated over multiple combinations of the pitch ( $\alpha$ ) and yaw ( $\beta$ ) planes to ensure the best accuracy for the measurements. Previous studies (Marasli *et al.*, 1993) have relied on analytical derivations to relate the probe signals to the velocity vector, but these methods have been shown to be the least accurate

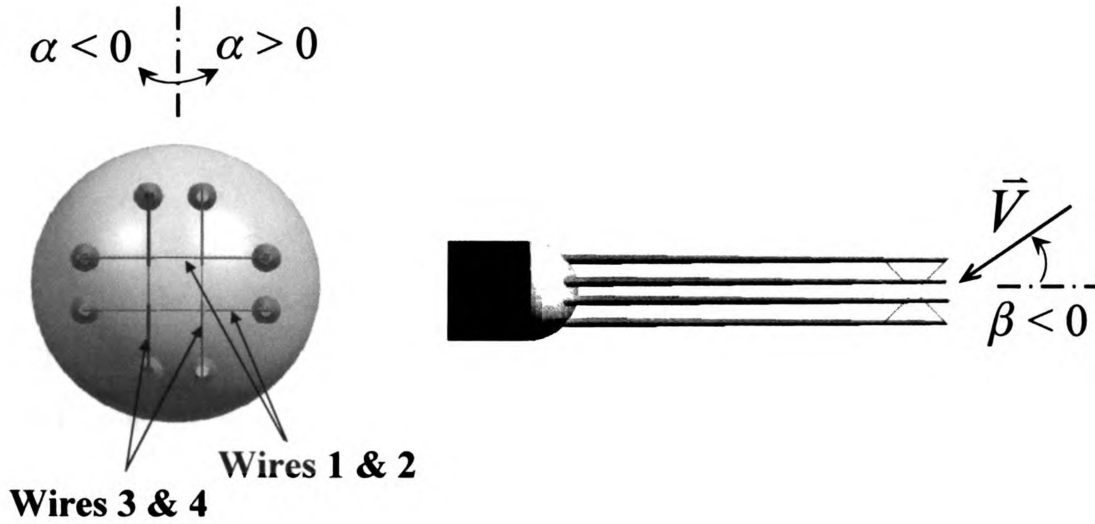


**Figure 4.28:** 2X-Probe (left - top view; right - side view)

(Lavoie & Pollard, 2003). Another approach is to use look-up tables and then use a method (i.e. effective cooling velocity concept, analytical functions, etc.) to decouple the velocity magnitude from the directional response of the probe (see Döbbeling *et al.* (1990b); Wittmer *et al.* (1998); Beharelle (1999); Maciel & Gleyzes (2000)). This approach requires a single velocity calibration (over a range of velocities) at one fixed orientation ( $\alpha = \beta = 0$ ) and a directional response calibration at one fixed velocity over a range of pitch and yaw angles that cover the extent of the desired calibration domain. These approaches can improve upon the accuracy of the analytical methods, but they still have higher errors at large incidence angles and they also require very long times for calibration (Lavoie & Pollard, 2003).

The approach used in this dissertation is to not decouple the velocity calibration from the directional response calibration. In addition, it makes use of the *quasi-steady* calibration technique described in Sec. 5.2.8 of Tropea *et al.* (2007) for standard X-probes and also previously described in Sec. 4.4.1. This quasi-steady calibration concept is performed for the 2X-probe at each unique combination of pitch and yaw over the entire calibration domain. The calibration domain used in this dissertation

is  $-36^\circ \leq \alpha, \beta \leq +36^\circ$ . The sensor output at each pitch and yaw orientation is correlated with the jet velocity using King's law:

$$E_i^2(\alpha, \beta) = A_i(\alpha, \beta) + B_i(\alpha, \beta)Q_i^{0.45} \quad \text{where } i = 1 : 4 \quad (4.13)$$

Note that the modification to fix  $n=0.45$  rather than 0.50, as suggested by Collis & Williams (1959) is used. Eq. 4.13 is different than the form used in Eq. 4.12 and the reasons are described later in this section. This procedure results in calibrations of 169 or 81 orientations for angle increments of  $6^\circ$  or  $9^\circ$ , resp. A previous study conducted in the TSFL (de Laborderie, 2007) indicated that comparable accuracies in conventional X-probes could be obtained by using an increment of  $9^\circ$ . The ability to adjust the  $\Delta\alpha$  and the  $\Delta\beta$  for the 2X-probe calibration was made possible by the 2X-probe facility shown in Fig. 4.29. The 2X-probe calibration facility can set the pitch and yaw orientations of the 2X-probe into any combination, down to a fraction of a degree. The ability to make these adjustments is different than the facility shown in Fig. 4.26, which uses precision machined holes to define the (yaw only) calibration angles. The facility in Fig. 4.29 uses a rotary potentiometers in conjunction with a voltage divider to generate a voltage which is proportional to the angle. The voltages corresponding to the pitch-yaw orientation of the probe are then recorded throughout the calibration process.

Given the ability to adjust the  $\Delta\alpha$  and  $\Delta\beta$ , the use of  $9^\circ$  angle increments (i.e.,  $\Delta\alpha = \Delta\beta = \pm 9^\circ$ ) allows for over 50% reduction in the number of calibration points. However, even with  $9^\circ$  angle increments, a full 81 point calibration (called the *full calibration*) will take approximately 4 hours. A standard practice in HWA is to collect a pre and post calibration just before and after a dataset. This practice ensures that the integrity of the calibration has been maintained throughout the dataset and also provides the user with a realistic idea of the error bounds caused by calibration drift.

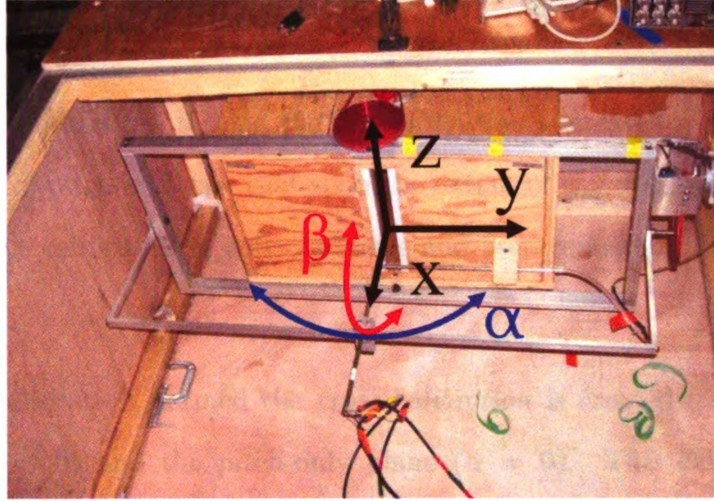


**Figure 4.29:** 2X-probe calibration facility

Since the time required for a full calibration (nominally 4-5 hours to collect an 81 point calibration) is long, it not feasible to collect a full calibration (or multiple full calibrations) each time the probe is used in an experiment.

Some researchers have attempted to shorten this long calibration cycle by performing a full velocity and angle calibration along only the pitch and yaw planes (Dusel, 2005; Rajagopalan *et al.*, 1998), noting that two X-arrays used in conjunction could logically be calibrated in such a manner. This significantly reduces the time for calibration since it only requires 18 pitch-yaw orientations (for  $\Delta\alpha = \Delta\beta = \pm 9^\circ$ ). The data are then processed using conventional X-probe methodologies, therefore processing each X-array separately. This approach introduces substantial errors in the resolved pitch and yaw angles and also the velocity magnitudes that are off-plane, as shown in Sec. 5.1 of this dissertation.

This problem can be solved by adopting a calibration strategy that is described in the following paragraphs. This approach assumes that the directional response calibration is unique to a particular probe and also a particular wire mounting of that probe, whereas the velocity calibration is determined by both the resistance of the individual sensors and also the particular sensor mounting of that probe. The

steps can be summarized as follows:

1. A master calibration, termed the *full calibration* is created over multiple combinations of pitch and yaw that span the extent of the domain,  $-36^\circ \leq \alpha, \beta \leq +36^\circ$ . This calibration is collected once and used repeatedly for the life of the probe.
2. A daily calibration, termed the *cross calibration* is created over the yaw-only plane ( $\beta = 0$ ) and the pitch-only plane ( $\alpha = 0$ ). This calibration can be performed directly before and just after the measurement campaign.
3. The cross and full calibrations are combined using the strategy described in Eqs. 4.14 and 4.15. This combined calibration is referred to as the *pseudo-full calibration*.

This calibration strategy allows for the full calibration, which is too time-consuming to be collected on a daily basis, to be collected once throughout the life of the probe. This full calibration will be used as the master calibration for the life of the probe, until a wire breaks and it must be repaired by mounting new wires. Data supporting this approach are presented in Sec. 5.1. Subsequent calibrations along only the yaw ( $\beta = 0$ ) and pitch ( $\alpha = 0$ ) planes, termed the *cross calibration* will be performed before and after each dataset. Each cross calibration requires approximately one hour, hence it is realistic to routinely collect pre and post cross calibrations. See the solid (interior) lines of Fig. 4.30 for the cross calibration locations. These two datasets are combined to create a new calibration, called the *pseudo-full calibration*. The pseudo-full calibration makes use of the one-time full calibration that adequately describes the coupled velocity calibration *and* the directional response functions, but it also incorporates the information from the frequent cross calibration. The pseudo-full calibration is created by maintaining the ratios of the calibration coefficients (A

and B from Eq. 4.13) for sensors 1 and 2 that exist along the  $-36^\circ \leq \alpha \leq +36^\circ$  and  $\beta = 0$  line for all successive rows ( $\beta \neq 0$ ). These ratios of the A and B coefficients for the yaw sensors (sensors 1 and 2) can be expressed as:

$$A_{m,k}^P = \frac{A_{m,k}^F}{A_{0,k}^F} A_{0,k}^C \quad (4.14)$$

In Eq. 4.14, the superscripts “F”, “C”, and “P” refer to the full, cross and pseudo calibrations respectively; whereas the subscripts “m” and “k” refer to the row and column as shown in Fig. 4.30. The  $n$  coefficient from Eq. 4.13 is fixed, so that  $n(\alpha, \beta) = 0.45$  throughout the entire calibration domain. The ratios calculated in Eq. 4.14 depend on  $n(\alpha, \beta) = 0.45$ . It follows that the B coefficients for sensors 1 and 2 in Eq. 4.13 are calculated similarly. Sensors 3 and 4 (the pitch sensors) get their values for the A coefficient from Eq. 4.13 by maintaining the ratios of the A and B values that exist along the  $-36^\circ \leq \beta \leq +36^\circ$  and  $\alpha = 0$  line for all successive columns ( $\alpha \neq 0$ ). These ratios are represented by the following expression:

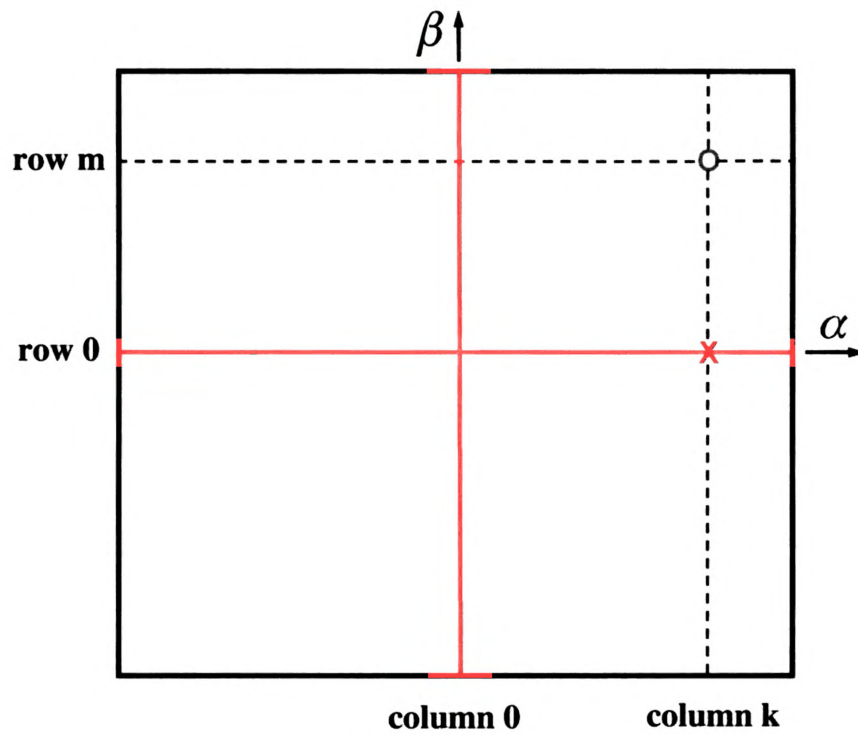
$$A_{m,k}^P = \frac{A_{m,k}^F}{A_{m,0}^F} A_{m,0}^C \quad (4.15)$$

Once again, it follows that the B coefficients for sensors 3 and 4 in Eq. 4.13 would be solved similarly.

## 4.5.2 A new data reduction technique for the 2X-probe: MSU spline search

The reduction of the four voltages measured by the 2X-probe into the sensed three-dimensional velocity vector is a complicated task. It requires taking a set of over-determined, non-linear equations and solving them either analytically or via look-up tables. A number of methods have been developed, but there are limitations to





**X: known in both the cross calibration and the full calibration**

**O: known only in full calibration**

**Figure 4.30:** Description of indexing algorithm for creating the pseudo-full calibration

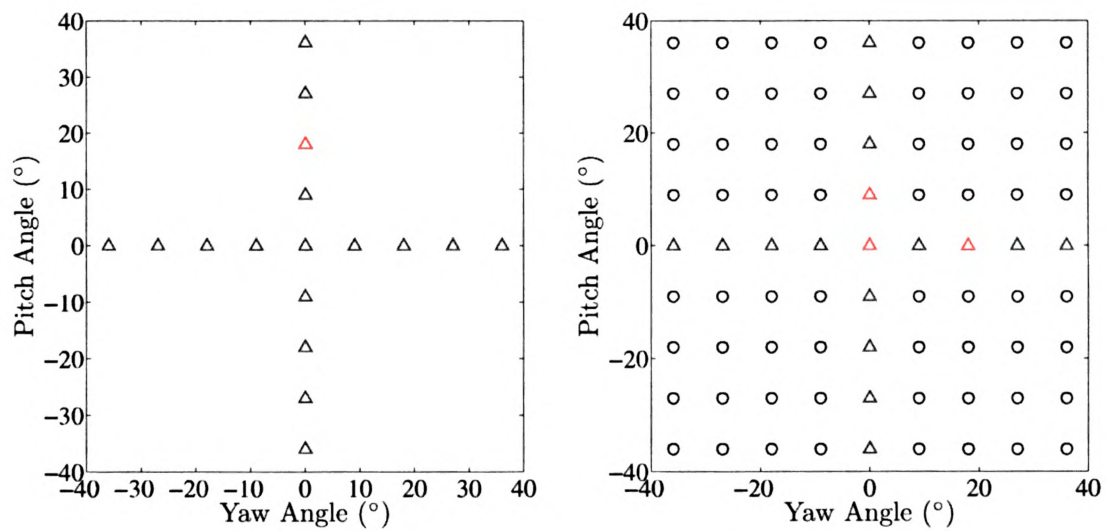


**Figure 4.31:** left - Cross calibration; right - Full calibration



these approaches. Specifically, the methods that rely on analytical derivations have low accuracies in highly turbulent flows (i.e. large incident angles for the measured velocity), as documented in Lavoie & Pollard (2003). The methods involving look-up tables provide greater accuracy in highly turbulent flows, but they have a high computational cost and also have lower accuracies for lower velocities. The latter observation can be directly attributed to the decoupling of the velocity and directional response functions. Lavoie & Pollard (2003) note that the accuracy of some of the published methods (Döbbeling *et al.*, 1990b; Wittmer *et al.*, 1998; Beharelle, 1999) at lower velocities can be improved by recoupling the velocity magnitude and direction. However this would require the use of an iterative algorithm and also that the directional response be known over a large enough range of velocities to accurately represent their variations with velocity. As Lavoie & Pollard (2003) note, this additional iteration step will greatly increase the time needed for data reduction.

The following section describes a new approach developed for this dissertation. The results of this new technique are described in Sec. 5.1 and a comparison with two published methods (Döbbeling *et al.*, 1990b; Wittmer *et al.*, 1998) are presented. The basic steps of the data reduction process can be summarized as follows:

1. The A and B coefficients of a pseudo-full calibration with  $\Delta\alpha = \Delta\beta = \pm 9^\circ$  or  $\pm 6^\circ$  are spline-fitted to a grid with  $\Delta\alpha = \Delta\beta = \pm 0.1^\circ$ .
2. A first guess is made by processing each X-array (pitch-oriented and yaw-oriented) using a cross calibration for standard X-probes as described in Sec. 4.4.
3. This estimate is refined by searching for the minimum value of the parameter,  $\Psi$ , as defined in Eq. 4.16. This search is efficiently performed by using the approach described in the following section.
4. The final value of the parameter,  $\Psi$ , is compared against a reference threshold

value. If the value is lower than the threshold level, the data reduction for that point is complete. If the value is higher, it is reprocessed using a more costly search over a limited domain.

5. The lower  $\Psi$  value from the previous two steps is chosen and its associated values of pitch ( $\alpha$ ) and yaw ( $\beta$ ) are recorded.

The items of the above list are described in detail below. In step #1, the coefficients (A & B) of the full or pseudo-full calibration are curve fitted via cubic splines over the entire domain to a resolution in both the pitch and yaw directions of  $\pm 0.1^\circ$ . This resolution can be altered to match the desired accuracy and a substantial reduction in the computational cost can be obtained by reducing the resolution of the spline grid. However, extensive testing of this method yielded  $\pm 0.1^\circ$  as a good trade-off. The calibration grid is also slightly extended to accommodate small fluctuations at the angle limits ( $\pm 36^\circ$ ), so the final grid is over the domain of  $-38^\circ$  to  $+38^\circ$ . Ultimately, the original calibration grid of 81 unique angle orientations ( $9 \times 9$  grid) becomes 579,121 orientations ( $761 \times 761$  grid). Each of these points are “knots” from the spline calculation.

The next step is to initially process each of the two X-arrays with a data reduction scheme that treats each array separately, identical to the data reduction described in Sec. 4.4. This process uses the cross calibration described previously and shown schematically in Fig. 4.31. This data reduction scheme does not account for the out-of-plane cooling effects on each array and results in substantial error, as shown in Sec. 5.1, but it serves two important purposes. First, it provides a very reasonable first estimate that gives a good starting point for the more advanced processing routine. This point is described in more detail and is supported by experimental results in Sec. 4.4. Second, it is very fast to process this first estimate, so the computational overhead to make this step is very low.

This initial first estimate is refined by evaluating a parameter that can be calculated for each location in the  $761 \times 761$  grid and searching for a minimum value of that parameter. The parameter is an extension of the concept first introduced by Browne *et al.* (1988) for standard X-probe processing and also developed in the TSFL at MSU and described in Sec. 5.2.8 of Tropea *et al.* (2007). The basic idea refers to processing the two voltages of the X-probe over the extent of the calibration range and locating the condition where  $Q_1 = Q_2$ , as shown in Fig. 4.27. For X-probes,  $E_1$  and  $E_2$  are both  $f(\alpha)$  (i.e. yaw angle) only and an intersection of the two curves can be solved for in a straightforward manner, as shown in Fig. 4.27. When this idea is extended to a 4-wire probe, where  $E_1$ ,  $E_2$ ,  $E_3$  and  $E_4$  are  $f(\alpha, \beta)$  (i.e. yaw and pitch), the curves of Fig. 4.27 become *planes* and a single point intersection does not, in general, exist. Therefore, the operating point of the probe for a particular combination of  $Q$ ,  $\alpha$ , and  $\beta$  can be cast as minimization problem, where the objective function to be minimized is defined as:

$$\Psi = |Q_1 - Q_2| + |Q_1 - Q_3| + |Q_1 - Q_4| + |Q_2 - Q_3| + |Q_2 - Q_4| + |Q_3 - Q_4| \quad (4.16)$$

Extensive tests were conducted to verify that  $\Psi$  is a suitable parameter to determine the directional orientation of the incoming flow vector. A typical mapping of Eq. 4.16 over all orientations is shown in Fig. 4.32. The arrow in Fig. 4.32 points to the minimum value of  $\Psi$ . This location is also in the very corner of the calibration domain, which typically is considered to be outside the acceptance domain of 4-wire probes (Lavoie & Pollard, 2003). The accuracy of locating the correct values for  $Q$ ,  $\alpha$ , and  $\beta$  are examined in detail in Sec. 5.1. A unique searching strategy to locate the minimum value of  $\Psi$  has been developed. This searching strategy uses an efficient series of searching steps to take the initial estimate of step #2 in the above processing stages and to find a more accurate final answer. The steps are shown graphically in

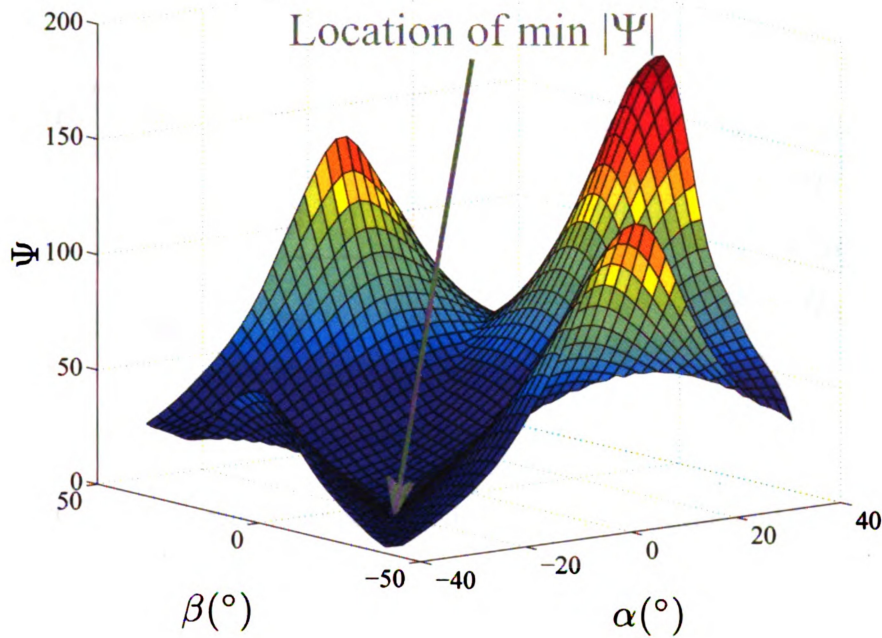


**Figure 4.32:** Mapping of  $\Psi(\alpha, \beta)$

Figs. 4.33–4.37.

1. The value of  $\Psi$  at the initial guess is evaluated against the values of  $\Psi$  at the two neighboring horizontal (yaw) knots separated by a distance “d”. If a lower value exists, then the current location is updated to the location with the lower value of  $\Psi$ . If no lower value exists, the location remains the same.
2.  $\Psi$  at the location from Step 1 is compared with the two adjacent vertical (pitch) knots (again separated by an increment in degrees “d”). If a lower value is found, the location is moved in either vertical direction.
3. The value of  $\Psi$  at the updated knot is now compared along a diagonal axis with the values of  $\Psi$  at the neighboring knots and reassigned if a lower value is found (it remains the same if no lower value is located).
4. Step #3 is repeated along the other diagonal direction

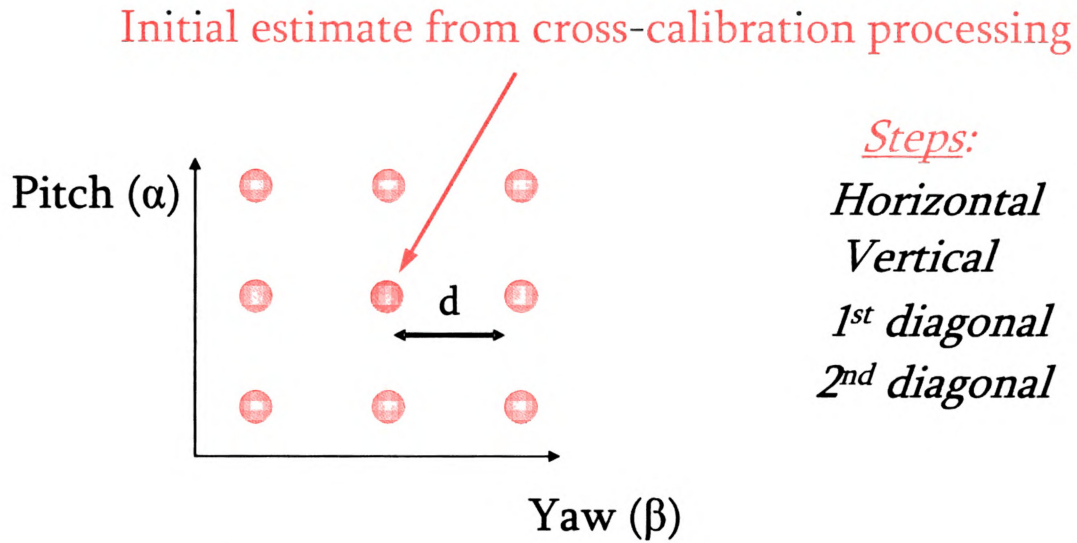


**Figure 4.33:** Spline search method. The initial guess is in the middle and neighboring knots are evaluated (“d” varies).

5. Steps #1–4 are repeated over a range of values for the increment in degrees, “d”. The number of cycles (different values of “d”) along with the values for “d” can be set by the user. This was evaluated empirically and an optimal set of values for “d” was used for this study.

Initial estimate from cross-calibration processing

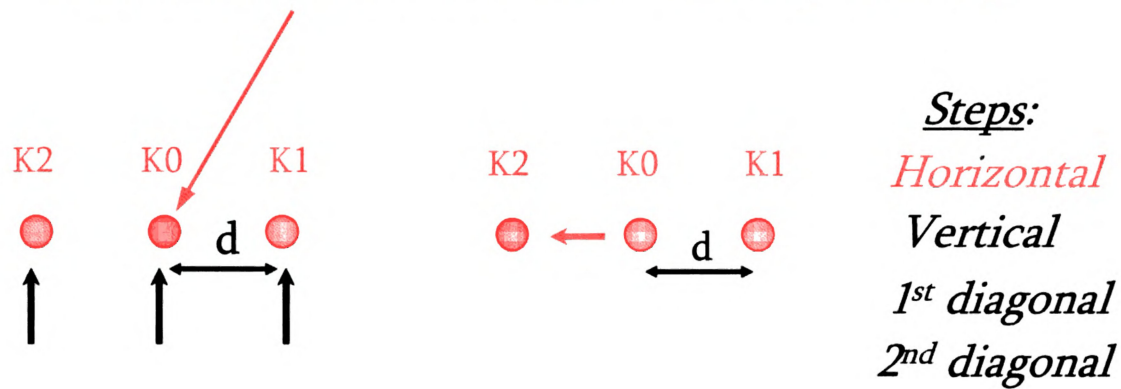


**Figure 4.34:** Left: Current location (K0) and neighbors (K1 & K2) Right: A lower value for  $\Psi$  is found and K1 is the new location.

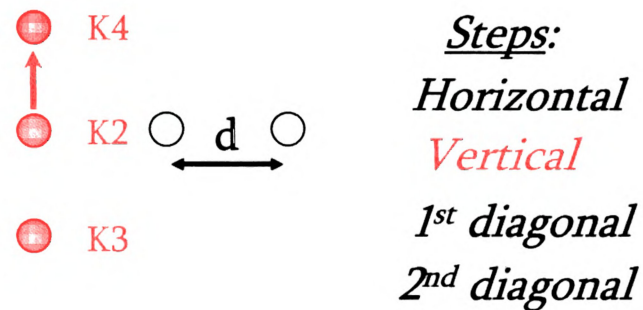


**Figure 4.35:** Neighboring vertical values of  $\Psi$  are evaluated and K4 becomes the new location.

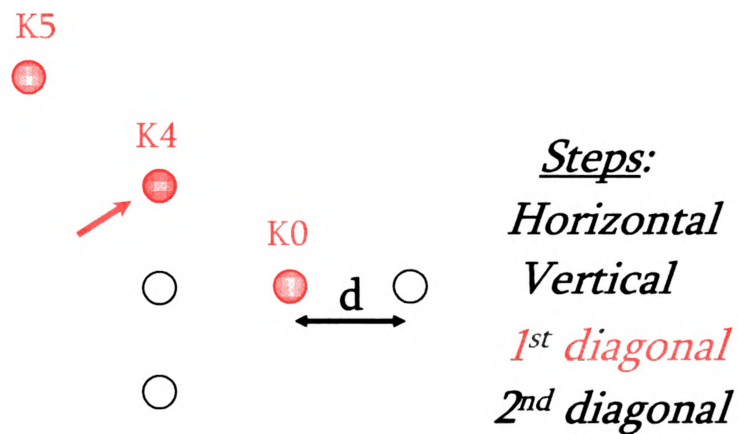


**Figure 4.36:** First diagonal check - location, K4 is retained since no lower value is found.

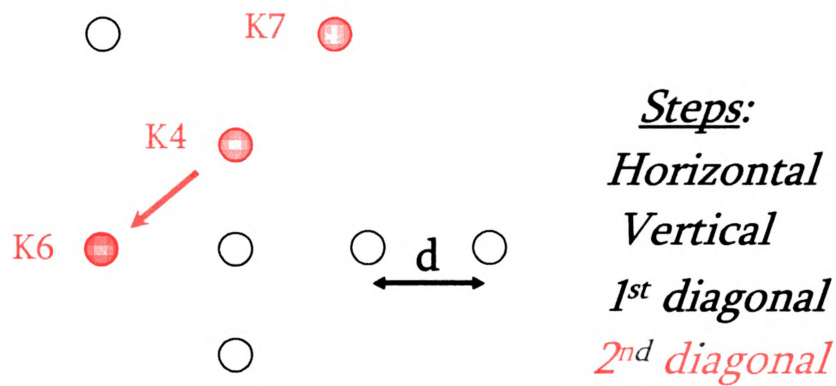


**Figure 4.37:** Second diagonal check - K6 is the new location. This cycle is repeated for multiple values of “d”.

# Chapter 5

## Results

### 5.1 Development of 2X-probe calibration and data reduction techniques

The methods developed in Sec. 4.4.1 for the 2X-probe are evaluated in this section. These methods are compared with two of the best approaches found in the literature (Döbbeling *et al.*, 1990b; Wittmer *et al.*, 1998), based on the conclusions of Lavoie & Pollard (2003). A comparison is provided in this section using an evaluation procedure similar to Lavoie & Pollard (2003). A summary of the methodologies of Döbbeling *et al.* (1990b) and Wittmer *et al.* (1998) can be found in Lavoie & Pollard (2003) and further details can be found in the original papers.

The accuracy of the calibration and data reduction schemes developed in this dissertation were determined by processing several different sets of test data. Since these data are collected in the calibration facility, they have known values of  $Q$ ,  $\alpha$ , and  $\beta$  and the accuracy of any particular data reduction scheme can be evaluated. The study from Lavoie & Pollard (2003) evaluated 4 different calibration and data reduction schemes using a similar approach. Lavoie & Pollard (2003) introduced the following definitions to compute the errors between the inferred and measured velocity



vectors:

1. Relative errors on velocities (%),

$$\varepsilon_{\Phi} = \left( \frac{\Phi_{\text{ref}} - \Phi_{\text{m}}}{\Phi_{\text{ref}}} \right) \times 100 \quad (5.1)$$

where  $\Phi$  is the velocity magnitude,  $Q$ . It could also be the streamwise component of the velocity magnitude ( $u$ ). The relative error of the two normal components,  $v$ ,  $w$ , are undefined (infinity) along the axes where  $\alpha = 0$  or  $\beta = 0$ . This is because their values along these axes are small ( $v \approx 0$  or  $w \approx 0$ ), so their relative errors become large. Therefore, defining a relative error for  $v$  and  $w$  does not make sense. The subscript “ref” is used for the reference quantities and the subscript “m” is used for the measured quantities.

2. Errors on directions, expressed in ( $^{\circ}$ ),

$$\varepsilon_{\Phi} = \Phi_{\text{ref}} - \Phi_{\text{m}} \quad (5.2)$$

here  $\Phi$  is either the yaw angle,  $\alpha$  or the pitch angle,  $\beta$ .

These errors were calculated over the entire extent of the calibration domain (all 81 combinations of pitch and yaw for this study). In order to summarize these errors for this large set of data, the average and the standard deviation of these errors were computed for each orientation. These errors were combined to give an overall estimate of the accuracy of the given data reduction scheme:

$$\vartheta = \sqrt{(\varepsilon_{\text{AVG}})^2 + (2\varepsilon_{\text{STD}})^2} \quad (5.3)$$

As Lavoie & Pollard (2003) write, the average value of the error can be considered an estimate of the bias error caused by the data reduction and calibration scheme,

while the standard deviation represents an estimate of the variation of the errors. The authors additionally state that if no other information is known about the variation of these errors, then the standard deviation can be interpreted as a source of precision error.

Another method of viewing the errors for pitch and yaw over a large number of test points is shown in the joint-angle error plot of Fig. 5.1. In this plot, the 'O' represents the actual (known) pitch-yaw orientation of the incoming velocity vector relative to the 2X-probe and the 'X' represents the resolved pitch-yaw orientation from the data reduction scheme. These two values are connected by a line so the related values can be easily discerned. Figure 5.1 is an example of a joint-angle plot and it shows a few sample orientations (measured and actual). In Fig. 5.1, the orientation on the left has the highest error (i.e. the longest connecting line) and the orientation on the right has the lowest error (nominally zero). The orientations in between these points have errors that are in between these extremes.

### 5.1.1 Data reduction using only the cross calibration

Some authors (Rajagopalan *et al.*, 1998; Dusel, 2005) have used 2X-probe data reduction schemes that only use the calibrations along the  $\alpha = 0$  and  $\beta = 0$  planes, effectively treating the probe as though it were 2 separate orthogonally arranged X-arrays. As discussed in Sec. 4.5.1, this is referred to as the *cross calibration* (noting the shape of the calibration orientations in Fig. 4.31). The accuracy of that approach is discussed here. A cross calibration using the quasi-steady calibration approach described in Sec. 4.5.1 was performed over a speed range of 3-17 m/s. The quasi-steady calibration occurred over a time of 60 secs, following guidelines that are found in Sec. 5.2.8 of Tropea *et al.* (2007).

Separate data sets with  $Q = 4, 8, 12$  and  $16$  m/s were also collected at the time of the calibration over a range of pitch and yaw angles. Using the data reduction

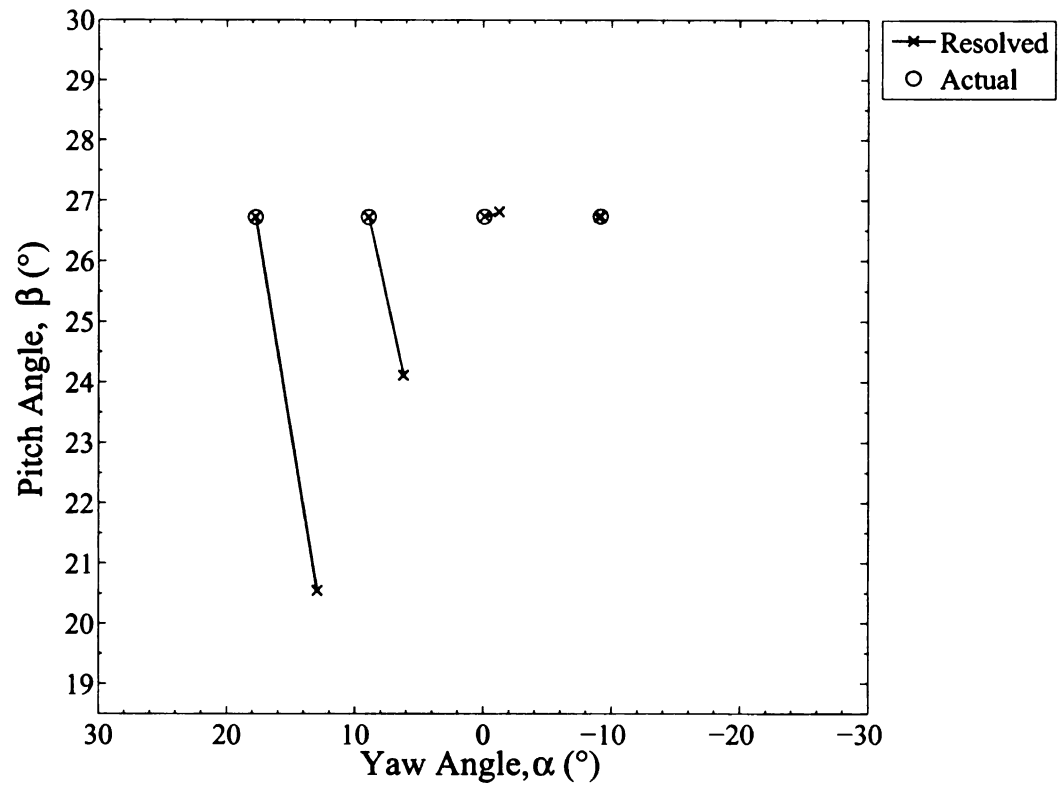


**Figure 5.1:** Example of the joint-angle error plotting used for 2X-probe results.

scheme described in Sec. 4.4 and treating each of the two X-arrays independently during the data reduction processing yields the results shown in the joint-angle error plot of Fig. 5.2. Figure 5.2 shows that for the points that lie along the planes

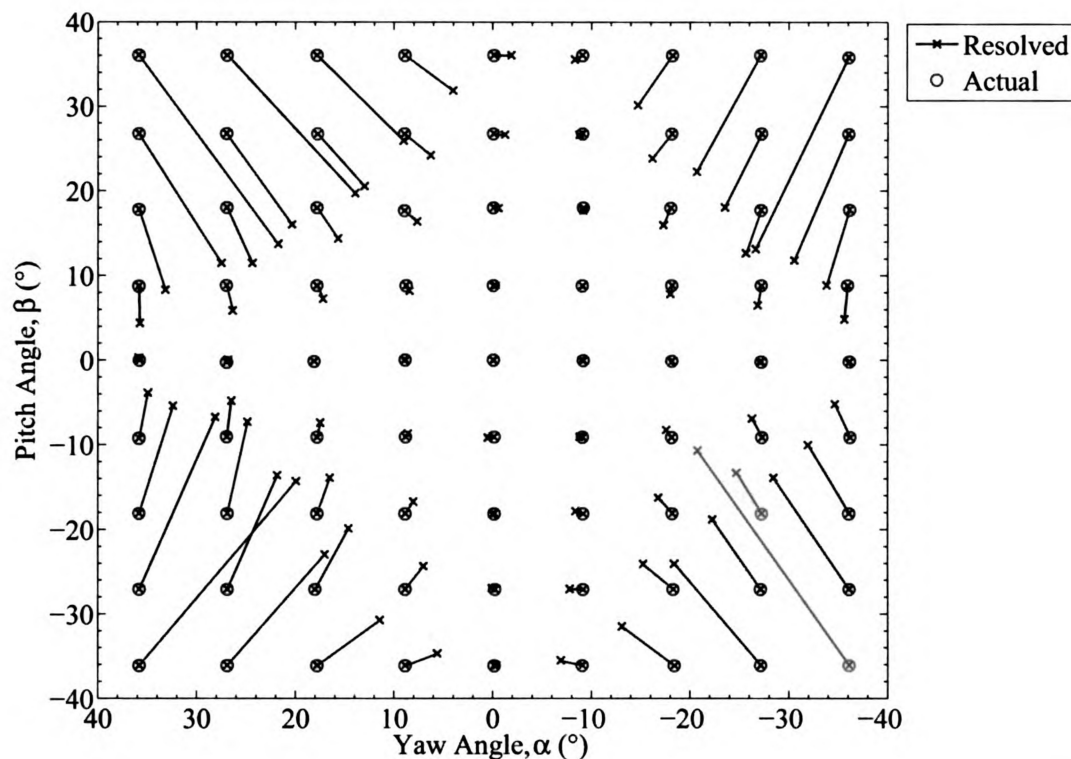


**Figure 5.2:** Pitch-yaw results for test data processed with a cross calibration ( $Q = 12$  m/s).

where  $\alpha = 0$  and  $\beta = 0$ , the angle errors in both pitch and yaw are very small. For the off-axis orientations, the angle error is initially small, but steadily increases as both  $\alpha \rightarrow \pm 36^\circ$  and  $\beta \rightarrow \pm 36^\circ$ . A few interesting details can be noted from these data. First, the effect of bi-normal cooling on a conventional X-probe can be well understood from this plot. For orientations where either  $\alpha$  or  $\beta$  is small (or both are small), the accuracy of the conventional X-probe data reduction scheme is quite acceptable. However, when either  $\alpha$  or  $\beta$  becomes large (or both are large), the errors become significant. Another important observation from these results is that the use of the cross calibration as a first-guess can be quite effective. This is because even the

points with the highest errors (i.e. in the corners) still remain in the correct quadrant where the actual orientation exists.

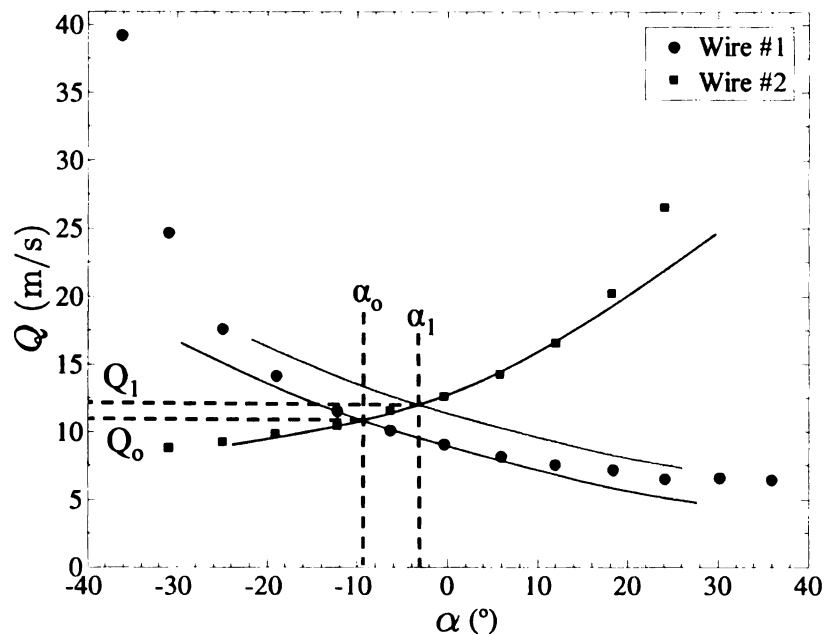


**Figure 5.3:** The effect of off-axis (bi-normal) cooling X-probe processing.

It can be seen in Fig. 5.2 that a very consistent pattern occurs over the entire extent of the calibration domain. There is a tendency for the points that do not accurately recover the pitch and yaw orientation to consistently have angles that are lower than the actual values. This is explained by examining the data reduction technique that is described in Sec. 4.4.2 and also in Sec. 5.2.8 of Tropea *et al.* (2007). Figure 5.3 shows a typical result of processing a single pair of voltages with this data reduction technique. This technique would normally be used for an X-probe that had minimal effects of bi-normal cooling and the intersection of the two curves in Fig. 5.3 would be the angle of the incoming velocity vector as measured by the probe (as shown by  $\alpha_0$ ). If the orientation of the probe were changed so that the in-plane (yaw angle) remained the same, but the probe was placed into an orientation where  $\beta > 0$ , then a bi-normal cooling effect is experienced by the sensors. When the yaw angle is high ( $\alpha \geq 18^\circ$ ), the orientation of the sensors causes this bi-normal cooling to

affect one sensor more than the other. The effect of this bi-normal cooling is shown in Fig. 5.3. The original angle from the data reduction scheme (when  $\beta = 0$ ) is represented by  $\alpha_0$  and the angle when  $\beta > 0$  is represented by  $\alpha_1$ . It can be seen in Fig. 5.3 that  $\alpha_1 > \alpha_0$ , as was also seen in Fig. 5.2. Additionally, it can be seen that  $Q_1 > Q_0$ . Although these results are shown for the sensors that are aligned in the yaw plane, a similar effect occurs for the two sensors that aligned in the pitch plane (where the off-axis cooling is caused by  $\alpha > 0$ ).

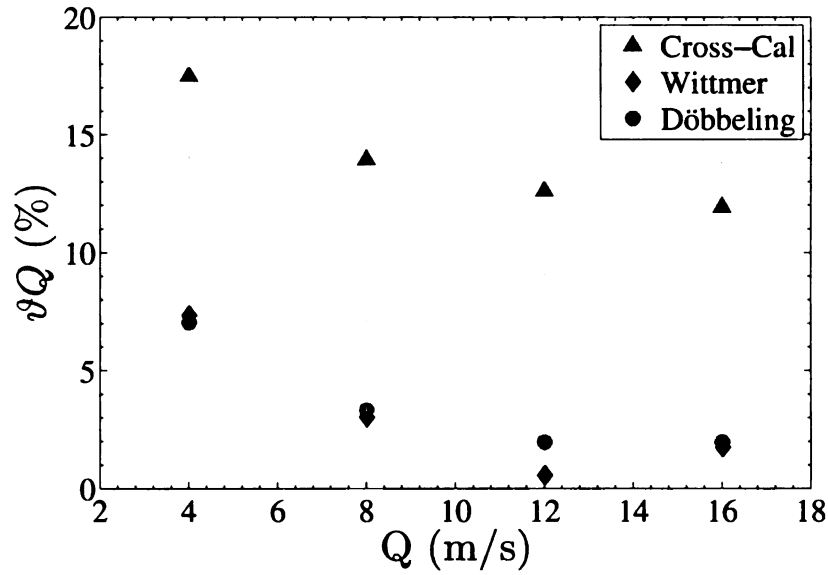


**Figure 5.4:** Overall uncertainty on the velocity magnitude for cross calibration.

The overall uncertainty of  $Q$  ( $vQ$ ) vs. velocity magnitude for the cross calibration data reduction is shown in Fig. 5.4. This figure also includes the results obtained from using methods of Wittmer and Döbbling. As expected, the test data at 4 m/s yields the greatest error for each of the methods and overall the cross calibration method has the highest uncertainty ( $v \geq 12\%$ ). The methods of Wittmer and Döbbling show consistently lower uncertainty at each of the test speeds and their results are nearly identical. Figures 5.5 and 5.6 show the uncertainty for the pitch and yaw ( $v\alpha$  &  $v\beta$ ) for these three methods. Again the cross calibration has the highest overall uncertainty for both pitch and yaw. The method of Döbbling consistently yields the

best results and shows slightly lower overall uncertainty than Wittmer. A consistent trend is found where the overall uncertainty at 12 m/s is the lowest for both Döbbeling and Wittmer. This result is expected since the data for 12 m/s were used to create the angle response calibration for these two methods. Therefore, 12 m/s is the only speed where the angle response and the velocity response remained coupled for Döbbeling and Wittmer.

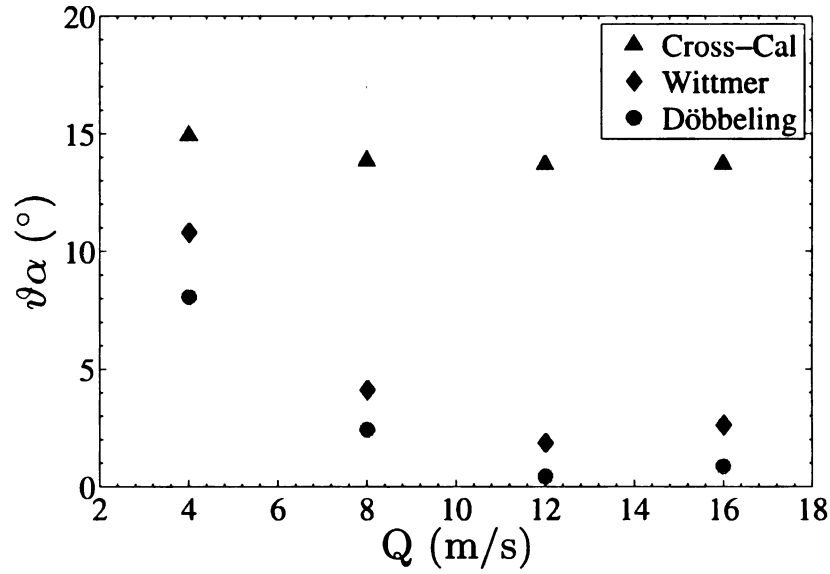


**Figure 5.5:** Overall uncertainty on the yaw angle for cross-calibration.

## 5.1.2 Data reduction using the TSFL Spline Search method

### 5.1.2.1 Comparisons with published results

The same test data that were used in Sec. 5.1.1 were used to evaluate the TSFL Spline Search method for data reduction that was introduced in Sec. 4.5.2. As described in that section, this method uses the cross calibration results as a first guess for the data reduction. This is because the cross calibration results, while limited in accuracy, provide a good initial guess with minimal computational cost. The joint-angle plot for the TSFL Spline Search method is shown in Fig. 5.7. This plot shows

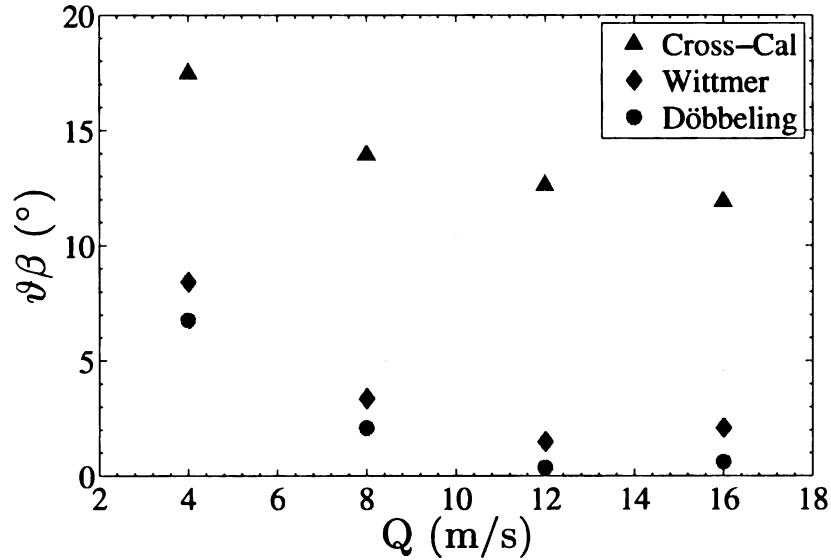


**Figure 5.6:** Overall uncertainty on the pitch angle for cross calibration.

that the error for the off-axis orientations are dramatically reduced through using the pseudo-full calibration. It also shows that the parameter:  $\Psi$  (Eq. 4.16), is a suitable parameter for the minimization problem. Additionally, it shows that the searching routine, described in Sec. 4.4.2 can reliably resolve the off-axis orientations that were problematic in the cross-calibration results.

### 5.1.3 Tests of elapsed time between cross and full calibrations

#### 5.1.3.1 Same-day tests (0 elapsed days)

The tests conducted in Sec. 5.1.2.1 were all performed with the calibrations (MSU, Wittmer and Döbbling) collected on the same day as the test data. These calibration require a long time to collect and it is not feasible to do these calibrations on a daily basis. This fact, coupled with the idea that it is standard practice in HWA is to collect a pre and post calibration just before and after a dataset, motivated the development of the pseudo-full calibration strategy described in Sec. 4.5.1. The pseudo-full strategy



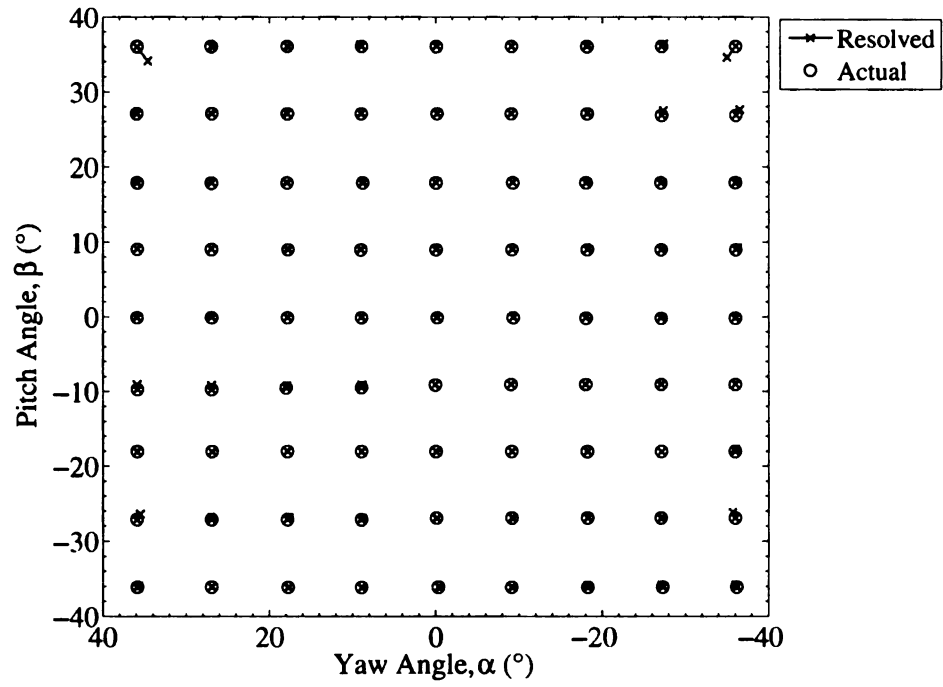


**Figure 5.7:** Pitch-yaw results for test data processed with TSFL Spline Search.

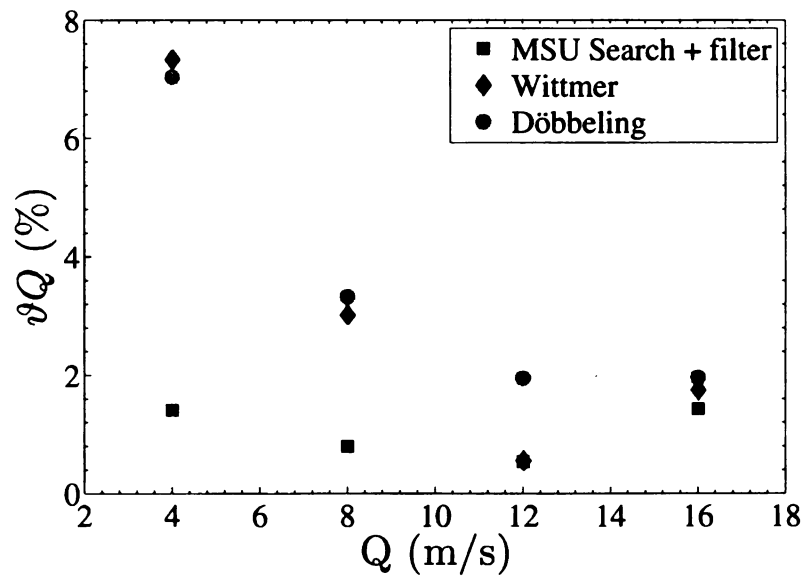


**Figure 5.8:** Overall uncertainty on the velocity magnitude for full calibration.

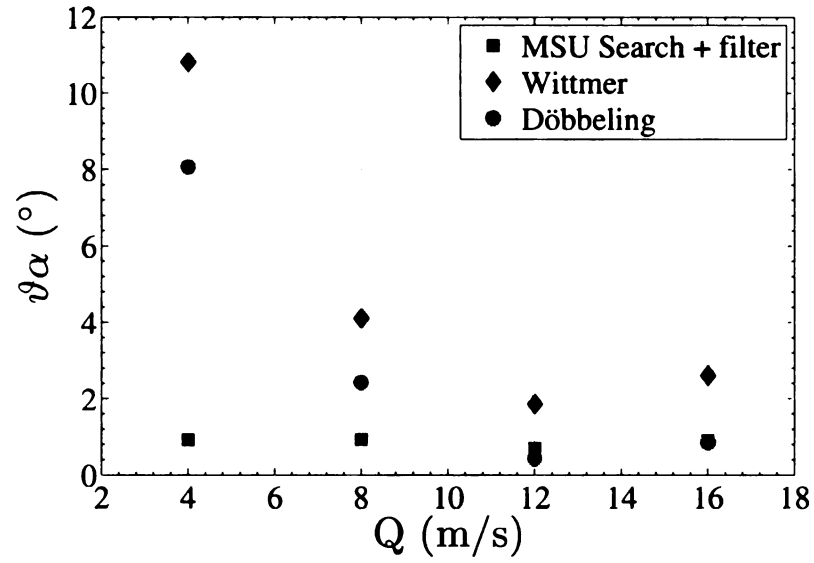


**Figure 5.9:** Overall uncertainty on the yaw angle for for full calibration.

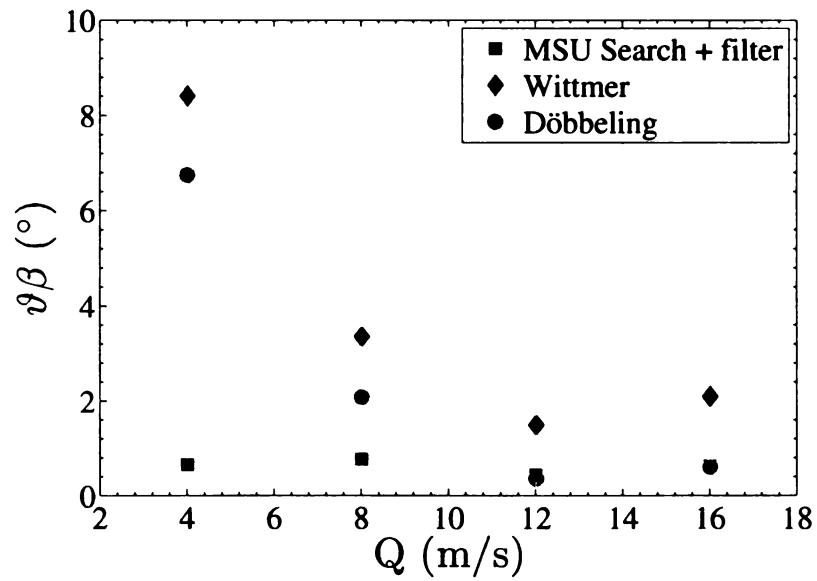


**Figure 5.10:** Overall uncertainty on the pitch angle for full calibration.

assumes that the directional response calibration can be collected once per the life of the probe (and a particular sensor mounting) and then daily cross calibrations (pre and post) can be collected. This section presents the results of studying the effect of the elapsed time between the full calibration and subsequent cross calibrations.

Additionally, the data tested in this section are for various yaw-pitch orientations at a single velocity ( $Q = 12 \text{ m/s}$ ). As shown in Sec. 5.1.2.1, the TSFL Spline Search method can resolve the incoming velocity magnitude, yaw and pitch angles with the lowest uncertainty. It is assumed that similar results would be found if these tests were conducted at those velocities. These test data are also deliberately positioned at orientations which are “off the grid” to test the effectiveness of making a fine grid (by cubic splines) from the original  $9 \times 9$  grid.

A single full calibration was collected on the first day (day 0), separate cross calibration and then test data (at random orientations) were collected. These data were processed with the cross calibration processing for the purpose of comparison (this is also the first step in the TSFL Spline Search method). A pseudo-full calibration was created from the cross and full calibrations, as described in Sec.4.5.1, and this calibration was used for the TSFL Spline Search method. The results are shown via the joint-angle plot of Figs. 5.11 & 5.12 and also the values for  $\vartheta Q$ ,  $\vartheta \alpha$  and  $\vartheta \beta$  are shown in Table 5.1. The joint-angle plots show that for the points that are on-axis (i.e. close to the planes where  $\alpha \approx 0$  or  $\beta \approx 0$ ), the cross calibration can resolve the correct angle. However, a substantial error is found for the points that exist off-axis, where the bi-normal cooling effects are significant. The TSFL Spline Search method can reliably resolve those off axis orientations. Table 5.1 shows the total uncertainty for the  $Q$  ( $\vartheta Q$ ) and it can be seen that this value is significantly lower for the TSFL Spline Search.

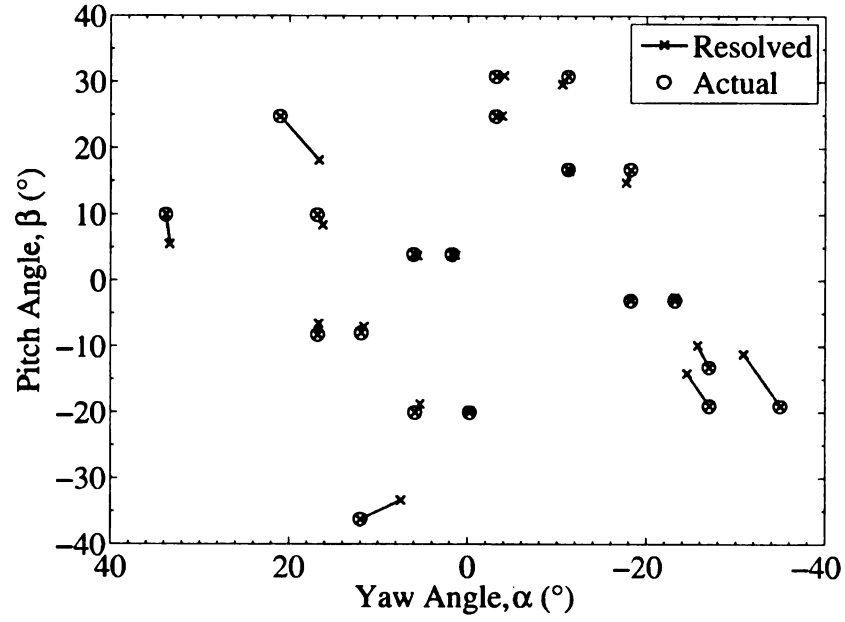


**Figure 5.11:** Pitch-yaw results for test data #1: processed with cross calibration.

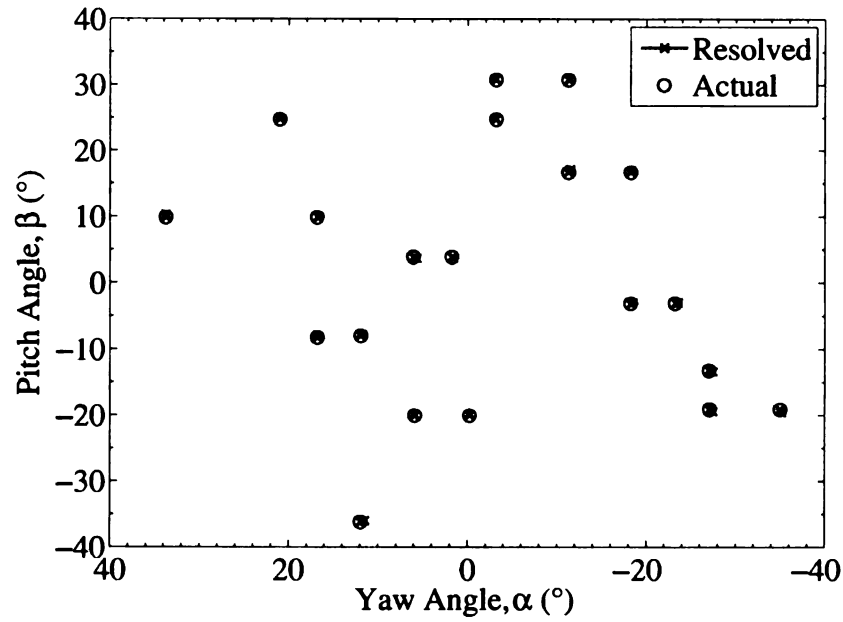


**Figure 5.12:** Pitch-yaw results for test data #1: processed with pseudo-full calibration (0 days elapsed between cross and full calibrations).

**Table 5.1:** Total uncertainty on test data #1: 0 elapsed days

Data reduction method	$\vartheta Q$ (%)	$\vartheta\alpha$ (°)	$\vartheta\beta$ (°)
Cross Calibration	3.71	6.15	3.73
TSFL Spline Search	0.76	0.41	0.38

### 5.1.3.2 Tests after 5 elapsed days

A second cross calibration was collected 5 days after the original full calibration. An additional set of test data were collected on this day for the same velocity ( $\approx 12$  m/s) for random orientations throughout the calibration domain. A pseudo-full calibration was created from this new cross calibration and the full calibration (from 5 days earlier). The test results are shown in Figs. 5.13 & 5.14. The joint-angle plots for the cross-calibration (Fig. 5.13) and the TSFL Spline Search (Fig. 5.14) show results consistent with the original tests (0 elapsed days). As seen in Table 5.2, there is a substantial difference in the overall uncertainty between the cross-calibration processing and the TSFL Spline Search. Slightly higher total uncertainties exist for the TSFL Spline Search processing (compared with Table 5.1), but the changes relative to the cross-calibration processing are quite comparable.

**Table 5.2:** Total uncertainty on test data #2: 5 elapsed days

Data reduction method	$\vartheta Q$ (%)	$\vartheta\alpha$ (°)	$\vartheta\beta$ (°)
cross-calibration	4.25	11.42	3.35
TSFL Spline Search	1.62	1.63	0.60

### 5.1.3.3 Tests after 7 elapsed days

A third cross-calibration was collected 7 days after the original full calibration, along with a new set of test data. The new cross-calibration and the full calibration from 7 days earlier were combined to form a new pseudo-full calibration. The new test data

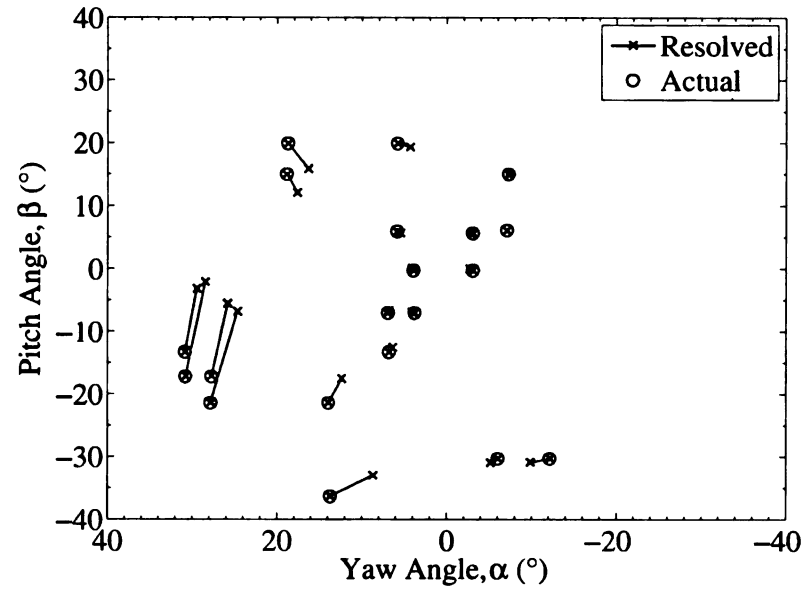


**Figure 5.13:** Pitch-yaw results for test data #2: processed with cross-calibration.

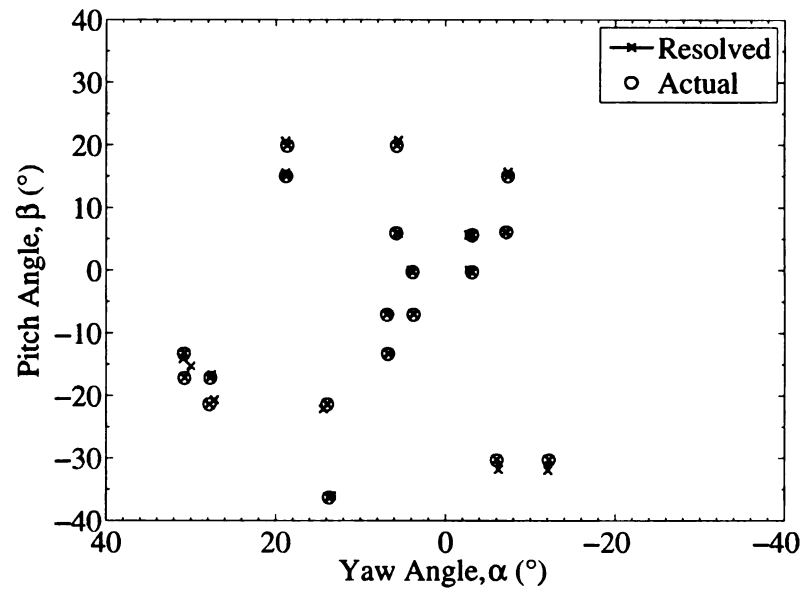


**Figure 5.14:** Pitch-yaw results for test data #2: 5 days elapsed between cross and full calibrations.

were again processed using the cross-calibration data reduction scheme and also the TSFL Spline Search method. Both the joint-angle plots and the values in Table 5.3 show results that are consistent with the results for 5 elapsed days.

**Table 5.3:** Total uncertainty on test data #3: 7 elapsed days

Data reduction method	$\vartheta Q$ (%)	$\vartheta\alpha$ ( $^{\circ}$ )	$\vartheta\beta$ ( $^{\circ}$ )
Cross-Calibration	2.45	5.77	3.19
TSFL Spline Search	1.85	2.80	0.83

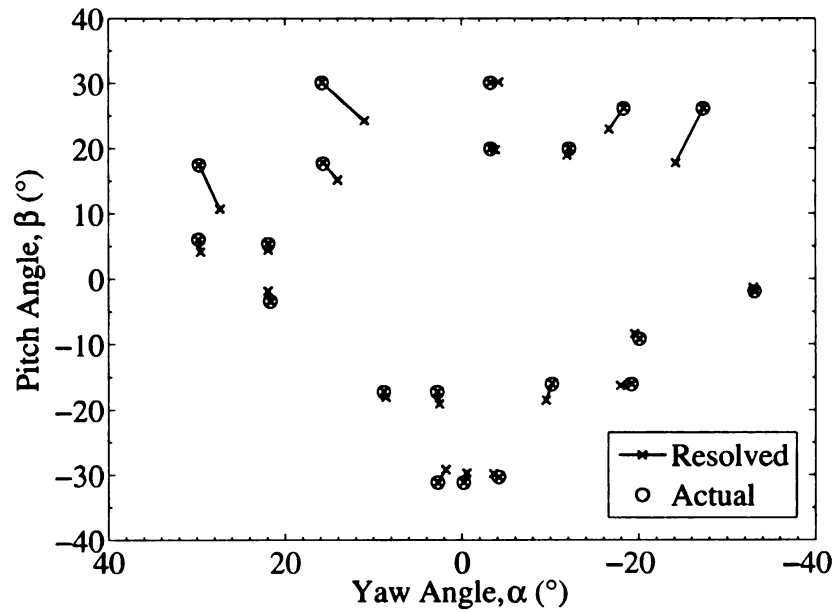


**Figure 5.15:** Pitch-yaw results for test data #3: processed with cross-calibration.

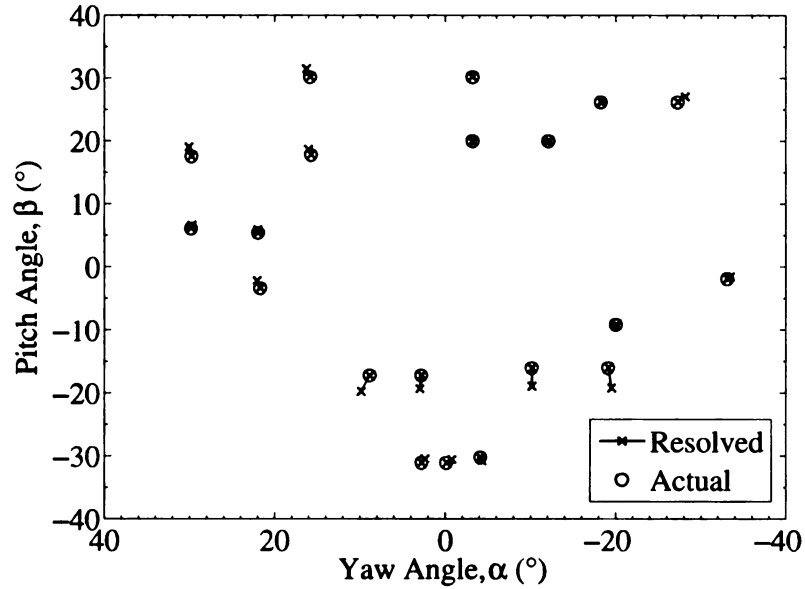


**Figure 5.16:** Pitch-yaw results for test data #3: 1 week elapsed between cross and full calibrations.

## 5.2 Controlled-Diffusion (CD) Airfoil

### 5.2.1 Inlet data

The CD airfoil experiment is set up in an open jet configuration as described in Sec. 4.1.2. A velocity survey using a single normal (SN) probe was performed to characterize the inlet flow for uniformity and also to measure the free-stream turbulence intensity. A similar survey had previously been undertaken at the ECL and a comparison of these inlet conditions are shown here. The SN probe was positioned just downstream of the separation edge of the nozzle, at a distance  $x/c = -2.5$ . The inlet nozzle, with dimensions  $50\text{ cm} \times 25\text{ cm}$ , spans the distance  $y/c = -1.75$  to  $y/c = 2.0$  (note with the origin at the trailing edge and a geometric angle of attack ( $\alpha_g$ ) of  $8^\circ$ , the airfoil trailing edge is not centered).

Figure 5.17 shows the mean inlet velocity profile from the near the center of the tunnel to the outer edge of the nozzle. The plot shows quite similar inlet velocities be-



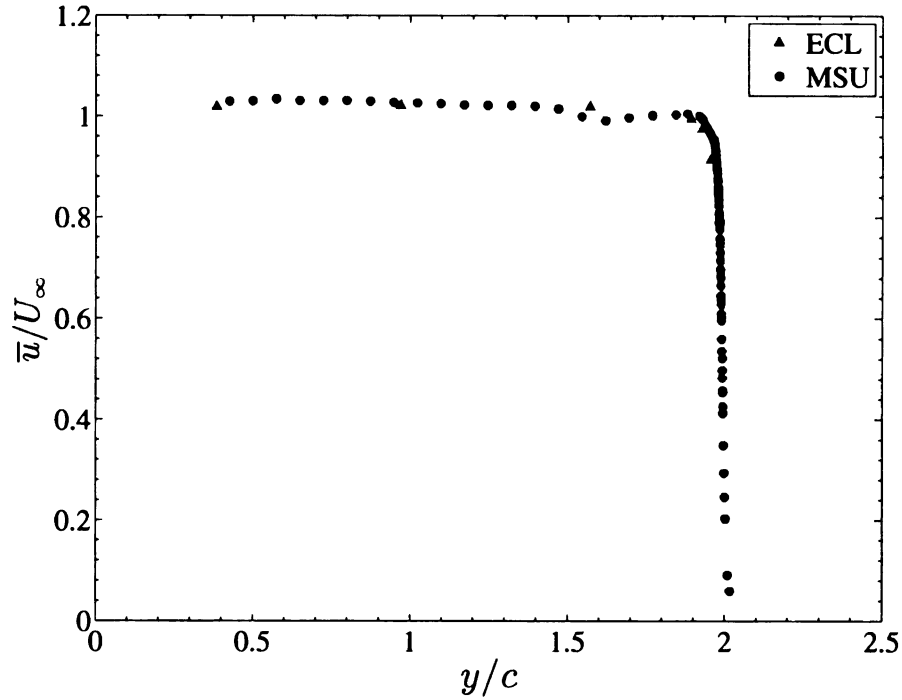


**Figure 5.17:** Comparison of the inlet ( $x/c = -2.5$ ) velocity profiles for the MSU and ECL experiments.

tween the two experimental configurations (ECL and MSU). The survey for the MSU configuration is comprised of significantly more points and it includes the boundary layer just after separation. This boundary layer becomes a shear layer which forms the upper (and lower) boundary conditions for the flow field around the airfoil. The inlet turbulence intensity can be seen in Fig 5.18. There exists slightly different values for the freestream turbulence intensity of the MSU facility (0.5%) and the ECL facility (0.7%). As expected, higher values of turbulence intensity exist in the separated boundary layer that exists between  $1.8 \leq y/c \leq 2.0$ .

### 5.2.2 Suction side boundary layer data

Data were collected at seven different  $x/c$  locations along the suction side to characterize the boundary layer and track its evolution. A single-normal (SN) probe was used for these data and the various measurement locations are shown in Fig. 5.19.

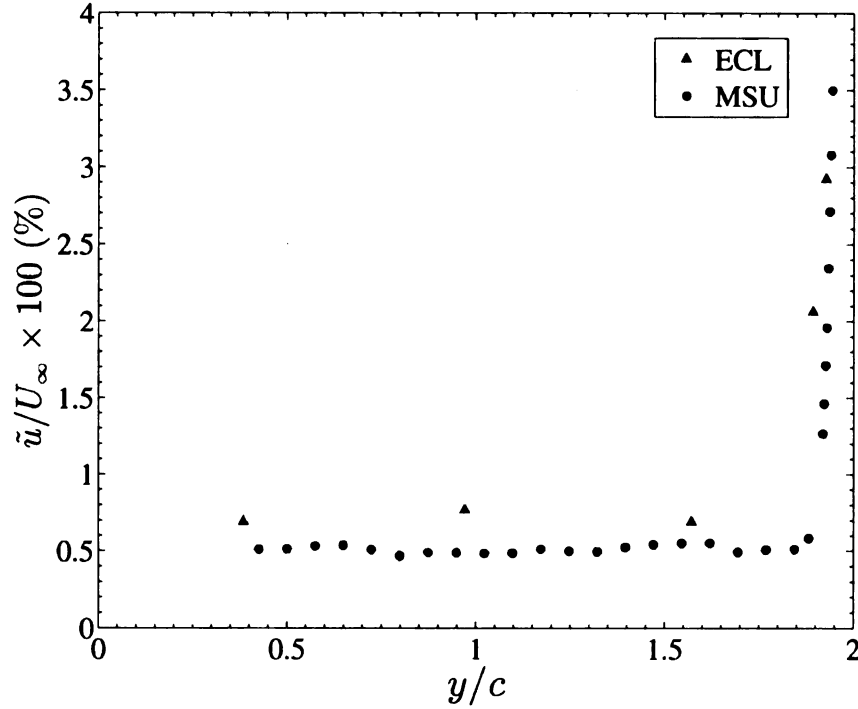


**Figure 5.18:** Comparison of the freestream turbulence intensity profiles for the MSU and ECL experiments (measured at  $x/c = -2.5$ ).

The numbers shown in Fig. 5.19 are the RMP numbers, which were also defined in Fig. 4.5. In all cases, the probe was traversed in a direction that was normal to the local tangent at the  $x/c$  location (i.e. wall normal direction). This was determined by using available CAD data and a rotary table connected to a standard 3-axis traverse. The mean velocity profile at the RMP #5 location is shown in Fig. 5.20. These data are compared with the LES of Wang that were published in Moreau *et al.* (2003) and also Moreau *et al.* (2006b) (The present author was involved with the latter publication, but the data from the boundary layer were not compared). The LES data are for nominally identical conditions - matching geometry, angle of attack and  $Re_c$ . The experimental data are normalized by the inlet velocity, in order to make the experimental values match those of the LES (also normalized by the inlet velocity). An alternative would be to select a free-stream velocity just outside of the boundary layer, but selecting this value is subjective and the free stream velocity is

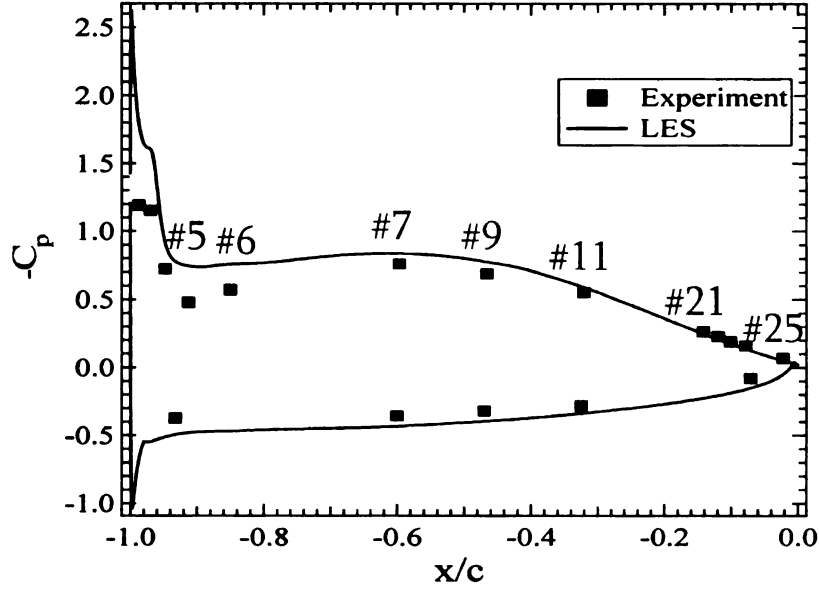


**Figure 5.19:** Measurement locations for boundary layer surveys above the RMP locations.

not constant (since there is an inviscid acceleration over the airfoil). Based on the  $C_p$  data shown in Fig. 4.7, it is apparent that this measurement station is very close to the downstream side of the laminar separation bubble. A normal mean boundary layer profile would monotonically decrease towards the wall. The data in Fig. 13 show a distinct increase in the mean velocity for  $y < 0.2 \text{ mm}$ . Since the hot-wire (SN-probe) can not distinguish between two different flow directions, the increase is likely the result of high velocity fluctuations, which would normally be associated with a separated region. This idea is reinforced in Fig. 5.21 where the plot shows a sharp peak in the normalized RMS velocity around  $y = 0.15 \text{ mm}$ . The LES data of Wang shows a normal turbulent velocity profile. This is likely because the laminar separation bubble of the LES is smaller than that of the experiment.

The normalized mean velocity profile at the RMP #6 location is shown in Fig. 5.22. These are again plotted against the LES of Wang at the same locations. The two curves are distinctly different - the LES shows a profile that is closer to a classical mean turbulent boundary layer, whereas the experimental data appear to be closer

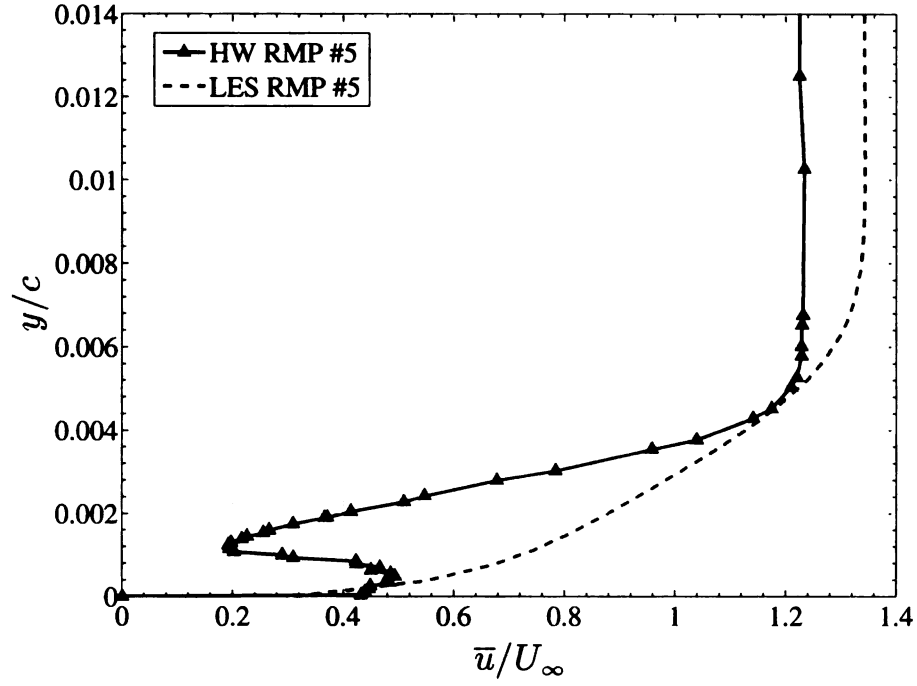


**Figure 5.20:** Normalized mean velocity profile at the RMP #5 location (HW and LES,  $c = 133.9$  mm).

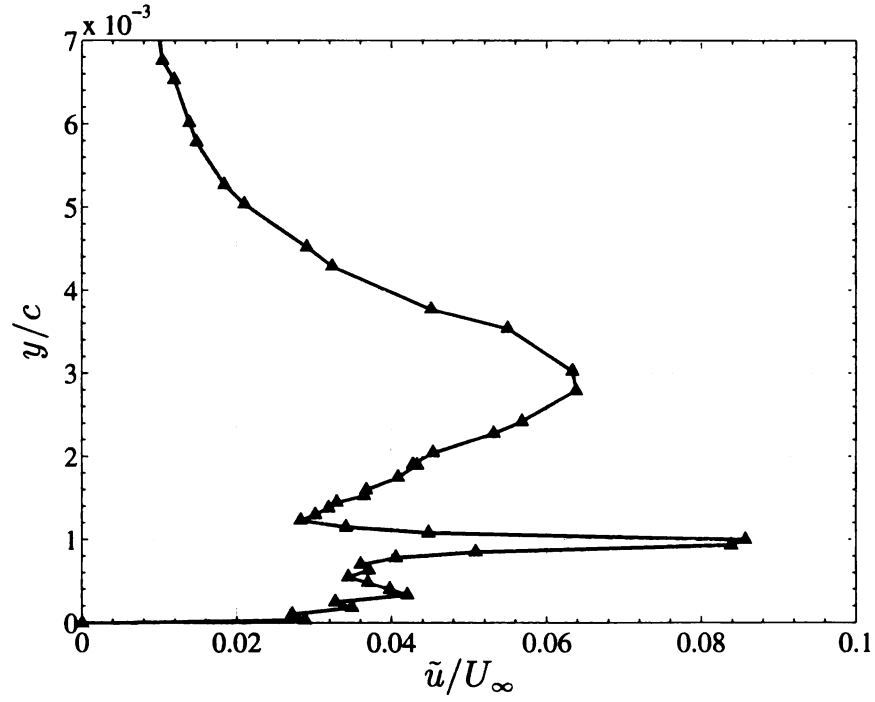


**Figure 5.21:** Normalized RMS velocity profile from HW data at the RMP #5 location.

to a mean laminar profile. The LES shows a much stronger acceleration outside of the boundary layer. The curves for the RMP #7 location, shown in Fig. 5.23, also show a profile normally associated with a mean turbulent boundary layer for the LES, while the experimental data have a lower mean velocity in the near wall region. The shape of the experimental profile was checked against a Blasius solution for the same (approximate downstream distance and free-stream velocity) and the results are shown in Fig. 5.24. The classical Blasius solution does not account for the curved wall and non-zero pressure gradient that exists in the experiment, although the pressure gradient, as seen in Fig. 5.19, is close to zero at the RMP #7 location (yet the upstream legacy of strong favorable and adverse pressure gradient exists at this location). Figure 5.24 also shows the result of a Falkner-Skan solution using the same free-stream velocity and a value of  $\beta = -0.018$ . Several different values for  $\beta$  were used (note that  $\beta < 0$  denotes an adverse or positive pressure gradient and  $\beta > 0$  denotes a favorable or negative pressure gradient). The Falkner-Skan solution can account for either a favorable or adverse pressure gradient, but it cannot account for the combined upstream legacy of both conditions. Falkner-Skan solution will also not account for the curved wall boundary condition that exists along the airfoil.

Figure 5.25 shows the normalized mean velocity profile at the RMP #9 location. In contrast to the RMP #7 location, the experimental boundary layer is closer to the one predicted by the LES, although the shape of the curves differ. The freestream velocity of the LES is higher than that of the experiments. This trend continues in Fig. 5.25 with the comparison between the LES and the experimental velocity profiles being similar in the approximate height of the boundary layer, although their respective shapes are different. In Fig. 5.26, the freestream velocity is lower than that of the experiments. Finally, closer to the trailing edge at RMP #21, shown in Fig. 5.27, the two profiles are quite similar, including good agreement on the freestream velocity. Interestingly, despite different initial profiles (in both shape and

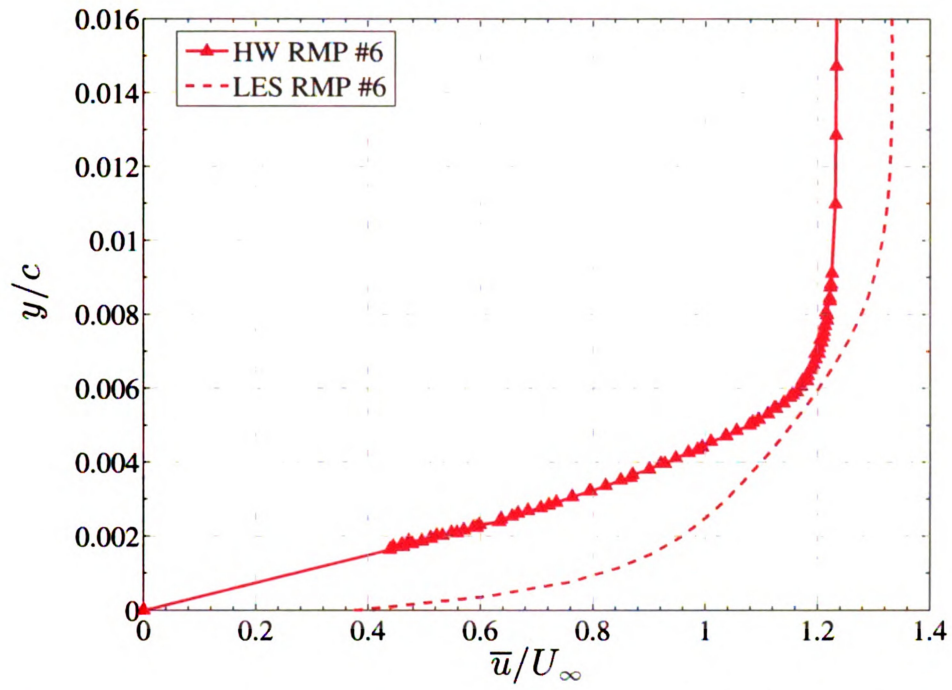


**Figure 5.22:** Mean velocity profile at RMP #6 (HW data and LES).

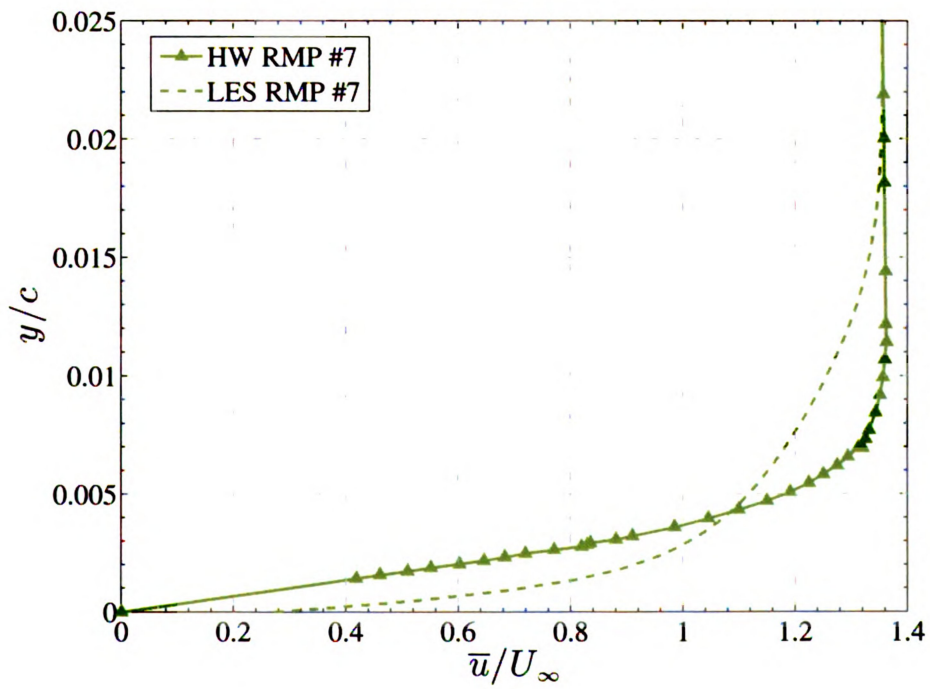


**Figure 5.23:** Mean velocity profile at RMP #7 (HW data and LES).

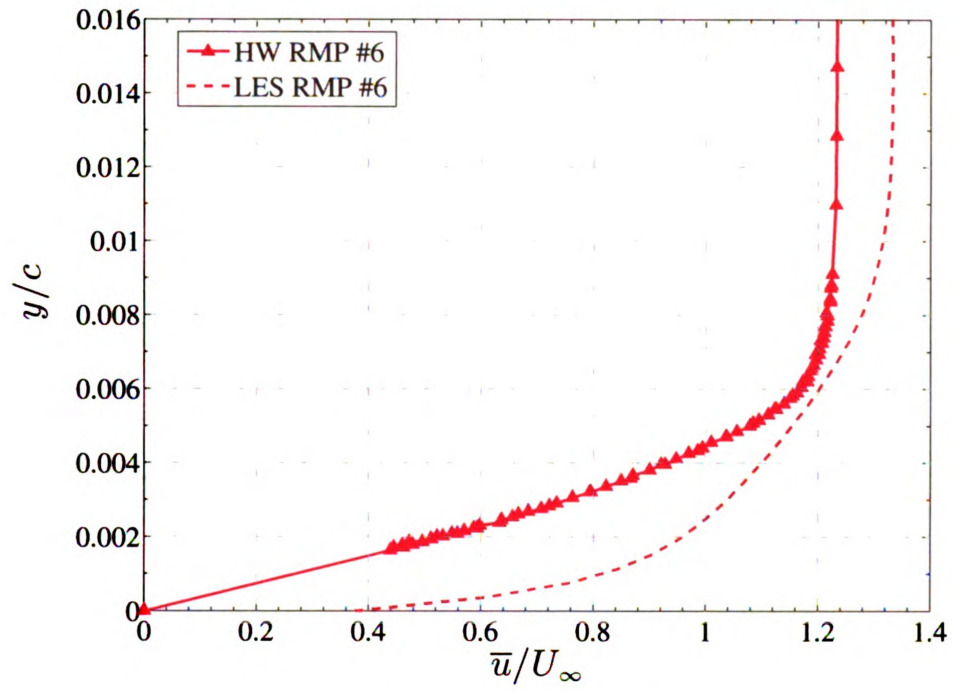


**Figure 5.22:** Mean velocity profile at RMP #6 (HW data and LES).

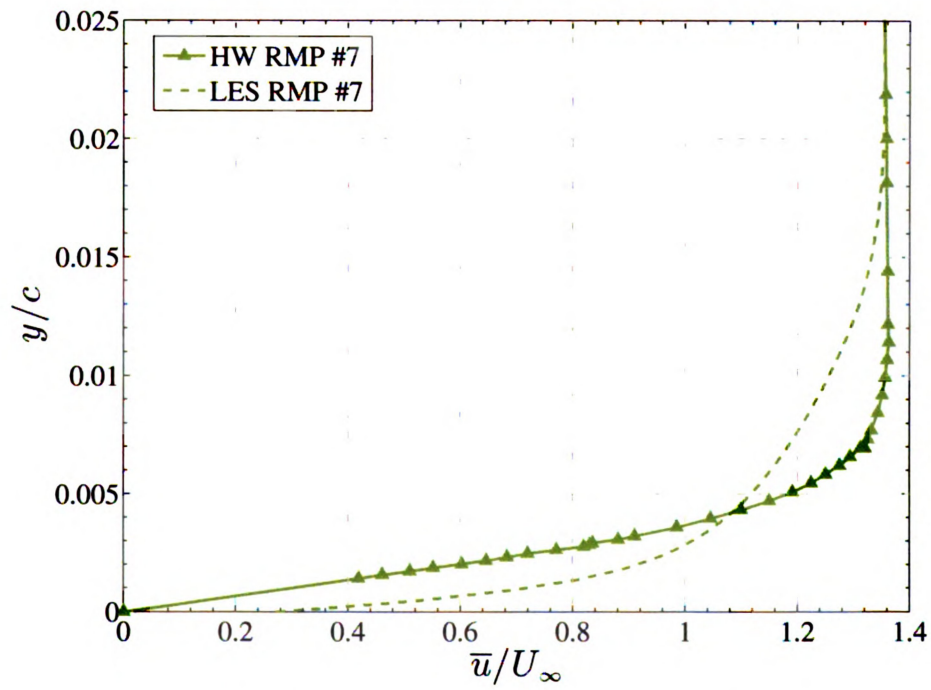


**Figure 5.23:** Mean velocity profile at RMP #7 (HW data and LES).

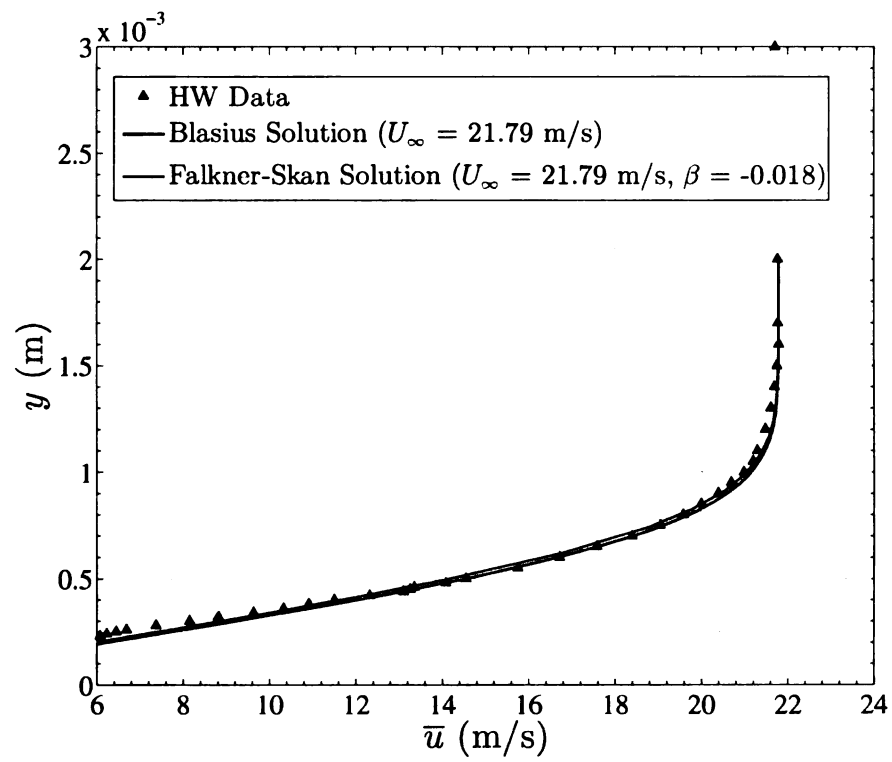


**Figure 5.24:** Mean velocity data at RMP #7 fitted to the Blasius and Falkner-Skan solutions.



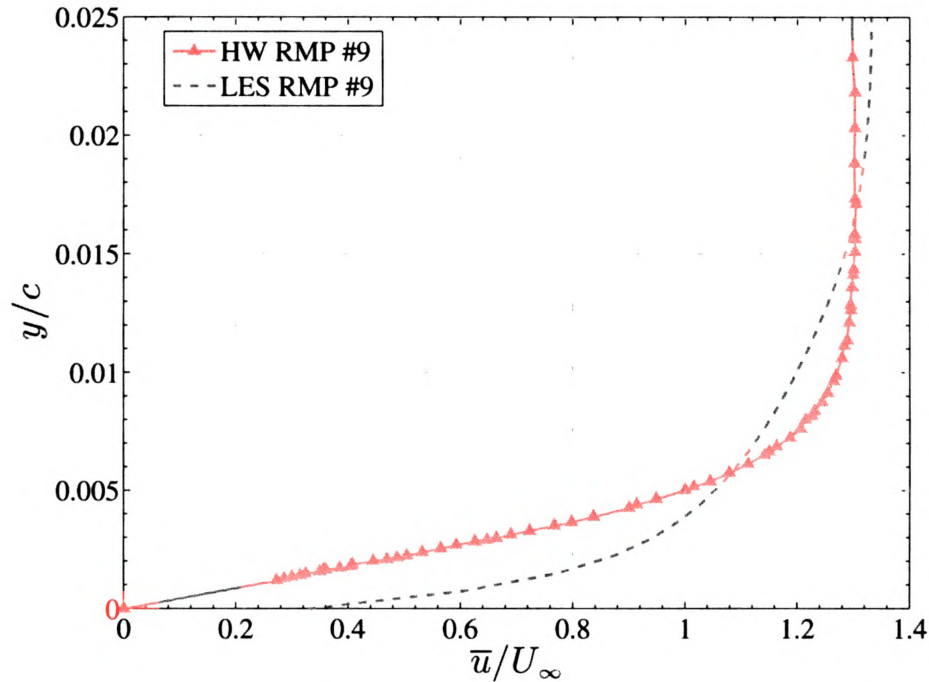


**Figure 5.25:** Mean velocity profile at RMP #9 (HW data and LES).

size of the boundary layer), the two boundary layers have evolved into very similar profiles before separation at the trailing edge. These data show that the boundary layer downstream of the laminar separation bubble does not immediately take on the characteristic of an “approximately normal turbulent boundary layer” as stated by Lissaman (1983). Instead the initial profiles after re-attachment are closer to those of a laminar boundary layer, yet with a higher RMS value within the profile. In contrast the LES shows a classical mean turbulent profile almost immediately, indicating that it has transitioned after the reattachment of the leading edge laminar separation. At the more downstream locations, the two profiles show good agreement, suggesting that the experimental boundary layer has transitioned somewhere near the mid-chord region and is showing a more turbulent profile by the time it reaches the trailing edge region. A composite of all the locations that were measured is shown in Fig. 5.28.

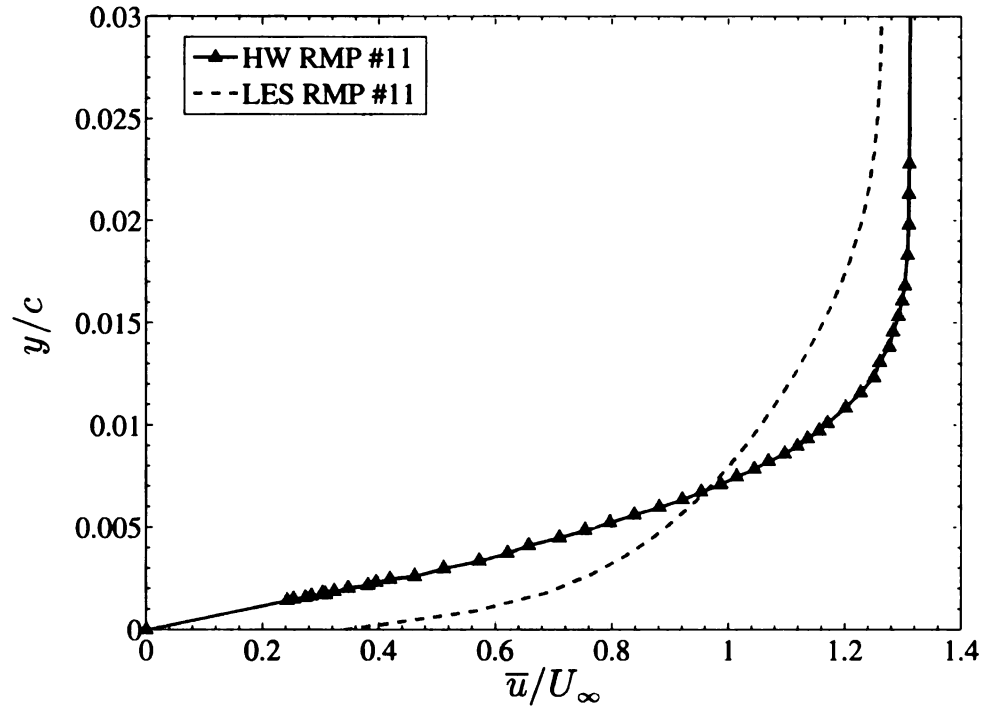


**Figure 5.26:** Mean velocity profile at RMP #11 (HW data and LES).

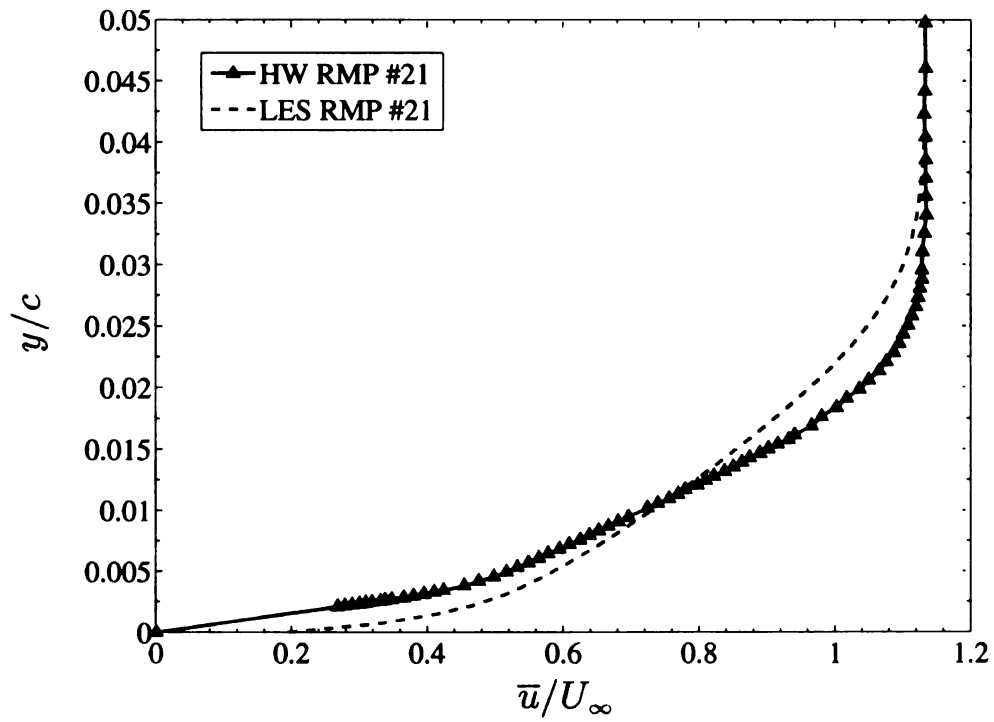


**Figure 5.27:** Mean velocity profile at RMP #21 (HW data and LES).

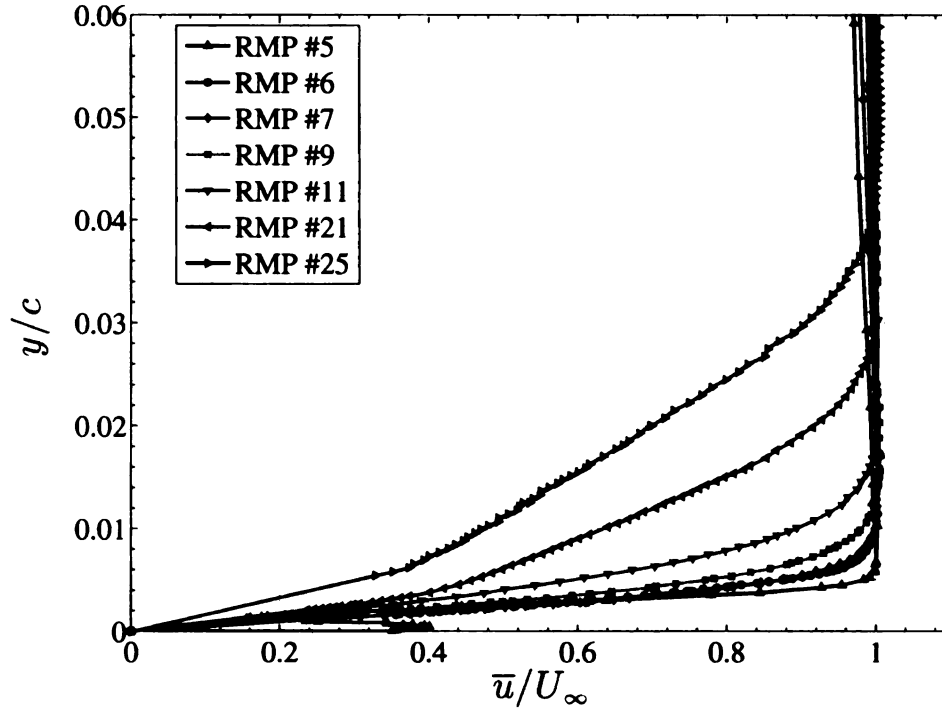


**Figure 5.28:** Composite of mean velocity profiles at the suction-side RMP locations.

### 5.2.3 Very near wake data

The terms used in the following sections: *very near wake*, *near wake*, and *far wake* are consistent with the definitions presented in Hah & Lakshminarayana (1982) and also described in detail in Sec. 2.3. A velocity survey was taken just downstream of the trailing edge ( $x/c \approx 0.00373$ ) to measure the near wake region just after boundary layer separation. The suction side and pressure side boundary layers in this region (that is very close to the trailing edge) should be very similar to the upstream boundary layer. This is because the boundary layer has not transitioned to a wake or a shear layer, as shown by Morris & Foss (2003). This finding was also reported for airfoils by Hah & Lakshminarayana (1982). A photograph showing the position of the SN-probe relative to the trailing edge region is shown in Fig. 5.29. The SN-probe was traversed in very small increments ( $\approx 0.01 \text{ mm}$ ) from the outer edge of the suction side boundary layer, past the trailing edge, and across the pressure

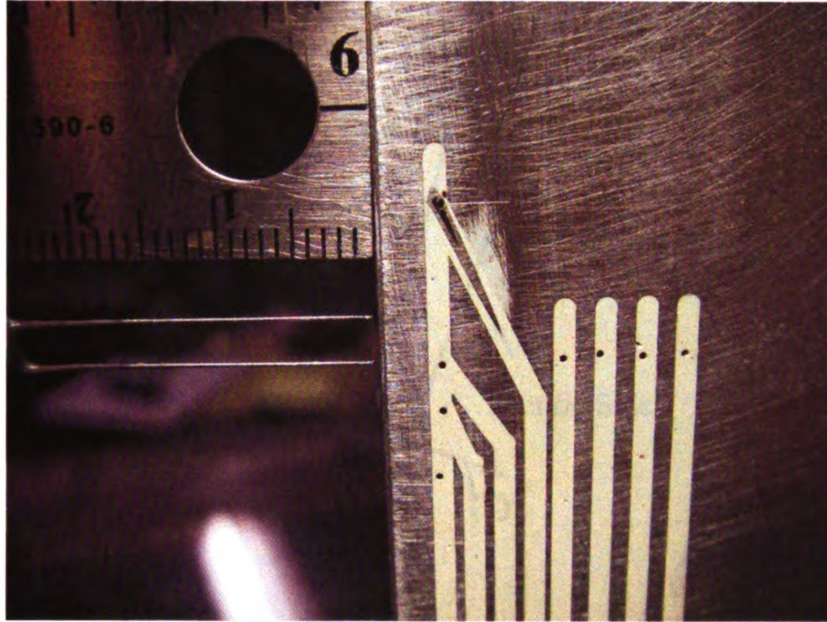


**Figure 5.29:** Orientation of HW probe near the TE for near wake experiments (mm units on reference scale).

side boundary layer. A top view of the traversing probe is shown in Fig. 5.31. A special coordinate system, different than the one used Fig. 4.3, was established for this survey. This special coordinate system was established because the probe was traversed along a line that was normal to streamwise direction at the trailing edge. This allowed the boundary layers to be characterized in wall-normal coordinates. A representation of this coordinate system is shown schematically in Fig. 5.30.

The results of the velocity survey are shown in Fig. 5.32. The location  $y'/c = 0$  is the location of the center of the trailing edge. The trailing edge has a thickness that is approximately 1.5 mm thick and spans the region of  $y'/c = \pm 0.007$ . In Fig. 5.32, the small region of nominally constant velocity either side of the line at  $y'/c = 0$  is in the small recirculation region behind the airfoil thickness and these data are not reliable (since a SN-probe does not reliably measure a flow in a recirculation region). Outside of this region, the boundary layers on the pressure and suction side can be clearly seen. On the suction side, the shape and size of the boundary layer is very

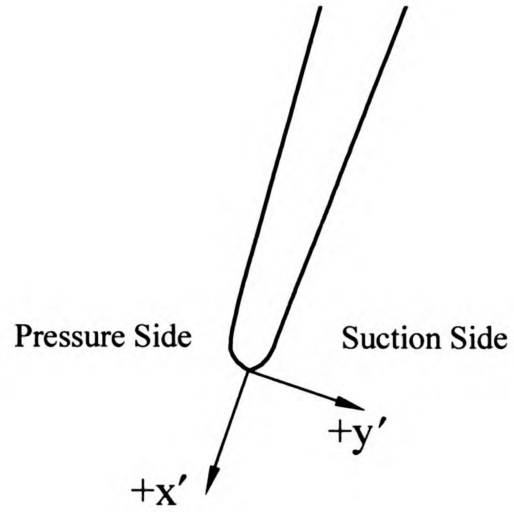


**Figure 5.30:** Coordinate system for near wake measurements.



**Figure 5.31:** Top view of HW probe traversing the near wake region.



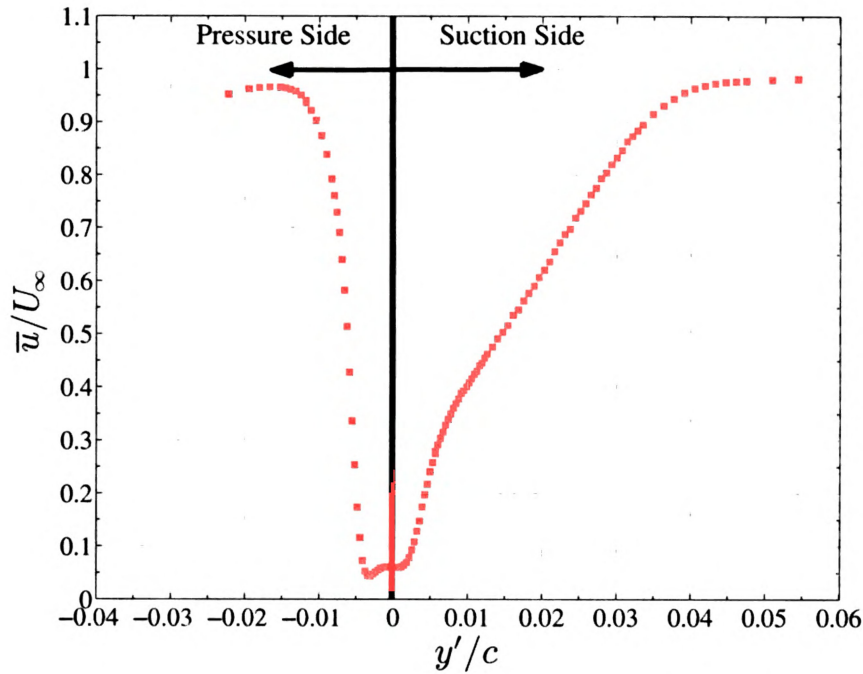


**Figure 5.32:** Mean streamwise velocity profile in the near wake region ( $x/c \approx 0.00373$ )

similar to the profile that was measured at the last RMP station. It appears from these data that the boundary layer does not separate before the trailing edge.

#### 5.2.4 Near and far wake data - mean velocity and related wake parameters

Detailed velocity surveys were carried out in the wake of the CD airfoil using both the 1X and 2X HWA probes, along with PIV. Because of the additional quantities that can be measured by the 2X-probe (compared with an X-probe), these results comprise the majority of the data that are presented here. Also, the 2X-probe, compared with an X-probe, is less susceptible to out-of-plane (i.e. bi-normal) cooling effects from the three-dimensional flow field which exists in the wake. A detailed comparison of the similarities (and differences) between the measurements collected in the wake with

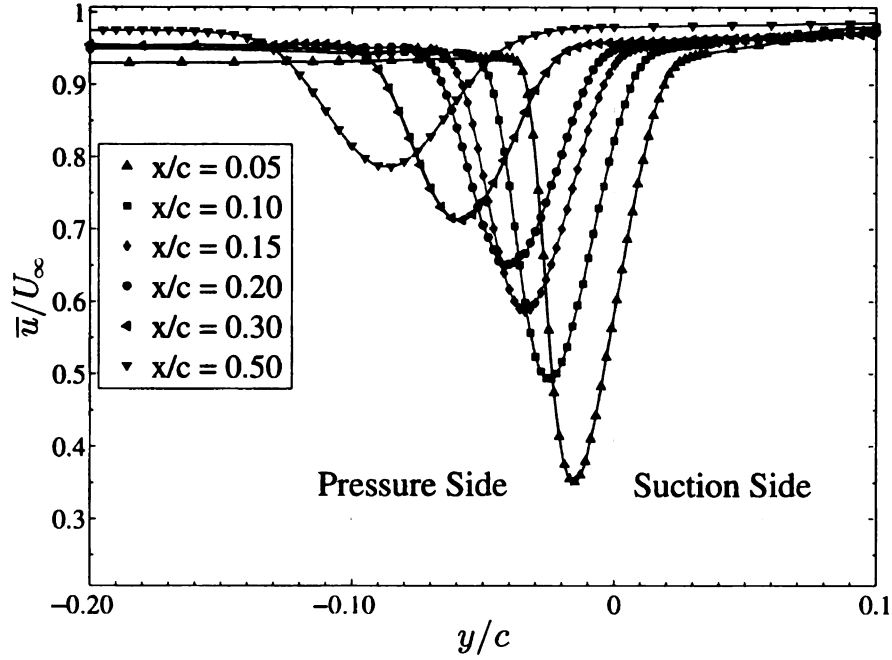


**Figure 5.33:** Mean streamwise velocity profiles.

the X-probe and 2X-probe are presented in Sec. 5.5. These differences are discussed and explained relative to the results shown in Sec. 5.1.

The mean streamwise velocity profiles, for several downstream ( $x/c$ ) locations, are shown in Fig. 5.33. These data are normalized by the upstream freestream velocity,  $U_\infty$ , which is measured by a Pitot-static probe at the exit of the upstream nozzle. The location  $y/c = 0$  is the trailing edge of the airfoil. These data show that the wake is deflected in the negative  $y/c$  direction as it moves in the streamwise direction. This trend continues for each of the downstream measurement stations. This deflection of the wake towards the pressure side is a direct result of the lift imparted on the blade by the fluid. The initial peak velocity deficit (where  $du/dy = 0$ ) at  $x/c = 0.05$  is approximately 35% of the freestream velocity and it recovers to 80% of the freestream velocity at the farthest downstream location:  $x/c = 0.50$ .

Figure 5.34 shows the mean streamwise velocity with the profiles plotted in a coordinate system that aligns the wake centers on the abscissa ( $n = y - y_c$ ). This allows for the salient features of the wake profiles to be more easily compared and

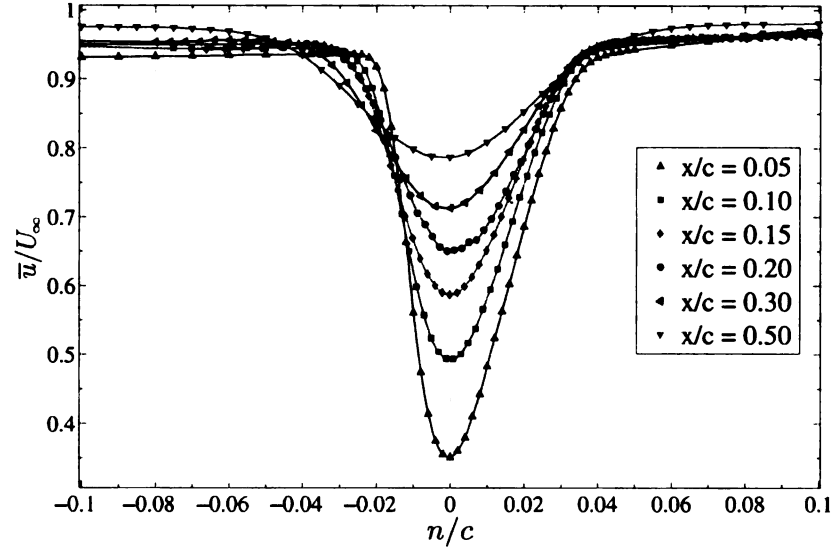


**Figure 5.34:** Mean streamwise velocity profiles, wake center aligned ( $n = y - y_c$ ).

contrasted. The velocity adjacent to the wake region, the wake edge velocity, (i.e. where  $((\overline{u'^2})^{\frac{1}{2}} \approx 0))$  is designated by  $U_e$ . The wake edge velocity increases in the  $+y/c$  direction and it converges to a common value in the adjacent freestream on the suction side. It is reasoned that this value will approach unity sufficiently far away ( $y/c \gg 0$ ) from the blade. The edge velocity on the pressure side shows a systematic increase with each downstream location. Also the adjacent freestream velocity shows a very constant value in the  $-y/c$  direction. A close-up view of this region is shown in Fig 5.35. This non-constant freestream velocity is explained by the illustration in Fig. 5.36. Since there is streamline curvature along the pressure side of the blade resulting from the higher pressure (relative to  $P_\infty$ ) on pressure side of the blade, there exists an inviscid deceleration in this region. This is inviscid since the freestream is not sheared by the surface on the pressure side. Farther downstream, this pressure will recover back to  $P_\infty$ , and there is a resulting inviscid acceleration occurring in the freestream velocity that is adjacent to the pressure-side of the wake.

The mean normal velocity component,  $v$  is shown in Fig. 5.37. at all of the downstream measurement locations. Referring to the coordinate system previously defined



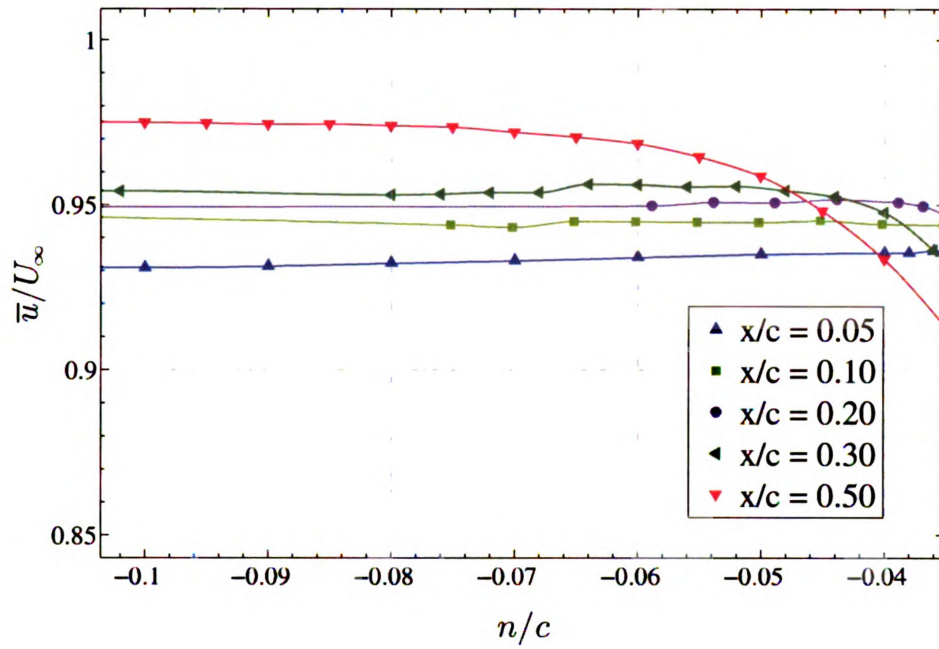


**Figure 5.35:** Close-up view of the velocity just outside the CD airfoil wake on the pressure side.

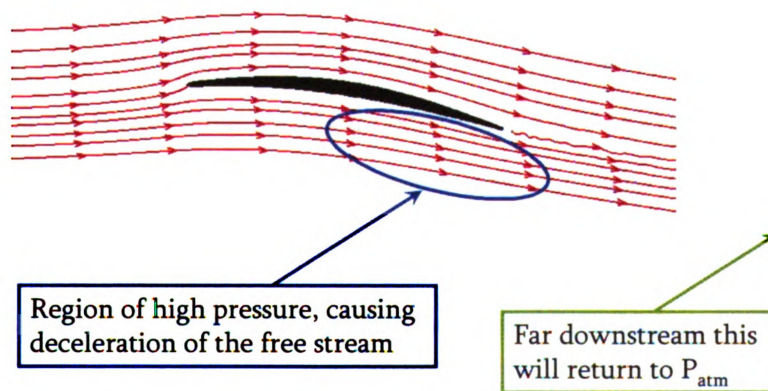


**Figure 5.36:** Explanation for increasing velocity on the pressure side of the CD airfoil.

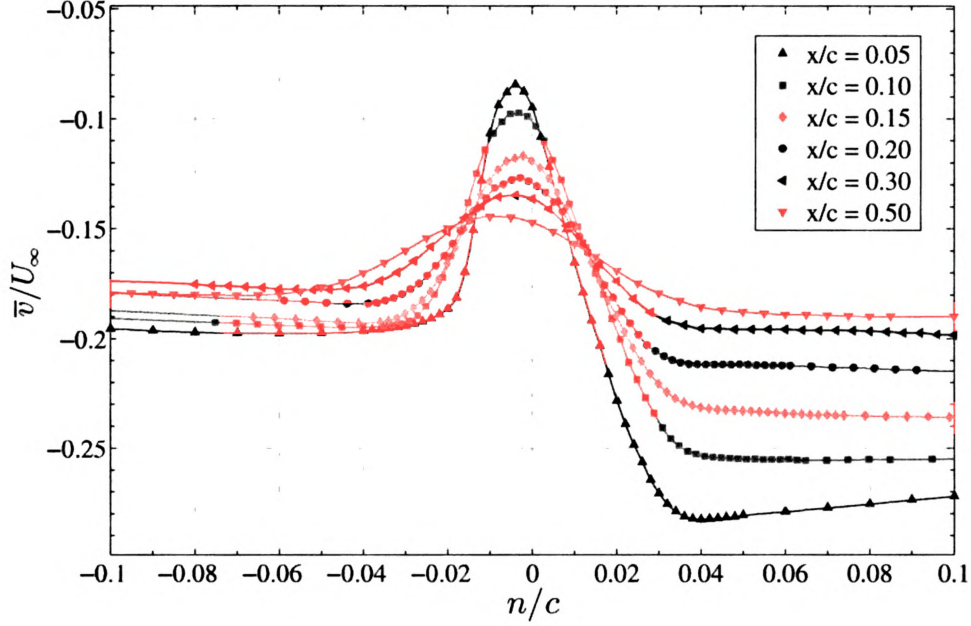


**Figure 5.37:** Mean transverse velocity profiles ( $n = y - y_c$ ).

in Fig. 4.3,  $v < 0$  indicates that the flow is deflecting towards the pressure side, consistent with the data shown in Fig. 5.33. The suction side freestream velocity ( $y/c > 0.04$ ) shows a systematic increase in  $v$  with downstream distance. This indicates the flow is deflecting less towards the pressure side as it moves downstream. A similar trend, but of smaller magnitude, is evident on the pressure side ( $y/c < -0.4$ ). This indicates that the inviscid fluid just outside of the wake is “straightening out” more on the suction side than on the pressure side. In the wake, it is evident that the  $v$  is increasingly negative with downstream direction. The values of  $v$  in the wake range from  $0.08 - 0.14U_\infty$ .

Figure 5.38 shows a composite of the mean spanwise velocity,  $w$  at various downstream locations. The freestream velocity, as expected, is nominally two-dimensional ( $\bar{w} \approx 0$ ). However, the wake region has a non-zero  $\bar{w}$  at all downstream locations. The pressure side ( $n/c < 0$ ) has a negative spanwise velocity,  $\bar{w} < 0$  and the suction side ( $n/c > 0$ ) has a positive spanwise velocity  $\bar{w} > 0$ . The extent of this non-zero spanwise

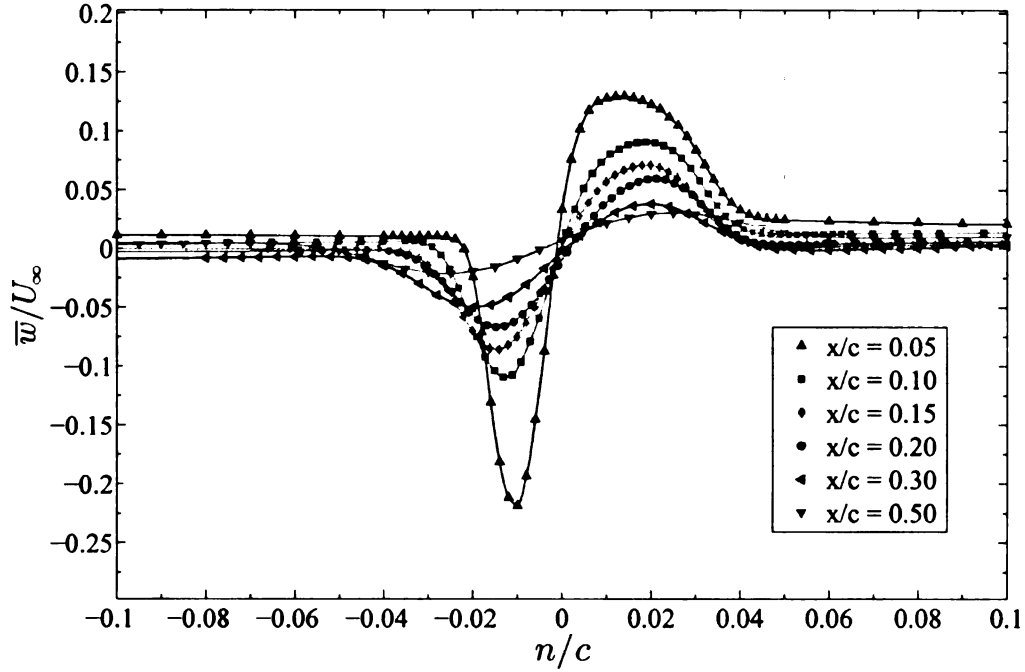


**Figure 5.38:** Mean spanwise velocity profiles ( $n = y - y_c$ ).

velocity region is consistent with the other velocity measurements (i.e. the suction side is wider). These data show that the airfoil imparts a three-dimensional flow from the near blade region. It is also apparent that the airfoil introduces a streamwise vorticity ( $\omega_x$ ) into the wake region. The  $\bar{w}$  inside the wake is quite strong at the  $x/c = 0.05$  location, where  $\bar{w} = -0.22U_\infty$  on the pressure side and  $\bar{w} = -0.13U_\infty$ . The spanwise velocity in the wake can be seen to be of the approximately the same order of magnitude as the transverse velocity for the upstream locations. This spanwise velocity decreases rapidly and is very small ( $\bar{w} \approx |0.025U_\infty|$ ) by the downstream distance of  $x/c = 0.50$ .

The mean streamwise velocity data were reduced to a single curve by introducing a scaling velocity and a scaling length. The choice of scaling velocity was the difference between the wake edge velocity and the wake centerline velocity,  $(U_e - U_c)$ . Because the wake is asymmetric, two different scaling lengths were selected,  $l_p$  and  $l_s$ . These lengths are defined at the distances from the wake centerline to the locations on

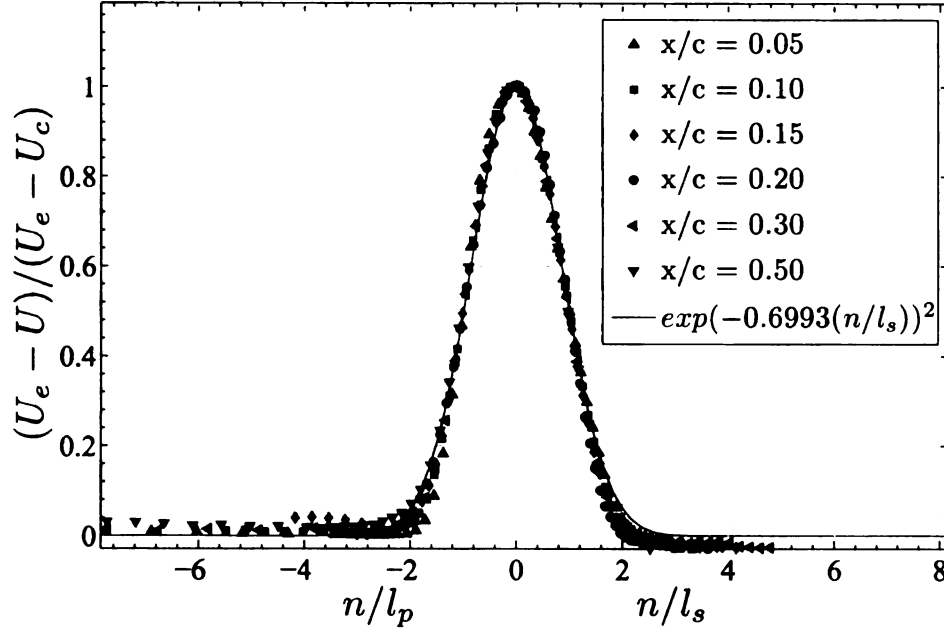


**Figure 5.39:** Self-similarity for the mean velocity profiles of the CD airfoil.

the pressure and suction sides where the velocity is  $\frac{1}{2}(U_e - U_c)$ . The scaled velocity profiles are shown in Fig. 5.39 which shows the existence of self-similarity in the mean streamwise velocity profiles.

The decay of the velocity defect at the center of the wake (wake centerline) is shown in Fig. 5.40. These data are cast as the normalized difference between the wake edge velocity and the wake centerline velocity. The data presented in Fig. 5.40 use the edge velocity on the pressure side, however, identical results are derived if the suction side edge velocity were used. The data from Hah & Lakshminarayana (1982) and Raj & Lakshminarayana (1973) are presented for comparison. Each of the three studies shown used different airfoil shapes and also had different experimental configurations. Hah & Lakshminarayana (1982) had a zero-camber symmetric airfoil in an isolated airfoil configuration (i.e. bounding side walls on the wind tunnel). Hah & Lakshminarayana (1982) used a cambered airfoil in a cascade configuration. These both differ from the open-jet configuration with a cambered airfoil that was used in the present study.

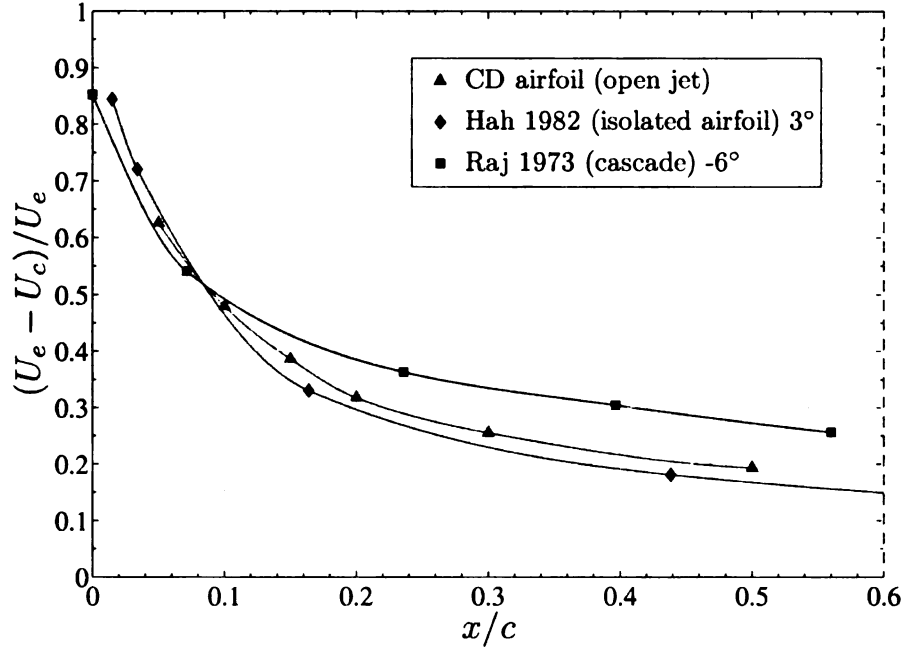


**Figure 5.40:** Decay of the wake centerline velocity defect for the CD airfoil.

The momentum thickness (Eq. 5.5) and the displacement thickness (Eq. 5.4) were used to define the shape factor:  $H = \delta^*/\theta$ . Because the wake is asymmetric, the edge velocity,  $U_e$ , is different for the pressure side and the suction side. This asymmetry requires that  $\theta$  (and also  $\delta^*$ ) be calculated separately for each side (using the appropriate  $U_e$ ). These definitions are shown in Eqs. 5.4 & 5.5, where  $\theta_-$  and  $\theta_+$  are the momentum thicknesses on the pressure and suction side, respectively. The total momentum thickness for the wake is the sum of the two sides, i.e.  $\theta = \theta_- + \theta_+$ . These results are compared with the isolated airfoil study of Hah & Lakshminarayana (1982) and the cascade study of Raj & Lakshminarayana (1973) in Fig. 5.41. As mentioned previously, each of these studies used a different airfoil shape (not the CD airfoil used in this study), so the experimental configuration is one of several differences that exist between these three studies.

$$\delta_-^* = \int_{-n_e}^0 \left(1 - \frac{u}{U_e}\right) dn; \quad \delta_+^* = \int_0^{+n_e} \left(1 - \frac{u}{U_e}\right) dn \quad (5.4)$$

$$\theta_- = \int_{-n_e}^0 \left(1 - \frac{u}{U_e}\right) \frac{u}{U_e} dn; \quad \theta_+ = \int_0^{+n_e} \left(1 - \frac{u}{U_e}\right) \frac{u}{U_e} dn \quad (5.5)$$

The values of  $\theta/c$  and  $H$  from the CD airfoil dataset were measured with a single X-probe. Very similar results were found from the same data measured with the 2X-probe. As mentioned in Raj & Lakshminarayana (1973), the behavior of  $\theta/c$  can be explained by the von Kármán momentum integral equation:

$$\frac{d\theta}{dx} + (H + 2) \frac{\theta}{U_e} \frac{dU_e}{dx} = \frac{\tau_o}{\rho U_e^2} \quad (5.6)$$

In the wake of the airfoil, the flow has separated from the surface of the airfoil and  $\tau_o = 0$ , so Eq. 5.6 reduces to:

$$\frac{d\theta}{dx} + (H + 2) \frac{\theta}{U_e} \frac{dU_e}{dx} = 0 \quad (5.7)$$

It can be seen that the increase or decrease of  $\theta/c$  in the streamwise direction depends on the variation of  $U_e$ , since the sign of  $d\theta/dx$  is the same as that for  $dU_e/dx$ . The trend for  $\theta/c$  vs.  $x/c$  varies for each of the three experiments. For the cascade (Raj & Lakshminarayana, 1973),  $\theta/c$  initially increases and then reaches a steady value. The isolated airfoil (Hah & Lakshminarayana, 1982) shows a nominally constant value for  $\theta/c$  at all downstream locations. The open-jet airfoil configuration (present study) shows an initial decrease in  $\theta/c$  followed by a slight increase at the farthest downstream location. Very different wake characteristics are exhibited by each of these three experimental configurations. Since the wake will vary depending on the blade loading, it is apparent that the boundary conditions imposed by these three experimental configurations are qualitatively different. Planar PIV data showing the normalized velocity magnitude for the CD airfoil are shown in Fig. 5.42. As described in Sec. 4.3.1, these data were measured at the mid-span of the airfoil, which is the same plane as all of the hot-wire velocity surveys. Streamlines are

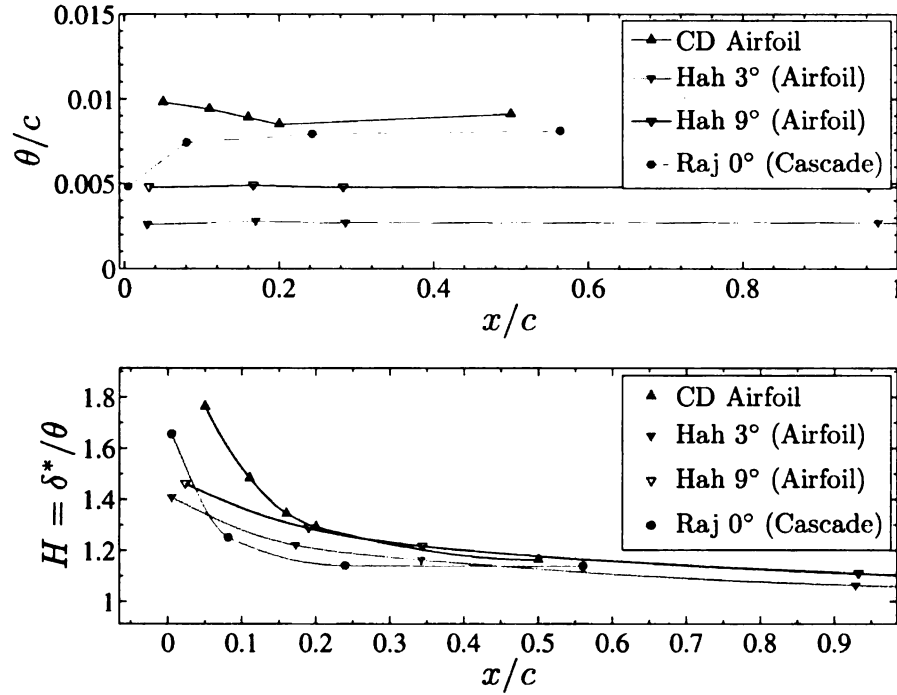


**Figure 5.41:** Momentum thickness and shape factor for the CD airfoil.

drawn using the two measured velocity components,  $u$  and  $v$ . A total of 600 image pairs were collected and averaged. The number of samples were substantially fewer than the number measured for the velocity time series of the 2X HW data ( $1.2 \times 10^6$  samples). However, good agreement was found for the mean velocity at the equivalent locations ( $x/c = 0.05, 0.10, \dots$ ). The PIV data provide the additional advantage of showing the overall flow field with good spatial resolution (a vector is measured every  $0.67 \text{ mm}$  over a field of view that is nominally  $0.5c \times 0.5c$ , or  $67 \text{ mm} \times 67 \text{ mm}$ ). Figure 5.42 shows the mean wake deflecting towards the pressure side and also that the transverse velocity,  $v$ , is negative throughout the entire wake region and in the freestream velocity downstream of the trailing edge. It can also be seen from the streamline angles that the transverse velocity on the suction side is slightly higher than on the pressure side, consistent with the data that were shown in Fig. 5.37. The region immediately downstream of the trailing edge (at  $(x/c, y/c = 0, 0)$ ) shows lower than expected velocities. This is the result of reflected laser light from the airfoil



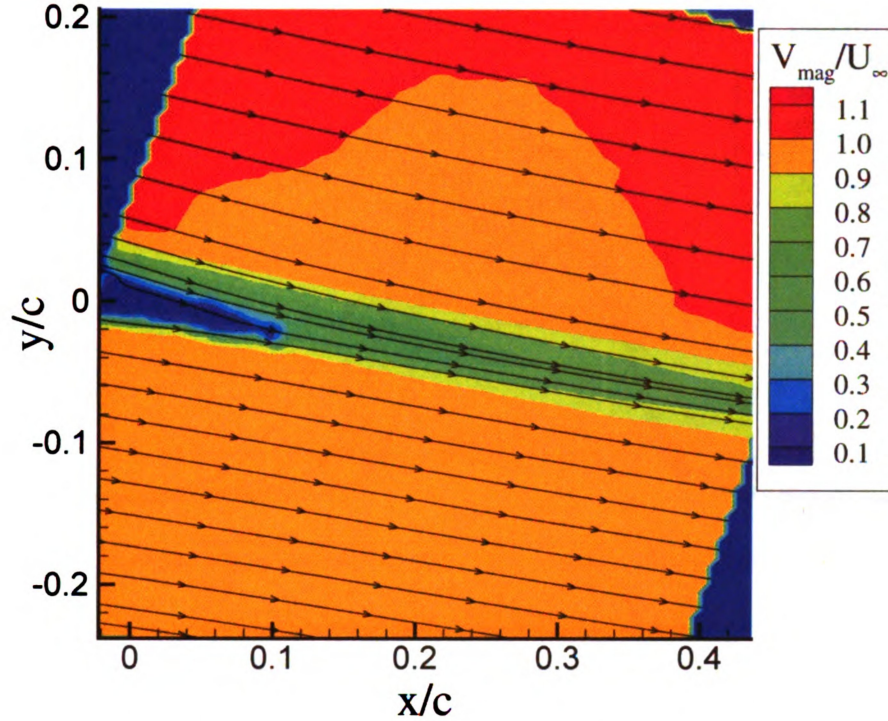


**Figure 5.42:** PIV data showing the normalized velocity magnitude.

surface that causes a region that cannot be reliably measured. It is estimated (by comparison with the HW surveys) that the region ( $x/c > 0.10$ ) is sufficiently far from the airfoil surface for the reflections to not adversely affect the PIV data. A second PIV plane, as described in Sec. 4.3.1, was also measured, but is not presented here. This second PIV plane was positioned farther downstream and had a slight overlap with this upstream plane ( $0.35 \leq x/c \leq 0.75$ ). These data are used for comparisons between the CD airfoil and RCDB that are presented in Sec. 5.4.

### 5.2.5 Near and far wake data - turbulence properties

The turbulence intensities in the streamwise  $((\overline{u'^2})^{\frac{1}{2}})$ , transverse  $((\overline{v'^2})^{\frac{1}{2}})$ , and span-wise  $((\overline{w'^2})^{\frac{1}{2}})$  directions are shown in Figs. 5.43–5.45. These will be referred to in the text as  $T_u$ ,  $T_v$ , and  $T_w$ , respectively. The data for both  $T_u$  (Fig. 5.43) and  $T_v$  (Fig. 5.44) show an asymmetry between the pressure side and suction side, with the



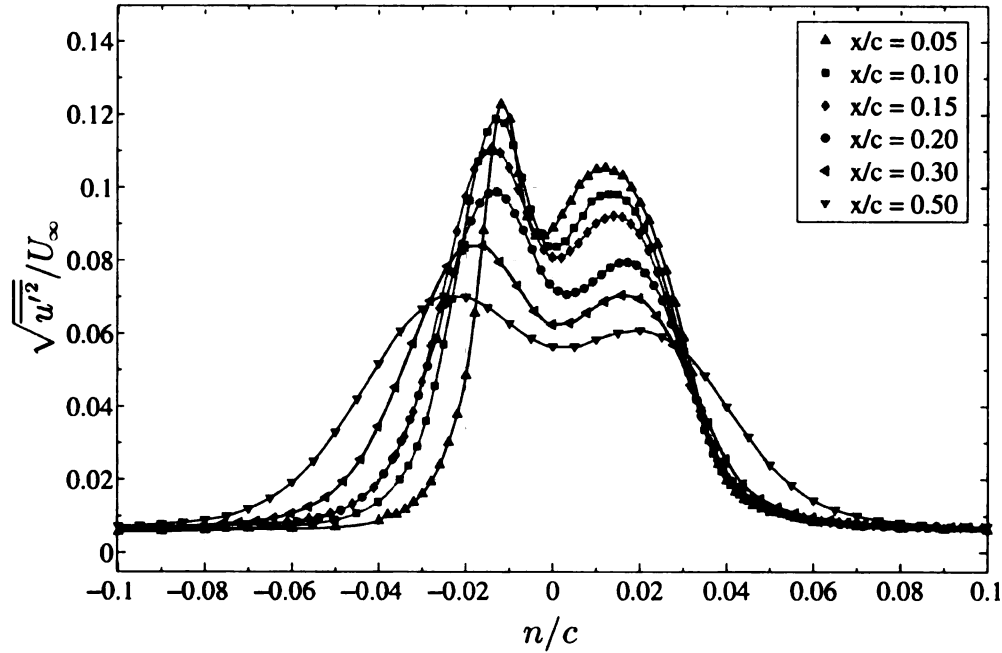


**Figure 5.43:** Streamwise turbulence intensity ( $n = y - y_c$ ).

values for turbulence intensities being higher on the pressure side for both components. This asymmetry decreases with downstream distance and by  $x/c = 0.50$ , the profiles are nominally symmetric. As was shown in Fig. 5.2.3, the boundary layer at separation is considered to be turbulent on the suction side and laminar on the pressure side.

These higher values for  $T_u$  and  $T_v$  on the pressure side can be understood by looking at the instantaneous PIV data in Fig. 5.46. The instantaneous velocity magnitude in the wake is shown; it can be seen that distinct regions of higher velocity fluid ( $\vec{V}/U_\infty > 1.0$ ) appear along the pressure side of the wake. These regions are marked by the black arrows in Fig. 5.46. The suction side also shows regions of higher velocity fluid, but these exist outside of the mean wake region, as seen in Fig. 5.42. In addition to the regions of higher velocity fluid on the pressure side, the instantaneous edge of the wake on the pressure side appears to vary in the  $y/c$  direction more strongly than the wake edge on the suction side.

These regions of higher velocity fluid on the pressure side can be further examined

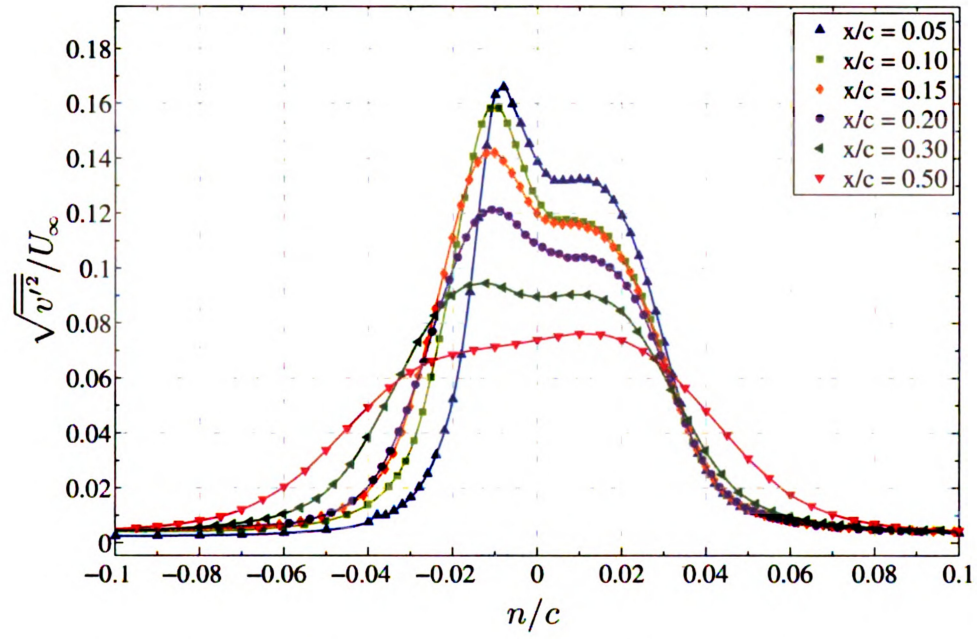


**Figure 5.44:** Transverse turbulence intensity ( $n = y - y_c$ ).

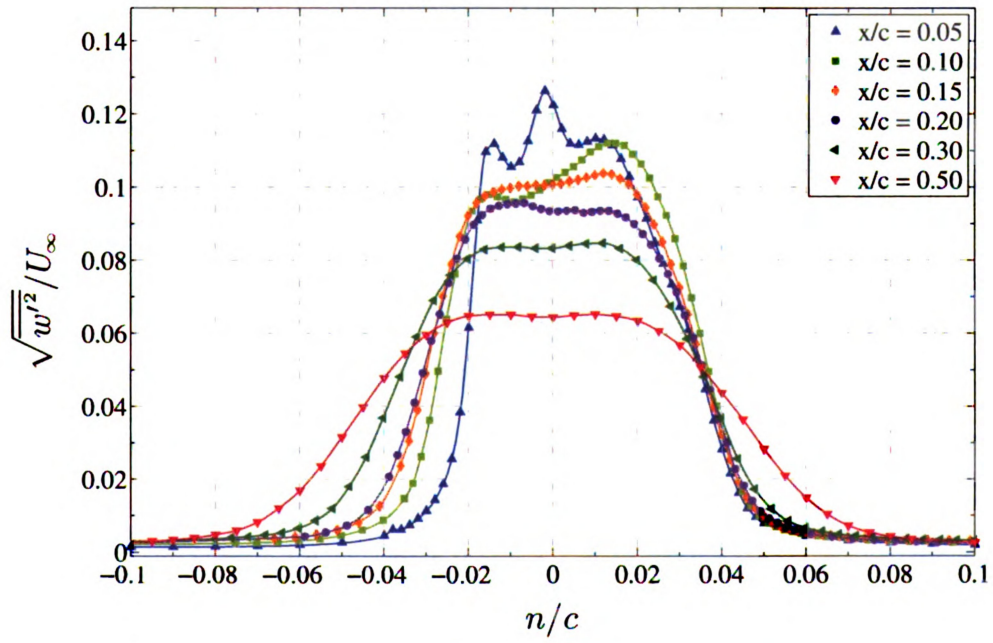


**Figure 5.45:** Spanwise turbulence intensity profiles ( $n = y - y_c$ )

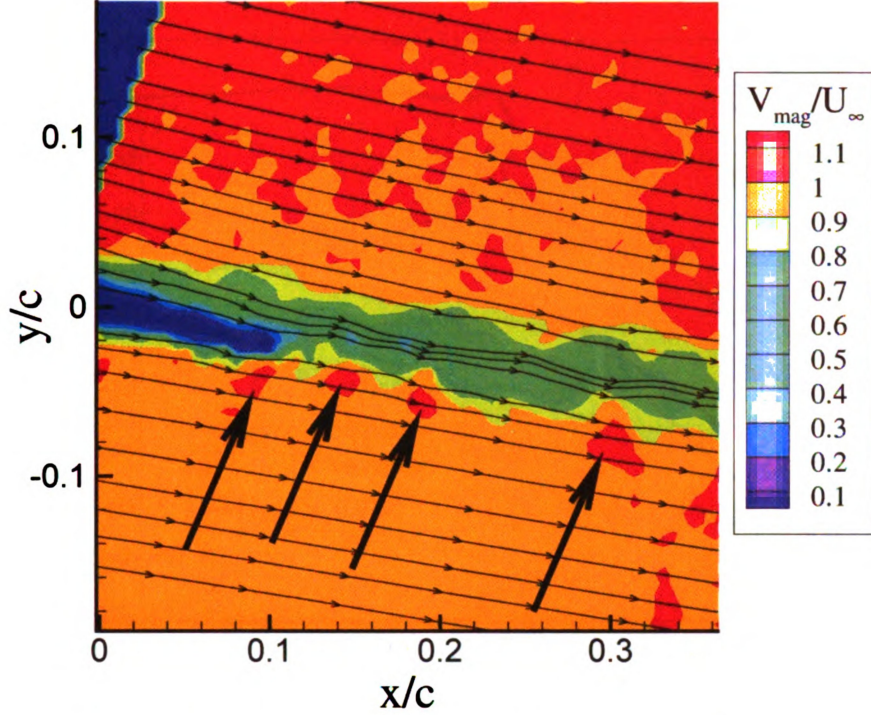


**Figure 5.46:** Instantaneous PIV data for the CD airfoil

by analyzing the streamwise velocity spectra from HW data measured at the downstream location of  $x/c = 0.075$ . These data, shown in Fig. 5.47 show the spectra at various  $y/c$  locations. Two suction side locations ( $y/c = 0.014$  and  $y/c = -0.0084$ ) and two pressure side locations ( $y/c = -0.030$  and  $y/c = -0.045$ ) are shown. A distinct peak exists on the pressure side around  $f = 1800$  Hz. Using the trailing edge thickness as a characteristic length scale yields a Strouhal number of about 0.2, typical of a vortex shedding phenomenon (a von Kármán vortex street).

The wake of the CD airfoil exhibits the trend  $T_v > T_u > T_w$  for the maximum values of each component. This is different than the results of Hah & Lakshminarayana (1982), who found  $T_u > T_w > T_v$  for the in the asymmetric wake of a symmetric airfoil (NACA 0012) with attached turbulent boundary layers leaving the trailing edge. This is also different than the findings of Raj & Lakshminarayana (1973), who found  $T_u > T_v$  (but only measured these two components) for a cascade study us-



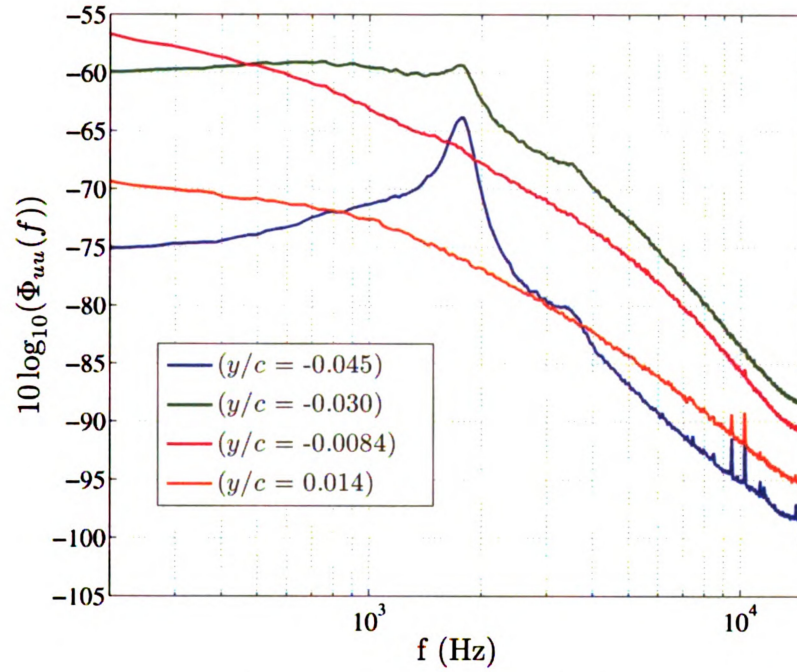


**Figure 5.47:** Streamwise velocity spectra in CD airfoil wake at  $x/c = 0.075$ .

ing cambered airfoils. The near wake region of the CD airfoil is highly anisotropic, but a much smaller degree of anisotropy exists at  $x/c = 0.50$ , where  $T_v \approx T_u \approx T_w$ . The profiles measured at the downstream locations also show that the asymmetry in the turbulence intensities measured upstream has diminished. A summary of these maximum values are shown in Table 5.4. This shows that  $T_v$  is decaying much more rapidly than  $T_u$  and  $T_w$ .

**Table 5.4:** Comparison of peak turbulence intensities at upstream and downstream locations (CD airfoil)

Turbulence Intensity Component	$x/c = 0.05$	$x/c = 0.50$
$((u'^2)^{1/2})_{\max}$	0.123	0.072
$((v'^2)^{1/2})_{\max}$	0.164	0.081
$((w'^2)^{1/2})_{\max}$	0.127	0.064

Each of the three Reynolds shear stresses have been measured using the 2X-probe:

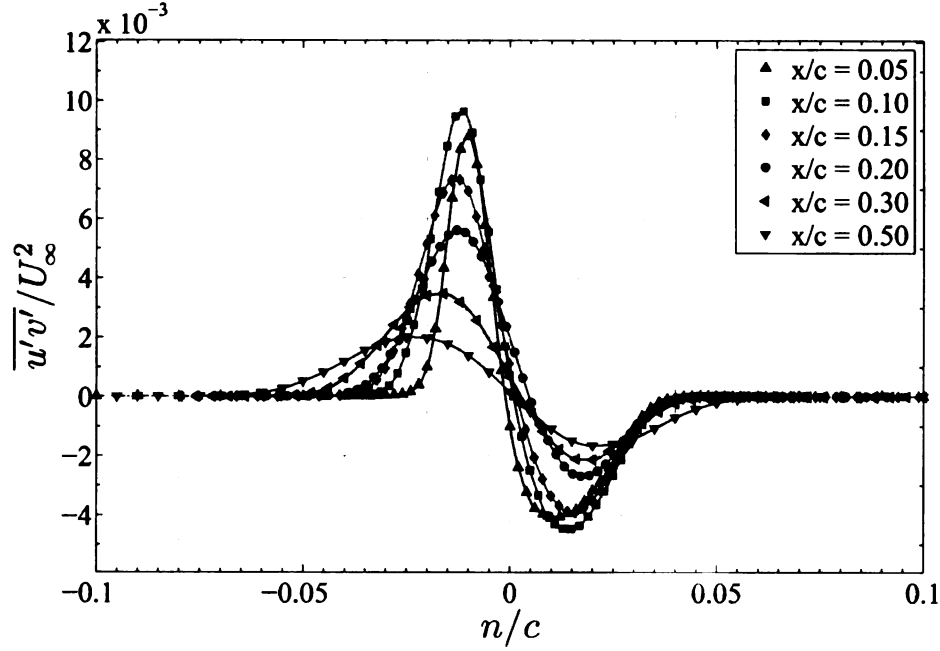


**Figure 5.48:**  $\overline{u'v'}$  shear stress distribution ( $n = y - y_c$ ).

( $\overline{u'v'}$ ), ( $\overline{v'w'}$ ), and ( $\overline{u'w'}$ ). Figure 5.48 shows the component  $\overline{u'v'}$  at various downstream locations. These values are normalized by the square of the freestream velocity upstream of the airfoil,  $U_\infty^2$  and they are presented in a wake-centered distribution, with ( $n = y - y_c$ ). The values for  $\overline{u'v'}$  at  $x/c = 0.05$  show negative values on the suction side and positive values on the pressure side. These signs are consistent with Prandtl's mixing-length concept ( $\overline{u'v'} > 0$  when  $du/dy < 0$ ). At the upstream locations, such as  $x/c = 0.05$ , the pressure and suction sides are asymmetric, both in terms of the overall width of the sheared region and also in the peak values at each  $x/c$  location. These initial asymmetries decrease farther downstream at  $x/c = 0.50$ , where the profile of  $\overline{u'v'}$  is nearly symmetric between the pressure and suction sides. Fig. 5.48 also shows that the absolute values for  $\overline{u'v'}$  on the pressure side are higher than the suction side and on both sides these values increase between  $x/c = 0.05$  and  $x/c = 0.10$ .

An interesting feature of Fig. 5.48 can be found by examining in detail the half-

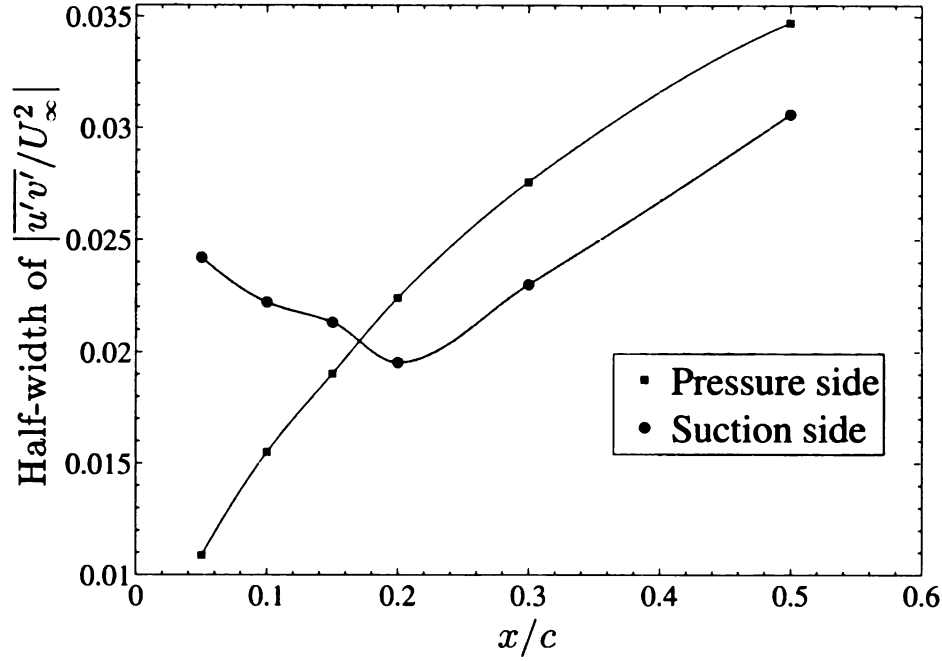


**Figure 5.49:** Wake half-width based on  $\left| \overline{u'v'} / U_\infty^2 \right| > 0$ .

width of the region where  $\left| \overline{u'v'} \right| > 0$ , which is plotted vs.  $x/c$  in Fig. 5.49. This  $\left| \overline{u'v'} \right|$  half-width is calculated for each downstream location by taking the peak value for both the pressure and suction side and subtracting out the freestream level ( $\overline{u'v'} \approx 0$  in this case) and dividing by 2. The width is then the lateral extent ( $n/c$  distance) at this  $\overline{u'v'}$  value (following a convention very similar to how the semi-wake width is calculated). It can be seen that the width of the sheared region on the pressure side steadily increases with downstream distance; however, on the suction side this width decreases (also its peak value decreases) from  $0.05 \leq x/c \leq 0.20$ . This behavior is explained by examining the effects of streamline curvature on turbulence structure, which has been documented by numerous researchers, most notably Bradshaw (1973) and also Lakshminarayana (1996). For a turbulent flow field with streamline curvature, a stabilizing or destabilizing condition will arise depending on the direction of the streamline curvature with respect to the mean velocity gradient. The concept is illustrated in Fig. 5.50, which shows a velocity gradient that is positive,

i.e.  $du/dy > 0$ , with streamline curvature such that  $u_B > u_A$  for  $r_A > r_B$ . Ignoring viscous effects and considering a simplified radial momentum equation:

$$\frac{\partial p}{\partial y} = \frac{\rho u^2}{R} \quad (5.8)$$

The effect of streamline curvature is explained using Prandtl's mixing-length concept. If an element of fluid that exists at location  $A$  (with a radius,  $r_A$ ) were suddenly displaced, via a turbulent fluctuation ( $u' > 0$ ), to location  $B$  (with a radius,  $r_B$ ), the Eulerian velocity fluctuation:  $u'$  would  $< 0$  at this new location. The observation that  $u' < 0$  is the result of the instantaneous velocity,  $u_A$  of the displaced fluid element being lower than the velocity of the surrounding fluid,  $u_B$ . At location  $B$ , the displaced fluid element will experience a restoring force that will further displace it towards the positive  $y$ -direction. This is the “destabilizing” effect of concave streamline curvature on turbulence.

For the CD airfoil, this streamline curvature decreases with downstream distance (evident from the decreasing  $v$  at each downstream location, see Fig. 5.37) and the corresponding unstable condition diminishes. Referring to Fig. 5.49, turbulent diffusion typically causes this region to steadily increase (as shown on the pressure side); however, an initially destabilized condition causes this region to initially decrease on the suction side. Once the streamlines straighten out (at  $x/c \approx 0.2$ ), the lateral extent of this sheared region increases. As seen in Fig. 5.49, for  $x/c \geq 0.2$ , the lateral extent of the pressure and suction side region increase at very similar rates.

The profiles of the Reynolds stress components  $\overline{u'w'}$  and  $\overline{v'w'}$  are shown in Figs. 5.51 and 5.52. The peak values for these are smaller than for  $\overline{u'v'}$  and they decay very rapidly. It can be seen that by  $x/c = 0.50$ , the peak values for these components,  $\overline{u'w'} \approx \overline{v'w'} \approx 1 \times 10^{-3}$ .

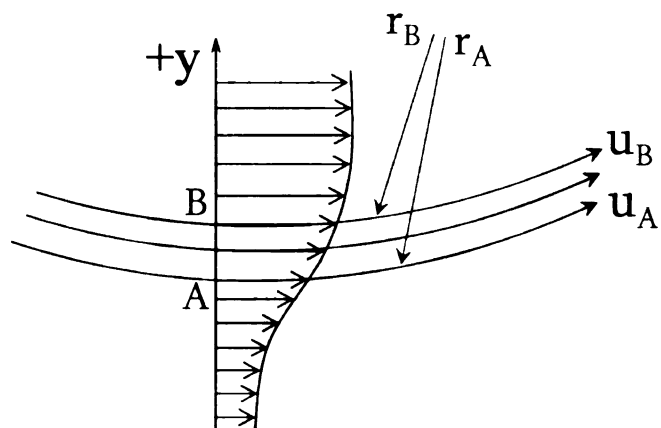


**Figure 5.50:** Sketch of the unstable condition for  $\overline{u'v'}$  region in curved streamlines.

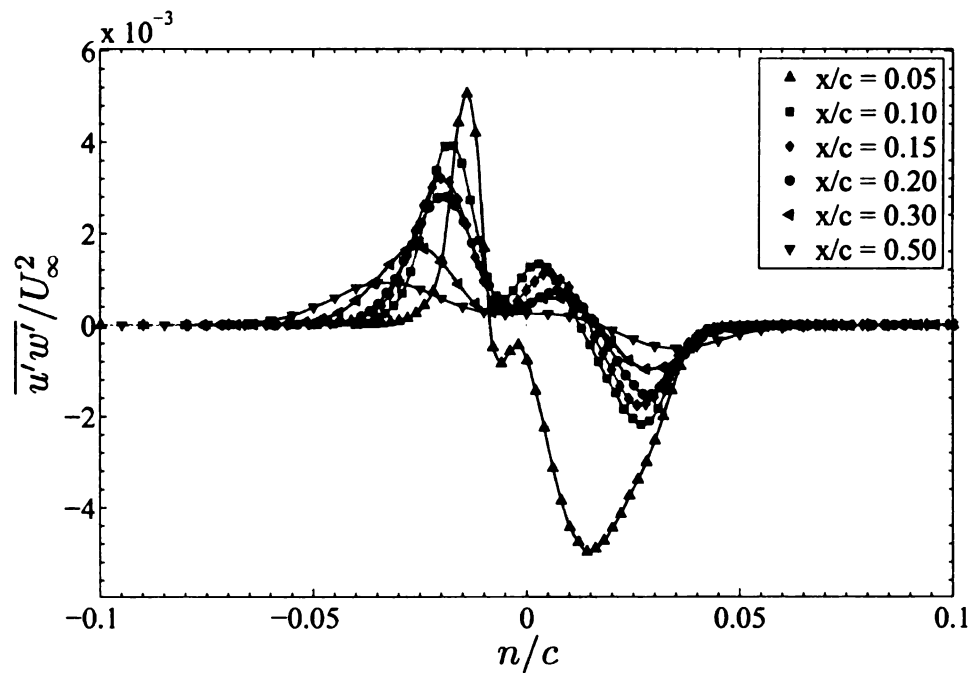


**Figure 5.51:**  $\overline{u'w'}$  shear stress distribution ( $n = y - y_c$ ).



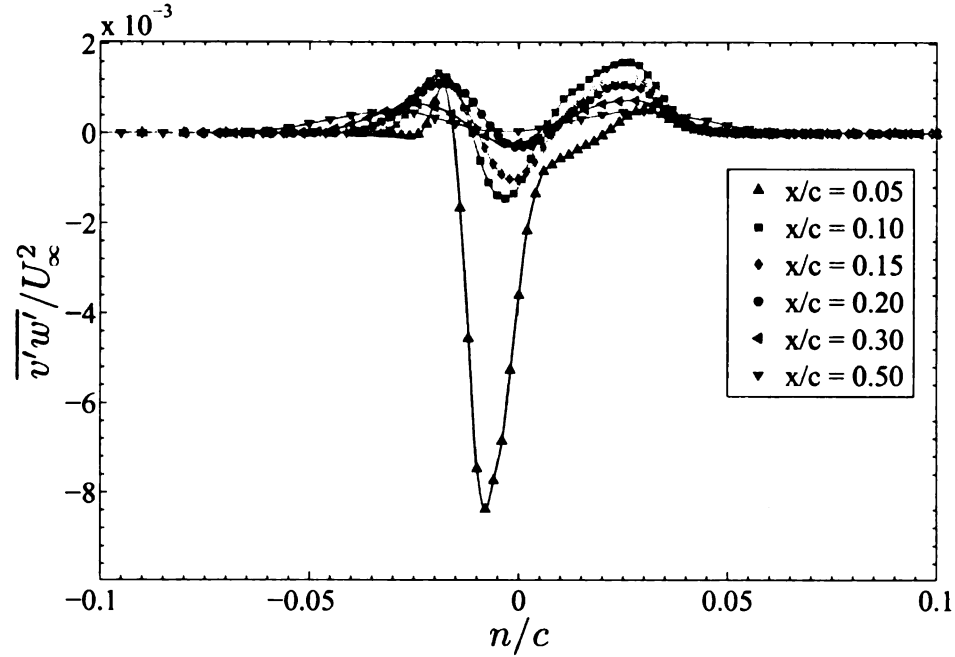


**Figure 5.52:**  $\overline{v'w'}$  shear stress distribution ( $n = y - y_c$ ).

## 5.3 Rotating CD Blade (RCDB)

### 5.3.1 Performance data ( $\Delta P$ vs. $\dot{m}$ )

The design of the RCDB was based on a specific mass flow rate,  $\dot{m} = 2.31 \text{ kg/s}$ . This flow rate, for the target rotational speed of  $\Omega = 437.5 \text{ RPM}$  provided the required upstream velocity (rotating reference frame) of  $W_\infty \approx 16 \text{ m/s}$ . A complete characterization of the pressure rise vs. mass flow was carried out in the AFRD facility. The results are shown in Fig. 5.53 for a series of tests conducted over a 10 month period. The design flow rate,  $\dot{m} = 2.31 \text{ kg/s}$ , is indicated in Fig. 5.53 by the black arrow. It can be seen from this figure that that RCDB must be run with a negative pressure rise to obtain the indicated flow rate. This means the auxiliary helper fan in the AFRD must draw a negative pressure from the upper receiver of the AFRD facility (see Fig. 4.8 for a description). The velocity surveys in this section were collected at this design flow rate, which must be maintained to create the rotating analog of

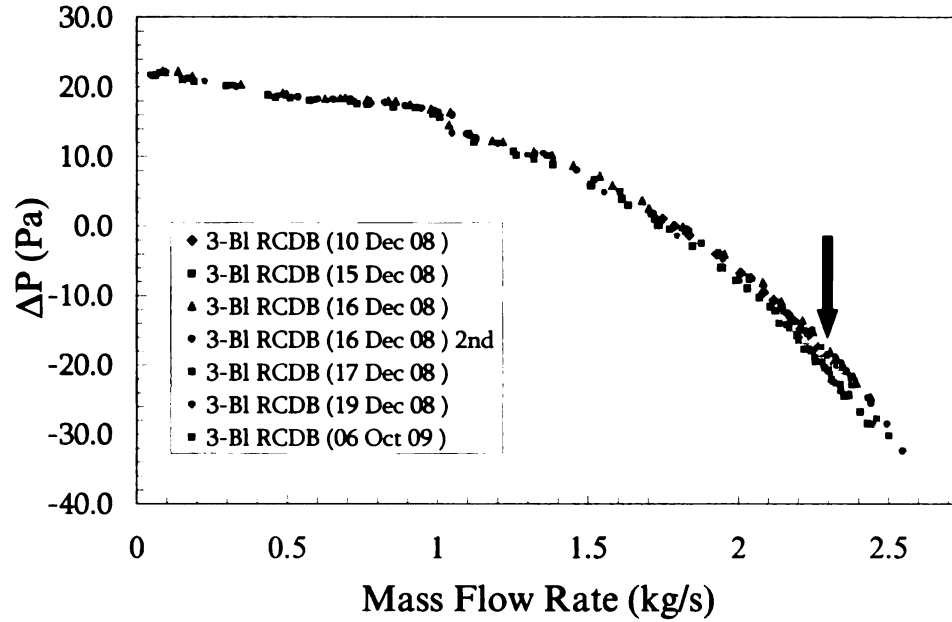


**Figure 5.53:** Performance data ( $\Delta P$  vs.  $\dot{m}$ ) for the 3-blade RCDB configuration.

the stationary CD airfoil. Additionally,  $\Delta P$  and  $\dot{m}$  data were collected during the velocity measurements to ensure that the proper design conditions were maintained.

### 5.3.2 Surface pressure ( $C_p$ ) data

The surface pressure distributions for several different RCDB configurations were measured and the results are shown in Fig 5.54. Each of these different configurations had a different solidity from a different number of installed blades (from 2–7). Also shown in Fig 5.54 are the  $C_p$  data for the stationary CD airfoil. These data show that the overall lift of a single blade of the RCDB device is affected by the solidity. The higher the solidity, the less lift is created by the blade. This result is similar to the finding, described in Sec. 3.3, that the blade loading of the stationary airfoil varied depending on the width of the jet used in the open jet experiments. The surface pressure distribution of the stationary CD airfoil is also plotted in the Fig 5.54. The

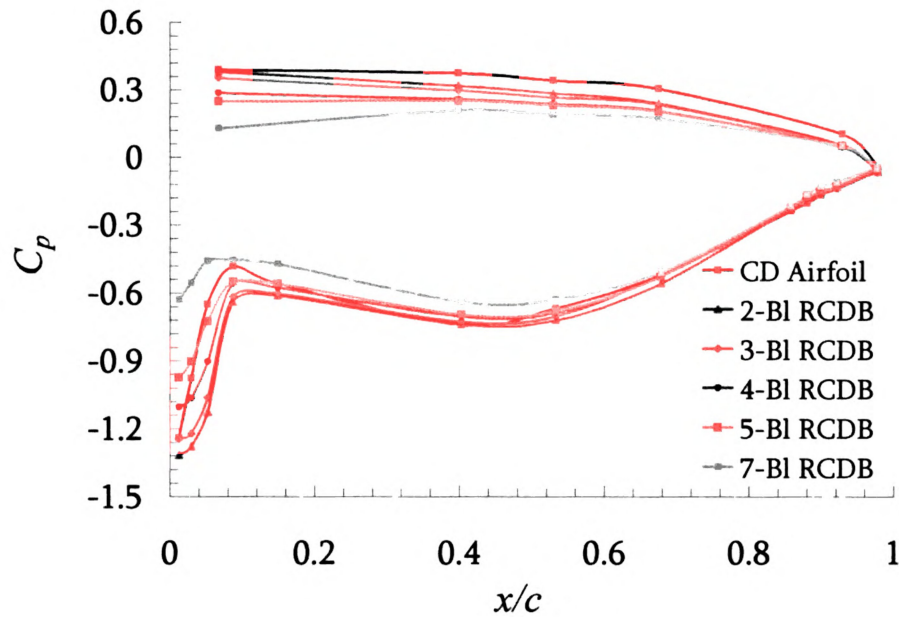


**Figure 5.54:** Comparison of the  $C_p$  distributions for various RCDB configurations.

data in the following sections are for the 3-blade RCDB configuration, which had the closest surface pressure distribution to the stationary CD airfoil, as shown previously in Sec. 3.3. Note that the 3-blade RCDB configuration does have a slightly lower pressure distribution on the suction side, indicating that it has a slightly lower lift than the stationary CD airfoil. Reasons for this are explained in Sec. 5.3.3. The 3-blade RCDB configuration, when operating at its design operating point, is a rotating analog of the stationary CD airfoil experiment (see Sec. 3.1 for the other criteria). This condition of being a rotating analog is true only for the mid-span region of the blade is as described in detail in Chap. 3.

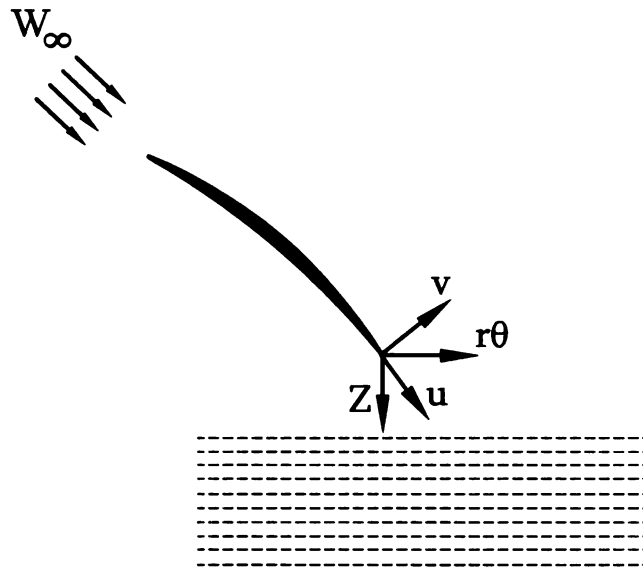
### 5.3.3 Phase-averaged mean velocity in the wake

The phase-averaged data measured in the RCDB are presented in this section. These data were measured with both an X-probe and a 2X-probe using a stationary probe that was mounted in an  $r$ - $\theta$ - $z$  traverse in the AFRD facility. It is conventional

to present turbomachinery velocity data as components in these directions ( $V_r$ ,  $V_\theta$ ,  $V_z$ ); however for the purpose of comparing with the CD airfoil, the RCDB data are presented in the same coordinate system used for the CD airfoil experiments,  $u$  and  $v$ , as shown in Fig. 5.55. The radial velocity (designated as  $V_r$  when  $V_z$  and  $V_{theta}$  are used and  $w$  when  $u$  and  $v$  are used) is the same in both coordinate systems and these two designations are interchangeable. The radial velocity in the RCDB will be referred to as  $w$ , to maintain consistency with the streamwise and transverse velocities,  $u$  and  $v$ , respectively. The velocity profiles of  $u$ ,  $v$  and  $w$  were measured at a fixed radial location ( $r = 303 \text{ mm}$ ) along lines of  $z$  and  $r\theta$ . The radius,  $r$  is multiplied by  $\theta$  to give the azimuthal ( $\theta$ ) direction a length dimension (mm). Note that  $w$ , the radial velocity, is different than  $W_\infty$ , the upstream approach velocity in the rotating reference frame in the RCDB experiment. Planar phase-averaged PIV data were also collected in the wake region at the blade mid-span. These data are also presented in this section.

A phase-averaged streamwise velocity profile for a full revolution is shown in Fig. 5.56. The abscissa,  $2\pi/\Omega$  is the time for one revolution. The phase reference is established on a once-per-revolution basis. These data are averaged from an ensemble of 2600 revolutions and each revolution is comprised of approximately 10,500 points, which yields a  $\Delta r\theta \approx 0.18 \text{ mm}$  (or a point every  $0.03^\circ$ ). The 3 wakes from each of the three blades are designated by the arrows in Fig. 5.56. This plot shows the very periodic behavior (blade-to-blade) of the RCDB experiment at this nearest location ( $z/c = 0.05$ ), a pattern which remains at subsequent downstream locations ( $0.05 \leq z/c \leq 0.50$ ). Also it is apparent from Fig. 5.56 that there is a non-constant free-stream velocity outside of the blade region (i.e. the region where the blade is shearing the flow). Instead, the free-stream has a constant velocity gradient,  $du/d(r\theta) < 0$ .

A single blade wake (for the blade that is instrumented with the pressure taps)



Wake Survey Locations

**Figure 5.55:** Locations of wake velocity surveys for the RCDB experiments. Note that  $u, v$  also specify the x,y directions. Also, the x-direction is parallel to  $W_\infty$ .

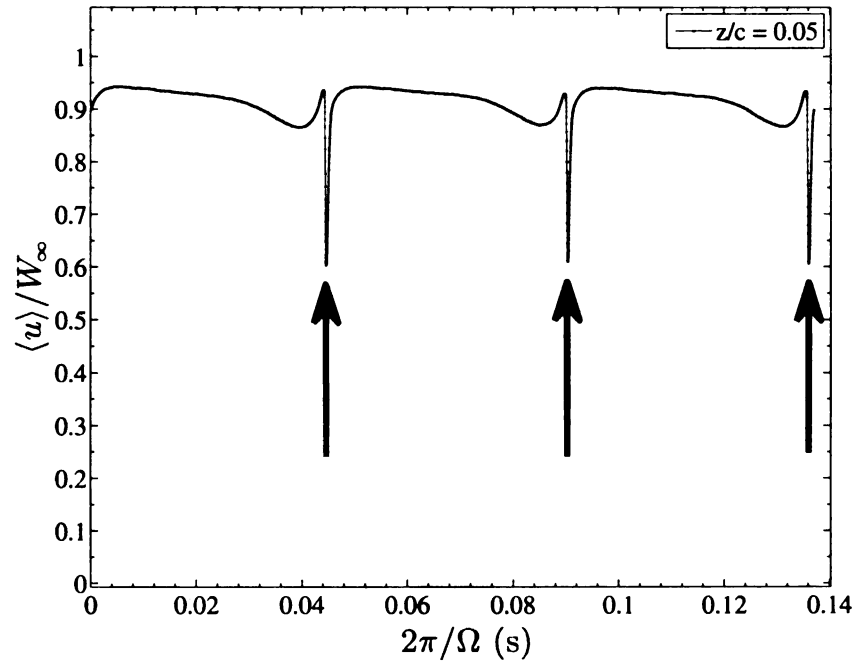


**Figure 5.56:** Phase-averaged  $\langle u \rangle$  data for all 3 blades of the RCDB experiment (wakes are indicated by the arrows).

is shown in Fig. 5.58. These data are the phase-averaged streamwise velocity at the furthest upstream ( $z/c = 0.05$ ) location and they are shown for an azimuthal distance of one chord in each direction ( $\pm 1c$ ). The pressure side and suction side of the wake are labeled in Fig. 5.58. The abscissa is converted from time (as seen in Fig. 5.56) to space using the following relationship:

$$\frac{r\theta}{c} = \frac{t \times \Omega \times r}{c} \quad (5.9)$$

These data are plotted in a coordinate system where the origin of the abscissa ( $r\theta/c = 0$ ) indicates the trailing edge of the blade. The position of the blade trailing edge was determined by fitting the wake centers at each  $r\theta/c$  location and extrapolating the curve fit to the  $z/c = 0$  location ( $z/c = 0$  is the trailing edge of the blade), see Fig. 5.57. Figure 5.58 clearly shows the width of the wake region and the free-stream velocity outside of the wake. The locations  $-1 \leq r\theta/c \leq -0.5$  on pressure side of the blade show a slight decrease in the  $+r\theta/c$ -direction (i.e.  $du/d(r\theta) < 0$ ). Between the locations  $-0.5 \leq r\theta/c \leq 0$ , there is a strong influence of the approaching blade and there is a strong increase in the velocity. The wake is between  $0 \leq r\theta/c \leq +0.25$  and the freestream velocity adjacent to the suction side is at the locations  $0.25 \leq r\theta/c \leq +1.0$

The streamwise velocity in the blade wake for multiple downstream locations are shown in Fig. 5.59. These data show the strong swirl component of the wake, as it is moving towards in the  $-r\theta$ -direction at each downstream location. Figure 5.63 shows these same data with the wake centers shifted ( $n = r\theta - r\theta_c$ ). This aligns the wake in a coordinate system that follows the wake centerline and allows for the wakes to be compared. This figure shows that the wake becomes increasingly asymmetric with downstream distance. The wake edge velocity,  $U_e$ , on the suction side decreases with each downstream measurement station, while the wake edge velocity on the pressure

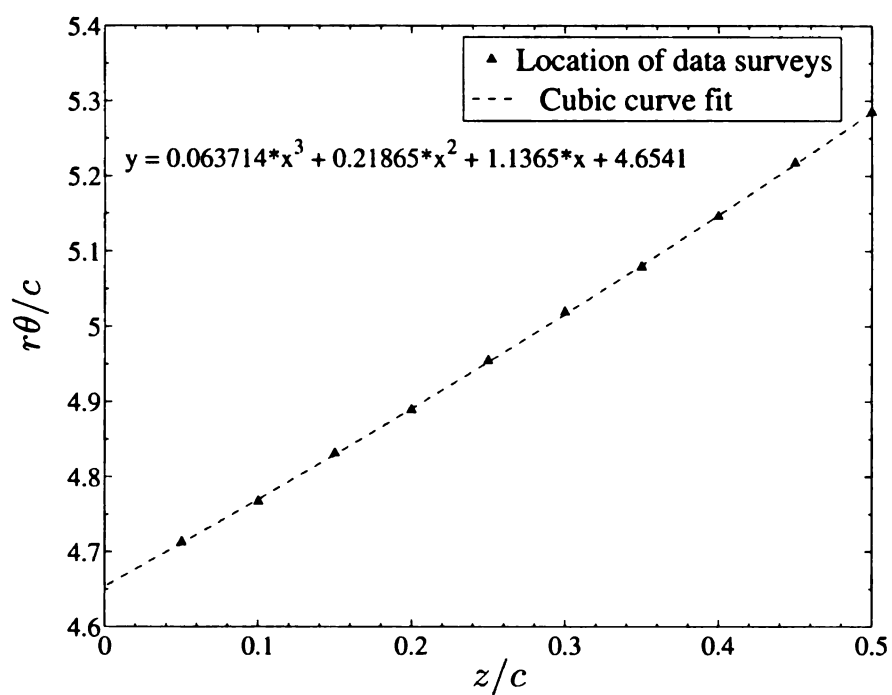


**Figure 5.57:** Data used to determine the location of the RCDB trailing edge.

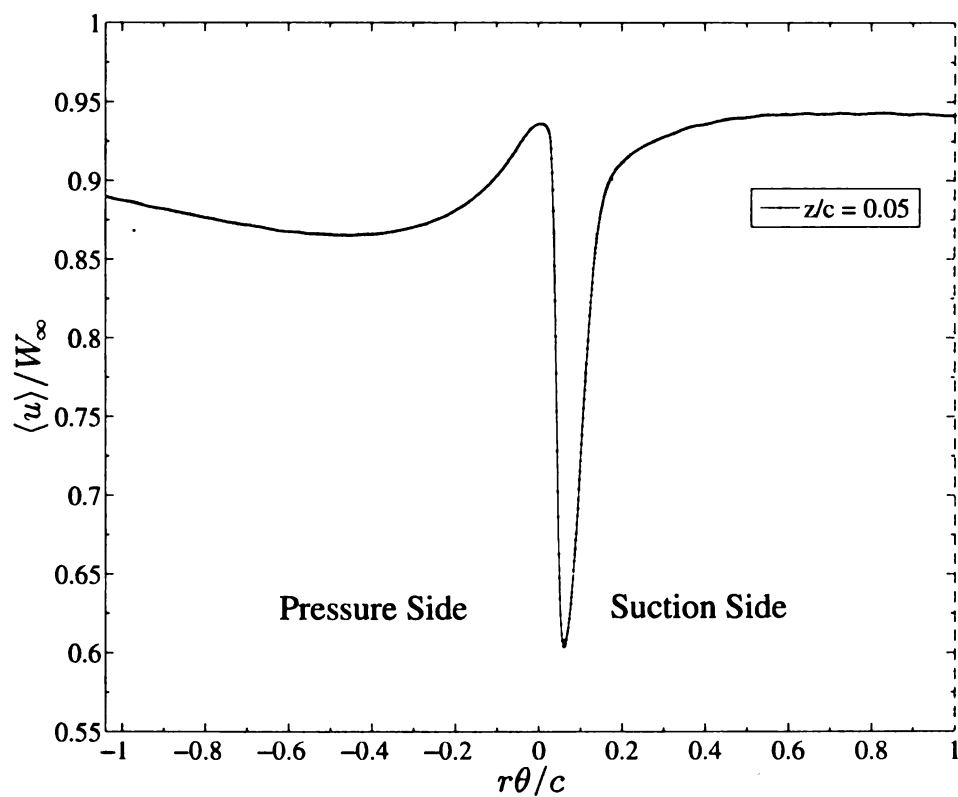


**Figure 5.58:** Phase-averaged  $\langle u \rangle$  data for a single blade of the RCDB experiment.

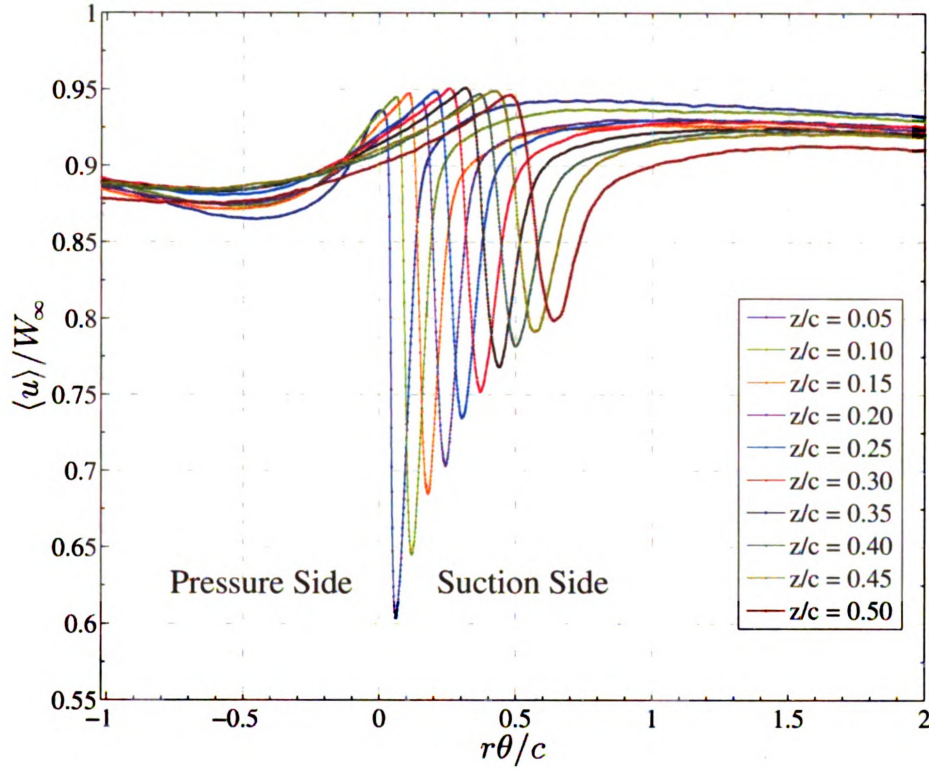


**Figure 5.59:** Phase-averaged  $\langle u \rangle$  for a single blade wake at multiple downstream locations.

side is nominally constant. The freestream velocity, farther from the edge of the wake, shows the opposite trend of the freestream velocity on the suction side.

The data of Fig. 5.59 show the center of the wake is moving in the  $+r\theta/c$ -direction (which is towards the suction side of the blade) with downstream distance  $+z/c$ . This would appear to be opposite of the trend seen in the stationary CD airfoil. However, this is a result of the coordinate system of the traverse ( $r - \theta - z$ ) that is used to collect these measurements. This can be seen by examining the phase-averaged PIV data that were also collected in the wake. Figure 5.60 shows the absolute velocity magnitude measured in the wake region. In the absolute reference frame, the velocity shows a slight swirl component ( $V_\theta < 0$ ). A region exists from the trailing edge of the blade (0,0) to along a diagonal line to the lower right hand side of the image. The



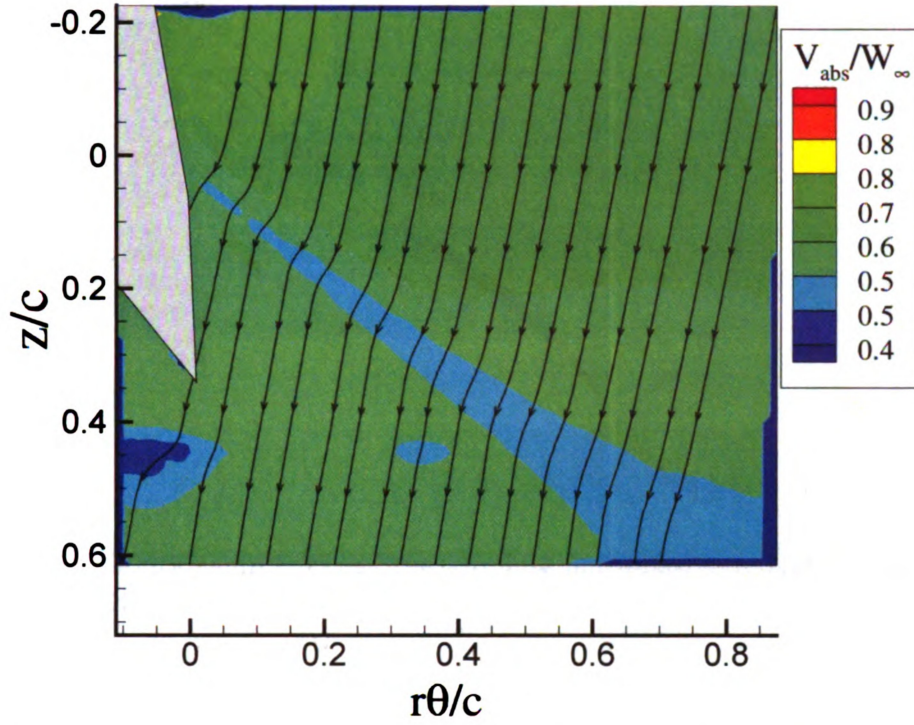


**Figure 5.60:** RCDB wake PIV data in the absolute velocity frame.

grey area in Fig. 5.60 is the area consumed, in the image, by the blade. Because of the changing blade stagger angle, the region that the blade occupies in the image is oddly-shaped and the grey region should not be interpreted as the shape of the RCDB profile at the mid-span. It can be seen that the streamlines have a slightly higher  $V_{\theta}$  in this region (as indicated by the change of the angle of the streamlines). This region is the airfoil wake, with the velocities represented in the absolute reference frame. The relationship between the relative and absolute velocity is:

$$\vec{V}_{abs} = \vec{V}_{rel} + \vec{r}\vec{\omega} \quad (5.10)$$

Which is shown graphically in Fig. 5.61. Since the rotational speed of the RCDB,  $r\omega$ , is measured at the same time as the PIV data were collected, Fig. 5.60 can be cast into a reference frame that is fixed to the moving blade, using the relationship in Eq. 5.10.

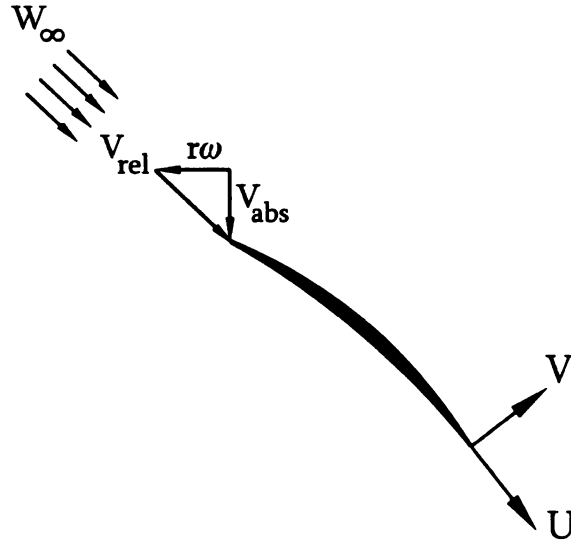


**Figure 5.61:** Relationship between the absolute and relative reference frame velocities in the RCDB.

The PIV measurements in the rotating frame of reference are shown in Fig. 5.62. Here the velocity contour is the relative (or fixed to the rotating blade) velocity magnitude,  $\vec{V}_{rel}$ . The streamlines in Fig. 5.62 are calculated from the velocity components,  $u$  and  $v$ , as shown schematically in Fig. 5.61. The streamwise (in the relative reference frame) velocity  $u$  is parallel to the upstream inlet velocity (in the relative reference frame),  $W_\infty$ . Note that  $u$  and  $v$  are identical to the definitions of  $u$  and  $v$  for the stationary CD airfoil. It can be seen in Fig. 5.62 that the wake moves towards the  $+r\theta$ -direction, as shown in Fig. 5.59.

The transverse component of velocity,  $v$ , is shown in Fig. 5.64. Referencing the coordinate system shown in Fig. 5.55,  $v < 0$  indicates that the fluid motion is deflecting towards the pressure side of the blade. This is consistent with the  $C_p$  data shown in Fig. 5.54, which shows the overall lift of the RCDB is very close to that of the stationary CD airfoil. Since the blade has a positive lift force, it must deflect the flow towards the pressure side of the blade, i.e. towards the  $-n/c$ -direction. This  $v < 0$  condition is seen at all of the measurement stations, but its magnitude is monotonically increasing with downstream distance (for a given  $n/c$  location). This indicates

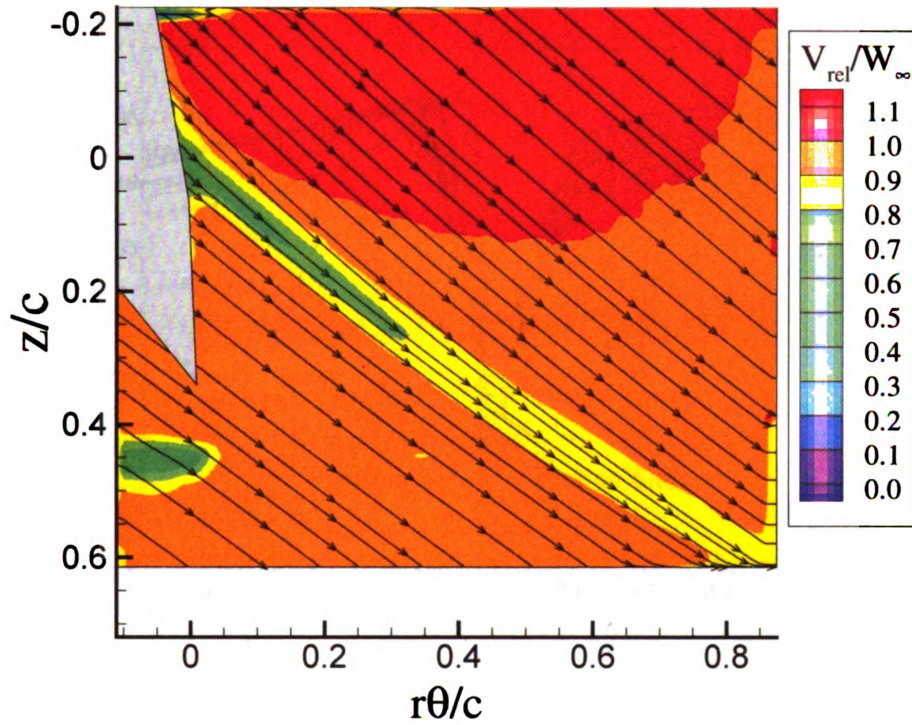


**Figure 5.62:** RCDB wake PIV data in the relative velocity frame.

that the wake is “straightening out” by moving towards the suction side as it moves farther from the wake. This decrease in  $v$  is a direct result of the negative pressure rise (as shown in Fig. 5.53) that is imparted on the blade to get the necessary flow conditions.

The radial velocity,  $w$ , for all downstream measurement planes is shown in Fig. 5.65. The radial velocity in the freestream is consistently negative, and is a small percentage (5-8%) of the freestream velocity:  $W_\infty$ . Outside of the wake region, the radial velocity is also consistently negative, which shows that the wake is moving towards the hub. This is a direct result of the Coriolis forces. In the wake region, the flow varies between the positive and negative directions, indicating that a complex flow exists in the RCDB wake. Overall, the radial velocity is very small downstream of the blade (including the region inside wake) which is consistent with the design objective (nominally 2D flow) outlined in Chap. 3. Figure 5.66 shows the radial velocity,



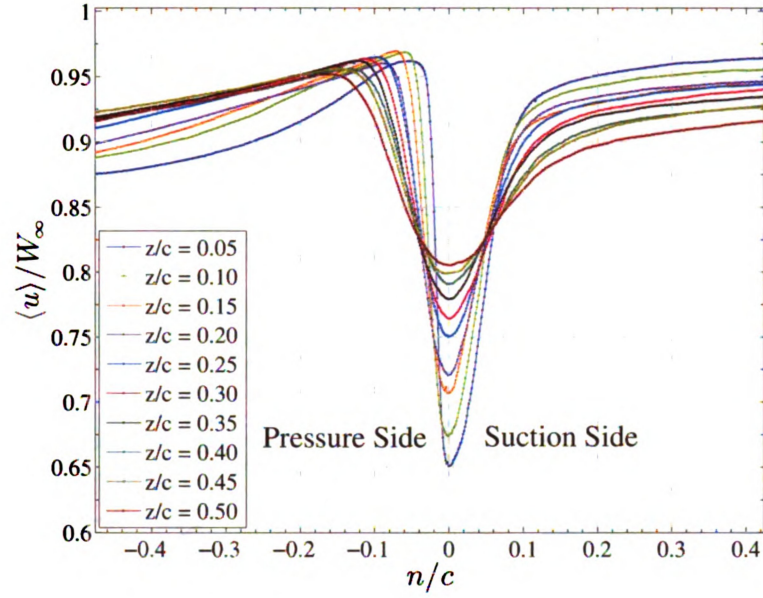


**Figure 5.63:** Wake-centered phase-averaged  $\langle u \rangle$  for a single blade wake ( $n = r\theta - r\theta_c$ ).

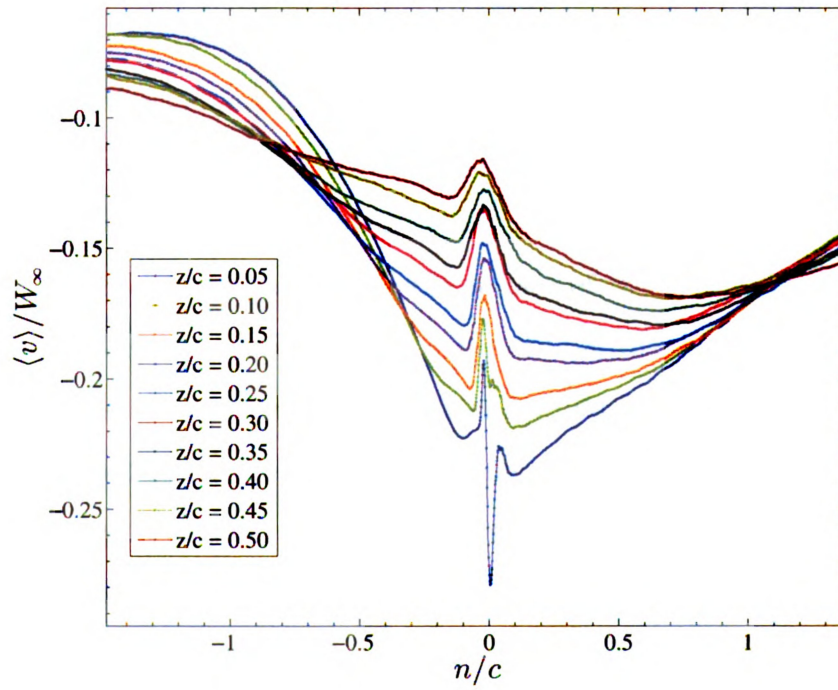


**Figure 5.64:** Phase-averaged  $\langle v \rangle$  for a single blade wake ( $n = r\theta - r\theta_c$ ).

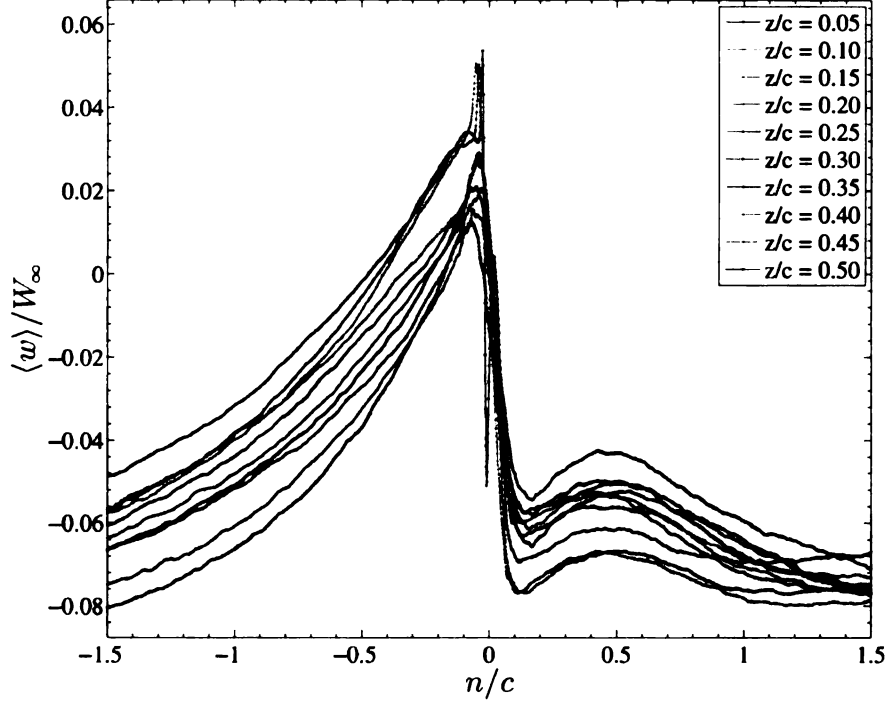


**Figure 5.65:** Phase-averaged  $\langle w \rangle$  in the wake of a single blade ( $n = r\theta - r\theta_c$ ).

$w$ , in a region very near the trailing edge. The locations where  $n/c > 0$  comprise the suction side region and the locations where  $n/c < 0$  are the pressure side. At the farthest upstream location, where  $z/c = 0.05$ , there is a non-zero velocity found on the pressure side (between  $-0.02 \leq n/c \leq 0.0$ ). This non-zero radial velocity will have a Coriolis acceleration into the surface of the blade. The resulting force in the rotating reference frame will be outward from the surface. This would cause the surface pressures measured on the suction side to be *lower* than an equivalent flow that was not under the effects of rotation. This is likely the cause of the lower pressure-side blade loadings that were shown in Fig. 5.54. The suction side region that is the wake center (between  $0.0 \geq n/c \geq 0.02$ ) has a nominally zero velocity, indicating that there is very little radial flow on the suction side. This is consistent with the  $C_p$  data shown in Fig. 5.54. It can also be seen that the radial velocity decays very quickly; the distinct peaks that were found at  $z/c = 0.05$  are gone by

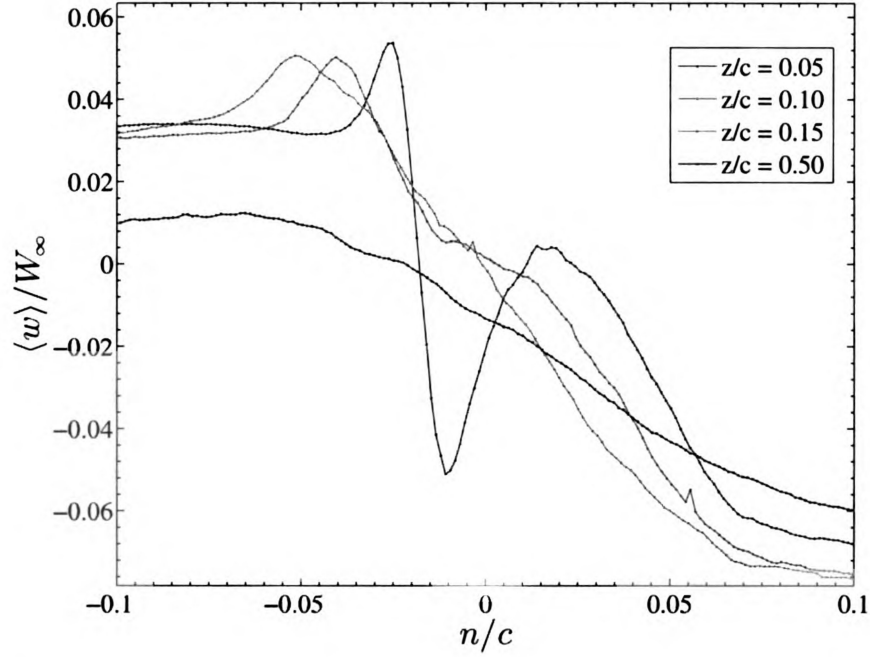


**Figure 5.66:** Close-up view of the phase-averaged  $\langle w \rangle$  in the wake of a single blade ( $n = r\theta - r\theta_c$ ).

$z/c = 0.10$ . It can be reasoned that the radial velocity further upstream ( $z/c \approx 0$ ) would have an even higher pressure-side radial velocity than what is measured at  $z/c = 0.05$ .

The phase-averaged streamwise velocity profiles for the RCDB were also reduced to a single curve by introducing a scaling velocity and a scaling length, identical to what was calculated in Sec. 5.2.4. The scaling velocity was again the difference between the wake edge velocity and the wake centerline velocity,  $(U_e - U_c)$ . The wake of the RCDB is also asymmetric (even more in the  $r - \theta - z$ -coordinate system), so again two different scaling lengths were selected,  $l_p$  and  $l_s$ , using identical definitions as defined previously. The scaled velocity profiles are shown in Fig. 5.67 which, similar to the CD airfoil, shows the existence of self-similarity in the mean streamwise velocity profiles. The region just outside of the wake edge velocity (on either side) does not reduce to a single curve like the CD airfoil. This is apparently the result of the large

asymmetries that exist from measuring the wake along a  $z/c=\text{constant}$  plane.

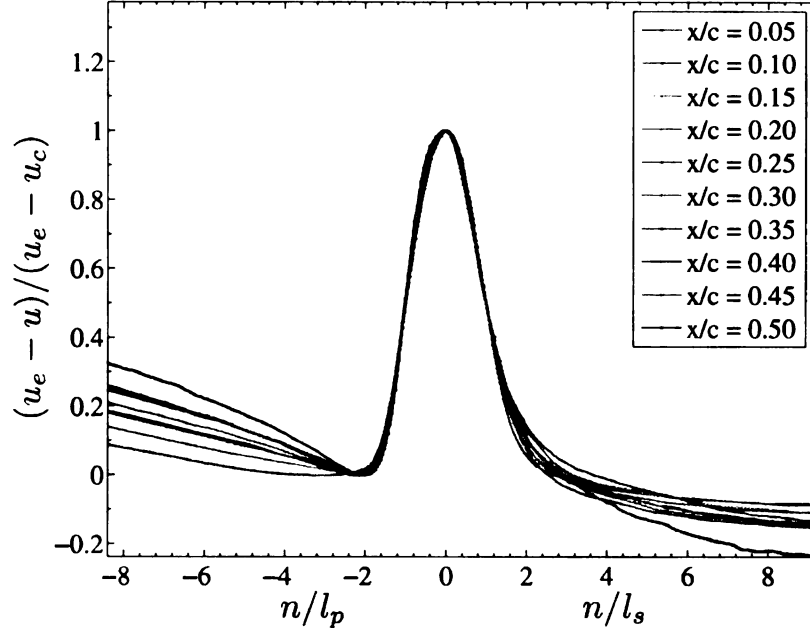


**Figure 5.67:** Similarity for the mean velocity profiles of the RCDB.

### 5.3.4 Phase-averaged turbulence properties

The phase-averaged turbulence intensities in the wake, as measured by the 2X-probe, are examined in this section. Similar to the mean velocity data, these quantities are phase-averaged from an ensemble of 2600 revolutions and each revolution is comprised of approximately 10,500 points, which yields a  $\Delta r\theta \approx 0.18 \text{ mm}$  (or a point every  $0.03^\circ$ ). The 2X-probe provides instantaneous 3-components of velocity, which can be phase-averaged to provide the full detail of the 3 components of turbulence intensity. These are in: the streamwise  $(\langle u'^2 \rangle)^{\frac{1}{2}}$ , transverse  $(\langle v'^2 \rangle)^{\frac{1}{2}}$ , and spanwise  $(\langle w'^2 \rangle)^{\frac{1}{2}}$  directions, as well as the 3 components of the Reynolds stress:  $\langle u'v' \rangle$ ,  $\langle v'w' \rangle$ , and  $\langle u'w' \rangle$ .

The turbulence intensities  $(\langle u'^2 \rangle)^{\frac{1}{2}}$ ,  $(\langle v'^2 \rangle)^{\frac{1}{2}}$ ,  $(\langle w'^2 \rangle)^{\frac{1}{2}}$  will be referred to as  $T_u$ ,  $T_v$ , and  $T_w$ , respectively. Their values across the wake region at several downstream

locations are shown in Figs. 5.68–5.70. These values are wake-shifted (aligned on wake center), where  $n = r\theta - r\theta_c$ . The downstream locations are along lines of constant  $z/c$ , following the coordinate system shown in Fig. 5.55. Figure 5.68 shows the values of  $T_u$  for  $z/c = 0.05 - 0.50$ . These data show an asymmetry with two distinct peaks (one on the pressure and one on the suction side), with a minimum value between the two very close to the TE location ( $n/c = 0$ ). These two peaks persist with downstream location and are clearly visible at  $z/c = 0.50$ . The upstream peak value for the normal turbulence intensity on the pressure side is  $T_u \approx 0.13$ .

The transverse turbulence intensities,  $T_v$ , are shown in Fig. 5.69. These values have a single peak for all values of  $z/c$ , again situated on the pressure side. The farthest upstream value ( $z/c = 0.05$ ) is slightly higher than the value of  $T_u$  at the same location; however at the farthest downstream location, the peak value of  $T_v$  is lower than  $T_u$ . This shows there is more rapid decay in the transverse direction as compared with the streamwise direction.

The data for the spanwise (radial) turbulence intensity,  $T_w$ , is shown in Fig. 5.70. These profiles show that there are initially two peaks at the  $z/c = 0.05$ , with the larger peak again being on the pressure side of the airfoil. The peak value at this location, is significantly higher than for the transverse and streamwise directions. These two peaks quickly become a single peak by  $z/c = 0.15$  and the final peak value at  $z/c = 0.50$  is slightly higher than  $T_u$  and  $T_v$ . These upstream and downstream values show that the decay rate for  $T_w$  is comparable to the decay rate for  $T_v$ , but lower than for  $T_u$ . A summary of the peak values for each component at their upstream and downstream locations is shown in Table 5.4.

The turbulence intensities in the wake of the RCDB show the trend  $T_w > T_v > T_u$  for the maximum values of each component in the upstream region. The values for  $T_u$  and  $T_v$  are approximately the same, with the radial component being significantly higher. Downstream, the different decay rates show that  $T_u > T_v$ , but  $T_w$  remains the



highest. These results are similar to those of Lakshminarayana & Reynolds (1980) who also found  $T_w > T_u$  throughout the wake, but they found that values of  $T_v > T_w$  at certain locations.

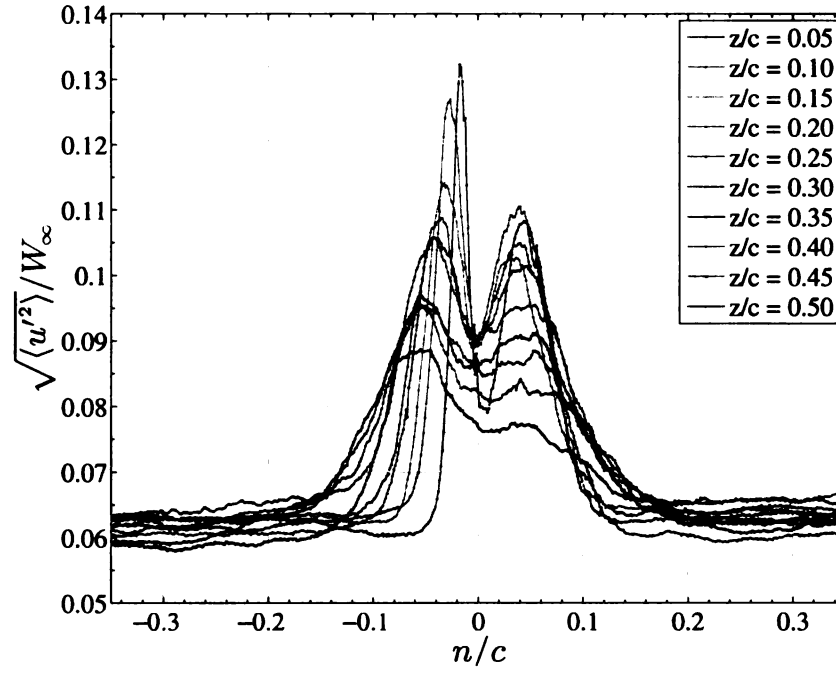


**Figure 5.68:** Phase-averaged streamwise turbulence intensity in the wake of a single blade ( $n = r\theta - r\theta_c$ ).

**Table 5.5:** Comparison of peak turbulence intensities at upstream and downstream locations (RCDB)

Turbulence Intensity Component	$z/c = 0.05$	$z/c = 0.50$
$(\langle u'^2 \rangle)^{1/2}  _{\max}$	0.1322	0.0887
$(\langle v'^2 \rangle)^{1/2}  _{\max}$	0.1393	0.076
$(\langle w'^2 \rangle)^{1/2}  _{\max}$	0.1665	0.0952

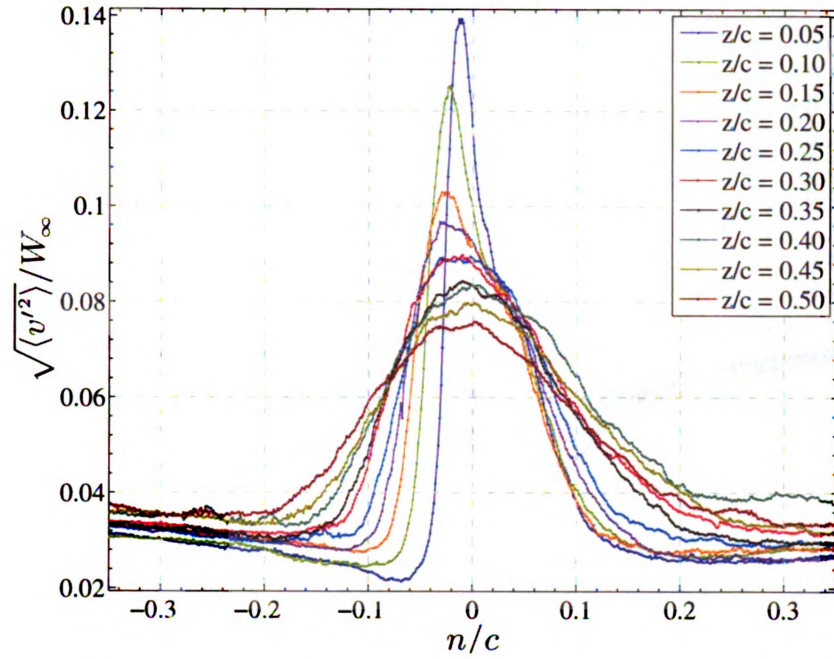


**Figure 5.69:** Phase-averaged transverse turbulence intensity in the wake of a single blade ( $n = r\theta - r\theta_c$ ).

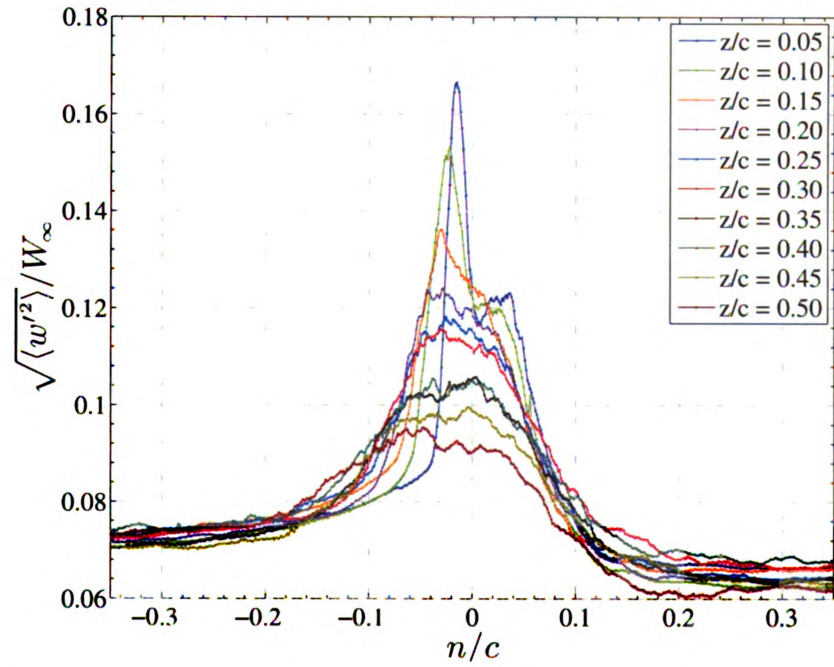


**Figure 5.70:** Phase-averaged radial (spanwise) turbulence intensity in the wake of a single blade ( $n = r\theta - r\theta_c$ ).

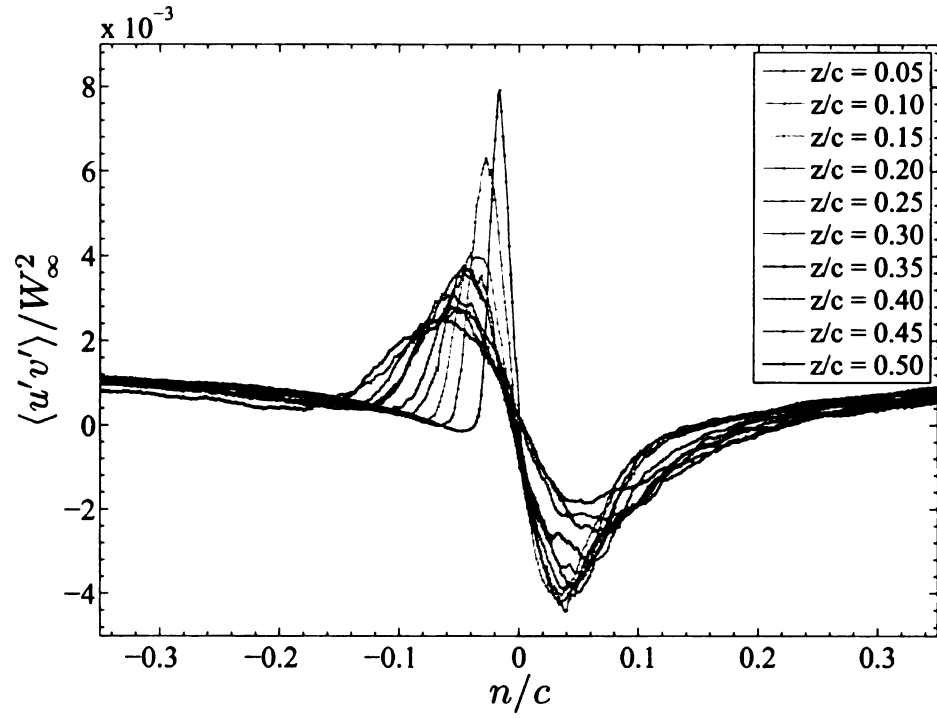


**Figure 5.71:** Phase-averaged Reynolds shear stress in the wake of a single blade ( $n = r\theta - r\theta_c$ ).

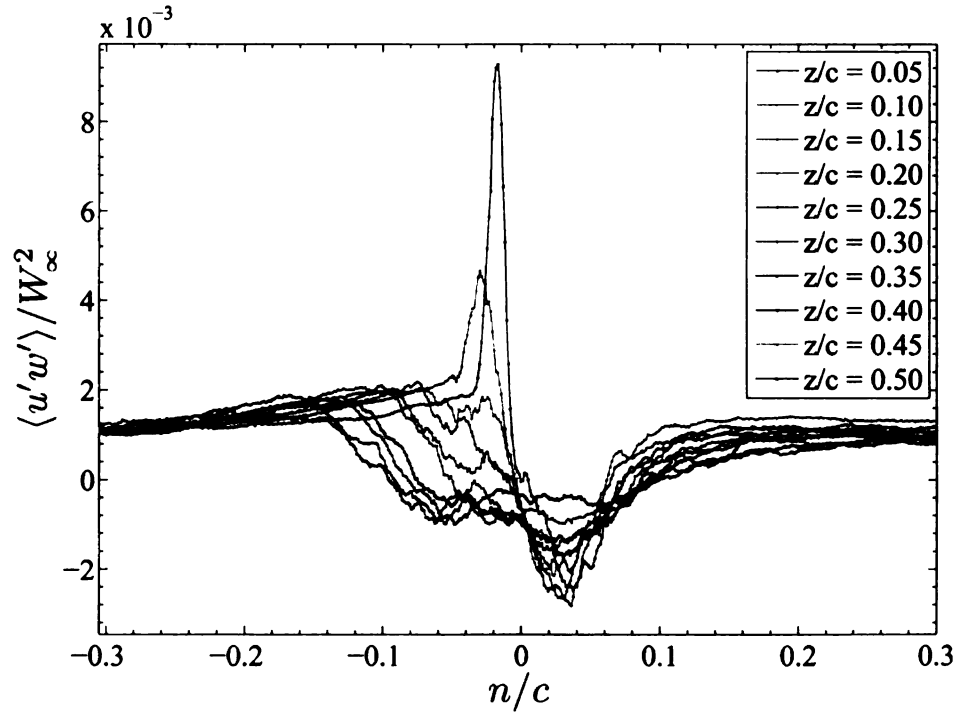


**Figure 5.72:** Phase-averaged Reynolds shear stress  $\langle u'w' \rangle$  in the wake of a single blade ( $n = r\theta - r\theta_c$ ).

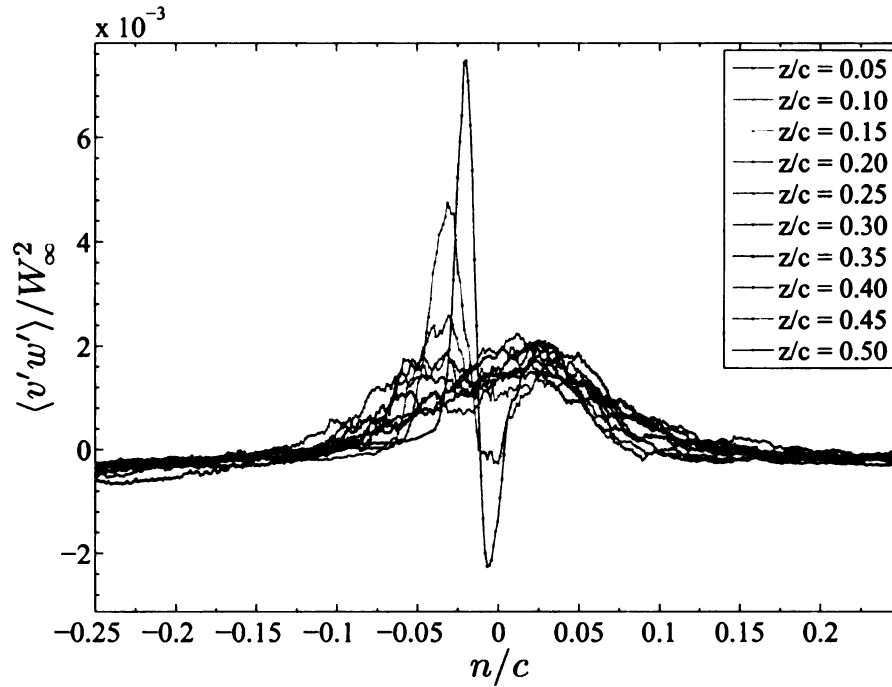


**Figure 5.73:** Phase-averaged Reynolds shear stress in the wake of a single blade ( $n = r\theta - r\theta_c$ ).

### 5.3.5 Time-resolved turbulence properties from the rotating X-probe measurements

The majority of the RCDB data were collected with the hot-wire probe in the stationary reference frame. This approach allows for the collection of phase-averaged measurements, which provide most of the parameters of interest. Time-resolved data, such as velocity spectra, require that the probe is moving with the rotating blade, such that the probe position is fixed to a specific blade location for a specified amount of time. These data required the special traverse that is described in Sec. 4.2.5. The space limitations for the instrument cluster inside the hub allowed for two channels of hot-wire anemometry. As a result, 1X-probe data were collected using a specialized X-probe (shown in Fig. 4.19).

Figure 5.74 shows the streamwise velocity spectra at various locations in the wake. The negative values of  $n/c$  represent locations on the pressure side of the wake and

the positive values of  $n/c$  are located on the suction side of the wake. This plot shows a result that is very similar to what was found previously for the stationary CD airfoil in Fig 5.47. Specifically, a distinct peak exists on the pressure side (at  $n/c = -0.02987$ ) around  $f = 1800$  Hz. This location corresponds to the outer edge of the wake on the pressure side, where the overall turbulence levels are relatively low. This peak is also evident at the location  $n/c = -0.0239$ , although the overall turbulence levels are higher and almost bury the peak. At  $n/c = -0.01195$ , which is still on the pressure side, the turbulence levels are too high to resolve the peak at  $f \approx 1800$  Hz. It also evident in Fig. 5.74 that there is no distinct peak on the suction side locations ( $n/c > 0$ ). These data show that the shedding phenomenon previously shown in the CD airfoil (and reasoned to be a von Kármán vortex shedding) also exists in the RCDB. This argues that the shedding is connected to the geometry and boundary conditions and not significantly affected by the Coriolis forces.

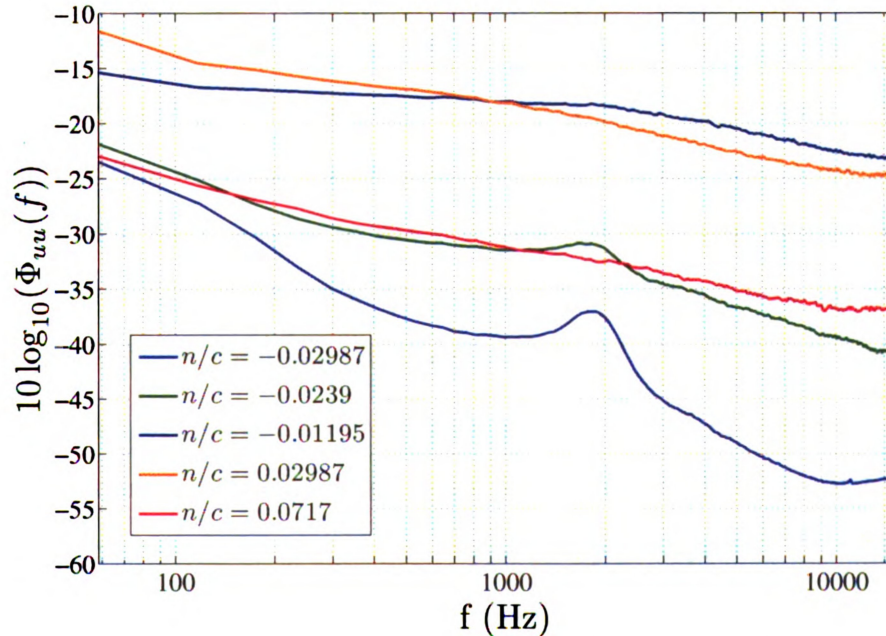


**Figure 5.74:** Streamwise velocity spectra in RCDB wake at  $z/c = 0.05$  ( $n = r\theta - r\theta_c$ ).

## 5.4 Comparison of the Rotating CD Blade (RCDB) and the CD Airfoil

### 5.4.1 Comparison of mean wake parameters

The Rotating CD Blade (RCDB) was designed specifically to be the rotating analog of the stationary CD airfoil. By carefully matching the parameters outlined in Sec. 3.1, a comparison of the detailed features of these two flow fields can be made. The mean streamwise profiles for these two flow fields are plotted in Fig. 5.75. The wake for the CD airfoil, on the left, can be seen to move in the  $-y/c$  direction, which is towards the suction side. This is consistent with the streamline patterns seen in the PIV data for the CD airfoil that is shown in Fig. 5.42. It is also consistent with the transverse ( $v$ ) velocity profiles shown in Fig. 5.37 showing that  $v < 0$  throughout the wake and the adjacent freestream. For the RCDB on the right of Fig. 5.75, it appears that the wake is moving to the right, in the  $+r\theta$  direction. This apparent discrepancy was partly explained by Fig. 5.62, where the orientation of the wake is visible in the PIV data in the rotating reference frame. The strong swirl of the wake is visible and the orientation of the wake relative to the  $\theta - z$  coordinate system can be seen. This orientation means that steps in the  $+z/c$  direction require nearly equal steps in the  $+r\theta$  direction to follow the wake centerline.

The HW data for the RCDB required the use of the  $r - \theta - z$  coordinate system to use the traverse in the AFRD facility. Also, for phase-averaged data, it is necessary for the rotating blade to be moved past a stationary HW probe. This requirement means that HW data will be collected in a plane that is perpendicular to the axis of rotation (i.e. constant  $z/c$ ). However, the uniform spatial resolution of PIV allow for the measurement plane to be rotated into coordinate systems that would otherwise be difficult in turbomachinery measurements. The limitation of planar PIV is that

the flow should be nominally 2-dimensional to limit the out of plane motions of the seeding particles (and the errors associated with these motions). This limitation is acceptable in the RCDB, where, as shown in Fig. 5.38, the spanwise/radial velocity,  $w$  is small relative to the streamwise and transverse velocities  $u$  and  $v$ . This allows for planar PIV data to be collected in the  $\theta$ - $z$  plane. This would be difficult in many conventional turbomachines, where the radial velocities can be substantial.

Figure 5.76 shows the PIV data in the relative reference frame cast into the coordinate system used in the CD airfoil experiments ( $x/c$ ,  $y/c$ ). When plotted in this coordinate system, it is evident that the wake is indeed deflecting towards the  $-y/c$  direction, consistent with the results from the stationary CD airfoil. However, at the downstream distance  $x/c \approx 0.7$  the wake appears to be “straightening out”. This idea is consistent with the HW data of Fig. 5.37 that show the  $v$  velocity is decreasing towards zero with downstream distance. The location of the wake centerline for the CD airfoil and the RCDB is shown in Fig. 5.77. These data show that the wake deflection for the CD airfoil has a consistent trajectory with downstream distance. The RCDB has a very similar initial trajectory; however, the wake deflection begins to decrease and the wake is moving in a straight line for locations where  $x/c > 0.65$ . This “straightening” out of the wake is the result of the operating condition of the AFRD facility. In order to meet the required flow rate at the required rotational speed (for the 3-blade version, which had the closest blade loading ( $C_p$ ) to the stationary airfoil), the AFRD facility had to be operated with a negative pressure rise across the inlet plane of the RCDB. Although this pressure rise was very small (-20 Pa) it was operating as a turbine. This negative pressure rise would normally cause the wake to deflect towards the suction side, and for the RCDB shape (highly cambered) it counteracts the strong pressure side deflection seen in the CD airfoil. This causes the RCDB blade wake to “straighten” from roughly  $x/c > 0.3$  onward.

The wake semi-width,  $L$ , is shown in Fig. 5.78. The wake of the RCDB is wider



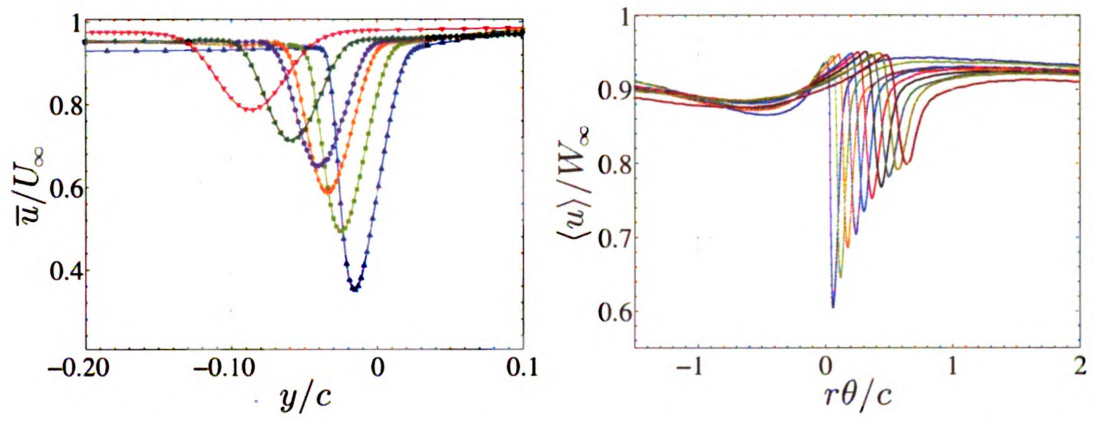


**Figure 5.75:** Streamwise velocity profiles. (left - CD airfoil, right - RCDB).

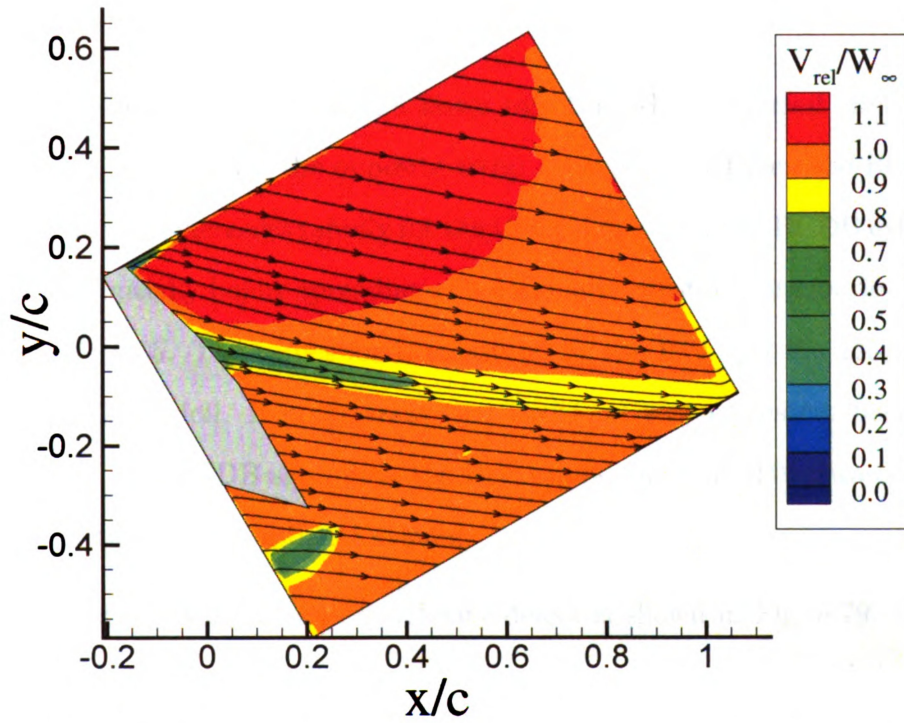


**Figure 5.76:** RCDB wake PIV data - relative velocity in  $(x/c, y/c)$  coordinates.



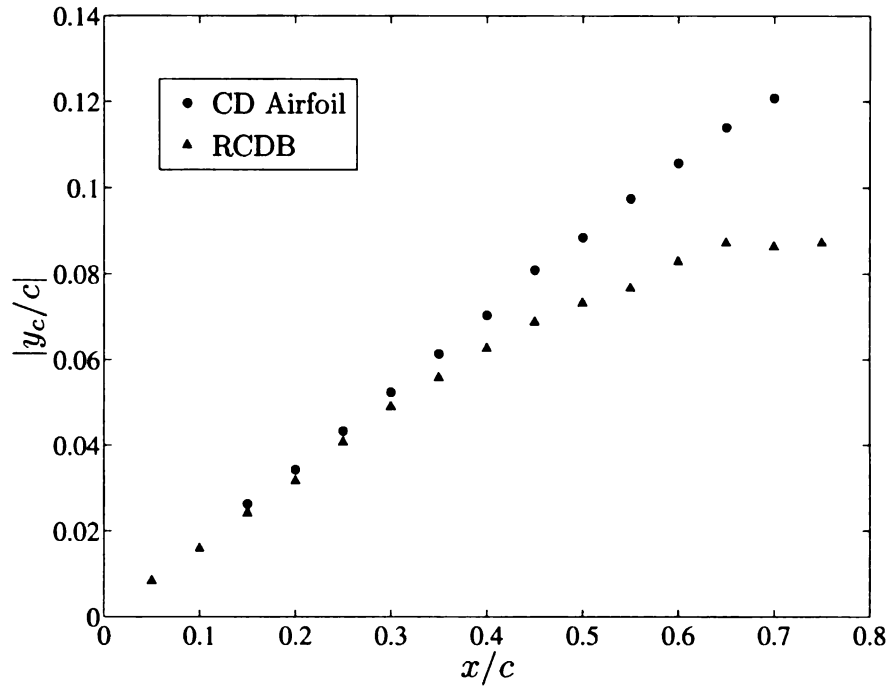


**Figure 5.77:** Location of the wake centerline for the CD and RCDB.

upstream and continues to spread at a faster rate than the CD airfoil. Between the locations  $0.05 \leq x/c \leq 0.15$ , the opposite trend is observed between the RCDB and CD airfoil. The wake increases rapidly for the CD airfoil, where the RCDB exhibits no wake spreading initially before spreading at a nominally constant rate for downstream locations  $x/c \geq 0.15$ . The values for  $L$  measured by the PIV and the 2X-probe are shown for the CD airfoil. It is apparent that these are very consistent between the two techniques. The RCDB show only the PIV values since the HW data could only be collected in the  $r - \theta$  coordinate system.

The decay of the wake centerline velocity defect is shown in Fig. 5.79. The centerline velocity defect is shown for the both the stationary CD airfoil and the RCDB, and these values are referenced to both the edge velocities on the pressure and suction side. The initial velocity defect is greater in the CD airfoil and it is evident that the wake is very symmetric. This decays to a value of 0.2 at the location  $x/c = 0.50$ ,

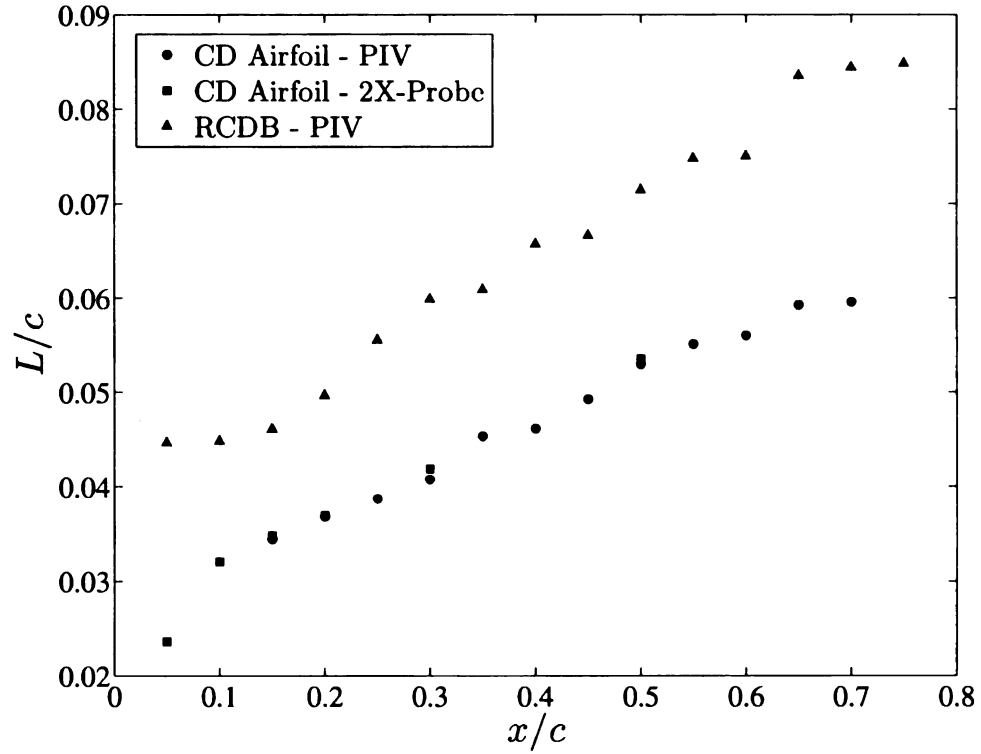


**Figure 5.78:** Wake semi-width for the RCDB and CD airfoil.

indicating that the centerline velocity has recovered to 80% of the edge velocity. This continues to a value of 17% at the farthest downstream location ( $x/c = 0.70$ ). The RCDB has a lower upstream centerline velocity defect and there is a slight initial asymmetry at this location ( $x/c = 0.15$ ). Different decay rates exist for the pressure side and suction side, causing additional asymmetry farther downstream ( $x/c = 0.75$ ). The suction side decay rate is approximately the same as for the CD airfoil, but the pressure side shows a more gradual decay. The asymmetry steadily increases with downstream distance. This shows that the Coriolis forces, shown to have a higher effect on the surface of the blade, continue to alter the turbulence structure in the wake, affecting the decay rate of the velocity defect.

The momentum thickness for the RCDB is shown in Fig. 5.80. The RCDB has a consistently higher momentum thickness, consistent with the wider wake width shown in Fig. 5.78. Both the RCDB and CD airfoil show a slightly decreasing  $\theta/c$ , which as

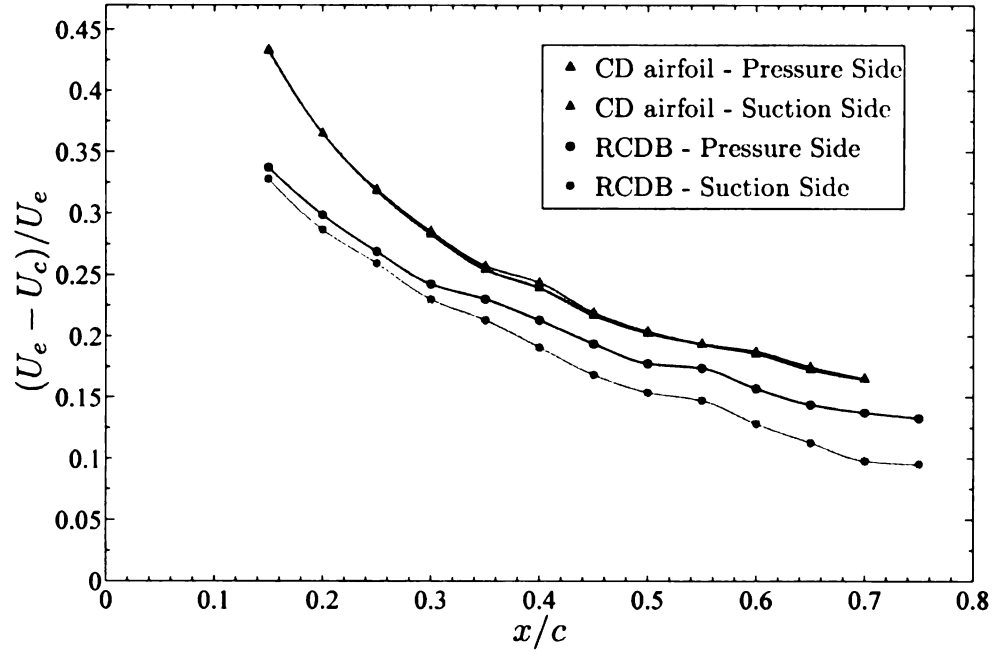


**Figure 5.79:** Decay of the wake centerline velocity defect for the CD airfoil and RCDB.

discussed above, indicates a slightly increasing  $U_e$ . The higher scatter in the RCDB data can be attributed to the difficulty in picking the  $U_e$  in the farther downstream locations, where the wake is increasingly asymmetric.

### 5.4.2 Comparison of turbulence parameters

The turbulence intensities in the wake of the RCDB show the trend  $T_w > T_v > T_u$  for the maximum values of each component in the upstream region. The wake of the CD airfoil exhibits the trend  $T_v > T_u > T_w$  at all locations throughout the wake. This much higher value of  $T_w$  as compared with the stationary CD airfoil can directly be attributed to the Coriolis forces, which act in the radial direction. The values for  $T_u$  and  $T_v$  in the CD airfoil are approximately the same, with the radial component being significantly higher. Downstream for the RCDB, the different decay rates show that  $T_u > T_v$ , but  $T_w$  remains the highest. These results are similar to those of

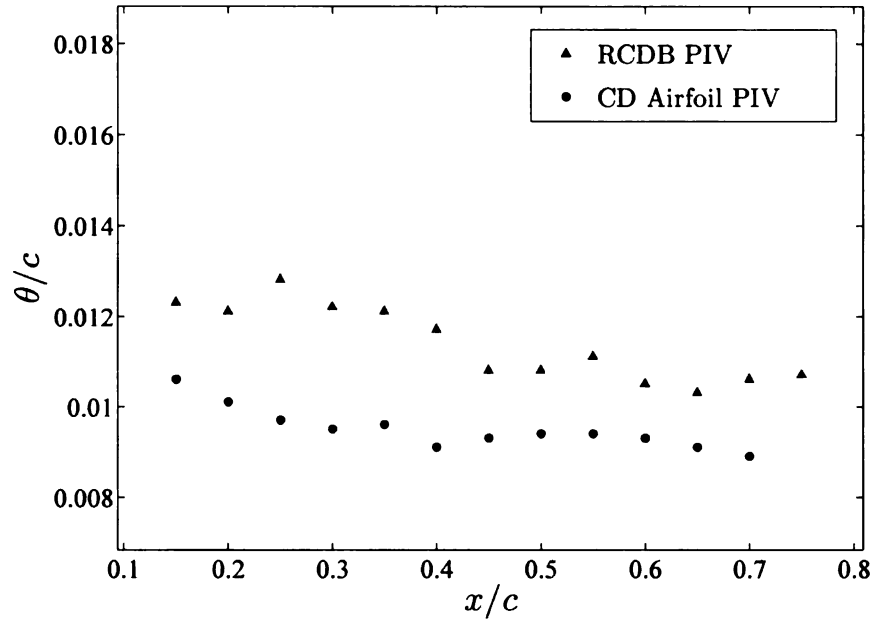


**Figure 5.80:** Momentum Thickness for the CD and RCDB.

Lakshminarayana & Reynolds (1980) who also found  $T_w > T_u$  throughout the wake, but they found that values of  $T_v > T_w$  at certain locations.

**Table 5.6:** Comparison of the peak turbulence intensities for the RCDB and CD airfoil

Turbulence Intensity Component	CD airfoil ( $x/c = 0.05$ )	RCDB ( $z/c = 0.05$ )
$T_u$	0.123	0.132
$T_v$	0.164	0.139
$T_w$	0.127	0.167

The Reynolds stress profiles show that the  $\overline{u'v'}$  (or  $\langle u'v' \rangle$  in the RCDB) component is the strongest. The other components  $\overline{u'w'}$  or  $\langle u'w' \rangle$  and  $\overline{v'w'}$  or  $\langle v'w' \rangle$  show high peak values in the near wake, but these decay quickly and are almost at the freestream value by a distance of  $\frac{1}{2}c$  downstream.

## 5.5 Comparison of the measurements from the 1X and 2X probes

### 5.5.1 Comparison of measured velocities: 1X and 2X

In this section, a comparison is made between the measurements collected using a conventional X-probe (1X) and the four sensor 2X-probe (2X). Measurements made with a conventional X-probe can only resolve two of the three velocity components (in a plane). As a result, the effect of unresolved (out-of-plane) velocities or binormal cooling effects are not accounted for in the X-probe measurements. This effect is described in detail in Zhao & Smits (2006) and the authors quantify its effects on the both mean flow and turbulent quantities collected in near-wall region of pipes and other boundary layers. The effect of unresolved velocity components on turbulent quantities has also been studied by Tutu & Chevray (1975); Hinze (1975); Cutler & Bradshaw (1991). Additionally, Ewing (2004) studied the effects of unresolved velocity components on one-dimensional velocity spectra and Shabbir *et al.* (1996) reported their effect for flows with turbulence intensity and low mean velocities. The effects of unresolved velocities in the wake of an airfoil are shown here through a detailed comparison of data collected for a 1X-probe and a 2X-probe. The 2X-probe has the distinct advantage of being able to resolve all three components of velocity; however, it is geometrically very similar to a 1X-probe and direct comparisons can be made between the two techniques.

Both the stationary CD airfoil and the rotating CD blade (RCDB) experiments had velocity surveys carried out at the same downstream locations in the wake. The 1X-probe data were used as a precursor to troubleshoot various parameters before using the 2X-probe. These parameters included the correct pitch and yaw orientations of the probe (i.e. positioning the HW probe so it was aligned with the mean flow)

and also determining the optimal locations to resolve the details of the wake while also spanning a sufficient distance (i.e. from the pressure side freestream to the suction side freestream). Since the 1X-probe is a relatively less expensive technique (lower processing time, lower calibration time, greater ease of use and less chance for calibration drift), it was more time effective to run several surveys with the 1X-probe and then use those results to determine the optimal experimental parameters for the 2X-probe. Additionally, the 1X-probe data provided a comparison against previous measurements that had been conducted on the same geometry (Moreau *et al.* (2006a) and other unpublished work).

Figure 5.81 shows the mean streamwise velocity ( $\bar{u}$ ) for the CD airfoil at various downstream locations that were measured with the 1X and 2X-probes. A distinct trend is observed in that the wake profiles measured with the 1X-probe show a higher streamwise velocity throughout the wake region. This difference is most pronounced in the region near the peak velocity deficit. These differences diminish in the outer region of the wake and they become very minimal in the freestream. This difference can be explained by recalling the results of Fig. 5.2 which showed the errors associated with bi-normal cooling effects. It is observed that a crossed-wire probe that is calibrated only along the pitch and yaw planes will resolve a lower angle for the measured velocity vector. This lower incident angle will result in a higher measured streamwise velocity, since the relationship between  $u$  and  $v$  and  $Q$  and  $\alpha$  are:

$$u = Q \cos(\alpha) \quad v = Q \sin(\alpha) \quad (5.11)$$

This effect will be most pronounced in regions where the flow is three-dimensional or in regions of high turbulence intensity. As seen in Fig. 5.38, the wake region has a high  $\bar{w}$  velocity. It also has the highest turbulent fluctuations, as shown in Figs. 5.43–5.45. This mean  $w$ , along with higher  $T_u$ ,  $T_v$ , and  $T_w$  will produce higher

bi-normal cooling effects on the 1X-probe. As expected, this difference decreases in the free-stream region adjacent to the wake. These out of plane errors are dramatically reduced for the 2X-probe, as seen in Fig. 5.7. Additionally, the bi-normal cooling also causes the  $Q$  measured by the 1X-probe to be erroneously higher. This erroneously higher  $Q$  combines with the erroneously lower  $\alpha$  to yield streamwise velocities,  $u$ , from which are higher (when measured with a 1X-probe) than those measured with the 2X-probe.

It is expected that if the  $u$  measured at a particular location is erroneously higher than expected (as the result of an  $\alpha$  that is too low), then by extension, the  $v$  should be smaller than expected. However, examining Eq. 5.11,  $v$  depends on the product of  $Q$  and  $\sin(\alpha)$ . Since  $Q$  is erroneously high and  $\alpha$  is erroneously low, the value of  $v$  will be higher or lower for the 1X-probe data depending on the magnitude of the  $Q$  and  $\sin(\alpha)$  terms. The data shown in Fig. 5.82 show that in the wake region, the  $\bar{v}$  measured by 1X-probe is approximately equal to the  $\bar{v}$  measured by the 2X-probe. However, in the adjacent freestream, the  $\bar{v}$  as measured by the 1X-probe is consistently lower. This result is counter-intuitive since the freestream region is where the two probes should show the best agreement (since the effects of bi-normal cooling are the smallest). This discrepancy can be explained by noting that two different calibration facilities, described in Chap. 4 and shown in Fig. 4.26 and Fig. 4.29, were used for the 1X and 2X calibrations. Although very precise techniques were used to position the probe in each facility, it is likely that a small bias error exists between the absolute probe positioning of each facility. Using the freestream data in Fig. 5.82, this bias error is estimated to be  $0.12^\circ$ . It can be further shown that a bias error is likely given that the trends on the pressure side and suction side are captured by each of the two techniques, with a very consistent offset observed throughout the entire freestream region. Given this offset in the freestream, the approximately equal values for  $\bar{v}$  in the wake region show that the erroneously higher  $Q$  measured by the

1X-probe has a greater magnitude than the erroneously lower  $\sin(\alpha)$  term.

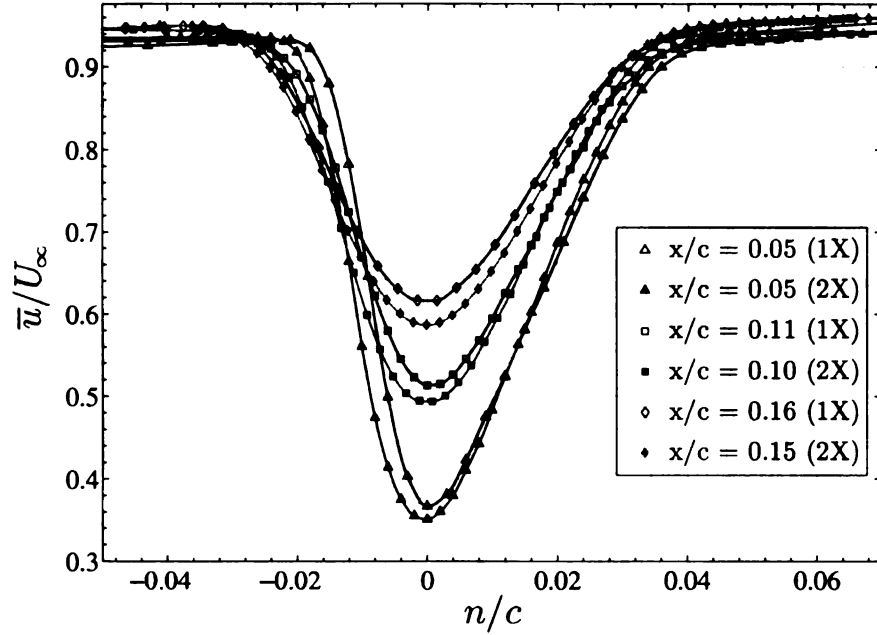


**Figure 5.81:** Streamwise velocity profiles for the CD airfoil measured by the 1X and 2X-probes ( $n = y - y_c$ ).

A comparison between the streamwise turbulence intensity ( $T_u$ ) measured with the 1X and 2X-probes is shown in Fig. 5.83. The data measured by both probes show very similar results throughout the entire wake region. Each dataset show the same salient features, specifically the peak value of  $T_u$  on the pressure side, a local minimum situated at  $n/c = 0$  and a second peak on the suction side. Also very comparable free-stream values are measured outside of the wake. Finally, a slightly higher value is measured by the X-probe, but this difference is within the uncertainty of the measurements.

The values of the transverse turbulence intensity ( $T_v$ ) measured by the 1X and 2X-probes are shown in Fig. 5.84. These data show a more substantial difference between the two measurement techniques. Overall, the same qualitative features are measured by each technique, but the relative heights of the two peaks (pressure and



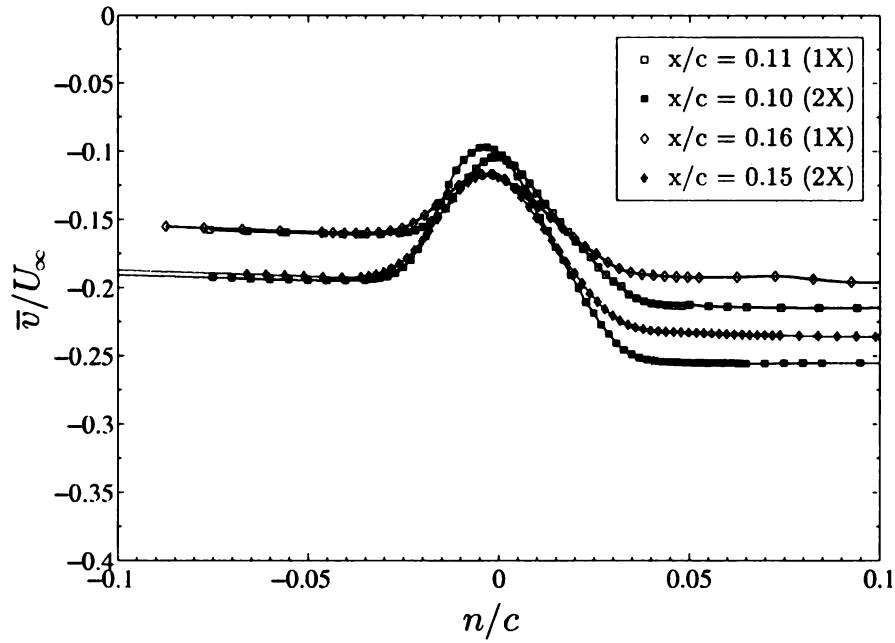


**Figure 5.82:** Transverse velocity profiles for the CD airfoil measured by the 1X and 2X-probes ( $n = y - y_c$ ).

suction side) and the levels are quite different. Also, the peak values measured by the 2X-probe are nearly 40% less than the values measured by the 1X-probe. The PIV data measured at the same location are also included and these show peak values that are even lower than the X-probe. It can be seen that the values at the edge of the wake (along with the gradients in these regions) are very similar. LES data taken from the paper of Moreau *et al.* (2006b) are also plotted. These data show values that are even higher than the 2X-probe.

As an additional diagnostic technique, the voltages from the horizontal X-array of the 2X-probe were processed using only the 1X-probe processing described in Sec. 4.4.1. This processing would produce the known errors shown in Fig. 5.7, but these results do not give the effect of a turbulent flow field, since these tests were carried out in the calibration facility (with minimal turbulence intensity). These data show levels that are lower than the results of the 2X-probe processing yet still higher

than the 1X-probe.

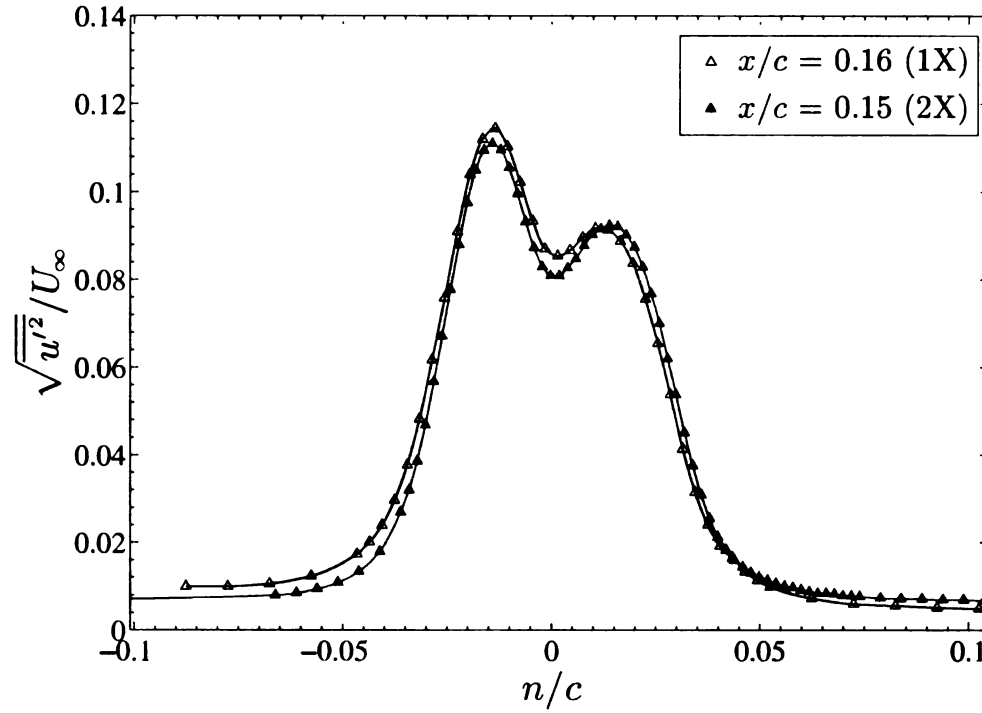


**Figure 5.83:** Streamwise turbulence intensity profiles for the CD airfoil measured by the 1X and 2X-probes ( $n = y - y_c$ ).

### 5.5.2 Uncertainty considerations: 1X and 2X

Estimates of the typical uncertainties for measured quantities are presented in this section. The typical sources of error associated with hot-wire anemometry are documented extensively by Bruun (1995) amongst others. Additionally, Burattini & Antonia (2005) reported the effects of different calibration schemes on turbulence statistics. The calibration methods for this study used the look-up table approach, so errors associated with analytical approximations were avoided. As Bruun (1995) notes, look-up table methods are affected by out-of-plane velocities (noted above in Sec. 5.5.1) and also interpolation errors caused by the finite number of points in the look-up table.

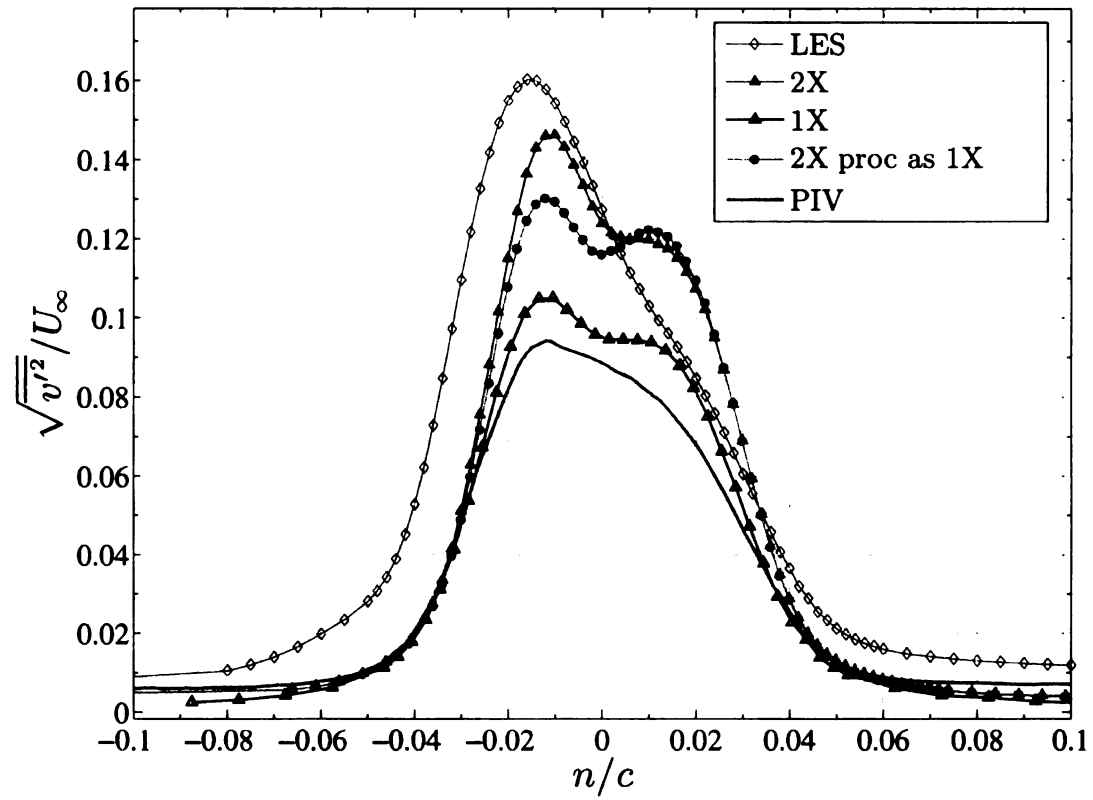


**Figure 5.84:** Streamwise turbulence intensity profiles for the CD airfoil measured by the 1X and 2X-probes ( $n = y - y_c$ ).

A more dominant source of error associated with measurements collected using 1X-probes and 2X-probes come from the calibration drift. Calibrations are collected before and after (pre-calibration and post-calibration) so the effect of calibration drift can be assessed. Several datasets were collected and discarded because of excessively large drift. The effects of drift are increasingly important for 2X-probes for two distinct reasons:

1. Four sensors are used instead of two. This increases the probability that one sensor will drift, which thereby alters the calibrated response of the probe.
2. The inability to perform full-calibrations regularly. Since these calibrations require a long time (nominally 4-5 hours to collect an 81 point calibration), the *pseudo-full calibration* approach described in Sec. 4.5.1 is used. This approach is shown to maintain its integrity as the time between the *full calibration* and the *pseudo-full calibration* increases (see Sec. 5.1.3). However, the uncertainty of the measurements increases over standard 1X-probe calibration techniques

Figure 5.85 shows the uncertainty of the  $\bar{u}/U_\infty$  data measured with both a 1X and 2X-probe. The symbols are the mean value between the velocities resulting from the pre-calibration and the velocities resulting from the post-calibration. The error bars indicate the upper and lower bounds from either the pre or post-calibration. These results show a higher uncertainty associated with the 2X-probe data compared with the 1X-probe data. Uncertainties as high as  $\approx 3\%$  (pre-post) were measured with the 2X-probe, whereas the maximum uncertainties from the 1X-probe were found to be  $\approx 2\%$ . Figure 5.85 also confirms that the systematic differences between the wake profiles measured with a 1X-probe and a 2X-probe (and described in detail in Sec. 5.5.1) are outside the uncertainty of the two techniques.

The uncertainty for the  $\bar{v}/U_\infty$  data are shown in Fig. 5.86. The higher uncertainties associated with the 2X-probe are shown by the longer error bars for those data as

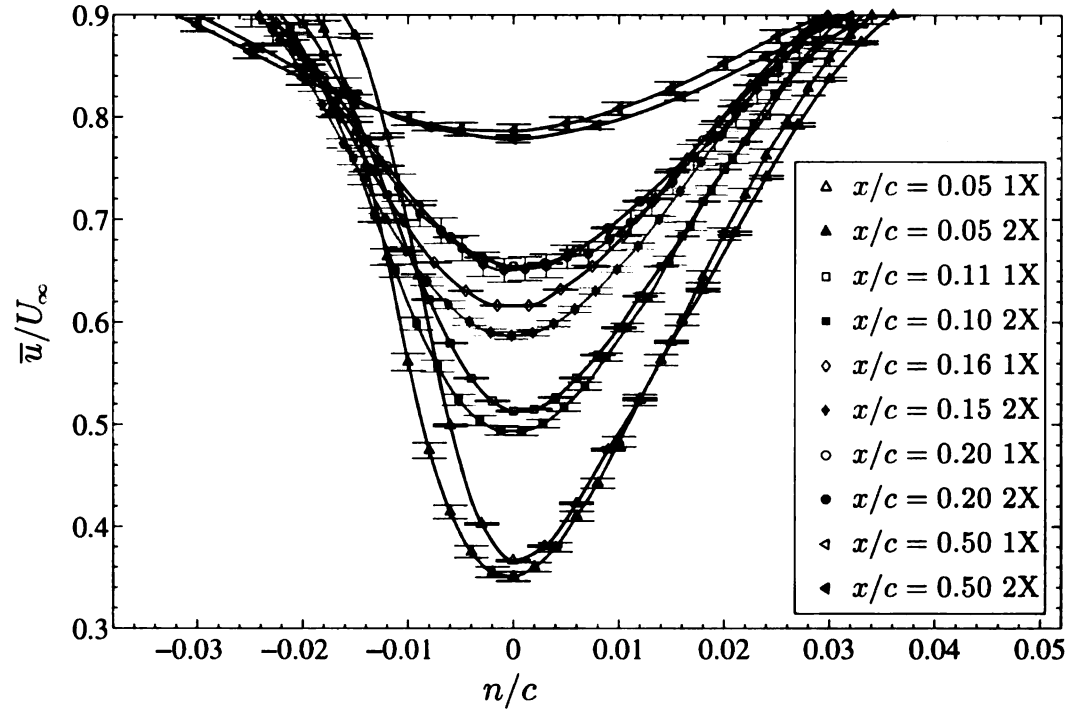


**Figure 5.85:** Effect of measurement uncertainties on  $\bar{u}$  data collected with a 1X and 2X-probe.

compared with the equivalent data measured using a 1X-probe. These data also show that the bias error estimated in Sec. 5.5.1 is much larger than the effect of uncertainties from the calibration drift. This bias error is the result of the differences absolute probe positioning between the 1X-probe and 2X-probe calibration facilities.

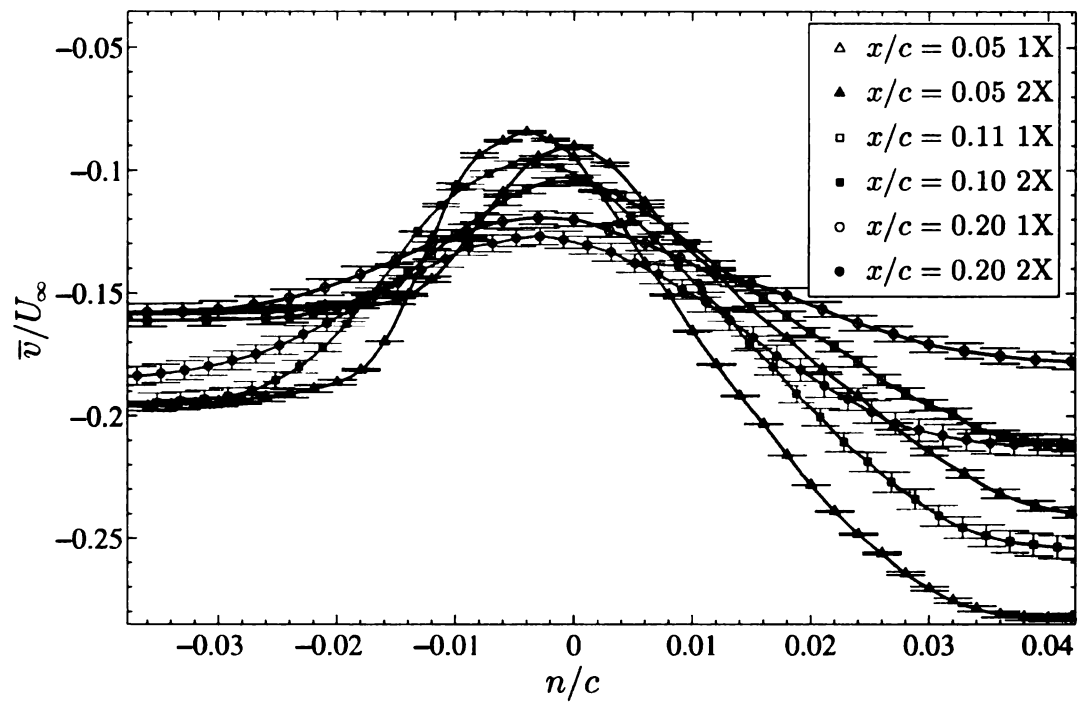


**Figure 5.86:** Effect of measurement uncertainties on  $\bar{v}$  data collected with a 1X and 2X-probe.

## Chapter 6

### Conclusions

A new calibration methodology and data reduction scheme have been developed for 4-sensor probes. The specific probe used in the research was the 2X-probe, designed and fabricated in the MSU-TSFL; however these techniques can be applied to any commercially available 4-sensor probe. These developments provide a comprehensive technique for 2X-probe calibration and data reduction. This technique has been compared with two of the best established techniques, Wittmer *et al.* (1998) and Döbbeling *et al.* (1990b), using an evaluation similar to that in the study conducted by Lavoie & Pollard (2003). It is shown that the new method provides superior accuracy in resolving the magnitude of the velocity vector as well as the pitch and yaw angles of the incident velocity vector. This new technique also has a substantially lower computational cost than the other two methods. This attribute makes it feasible for use in challenging experiments, such as the rotating CD blade (RCDB) experiment, which requires long time series of data to be properly phase-averaged with converged statistics. Comparisons have been made for wake data collected with a 2X-probe (using this calibration and processing technique) and data collected using a conventional 1X-probe (and standard calibration and processing techniques). Differences in the data collected using these two techniques have been found. These

differences are well-understood by examining the effects of the out-of-plane velocity component, which is also commonly referred to as binormal cooling. Since a conventional 1X-probe is only calibrated in a single plane, the binormal cooling effects create errors when using this probe in a highly three-dimensional flow field. These errors are greatly reduced by using the calibration and data reduction techniques described in Secs. 4.5.1 and 4.5.2 and verified in Sec. 5.1.

The open-jet experimental configuration shows distinct differences between an isolated airfoil configuration (Hah & Lakshminarayana, 1982) and a cascade configuration (Raj & Lakshminarayana, 1973). Although all three of these experiments used a different airfoil geometry, the angles of attack that were studied were similar and conditions at the trailing edge (attached boundary layers) were also similar. The CD airfoil has a laminar boundary layer on the pressure side that remains attached the entire length of the profile and a turbulent boundary layer on the suction side. The suction side boundary layer is much thicker than the pressure side boundary layer, as shown by velocity measurements at the trailing edge.

The wake of the CD airfoil exhibits the trend  $T_v > T_u > T_w$  for the maximum turbulence intensity values of each component. This result is different than the results of Hah & Lakshminarayana (1982), who found  $T_u > T_w > T_v$  for the maximum turbulence intensity values in the asymmetric wake of a symmetric airfoil (NACA 0012) with attached turbulent boundary layers leaving the trailing edge. This is also different than the findings of Raj & Lakshminarayana (1973), who found  $T_u > T_v$  (but only measured these two components) for a cascade study using cambered airfoils. The pressure side of the wake of the CD airfoil shows consistently higher values for turbulence intensities and Reynolds shear stress. Velocity spectra data indicate the existence of a Strouhal shedding phenomenon on the pressure side of the wake. These observations are confirmed through analysis of the instantaneous PIV data. This Strouhal shedding contributes to these higher fluctuations on the pressure side, and



the locations that show this distinct peak in the velocity spectra are consistent with the locations found in the PIV data.

The effects of streamline curvature are shown in the near-wake and wake of the stationary CD airfoil. These effects are most pronounced in the  $\overline{u'v'}$  component of the Reynolds stress. Here a unstable condition exists in the upstream region of the wake, which causes the region of  $-\overline{u'v'}$  to remain approximately the same size (in lateral extent) and have the same peak magnitude. This is in contrast to the normal evolution expect from the effects of turbulent diffusion. Farther downstream this effect is less pronounced and the unstable condition diminishes. Similarly, the pressure side shows the existence of a stable condition, although this effect is less pronounced since the streamline curvature (as seen in the  $\bar{v}$  profiles in the wake) is less pronounced on the pressure side.

The rotating CD blade (RCDB) experimental configuration has been conceived, designed, instrumented and validated. This experimental apparatus represents a modular turbomachine that can be used to study basic parameters of interest for the study of axial turbomachinery. This device can have a variable number of blades, from 2–8, that can be symmetrically installed. The blades in existence use the CD airfoil shape for their cross-section, and this shape remains constant (in both chord and camber) throughout the radial span. Additional blades, using sweep, variable camber and blade shape, or different tip geometries could be fabricated and incorporated into the existing facility. Given the large number of design complexities that exist in a modern turbomachine, the RCDB experiment provides a way to study, in a systematic manner, basic phenomenon associated with turbomachinery.

The RCDB experiment has been equipped so that it can make measurements in both the stationary and rotating reference frames. Measurement capabilities in the rotating reference frame include 22 pressure transducers, two thermocouples, 22 amplifiers for use with microphones (unsteady pressure), and two channels of hot-wire

anemometry. These channels can be measured in the rotating reference frame via a 64 channel analog-to-digital (A/D) board. The stationary and rotating reference frames are linked by a 20 channel slip ring. This allows for electrical power to be sent into the hub and also data to be retrieved (via USB 2.0) from the on-board A/D board. The slip ring also allows for the rotating reference frame A/D board to be synchronized with a stationary A/D board. This ensures that data measured in both reference frames can be evaluated together.

Direct comparisons between the stationary CD airfoil and the RCDB are non-trivial. This is largely a result of the different coordinate systems and the associated traversing equipment that is used in these experiments. A general Cartesian coordinate system, with the  $x$ -axis aligned with the upstream free-stream velocity, is typically used in airfoil studies. Studies of rotating machinery typically employ a polar coordinate system, with the  $z$ -axis aligned with the upstream free-stream velocity in *stationary* reference frame. Proper comparisons between the flow field in the CD airfoil and the RCDB require that the flow field of the RCDB be analyzed in the *rotating* reference frame. This poses challenges for making phase-averaged measurements by measuring the velocity past the moving blade with a stationary probe (necessarily taking surveys at  $z/c = \text{constant}$ ). Additionally, this poses challenges for the rotating reference frame hot-wire measurements, since the relative probe-to-blade spacing can most easily adjusted in the  $\theta$ -direction. The use of particle image velocimetry (PIV) was very effective for analyzing the mean flow features of the wake, since its good spatial resolution allowed for the wake to be analyzed in a Cartesian coordinate system (that was identical to the one used for the stationary CD airfoil). The wake of the RCDB is more energetic and also wider, as confirmed by measurements of the centerline velocity peak deficit, the wake half-width and the momentum thickness.

The turbulence intensities in the wake of the RCDB show the trend  $T_w > T_v > T_u$  for the maximum values of each component in the near-blade region. This much higher

value of  $T_w$  as compared with the stationary CD airfoil can directly be attributed to the Coriolis forces, which act in the radial direction. The values for  $T_u$  and  $T_v$  in the CD airfoil are approximately the same, with the radial component being significantly higher. Downstream for the RCDB, the different decay rates show that  $T_u > T_v$ , but  $T_w$  remains the highest. These results are similar to those of Lakshminarayana & Reynolds (1980) who also found  $T_w > T_u$  throughout the wake, but they found values of  $T_v > T_w$  at certain locations.

The Reynolds stress profiles show that the  $\overline{u'v'}$  (or  $\langle u'v' \rangle$  in the RCDB) component is the strongest. The other components ( $\overline{u'w'}$  or  $\langle u'w' \rangle$ ) and ( $\overline{v'w'}$  or  $\langle v'w' \rangle$ ) show high peak values in the near wake, but these decay quickly and are almost at the freestream value by a distance of  $\frac{1}{2}c$  downstream.

This research is the first study to compare, in detail, the wake of a cambered airfoil and an identical profile in a rotating environment. This comparison was carried out under conditions that were matched in both the stationary and rotating environments. Previous studies have had different blade shapes between the stationary and rotating environments or did not take extensive measures to keep the flow fields the same (nominally 2D). The results presented here provide detailed information on the effects of rotation in a low-speed, subsonic axial turbomachine. These data can be used as validation data for aeroacoustic models for rotating machinery or for advanced CFD simulations, such as a large eddy simulations (LES) on this geometry. The relative simplicity of the blade profile across the radial span makes this experiment of particular value for such modeling efforts.

Future studies can continue to utilize the highly modular capabilities of the RCDB experiment. The particular focus of this work was to provide a fundamental understanding of the effects of Coriolis forces on an airfoil. However, the RCDB experiment was designed to be a step up in complexity from a stationary airfoil, yet still far simpler than a modern axial turbomachine. The idea is that a simplified turbomachine

allows for the systematic study of basic physical phenomena, without being overwhelmed by a confluence of parameters. The midspan of the blade was the only region measured in this study since, under the right operating conditions, it was the rotating equivalent of the stationary CD airfoil. Future studies could focus on fundamental concerns for the axial turbomachinery community without needing to connect back to the stationary CD airfoil. One logical next step would be to examine the hub and tip regions on the RCDB. This would provide details on how operating conditions (blade loading, rotational speed, flow rate, etc.) affect the wake profile near an end wall. Additionally the effects of solidity could be examined in relation to the mean wake profiles and also the turbulent structure in the wake. This could be studied for any blade combination between 2-8 blades with the existing infrastructure. This study utilized 3 blades total, one of which had pressure taps mounted along the midspan of the blade. There are an additional 4 instrumented blades available (2 with pressure taps closer to the hub and another 2 with pressure taps closer to the tip).

Another logical progression for this work is to fully implement the RMP concept into the RCDB experiment. Presently pressure tubing exists on each of the 5 instrumented blades (discussed in the previous paragraph). The current configuration allows for the measurement of steady pressures; however, adding embedded microphones to the pressure taps as described in Sec. 4.1.3 will also allow for unsteady pressure measurements. Since the AFRD facility is not an aeroacoustic wind tunnel, signal contamination from the background noise could prove to be an issue. This problem has been addressed for unsteady pressure measurements on stationary surfaces (Naguib *et al.*, 1996). This method is of particular interest for the RCDB (and also the CD airfoil) since it is specifically intended for low Reynolds numbers flows where the noise signature overwhelms the low-level turbulent fluctuations. Unsteady surface pressure measurements and coherence at the trailing edge are of particular interest for aeroacoustic studies on both stationary and rotating blades, see Roger &

Moreau (2004).

Finally, the three-dimensional effects measured in the wake of the CD airfoil are of interest since it shows that a cambered airfoil (nominally two-dimensional) can induce strong three-dimensional effects on an upstream two-dimensional flow. This idea could be further studied by varying the length of the span (presently  $L \approx 3.7c$ ) to see if the endwall boundary conditions are inducing three-dimensional (spanwise velocities) features at the midspan. Additionally, velocity surveys on planes adjacent to the midspan could provide additional details on these three-dimensional features. The open-jet configuration of the CD airfoil experiment makes it quite feasible for PIV studies that utilize more camera views and provide additional velocity information (stereo PIV or tomographic PIV). This would provide additional information on the three-dimensional structure of the wake of the stationary CD airfoil. Tomographic PIV would be especially attractive since it would provide three-dimensional data on multiple planes and also yield multiple velocity gradients. The open-jet configuration would allow for the 4 camera view required for these experiments. The vibrations from the AFRD facility and the more limited optical access make tomographic PIV extremely difficult for the RCDB. In this case, 4-sensor hot-wire probes are still the best measurement tool for this experiment.

# Appendix A

## Effect of probe quality on data reduction methodologies for 4-wire probes

The effect of probe quality was discovered to have a profound effect on the results obtained for the 2X-probe. All of the hot-wire probes used in this study were custom fabricated in the Turbulent Shear Flows Laboratory (TFSL) at Michigan State University. The design of the 2X-probe is shown in Fig. 4.28. Both the 2X-probes and the 1X-probes have 1 mm long  $5\mu\text{m}$  diameter active length tungsten sensors. These are supported, at  $\pm 45^\circ$  from the probe axis, by copper-plated ends that are attached to the prongs, which are separated by 3 mm. The design of this probe follows on the recommendations of Strohl & Comte-Bellot (1973). The mounting of the sensors for the 2X-probe is quite difficult, since the fourth sensor must be “threaded” or passed under one of the existing sensors. This design allows the probe to be spatially compact and it differs slightly from other 4-wire probe designs (see the probe used in Lavoie & Pollard (2003) for an example of a commercially available probe, or reference the pyramidal geometry developed and well-utilized by Vukoslavcevic & Wallace (1981)).

The complexity of the wire mounting for the present design makes it susceptible to wires which are not necessarily straight. Figure A.1 shows this so-called “S-wire” defect. Validation tests conducted (following the methodologies described in Sec. 5.1)

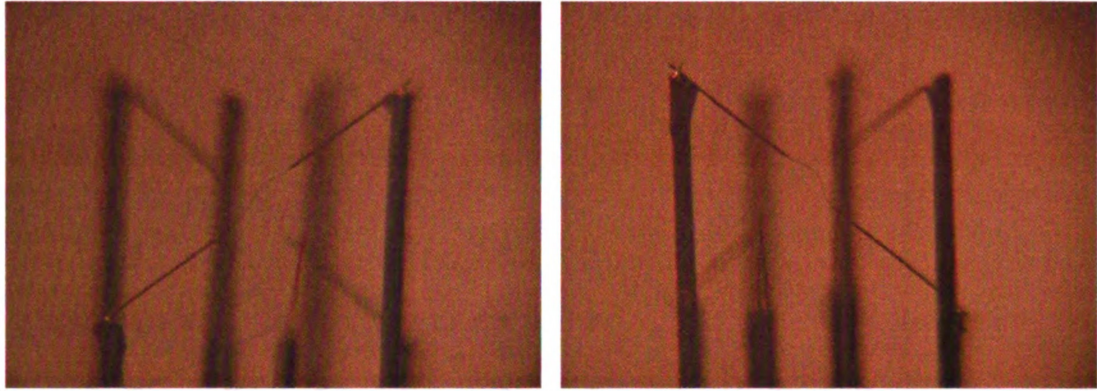


**Figure A.1:** Close-up view of 2X-probe with “S-wire” defect.

with this particular probe showed significant errors for probe orientations with simultaneous large pitch angles and large yaw angles. These results are shown in Fig. A.2 and the corner regions of this plot are the probe orientations with simultaneous large pitch and yaw angles. Additionally, it is apparent that there is significant asymmetry in these regions of higher error. Genin (2008) conducted a study where the probe was calibrated and used to process test data and then subsequently rotated  $90^\circ$  and the same process repeated. It was found that these regions of asymmetry tended to rotate with the probe orientation. This suggested that an intrinsic feature of a particular probe was affecting the results in the corner regions of the calibration domain.

The same probe (from Fig. A.1) was re-mounted with different sensors and a close-up view is shown in Fig. A.3. This figure shows the sensors mounted such that the active region is straighter, without significant “S-wire” defects. The results of validation tests carried out with this probe (and its re-mounted sensors) are shown in Fig. A.4. These data show significantly smaller errors for probe orientations with simultaneous large pitch and yaw angles (i.e. the corner regions).

These results are plotted side-by-side to show the striking contrast of identical



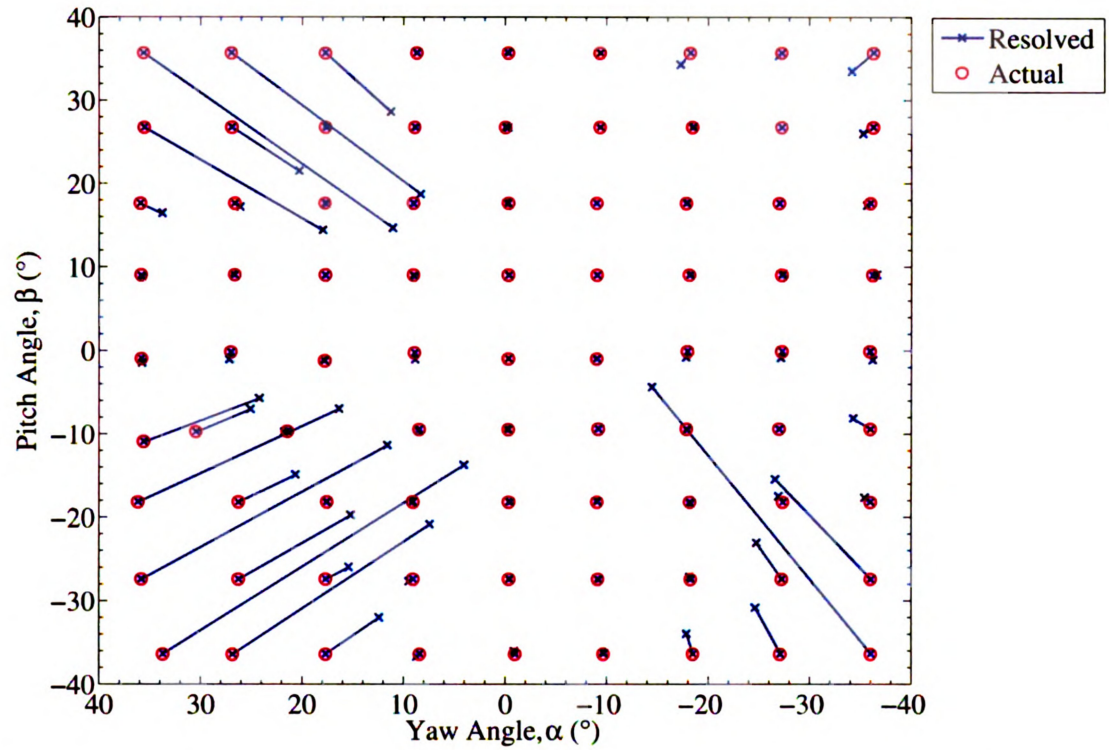


**Figure A.2:** Pitch-yaw results for test data processed with TSFL Spline Search using the probe shown in Fig. A.1.

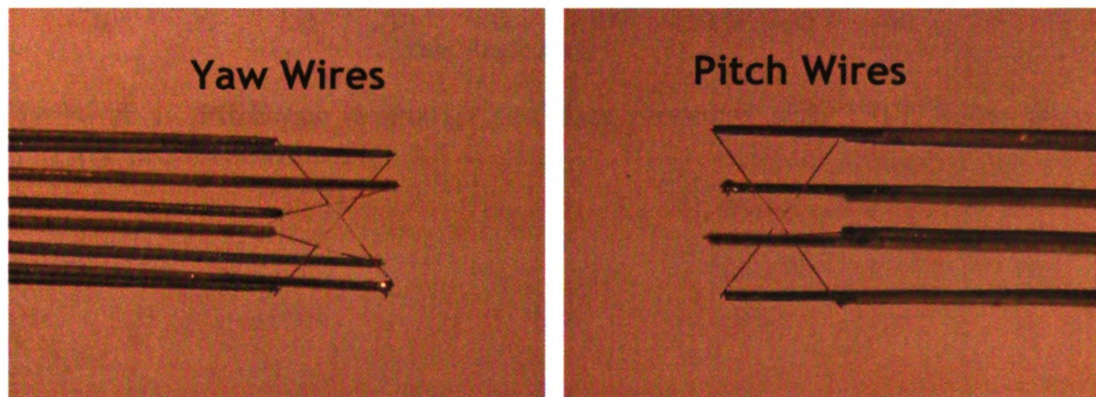


**Figure A.3:** Close-up view of 2X-probe with improved sensor mounting (note the absence of the “S-wire” defect seen in Fig. A.1)



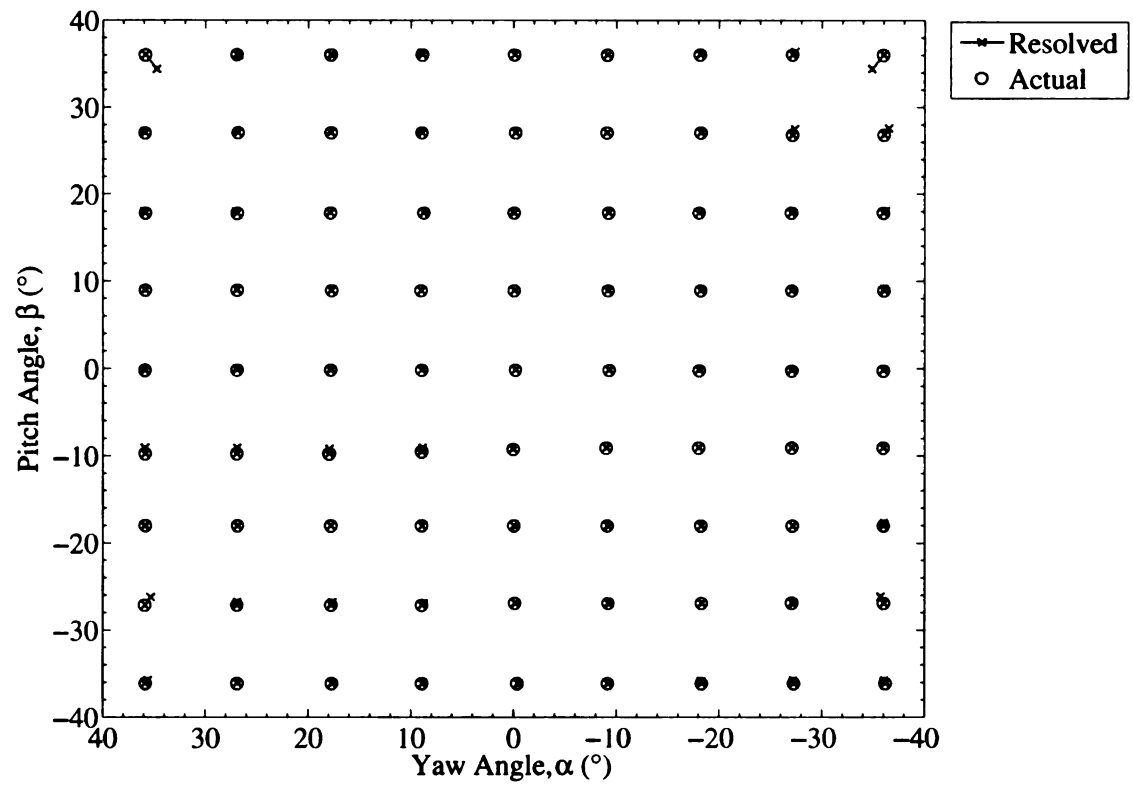


**Figure A.4:** Pitch-yaw results for test data processed with TSFL Spline Search using the probe shown in Fig. A.3

tests with the same probe (only with different sensor mountings). These data confirm the influence of mounting the sensors such that there is sufficient tension to ensure the wires are straight. Since other 4-wire probes (including those available commercially) have a similar relative configuration of their sensors, the calibration and data reduction methodologies developed in this dissertation are applicable to measurement campaigns. It is also suggested that these guidelines for sensor mounting will be similarly applicable.

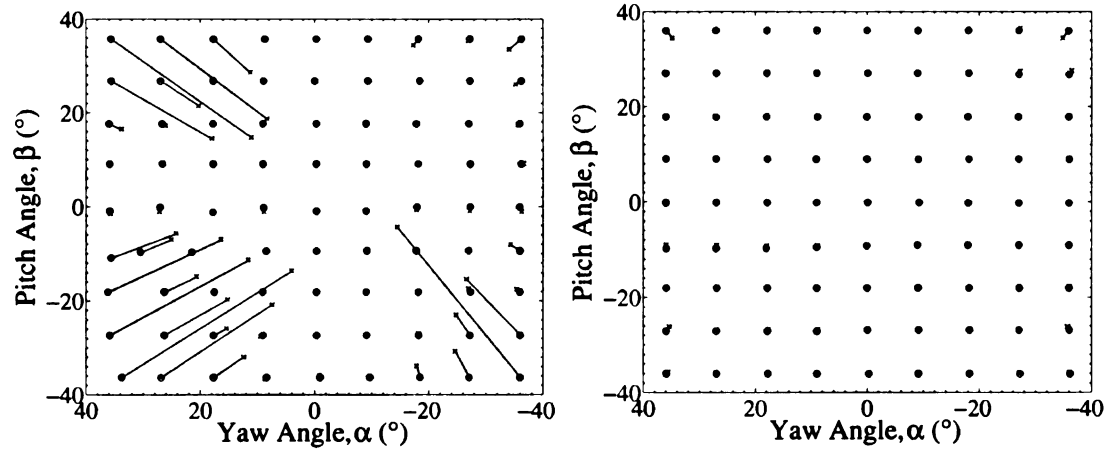


**Figure A.5:** Comparison of pitch-yaw results for test data processed with TSFL Spline Search. Left: Original wire-mounting, Right: Improved wire-mounting.

# References

- AMIET, RK. 1976. Noise due to turbulent flow past a trailing edge. *Journal of Sound and Vibration*, **47**, 387–393.
- ARBET, H., & BATAILLE, J. 1983. Noise generated by airfoil profiles placed in a uniform laminar flow. *Journal of Fluid Mechanics*, **134**, 33–47.
- BEHARELLE, S. 1999. *Influence du cisaillement transversal sur le d'evloppement d'une couche cisailée libre turbulente incompressible*. Ph.D. Thesis, Université de Poitiers.
- BLAKE, W.K. 1975 (Dec.). *A Statistical Description of Pressure and Velocity Fields at the Trailing Edges of a Flat Strut*. David W Taylor Naval Ship Research and Development Center, DTNSRD Rept. 4241, BETHESDA MD.
- BRADSHAW, P. 1973. *Effects of Streamline Curvature on Turbulent Flow*. AGAR-Dograph 169.
- BROOKS, TF, & HODGSON, TH. 1981. Trailing edge noise prediction from measured surface pressures. *Journal of Sound and Vibration*, **78**(1), 69–117.
- BROWNE, L.W.B., ANTONIA, R.A., & CHUA, L.P. 1988. Calibration of X-probes for turbulent flow measurements. *Experiments in Fluids*, **7**(3), 201–208.
- BRUUN, H. H. 1995. *Hot-wire Anemometry*. Oxford University Press.
- BURATTINI, P., & ANTONIA, R. A. 2005. The effect of different X-wire calibration schemes on some turbulence statistics. *Experiments in Fluids*, **38**(1), 80–89.
- CARO, S., & MOREAU, S. 2000. Aeroacoustic modeling of low pressure axial flow fans. *Pages 2000–2094 of: 6th AIAA/CEAS Aeroacoustics Conference, Lahaina, Hawaii*.
- CASPER, J., & FARASSAT, F. 2004. Broadband trailing edge noise predictions in the time domain. *Journal of Sound and Vibration*, **271**(1-2), 159–176.
- COLLIS, DC, & WILLIAMS, MJ. 1959. Two-dimensional convection from heated wires at low Reynolds numbers. *Journal of Fluid Mechanics*, **6**, 357–384.

- CUTLER, AD, & BRADSHAW, P. 1991. A crossed hot-wire technique for complex turbulent flows. *Experiments in Fluids*, **12**(1), 17–22.
- DE LABORDERIE, J. 2007. *Development of processing codes for hot-wire anemometry data*. Student Thesis, Ecole Catholique d'Arts et Métiers.
- DI SANTE, A., THEUNISSEN, R., & VAN DEN BRAEMBUSSCHE, R.A. 2008. A new facility for time-resolved PIV measurements in rotating channels. *Experiments in Fluids*, **44**(2), 179–188.
- DÖBBELING, K., LENZE, B., & LEUCKEL, W. 1990a. Basic considerations concerning the construction and usage of multiple hot-wire probes for highly turbulent three-dimensional flows. *Measurement Science and Technology*, **1**, 924–933.
- DÖBBELING, K., LENZE, B., & LEUCKEL, W. 1990b. Computer-aided calibration and measurements with a quadruple hotwire probe. *Experiments in Fluids*, **8**(5), 257–262.
- DUSEL, M. D. 2005. *An experimental investigation of the aerodynamic shroud with an off-highway engine cooling fan*. M.S. Thesis, Michigan State University.
- EWING, D. 2004. The effect of cross flow on one-dimensional spectra measured using hot wires. *Experiments in Fluids*, **36**(5), 675–684.
- FUKANO, T., & JANG, C.M. 2004. Tip clearance noise of axial flow fans operating at design and off-design condition. *Journal of Sound and Vibration*, **275**(3-5), 1027–1050.
- FUKANO, T., KODAMA, Y., & SENOO, Y. 1977. Noise generated by low pressure axial flow fans, I: Modeling of the turbulent noise. *Journal of Sound and Vibration*, **50**(1), 63–74.
- GELDER, T.F., SCHMIDT, J.F., SUDER, K.L., & HATHAWAY, M.D. 1987. *Design and performance of controlled-diffusion stator compared with original double-circular-arc stator*. Tech. rept. NASA.
- GENIN, J. 2008. *Development and validation of calibration and processing techniques for multi-wire hot-wire anemometry probes*. Student Thesis, Ecole Catholique d'Arts et Métiers.
- GLEGG, SAL, BAXTER, SM, & GLENDINNING, AG. 1987. The prediction of broadband noise from wind turbines. *Journal of sound and vibration*, **118**(2), 217–239.
- GODEFERD, FS, & LOLLINI, L. 1999. Direct numerical simulations of turbulence with confinement and rotation. *Journal of Fluid Mechanics*, **393**, 257–308.
- HAH, C., & LAKSHMINARAYANA, B. 1982. Measurement and Prediction of Mean Velocity and Turbulence Structure in the Near Wake of an Airfoil. *Journal of Fluid Mechanics*, **115**, 251–282.

- HINZE, J. O. 1975. *Turbulence*. McGraw-Hill, New York.
- HOARAU, C., BORÉE, J., LAUMONIER, J., & GERVAIS, Y. 2006. Analysis of the wall pressure trace downstream of a separated region using extended proper orthogonal decomposition. *Phys. Fluids*, **18**, 055107.
- HOWE, MS. 1978. A review of the theory of trailing edge noise. *Journal of Sound and Vibration*, **61**(3), 437–465.
- HUBBARD, H.H., & SHEPHERD, K.P. 1991. Aeroacoustics of large wind turbines. *The Journal of the Acoustical Society of America*, **89**, 2495.
- JOHNSON, R.W. 1998. *The handbook of fluid dynamics*. CRC Press, Boca Raton, FL (US).
- JOHNSTON, J.P. 1998. Effects of system rotation on turbulence structure: a review relevant to turbomachinery flows. *International Journal of Rotating Machinery*, **4**(2), 97–112.
- JOHNSTON, J.P., HALLEENT, R.M., & LEZIUS, D.K. 1972. Effects of spanwise rotation on the structure of two-dimensional fully developed turbulent channel flow. *Journal of Fluid Mechanics*, **56**(03), 533–557.
- KOYAMA, H., MASUDA, S., ARIGA, I., & WATANABE, I. 1979. Stabilizing and destabilizing effects of Coriolis force on two-dimensional laminar and turbulent boundary layers. *ASME Transactions Journal of Engineering Power*, **101**, 23–29.
- KOYAMA, H.S., KITAGAWA, K., & CHEN, K. 1995. Secondary flow and stability effects of Coriolis force on turbulent boundary layer in a rotating channel. *Pages 8.7–8.12 of: Symposium on Turbulent Shear Flows, 10th, Pennsylvania State Univ, University Park*.
- LAKSHMINARAYANA, B. 1996. *Fluid dynamics and heat transfer of turbomachinery*. John Wiley & Sons, Inc., New York.
- LAKSHMINARAYANA, B., & REYNOLDS, B. 1980. Turbulence characteristics in the near wake of a compressor rotor blade. *AIAA Journal*, **18**(11), 1354–1362.
- LAKSHMINARAYANA, B, GOVINDAN, TR, & REYNOLDS, B. 1982. Effects of rotation and blade incidence on properties of turbomachinery rotor wake. *AIAA Journal*, **20**(2), 245–253.
- LAVOIE, P., & POLLARD, A. 2003. Uncertainty analysis of four-sensor hot-wires and their data-reduction schemes used in the near field of a turbulent jet. *Exp Fluids*, **34**(3), 358–370.
- LISSAMAN, PBS. 1983. Low-Reynolds-number airfoils. *Annual Review of Fluid Mechanics*, **15**(1), 223–239.

- MACIEL, Y., & GLEYZES, C. 2000. Survey of multi-wire probe data processing techniques and efficient processing of four-wire probe velocity measurements in turbulent flows. *Experiments in Fluids*, **29**(1), 66–78.
- MANOHA, E., REDONNET, S., DELAHAY, C., KHELIL, SB, & GUILLEN, P. 2001. Numerical prediction of the unsteady flow and radiated noise from a 3D lifting airfoil. *In: AIAA Paper 2001-2133*.
- MARASLI, B., NGUYEN, P., & WALLACE, JM. 1993. A calibration technique for multiple-sensor hot-wire probes and its application to vorticity measurements in the wake of a circular cylinder. *Experiments in Fluids*, **15**(3), 209–218.
- MOREAU, S., & ROGER, M. 2005. Effect of Airfoil Aerodynamic Loading on Trailing-Edge Noise Sources. *AIAA Journal-American Institute of Aeronautics and Astronautics*, **43**(1), 41–52.
- MOREAU, S., & ROGER, M. 2007. Competing broadband noise mechanisms in low-speed axial fans. *AIAA journal*, **45**(1), 48.
- MOREAU, S., HENNER, M., IACCARINO, G., WANG, M., & ROGER, M. 2003. Analysis of flow conditions in freejet experiments for studying airfoil self-noise. *AIAA Journal*, **41**(10), 1895–1905.
- MOREAU, S., NEAL, D., & FOSS, J. 2006a. Hot-Wire Measurements Around a Controlled Diffusion Airfoil in an Open-Jet Anechoic Wind Tunnel. *Journal of Fluids Engineering*, **128**, 699.
- MOREAU, S., NEAL, D., KHALIGHI, Y., WANG, M., & IACCARINO, G. 2006b. Validation of unstructured-mesh LES of the trailing-edge flow and noise of a controlled-diffusion airfoil. *In: Studying Turbulence Using Numerical Simulation Databases - XI: Proceedings of the Summer Program 2006, Center for Turbulence Research, Stanford University*.
- MOREAU, S., HENNER, M., CASALINO, D., GULLBRAND, J., IACCARINO, G., & WANG, M. 2006c. Toward the prediction of low-speed fan noise. *In: Studying Turbulence Using Numerical Simulation Databases - XI: Proceedings of the Summer Program 2006, Center for Turbulence Research, Stanford University*.
- MORRIS, S.C., & FOSS, J.F. 2001. An Aerodynamic Shroud for Automotive Cooling Fans. *Journal of Fluids Engineering*, **123**, 287.
- MORRIS, S.C., & FOSS, J.F. 2003. Turbulent boundary layer to single-stream shear layer: the transition region. *Journal of Fluid Mechanics*, **494**, 187–221.
- MORRIS, S.C., NEAL, D.R., FOSS, J.F., & CLOUD, G.L. 2001. A moment-of-momentum flux mass air flow measurement device. *Measurement Science and Technology*, **12**(2), N9–N13.

- NAGUIB, AM, GRAVANTE, SP, & WARK, CE. 1996. Extraction of turbulent wall-pressure time-series using an optimal filtering scheme. *Experiments in Fluids*, **22**(1), 14–22.
- NEAL, D.R., & FOSS, J.F. 2007. The application of an aerodynamic shroud for axial ventilation fans. *Journal of Fluids Engineering*, **129**, 764.
- OBERAI, AA, ROKNALDIN, F., & HUGHES, T. 2002. Computation of trailing-edge noise due to turbulent flow over an airfoil. *AIAA journal*, **40**(11), 2206–2216.
- OVINK, R., LAMERS, A., VAN STEENHOVEN, AA, & HOEIJMAKERS, HWM. 2001. Correction for binormal velocity fluctuation. *Measurement Science and Technology*, **12**, 1208–1213.
- PARCHEN, R., HOFFMANS, R., GORDNER, A., BRAUN, KA, & VAN DER BORG, NJ. 1999. C., Dassen, M. & AGM 1999 Reduction of airfoil self-noise at low Mach number with a serrated trailing edge. *Pages 3433–3440 of: Sixth International Congress on Sound and Vibration, Copenhagen, Denmark.*
- PÉRENNÈS, S., & ROGER, M. 1998. Aerodynamic noise of a two-dimensional wing with high-lift devices. *Pages 772–782 of: AIAA/CEAS Aeroacoustics Conference, 4th(19th AIAA Aeroacoustics Conference), Toulouse, France.*
- RAJ, R., & LAKSHMINARAYANA, B. 1973. Characteristics of the wake behind a cascade of airfoils. *Journal of Fluid Mechanics*, **61**(Part 4), 707–730.
- RAJ, R., & LAKSHMINARAYANA, B. 1976. Three Dimensional Characteristics of Turbulent Wakes Behind Rotors of Axial Flow Turbomachinery. *ASME Journal of Engineering for Power*, **98**, 218–228.
- RAJ, R., & LUMLEY, J.L. 1978. A theoretical investigation on the structure of fan wakes. *Journal of Fluids Engineering*, **100**, 113–119.
- RAJAGOPALAN, S., ZHOU, T., & ANTONIA, RA. 1998. Three-component turbulence measurements using a four-wire probe. *Flow Measurement and Instrumentation*, **9**(4), 211–216.
- RAVINDRANATH, A., & LAKSHMINARAYANA, B. 1980. Mean velocity and decay characteristics of the near- and far-wake of a compressor rotor blade of moderate loading. *Journal of Engineering for Power*, **102**, 535–548.
- RAVINDRANATH, A., & LAKSHMINARAYANA, B. 1981. Structure and decay characteristics of turbulence in the near- and far-wake of a moderately loaded compressor rotor-blade. *Journal of Engineering for Power*, **103**, 131–140.
- REYNOLDS, B., LAKSHMINARAYANA, B., & RAVINDRANATH, A. 1980. Characteristics of the Near Wake of a Compressor of a Fan Rotor Blade. *AIAA Journal*, **17**, 959–967.

- ROGER, M., & MOREAU, S. 2004. Broadband self-noise from loaded fan blades. *AIAA journal*, **42**(3), 536–544.
- ROTHER, P.H., & JOHNSTON, J.P. 1979. Free shear layer behavior in rotating systems. *Journal of Fluids Engineering, Trans. ASME*, **101**, 117–120.
- ROZENBERG, Y. 2007. *Modélisation analytique du bruit aérodynamique à large band des machines tournantes: utilisation du calculs moyennés du mécanique des fluides*. Ph.D. Thesis, Ecole Centrale de Lyon.
- SCHLINKER, R.H., & AMIET, R.K. 1981. Helicopter rotor trailing edge noise. In: *AIAA, Astrodynamics Specialist Conference*.
- SHABBIR, A., BEUTHERT, P.D., & GEORGE, W.K. 1996. X-wire response in turbulent flows of high-intensity turbulence and low mean velocities. *Experimental Thermal and Fluid Science*, **12**(1), 52–56.
- SHARLAND, I.J. 1964. Sources of noise in axial flow fans. *Journal of Sound and Vibration*, **1**(3), 302–322.
- SINGER, B.A., LOCKARD, D.P., BRENTNER, K.S., KHORRAMI, M.R., BERKMAN, M.E., & CHOUDHARI, M. 2000. Computational aeroacoustic analysis of slat trailing-edge flow. *AIAA journal*, **38**(9), 1558–1558.
- STANISLAS, M., OKAMOTO, K., KÄHLER, C.J., WESTERWEEL, J., & SCARANO, F. 2008. Main results of the third international PIV challenge. *Experiments in Fluids*, **45**(1), 27–71.
- STROHL, A., & COMTE-BELLOT, G. 1973. Aerodynamic effects due to configuration of X-wire anemometers. (*American Society of Mechanical Engineers, 1973.*) *ASME, Transactions, Series E- Journal of Applied Mechanics*, **40**, 661–666.
- TROPEA, C., YARIN, A.L., & FOSS, J.F. 2007. *Springer handbook of experimental fluid mechanics*. Springer Verlag.
- TUTU, N.K., & CHEVRAY, R. 1975. Cross-wire anemometry in high intensity turbulence. *Journal of Fluid Mechanics*, **71**(Pt 4), 785–801.
- VUKOSLAVCEVIC, P., & WALLACE, J.M. 1981. Influence of velocity gradients on measurements of velocity and streamwise vorticity with hot-wire X-array probes. *Review of Scientific Instruments*, **52**(6), 869–879.
- WANG, M., & MOIN, P. 2000. Computation of trailing-edge flow and noise using large-eddy simulation. *AIAA journal*, **38**(12), 2201–2209.
- WATMUFF, J.H., WITT, H.T., & JOUBERT, P.N. 1985. Developing turbulent boundary layers with system rotation. *Journal of Fluid Mechanics*, **157**, 405–448.



- WILSON, D. G., & KORAKIANITIS, T. 1998. *The Design of High-Efficiency Turbo-machinery and Gas Turbines*. Prentice Hall.
- WITT, HT, & JOUBERT, PN. 1985. Effect of rotation on a turbulent wake. *Page 21 of: 5th Symposium on Turbulent Shear Flows, Ithaca, NY, August 7-9, 1985, Proceedings (A86-30201 13-34). University Park, PA, Pennsylvania State University, 1985, p. 21.25-21.30.*
- WITTMER, KS, DEVENPORT, WJ, & ZSOLDOS, JS. 1998. A four-sensor hot-wire probe system for three-component velocity measurement. *Experiments in Fluids*, **24**(5), 416–423.
- WRIGHT, SE. 1976. The acoustic spectrum of axial flow machines. *Journal of Sound and Vibration*, **45**(2), 165–223.
- ZHAO, R., & SMITS, A.J. 2006. Binormal cooling errors in crossed hot-wire measurements. *Experiments in Fluids*, **40**(2), 212–217.
- ZHOU, Q., & JOSEPH, P. 2007. A frequency domain numerical method for airfoil broadband self-noise prediction. *Journal of Sound and Vibration*, **299**(3), 504–519.
- ZHOU, Q., & JOSEPH, RF. 2006. Frequency-Domain Method for Rotor Self-Noise Prediction. *AIAA Journal*, **44**(6), 1197–1206.



MICHIGAN STATE UNIVERSITY LIBRARIES



3 1293 03220 8682